Bismuth Halide Perovskites: Tuning the Optoelectronic Properties Using Functional Organic Cations

By

Johnpaul K. P.

10CC16A39003

A thesis submitted to the
Academy of Scientific and Innovative Research
for the award of the degree of
DOCTOR OF PHILOSOPHY
in
SCIENCE

Under the supervision of
Dr. Vijayakumar Chakkooth

**CSIR-National Institute for Interdisciplinary
Science and Technology (CSIR-NIIST),
Thiruvananthapuram – 695 019**

Academy of Scientific and Innovative Research
AcSIR Headquarters, CSIR-HRDC campus
Sector 19, Kamla Nehru Nagar,
Ghaziabad, Uttar Pradesh – 201 002, India

July 2021

CSIR-National Institute for Interdisciplinary Science and Technology (NIIST)
Council of Scientific and Industrial Research, Thiruvananthapuram – 695 019, INDIA

Dr. Vijayakumar Chakkooth, PhD

Principal Scientist, Photosciences and Photonics, Chemical Sciences and Technology Division
Associate Professor, Academy of Scientific and Innovative Research (AcSIR)
Tel: +91-471-2515-484 (O) +91-9447-835-815 (M); E-mail: cvijayakumar@niist.res.in

July 02, 2021

CERTIFICATE

This is to certify that the work incorporated in this Ph.D. thesis entitled, *"Bismuth Halide Perovskites: Tuning the Optoelectronic Properties Using Functional Organic Cations"*, submitted by *Mr. Johnpaul K. P.* to the Academy of Scientific and Innovative Research (AcSIR) in fulfilment of the requirements for the award of the Degree of *Doctor of Philosophy in Sciences*, embodies original research work carried-out by the student. We further certify that this work has not been submitted to any other University or Institution in part or full for the award of any degree or diploma. Research materials obtained from other sources and used in this research work have been duly acknowledged in the thesis. Images, illustrations, figures, tables etc., used in the thesis from other sources, have also been duly cited and acknowledged.
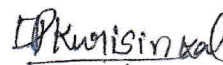
Dr. Vijayakumar C.

(Thesis Supervisor)

Johnpaul K. P.

STATEMENTS OF ACADEMIC INTEGRITY

I **Johnpaul K. P.**, a Ph.D. student of the Academy of Scientific and Innovative Research (AcSIR) with Registration No. 10CC16A39003 hereby undertake that, the thesis entitled *"Bismuth Halide Perovskites: Tuning the Optoelectronic Properties Using Functional Organic Cations"* has been prepared by me and that the document reports original work carried out by me and is free of any plagiarism in compliance with the UGC Regulations on *"Promotion of Academic Integrity and Prevention of Plagiarism in Higher Educational Institutions (2018)"* and the CSIR Guidelines for *"Ethics in Research and in Governance (2020)".*

Johnpaul K. P.

July 02, 2021

Thiruvananthapuram

It is hereby certified that the work done by the student, under my supervision, is plagiarism-free in accordance with the UGC Regulations on *"Promotion of Academic Integrity and Prevention of Plagiarism in Higher Educational Institutions (2018)"* and the CSIR Guidelines for *"Ethics in Research and in Governance (2020)".*
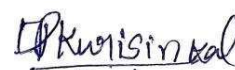
Dr. Vijayakumar C.

July 02, 2021

Thiruvananthapuram

DECLARATION

I hereby declare that the matter embodied in the Ph.D. thesis entitled: "**Bismuth Halide Perovskites: Tuning the Optoelectronic Properties Using Functional Organic Cations**" is the result of an independent work carried out by me at the Photosciences and Photonics Section, Chemical Sciences and Technology Division of the CSIR-National Institute for Interdisciplinary Science and Technology (CSIR-NIIST), Thiruvananthapuram, under the supervision of Dr. Vijayakumar C. and the same has not been submitted elsewhere for any other degree or diploma.

In keeping with the general practice of reporting scientific observations, research materials obtained from other investigations has been duly cited and acknowledged in the thesis.

Johnpaul K. P.

Thiruvananthapuram

July 02, 2021

ACKNOWLEDGEMENTS

CONTENTS

PREFACE

Lead-free Bi-based perovskites are currently receiving intense research interest for optoelectronic device applications due to their less toxicity and better moisture stability compared to lead-based analogues. Bismuth-based perovskites are reported to be suitable for solar cells, photodetectors, X-ray detectors, and memory device applications. Their superior photophysical properties such as high molar extinction coefficient, defect tolerance, and tunable optical bandgap are underpinned by the presence of ns^2 electrons at the Bi-site. Importantly, the optical and electronic properties of these materials can be easily tuned by manipulating the connectivity of inorganic units as well as via varying the organic spacer cations. The current thesis makes an effort to shed insights to disentangle the intriguing optoelectronic properties of these wondrous materials. Moreover, the potential perovskite candidates were tested for their utility in various device applications.

The thesis is organized into four chapters. The first Chapter gives a comprehensive overview of lead-free perovskite materials with a special emphasize on Bi-based perovskites and their applications. In Chapter 2, we discuss about the quantum and dielectric confinement effects in Bi-based zero-dimensional perovskite materials, (1,3-propanediammonium)$_2$Bi$_2$I$_{10}$·2H$_2$O (PDBI) and (benzylammonium)$_3$Bi$_2$I$_9$ (BBI), respectively. Single crystal XRD (SCXRD) analysis revealed that the PDBI featured a quantum-well crystal structure with orderly arranged Bi$_2$I$_{10}^{4-}$ inorganic clusters partitioned by propanediammonium cations. The short inorganic cluster separation enabled efficient charge transport in PDBI thin films even at a low bias voltage (1 V). The appreciably good on/off ratio (2.1) and responsivity (1.14 mA/W) of PDBI

photodetector devices were ascribed to its weak quantum confinement. In the next part of this chapter, we have attempted to circumvent the dielectric confinement in (methylammonium)$_3$Bi$_2$I$_9$ (MBI) perovskite by chemically substituting methylammonium with a more polarizable benzylammonium. This new perovskite material (benzylammonium)$_3$Bi$_2$I$_9$ (BBI) exhibited high photoconductivity compared to its congener MBI. The photoconductivity enhancement in BBI is stemmed from the efficient exciton screening by the dielectric benzylammonium cation.

In Chapter 3, we have reported a one-dimensional perovskite material (naphthalimide ethylammonium)$_2$BiI$_5$ (NBI) featuring anisotropic photoconductivity. Importantly, this material exhibited a long free charge carrier lifetime of 18 ms. Density functional theory (DFT) calculations suggested that Type-IIa heterojunction at the organic-inorganic interface of NBI is responsible for the long carrier lifetime. Followed by this report, we have studied the effect of self-assembled π-conjugated organic spacer cations on the structure and optoelectronic properties of zero-dimensional perovskites, (biphenyl bis(methylammonium)$_{1.5}$BiI$_6$.2H$_2$O (BPBI) and naphthalene diimide bis(ethylammonium)$_{1.5}$BiI$_6$.2H$_2$O (NDBI). NDBI showed extended visible-spectral response and superior photoconductivity compared to that of BPBI. SCXRD, Raman spectroscopy, and DFT calculations unambiguously proved that the band edge contribution of naphthalimide cations is underpinned by their excellent photophysical properties.

In Chapter 4, we have evaluated the utility of the zero-dimensional perovskite, (CH$_3$NH$_3$)$_3$Bi$_2$I$_9$ for electrochemical double layer capacitor (EDLC) application. The

capacitor device exhibited a low series resistance (R_S = 21 Ω) and charge transfer resistance (R_{CT} = 50 Ω). The fabricated EDLC delivered a maximum areal capacitance of 5.5 mF cm^{-2} at a scan rate of 5 mV s^{-1}. The device retained 84.8% of its initial capacitance even after 10,000 galvanostatic charge-discharge cycles.

LIST OF ABBREVIATIONS

1. Å - Angstrom

2. AFM - Atomic force microscopy

3. CBM - Conduction band minimum

4. c-Si - Crystalline silicon

5. CT - Charge transfer

6. CIGS - $Cu(In,Ga)Se_2$

7. CV - Cyclic voltammetry

8. DFT - Density functional theory

9. DMF - *N,N*-Dimethyl formamide

10. DOS - Density of states

11. DSC - Differential scanning calorimetry

12. °C - Degree Celsius

13. EIS - Electrochemical impedance spectroscopy

14. *et al.* - *Et allii/alia*

15. *etc.* - Et cetera

16. eV - Electron volt

17. FFT - Fast Fourier transform

18. FTIR - Fourier-transform infrared spectroscopy

19. FTO - Fluorine tin oxide

20. FPTRMC- Flash photolysis time resolved microwave conductivity

21. HI – Hydroiodic acid

22. µs - Microsecond

23. mg - Milligram

24. mL - Milliliter

25. mmol - Millimole

26. ms - Millisecond

27. nm - Nanometer

28. NMR - Nuclear magnetic resonance

29. PDOS - Partial density of states

30. PL - Photoluminescence

31. PLQY - Photoluminescence quantum yield

32. PV - Photovoltaic

33. R_s - Solution resistance

34. R_{CT} - Charge transfer resistance

35. SEM - Scanning electron microscopy

36. SCXRD - Single crystal XRD

37. TEM - Tunneling electron microscopy

38. TGA - Thermo gravimetric analysis

39. UV - Ultraviolet

40. V - Voltage

41. VBM - Valence band maximum

42. XPS - X-ray photoelectron spectroscopy

43. XRD - X-ray diffraction

Chapter 1

An Overview of Halide Perovskites: Crystal Structure, Optoelectronic Properties, and Applications

1.1. Abstract

Organometal halide perovskites captured significant research attention owing to their excellent intrinsic properties such as long charge carrier diffusion length, high carrier mobility, low exciton binding energy, defect tolerance, high absorption coefficient, tunable optical bandgap, and low-temperature solution processability. These properties enabled a widespread application of these materials in various fields such as solar cells, photodetectors, memory devices, light-emitting diodes, supercapacitors, Li-ion batteries, and so on. The state-of-the-art performing perovskite materials are based on Pb^{2+} metal ions. The toxicity and instability issues associated with these materials restricted their commercial applications. To address these issues, significant research has been devoted to lead-free perovskite materials. Interestingly, Bi-based perovskites exhibited excellent moisture and chemical stability compared to Sn^{2+} and Ge^{2+} perovskites and featured appreciable semiconducting properties, ideal for optoelectronic applications. This chapter provides an overview of the crystal structure, optoelectronic properties, and applications of halide perovskites, with a particular emphasis on bismuth-based perovskite structures reported to date.

1.2. Introduction

1.2.1. History of metal halide perovskites

The word perovskite was coined to name the naturally occurring mineral $CaTiO_3$, which was discovered in 1839 by German mineralogist Gustav Rose.[1] The name was given to this material in honor of a renowned Russian mineralogist Lev A. Perovski. Any material isostructural to that of $CaTiO_3$ is termed as a perovskite. The most explored metal oxide perovskites are $BaTiO_3$, $PbTiO_3$, $BiFeO_3$, $SrTiO_3$. Even though some of these materials exhibited photovoltaic properties due to their ferroelectric polarization, the wider optical bandgap limited their applications in photovoltaics. However, these metal oxide perovskites are widely used for ferroelectric, piezoelectric, pyroelectric, and dielectric applications.[2] The substitution of oxide anions in the perovskite structure with halides resulted in a new class of materials, *viz.* halide perovskites. A large variety of fully inorganic and organic-inorganic hybrid metal halide perovskites have been reported over the years.

The first all-inorganic perovskite materials, $CsPbCl_3$ and $CsPbBr_3$, were characterized by the Danish researcher C. K. Møller.[3] The simple solution processability of these materials inspired the researchers to replace the Cs with other organic and inorganic cations. Weber replaced the Cs with methylammonium cation and synthesized the first set of hybrid halide perovskites, $CH_3NH_3MX_3$ (M = Pb, Sn, X = I, Br).[4] Followed by these reports, Mitzi incorporated bulkier organic cations based on thiophenes into the perovskite crystal structure, which resulted in the formation of

layered perovskite materials.[5] Unlike metal oxide perovskites, these halide perovskites have excellent semiconducting properties such as long electron and hole diffusion length, high carrier mobility, weakly bound excitons, etc. and hence are suitable for photovoltaic (PV) applications.[6-10] In 2009, Miyasaka *et al.* introduced $CH_3NH_3PbI_3$ as the photosensitizer in dye-sensitized solar cell architecture, and the device exhibited a decent power conversion efficiency (PCE) of 3.8%.[11] However, the PCE was dropped immediately due to the dissolution of the perovskite in the liquid electrolyte. The efficiency of the perovskite solar cell was further improved to 6.5% by Park *et al.* by increasing the concentration of the perovskite ink.[12] Snaith and coworkers replaced the conventional liquid electrolyte and used a solid organic hole transporting material (HTM), spiro-OMeTAD (2,2′,7,7′-tetrakis(*N*,*N*-dimethoxyphenylamine)-9,9′-spirobifluorene) for fabricating perovskite solar cells.[13] The mixed halide perovskite, $CH_3NH_3PbI_{3-x}Cl_x$ exhibited a PCE of 10.9% with spiro-OMeTAD as the HTM. The PCE of perovskite solar cells skyrocketed to an efficiency of 25.5% within a decade.[14] The perovskite solar cell efficiency is approaching the theoretical Shockley-Queisser limit of 33.7% and has already surpassed many of the existing PV technologies such as polycrystalline silicon, CdTe, and CIGS (copper indium gallium diselenide).[15, 16]

Apart from its PV applications, Karunadasa and coworkers reported highly luminescent two-dimensional (2D) layered perovskite materials, which are promising for solid state lighting applications. They found that emission in these low dimensional materials arises from the transient self-trapped excitonic states.[17] Moreover, the order-

disorder transitions between the organic and inorganic components in the perovskite materials resulted in showing ferroelectric properties at room temperature, which is extensively studied by the research group of Xiong.[18-21] The low activation energy for ion migration and conductive filament formation in perovskite materials has been exploited for memory device applications. These materials are also widely used for photodetector, photocatalysis, sensing, X-ray detection, and energy storage applications.[22-26] The low-temperature solution processability and abundance of the inorganic salts on the earth's crust made these materials cost-effectively scalable.

1.2.2. Crystal structure of perovskites
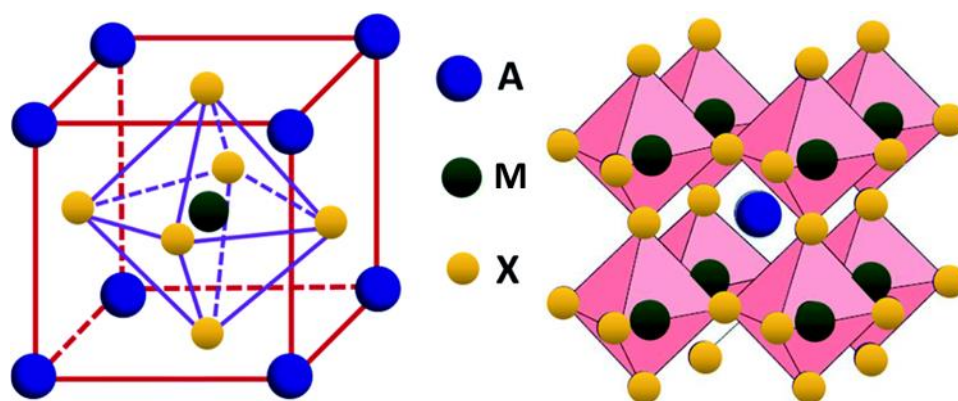
Figure 1.1. Crystal structure of AMX_3 type 3-dimensional (3D) perovskite (Adapted from reference 27).

Perovskites are having a general formula AMX_3 where A is a monovalent cation (Cs^+, $CH_3NH_3^+$ (MA^+), $NH_2CH=NH_2^+$ (FA^+), etc.) M is a divalent metal ion (Pb^{2+}, Sn^{2+}, Ge^{2+}, etc.), and X is a halogen (Cl^-, Br^-, I^-). The unit cell of a 3D perovskite consists of eight metal-halide octahedrons (MX_6^{3-}) connected through corner-sharing to form a

cubo-octahedral cavity with an overall negative charge. The A cation sits in the cavity, and the negative charge of the inorganic framework is counterbalanced (**Figure 1.1**).[27] The cavity can hold organic or inorganic cations having a size maximum of up to 2.6 Å. The coordination number of 'A' cation is 12, 'M' cation is 6, and 'X' anion is 2.

Various perovskite analogues were reported over the years. For instance, Karunadasa *et al*. replaced two equivalent of the divalent metal ions with trivalent and monovalent metal ions (Bi^{3+} and Ag^+) to form a new class of perovskite material ($Cs_2AgBiBr_6$) known as double perovskites.[28] Recently, they have reported expanded 3D perovskite materials consisting of sizeable organic spacer cations based on pyrazine; such a 3D inorganic framework was previously inaccessible with large organic spacer cations.[29] However, In general, 3D perovskite materials are highly unstable in the presence of moisture and oxygen;[30] this prompted the researchers to develop 2D perovskites incorporating hydrophobic organic spacer cations. These organic cations prevented the ingression of water into the inorganic lattice and improved the stability of the materials. There are two types of 2D perovskites: the Ruddlesden-Popper (RP) and Dion-Jacobson (DJ) phases.[31] RP and DJ perovskites have general formula $(A')_2A_{n-1}M_nX_{3n+1}$ (A' - mono cation) and $(A'')A_nM_nX_{3n+1}$ (A'' - dication) respectively. Here, the A cations fit in the voids of the inorganic layers, whereas A' and A'' cations occupy the space between the inorganic slabs. In RP perovskites, the adjacent inorganic slabs will be shifted by a half octahedral unit. In the case of DJ perovskites, the adjacent inorganic layers will be in an eclipsed conformation.[32] Compared to the DJ phase, the

RP perovskites exhibited improved electronic conductivity owing to their small van der Waals spacing between the adjacent inorganic layers.

The semi-empirical geometrical parameter, Goldschmidt tolerance factor, is relaxed in 2D perovskites so that the inorganic layers could hold bulkier organic cations in their cubo-octahedral cavity, and hence diverse structures are accessible. Even though 3D and 2D perovskites are well explored, less research attention was paid to one-dimensional (1D) and zero-dimensional (0D) perovskite materials. 1D perovskites have a quantum wire electronic dimensionality with MX_6 octahedrons connected via corner or edge-sharing to form zig-zag or linear inorganic chains. 0D perovskites consist of isolated MX_6 octahedrons results in a molecular salt-like structure. The lower dimensionality of these materials resulted in strong charge carrier confinements, and a wide optical bandgap subsequently resulted in poor photovoltaic performance.

1.2.3. Formability and stability of perovskites

Goldschmidt introduced a semi-empirical parameter called tolerance factor (*t*) to predict the stability and formability of the 3D perovskite phase. The Goldschmidts tolerance factor is described as

$$t = \frac{(R_A + R_X)}{\sqrt{2}(R_M + R_X)}$$

R_A, R_X and R_B are ionic radii of A, X, and M. The ideal range of *t* for cubic metal halide perovskites is $0.89 < t < 1$ (**Figure 1.2**a). Any deviation from this tolerance value range results in perovskites having low crystal symmetry, such as tetragonal,
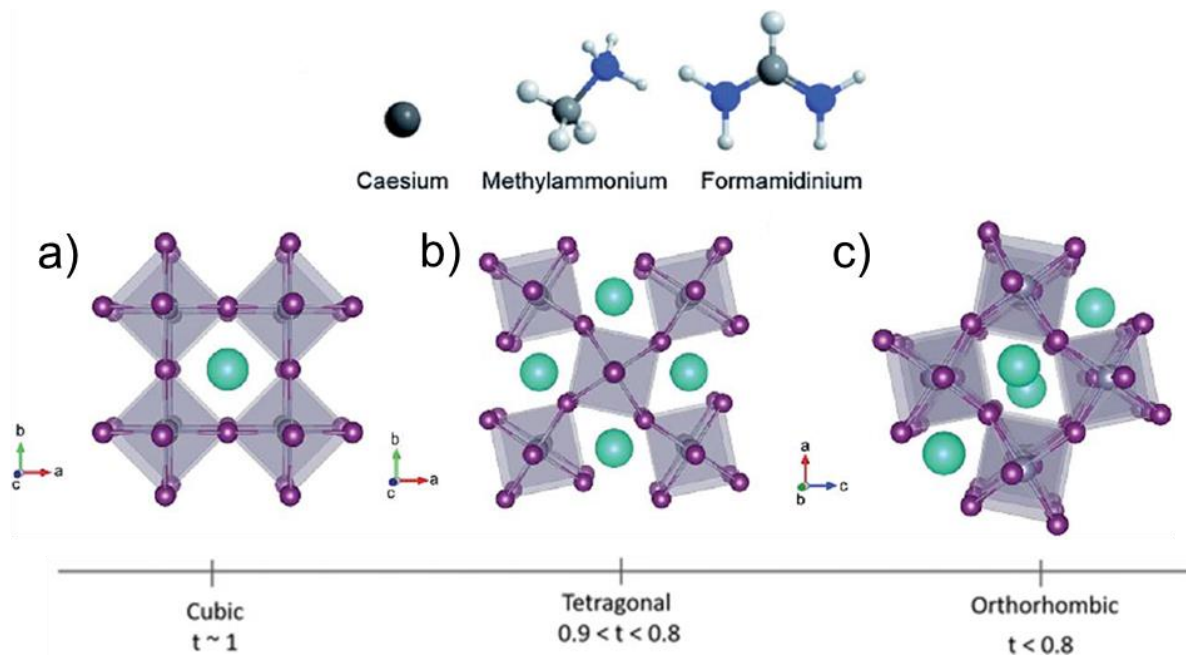
Figure 1.2. a), b), and c) are crystal structures of APbI$_3$ perovskites, where A is cesium, methylammonium, and formamidinium, respectively (Adapted from reference 34).

orthorhombic, and hexagonal (**Figure 1.2**b and c). The major assumption while deriving Goldschmidts tolerance factor was that the cations and anions are considered hard spheres. This approximation will be appropriate for all inorganic halide perovskites and will not be suitable for hybrid perovskites incorporating nonspherical organic cations or charge-transfer complexes. Therefore, this geometrical parameter is relaxed in 2D hybrid perovskite materials and expanded 3D perovskites.

Another parameter describing the stability of metal halide octahedrons and the formability of the perovskite phase is the octahedral factor (μ).[35] The octahedral factor is expressed as $\mu = \frac{R_M}{R_X}$, where R_M and R_X are ionic radii of M and X. The ideal MX$_6$

octahedron formation is favorable when the value of $\mu > 0.442$. Otherwise, the MX_6 octahedron will be distorted and have a detrimental impact on the photophysical properties of the perovskites. The extend of octahedral distortion could be estimated using two parameters called octahedral distortion (Δd) and bond angle variance (σ^2).[36] Octahedral distortion, $\Delta d = \left(\frac{1}{6}\right) \sum (d_i - d)^2 / d^2$. Where d_i denotes the six individual M-X bond lengths and d is the average M-X bond length. Bond angle variance (σ^2) is expressed by the formula $\sigma^2 = \frac{1}{11} \sum_{i=1}^{12} (\alpha_i - 90)^2$. Where α_i is the X-M-X bond angles of the octahedra. Large octahedral distortion and bond angle variance lead to insufficient overlapping of metal and halide atomic orbitals, resulting in a wider optical bandgap and poor electronic conductivity.

1.2.4. Optoelectronic properties of Pb-based perovskites

Metal halide perovskites exhibit unique physical properties such as narrow optical bandgap, high molar extinction coefficient, long carrier diffusion length, high electron and hole mobility, weakly bound excitons, and defect tolerance. These attractive properties made them promising for various applications such as solar cells, photodetectors, memory devices, etc. The band structure analysis using density functional theory (DFT) calculations revealed that the valence band maximum (VBM) states are derived from the anti-bonding interaction between the 6s atomic orbital of lead and np atomic orbital of halogen. In contrast, the conduction band minimum (CBM) states are composed of Pb-6p and halogen-np orbitals (**Figure 1.3**). The
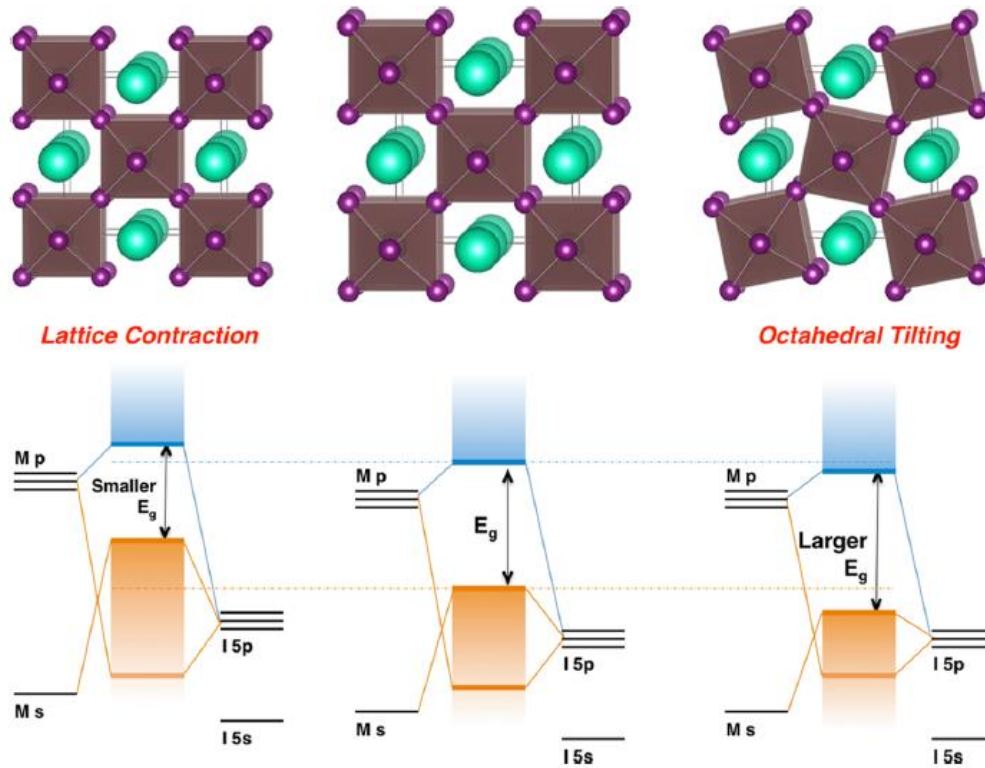
Figure 1.3. The upper panel shows the crystal structures of distorted (left and right ends) and ideal cubic (center) perovskites. The molecular orbital diagram explaining the bandgap variation is shown below the corresponding perovskite structures (Adapted from reference 37).

Commonly used 'A' site cations such as MA, FA, and Cs have only the electronic contribution in the deep valence band and conduction band states. This band structure allows modulating the optical bandgap by changing the metal ions and halogens. For instance, by changing the halogen from Cl → Br → I, the bandgap will become narrow because of the gradual lowering of the ionization energy.[38] Similarly, partial substitution of Pb with Sn allows the fine-tuning of the absorption onset from 1000 to 1300 nm. Since the VBM and CBM states are composed of p-orbitals, the material usually exhibits a direct bandgap, and the symmetry allowed p-p transition benefits for

its high absorption coefficient (10^5 cm^{-1}).[39] The absorption coefficient of perovskite is one order magnitude higher than that of the conventional photoabsorber such as GaAs; thus, thin films (~300 nm thickness) of perovskites are enough to harvest sufficient solar radiation.

The electron and hole diffusion length in solution-processed thin films of MAPbI$_3$ is 100 nm, as revealed by time-resolved photoluminescence (PL) measurements.[40] Snaith *et al*. reported a much-improved carrier diffusion length (>1 µm) in the mixed halide perovskite material, MAPbI$_{3-x}$Cl$_x$, suggesting that compositional engineering could deliver optimal carrier mobility.[41] In general, perovskite single crystals exhibit long carrier diffusion lengths compared to polycrystalline films owing to the reduced defect states and grain boundaries. For example, the single crystals of MAPbI$_3$ showed a carrier diffusion length over 175 µm.[42] The doctor-bladed thin films of MAPbI$_3$ exhibited a long carrier diffusion length of 3.5 µm, which is attributed to the large grain size of perovskite crystallites.[43] Instantaneous free charge carrier generation (~2 ps) upon one sun illumination was observed in MAPbI$_3$ thin films. The carrier mobility of MAPbI$_3$ perovskite thin films was evaluated using time-resolved terahertz and microwave techniques as 8 cm^2 V^{-1} s^{-1}.[44] The exciton binding energy of perovskites is dependent on quantum and dielectric confinement effects. The 2D perovskite, (C$_{10}$H$_{21}$NH$_3$)$_2$PbI$_4$, exhibits high exciton binding energy (370 meV) compared to the 3D analogue, MAPbI$_3$ (37 meV), due to the weak quantum confinement in the latter.[45,46] In 2D perovskites, the polarizability of organic spacer cations has a significant influence in

tuning the dielectric confinement and thereby the exciton binding energy. For instance, the (ethanolammonium)$_2$PbI$_4$ 2D perovskite material with polarizable organic spacer cation exhibits low exciton binding energy (13 meV) compared to (phenylethylammonium)$_2$PbI$_4$ (250 meV) owing to the poor image charge effect[47] (image charge effect defines the strength of electrostatic attraction between the two-point charges located on either side of the planar interface separating two dielectric mediums) in the former. In general, the lead halide perovskite materials are highly defect-tolerant, and this could be explained by the molecular orbital theory. The anti-bonding interaction between Pb-6s and I-5p orbitals shifts the VBM to higher energy, and the spin-orbit coupling effect broadens the conduction bandwidth; thereby, the defect states will be shallow or reside within the VB or CB energy states. Moreover, the high dielectric constant of these materials could screen the charged defect states and thereby reduces the trap state density.

1.2.5. Toxicity of Pb-halide perovskites

The best performing perovskite materials for solar cell application is based on highly toxic metal ion, Pb^{2+}. The toxicity of these materials hindered their practical application and commercialization. According to the world health organization, the safe upper limit of lead content in the blood is 5 µg dL^{-1}. The disintegration product of this perovskite is PbI$_2$, which is readily soluble in water (1.6 mM at 25 °C), and hence its bioavailability is high.
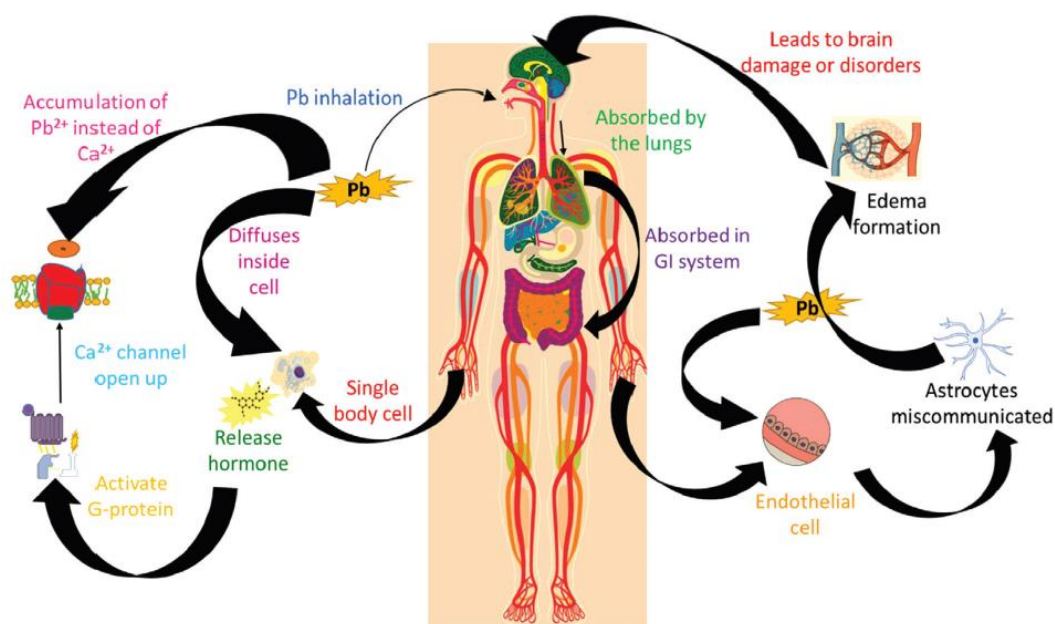
Figure 1.4. Schematic diagram showing the various possible ways of lead intoxication in humans and the health hazards associated with lead poisoning (Adapted from reference 48).

Moreover, lead intoxication can also occur through inhalation, dermal contact, breastfeeding, etc. (**Figure 1.4**). Acute toxicity of lead can cause neurological disorder, brain damage, decreased intelligence, etc. Proper encapsulation of the perovskite solar cell modules and strict recycling of the active perovskite layer could reduce the toxicity concern associated with these materials to some extent. Researchers have studied the toxicological impact of degraded perovskite material on plants and aquatic organisms. Antonio and coworkers found that the bioavailability of lead in perovskite is ten times higher than that of other lead contaminants.[49] They have observed that the intake of lead is high in mint plants grown in perovskite contaminated soil because of the increased acidity caused by hydriodic acid (side product during the degradation of perovskite).

This study revealed that lead could enter into the food cycle through plants if there is a potential leakage in the solar cell panels. Laszlo *et al*. studied the effect of $CH_3NH_3PbI_3$ perovskite on primary neurons, neuroblastoma cells, and lung epithelial cells.[50] Primary neurons and neuroblastoma cells were undergone a complete cell death, whereas cellular morphology and metabolic activities of lung epithelial cells were altered after exposure to perovskites. The environmental impact of perovskites was studied by Conings *et al*. using the Zebrafish as the model system.[51] The embryo of Zebrafish exposed to PbI_2 resulted in brain haemovascular defect, heart oedema, and dorsal curvature. These reports suggest that the hazardous impact of lead toxicity on humans and the environment will restrict the widespread application of lead halide perovskites.

1.2.6. Instability of Pb-based perovskites
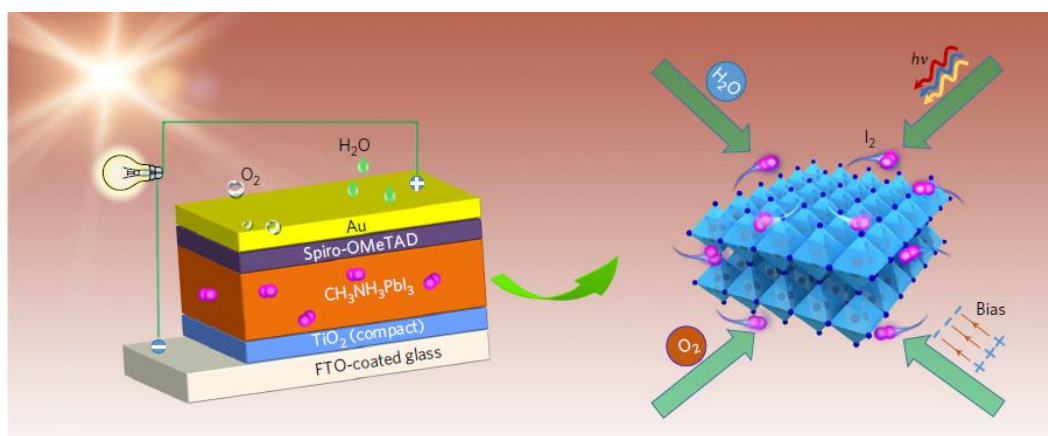
Figure 1.5. Schematic representation of the device architecture of a $MAPbI_3$ based perovskite solar cell and various external factors such as moisture, oxygen, light irradiation, and applied bias voltage affecting the stability of the perovskite layer (Adapted from reference 52).

Lead halide perovskites are highly unstable towards heat, moisture, and oxygen owing to their low formation energy of 0.11 - 0.14 eV (**Figure 1.5**). The formation energy of perovskites is equivalent to the energy corresponding to 85 °C; hence, an accelerated decay of these materials was observed at elevated temperatures. Since most of the organic ammonium cations in hybrid perovskites are hygroscopic, moisture will dissolve the organic components and disintegrate the perovskite structure. Frost *et al.* proposed that the degradation of $CH_3NH_3PbI_3$ perovskite is initiated by the formation of an aqua complex.[53] The detailed mechanism is as follows:

$$[(CH_3NH_3^+)PbI_3]_n + H_2O \rightleftharpoons [(CH_3NH_3^+)_{n-1}PbI_3]_n[H_3O^+] + CH_3NH_2$$

$$[(CH_3NH_3^+)_{n-1}PbI_3]_n[H_3O^+] \rightleftharpoons HI + PbI_2 + [(CH_3NH_3^+)PbI_3]_{n-1} + H_2O$$
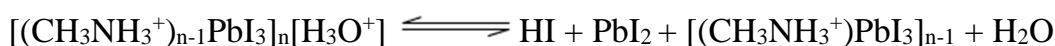
Since methylamine and hydriodic acid are gases, the equilibrium of the reaction will shift towards the product side, and hence the rate of decomposition of perovskite will be higher. In solar cell devices, due to the presence of hole transporting layer, spiro-OMeTAD, poly[bis(4-phenyl)(2,4,6-trimethylphenyl)-amine] (PTAA), and poly(3-hexylthiophene) (P3HT) over the perovskite thin film, moisture ingression will be reduced to some extent. However, it is reported that the additives such as Li-TFSI and 4-*tert*-butylpyridine in the hole transporting materials could accelerate the decomposition process of the underlying perovskite layer.[54,55]

Another factor for perovskite degradation is O_2; the atmospheric O_2 can diffuse into the perovskite lattice and cause its degradation under illumination conditions. Rappich

and coworkers proposed a degradation mechanism of perovskite in the presence of O_2 upon shining light on the perovskite layer.[56] The degradation is initiated by the formation of superoxide by an electron capture of O_2 from the conduction band of perovskite. This step is followed by the abstraction of a proton from the Brønsted-Lowry acid, $CH_3NH_3^+$. The degradation mechanism is as follows

$$O_2 \xrightarrow{hv > E_g} O_2^-$$

$$CH_3NH_3^+ + O_2^- \longrightarrow HO_2 + CH_3NH_2 \uparrow$$

$$2HO_2 \longrightarrow 2O_2 + H_2 \uparrow$$
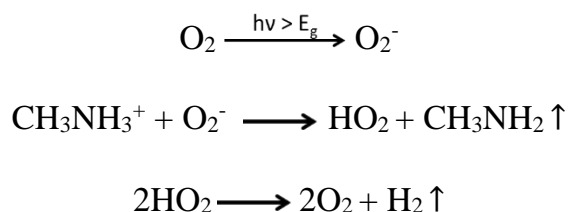
The instability of lead halide perovskites resulted in a sharp drop in the PCE of perovskite-based solar cells under ambient conditions. In contrast to 3D perovskites, 2D lead halide perovskites exhibited superior stability under ambient conditions due to alternative hydrophobic organic layers in their structure.

1.2.7. Ge and Sn-based perovskites

Due to the toxicity and instability of lead halide perovskites, researchers started looking for alternative elements to replace Pb^{2+} in the perovskite structure. The priority was given to the elements that belong to the same group of lead, and hence, Ge^{2+} and Sn^{2+} were at the frontline of choice. However, Ge^{2+} based perovskites have a wider optical bandgap than Pb^{2+} and Sn^{2+} based perovskites due to weak spin-orbit coupling. The DFT calculations revealed that the VBM states are derived from the anti-bonding states arising from Ge s and I p atomic orbitals.
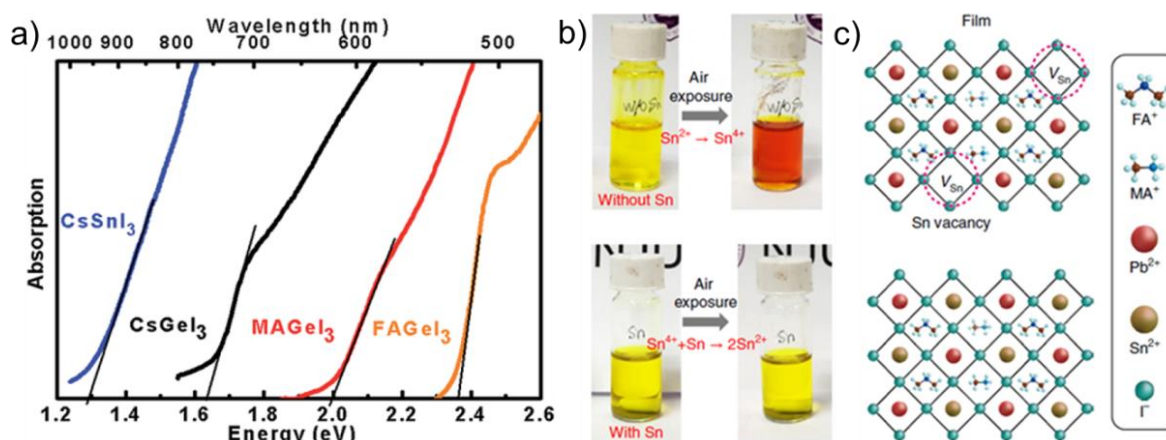
Figure 1.6. a) Optical bandgap of Sn and Ge- based perovskites b) photographs of Sn^{2+} oxidation in solvent DMSO (upper) and metallic Sn inhibiting the undesired oxidation of Sn^{2+} in the precursor solution (lower). c) Schematics of the Sn vacancy formation in the perovskite structure (upper) and the Sn vacancy suppressed crystal structure (lower). Adapted from references 57 and 63.

The CBM energy levels are primarily contributed by the non-bonding Ge p atomic orbitals. The optical bandgap of Ge-based perovskites is highly dependent on the size of the organic cation. For instance, the optical bandgap follows the trend $CsGeI_3 < MAGeI_3 < FAGeI_3$ (**Figure 1.6.**a).[57] Kanatzidiz *et al.* reported a series of hybrid Ge-based perovskites by varying the organic spacer cation such as methylammonium, formamidinium, acetamidinium, guanidinium, trimethylammonium, and isopropylammonium.[58] When the size of the organic cation is increased beyond acetamidinium, the dimensionality of the perovskite changed from 3D to 1D. The 3D materials exhibited a direct bandgap, whereas the 1D materials showed indirect bandgap transition. The optical bandgap of these perovskites showed a strong dependence on the size of the spacer cation. With the increase in the size of the organic

cations, the atomic orbital overlapping between the adjacent $[GeI_3]^-$ units were weakened and subsequently resulted in a widening of the optical bandgap. Theoretical study on $CsGeI_3$ revealed that this material has a large static dielectric constant of 18.5.[59] The observed large dielectric constant in $CsGeI_3$ is due to the mixed ionic-covalent nature of the lattice, which is beneficial for screening the charged defects and impurity defects in the perovskite lattice. However, the iodide vacancy in Ge-based perovskites could create deep trap states due to the more covalent nature of Ge-Ge bonding compared to Pb-Pb and Sn-Sn interactions in lead and tin halide perovskites, respectively. The solar cell devices fabricated using these materials exhibited low PCE due to the wide optical bandgap and poor film morphology. However, the $CsGeI_3$ quantum rods synthesized via a solvothermal approach yielded a decent solar cell PCE of 4.92%.[60]

The most explored lead-free perovskite materials are tin halide perovskites, owing to their narrow optical bandgap (1.21 eV), high mobility of charge carriers (2320 cm^2 V^{-1} s^{-1} for electrons and 322 cm^2 V^{-1} s^{-1} for holes), and long charge carrier diffusion length (> 500 nm).[61,62] The optical bandgap of Sn^{2+} perovskites can be fine-tuned by changing the organic spacer cation. For example, $MASnI_3$ exhibits a narrow optical bandgap than $FASnI_3$. It was attributed to the large octahedral strain in $FASnI_3$ compared to $MASnI_3$ due to the bigger size of FA cation in the former. More importantly, the synthetic conditions have considerable influence on the bandgap and photoluminescence (PL) properties of these materials. The major problem associated with Sn^{2+} perovskites is the

facile oxidation of Sn^{2+} to Sn^{4+} state due to the presence of high energy lying $5s^2$ atomic orbitals. This oxidation process will lead to inherent p-type doping in tin halide perovskites and is detrimental to its PV performance. Another limitation of these materials is the poor film morphology due to fast crystallization kinetics. Several successful methods were reported for preventing the oxidation of Sn^{2+} to Sn^{4+}; among them, the promising routes are the addition of reducing agents such as SnF_2 and metallic Sn to the perovskite precursor solution (**Figure 1.6**b).[63]   The kinetics of perovskite crystallization can be slowdown by the additives 2-fluoro-phenylethylammonium and poly(vinyl alcohol).[64,65] The additive modified perovskite layer exhibited low trap state density (**Figure 1.6**c), improved device stability, and high PCE compared to the pristine sample. The partial substitution of FA with ethylammonium in the Sn halide perovskite structure resulted in forming a stable perovskite phase due to the closeness of the tolerance factor to 1. This material exhibited a solar cell PCE of 13.24%, which is the highest efficiency so far reported for a Sn halide perovskite material.[66]

1.2.8. Bi-Based Perovskites

Apart from the synthetic advancements in the Ge and Sn-based perovskites, the instability of these materials remains an unsolved issue.[67] This prompted the researchers to search for metal ions other than Ge and Sn. The next nearest element to lead in the periodic table is bismuth, which is known to replace lead in many fields such as

pharmaceuticals, cosmetics, and pigments. Bismuth (Bi^{3+}) is the heaviest non-radioactive element in the periodic table, which is isoelectronic and having comparable ionic radii to Pb^{2+}. Moreover, the element bismuth is non-toxic. These features made Bi^{3+} an ideal substitute for Pb^{2+} in the perovskite structure. Due to the +3 oxidation state of Bi, it cannot form the conventional 3D perovskite structure of $CaTiO_3$. Instead, it forms low dimensional perovskites with a generic formula of $A_3Bi_2X_9$ (A= Cs^+, MA^+, FA^+, etc. and X= Cl^-, Br^-, I^-).[68-71] The advantages of bismuth perovskites are environment friendliness, excellent moisture and chemical stability, structural diversity ranging from 0D to 3D, and tunable optoelectronic properties.

1.2.8.1. 0D and 1D Bi-based Perovskites

The most widely explored perovskite material is $(MA)_3Bi_2I_9$ (MBI), which is having a zero-dimensional crystal structure and belongs to *P6₃/mmc* space group. It consists of isolated $Bi_2I_9^{3-}$ dimer units formed by the face sharing of two BiI_6^{3-} octahedrons (**Figure 1.9**a). The negative charge on the inorganic framework is counterbalanced by methylammonium cations. Due to the isolated nature of $Bi_2I_9^{3-}$ dimer units in MBI, the electronic wave function is localized in the inorganic clusters. However, the distance between the iodine atoms of adjacent inorganic clusters is lesser than the van der Waals diameter of elemental iodine, which will provide potential charge transport pathways in this molecular salt-like perovskite. Irvine *et al.* revealed that the inter dot electronic coupling between the $Bi_2I_9^{3-}$ dimer units is favorable because of the small size of the
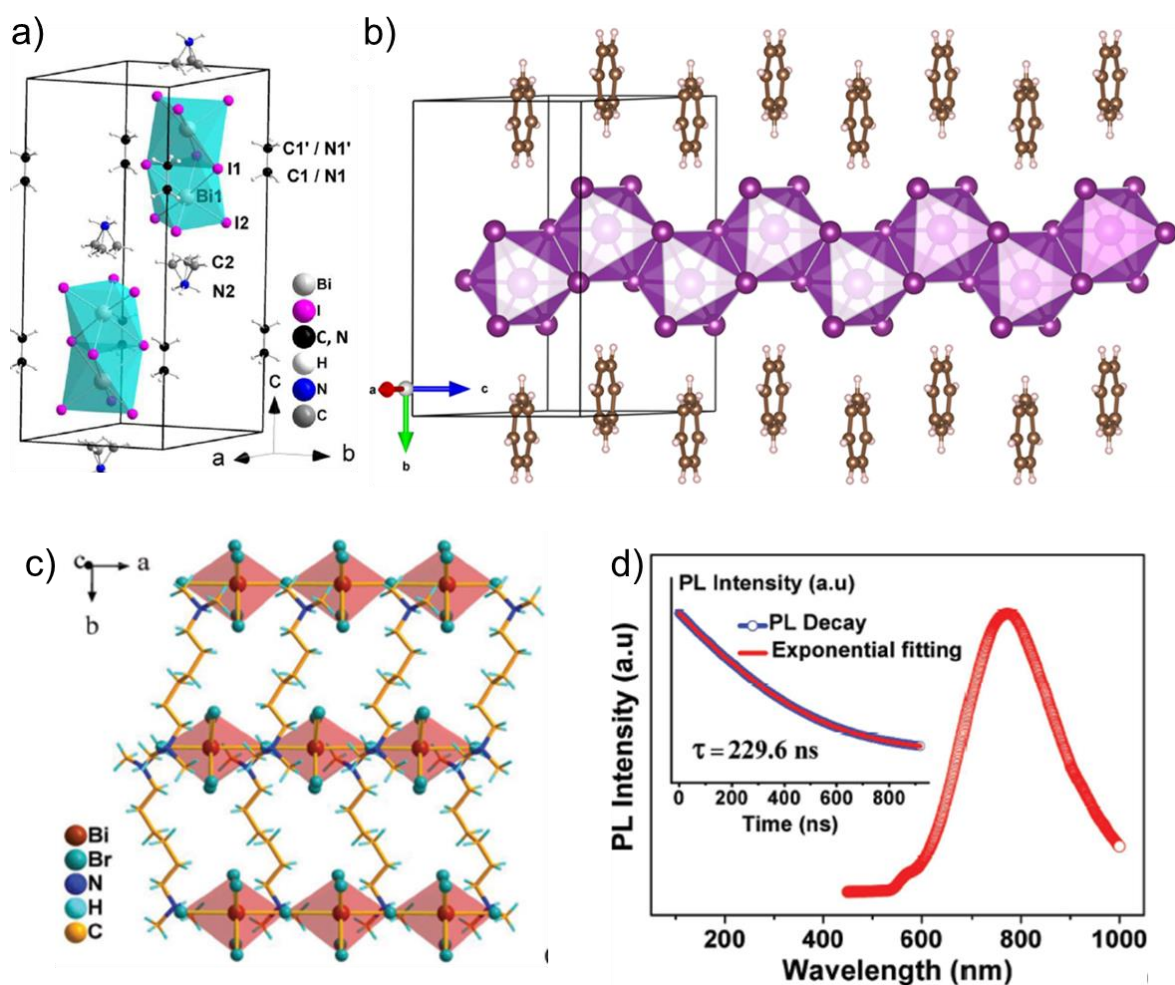
Figure 1.9. a) Unit cell representation of zero-dimensional $MA_3Bi_2I_9$ perovskite consisting of isolated $Bi_2I_9^{3-}$ dimers separated by methylammonium cations. $MA_3Bi_2I_9$ crystallizes in a hexagonal phase with *P6₃/mmc* space group symmetry. b) and c) are 3D crystal packing of $(CN_2SH_5)_3BiI_6$ and (*N,N,N,N*-tetramethyl-1,6-hexanediammonium)$_2BiBr_5$ perovskite materials. d) PL and time-resolved PL decay kinetics of (*N,N,N,N*-tetramethyl-1,6-hexanediammonium)$_2BiBr_5$ single crystals. Adapted from references 72, 73, and 74.

spacer MA cation, which will facilitate homo-Förster resonance energy transfer across the inorganic moieties and increases the lifetime of the excitons.[75] Hoye *et al*. reported an improved carrier lifetime in vapor-deposited MBI film (0.76 ns) compared to the

solution-processed one (0.12 ns).[76] The increased carrier lifetime in vapor-deposited MBI is attributed to its reduced defect state density. Kawai *et al*. estimated the exciton binding energy of MBI from the low-temperature absorption measurements.[77] At low temperature (78 K), the band continuum and excitonic peak are well isolated in the absorption spectrum, and the calculated exciton binding energy for MBI is over 300 meV. PL quenching studies of MBI thin films using spiro-OMeTAD and TiO_2 layers revealed the hole and electron diffusion length as 113 nm and 189 nm, respectively.[78] The DFT calculations showed a splitting in the CBM states due to spin-orbit coupling, resulting in a direct bandgap of 2.1 eV and an indirect bandgap of 2.04 eV for MBI.[76]

The poor visible light absorption ability of MBI due to its wide optical bandgap is one of the significant limitations associated with the poor photovoltaic performance of this material. Hayase *et al*. reported that in situ sulfur doping via bismuth(ethyl xanthate)$_3$ precursor is an efficient strategy to narrower the bandgap of MBI.[79] The sulfur-doped MBI films featured an optical bandgap of 1.45 eV and improved carrier density (2.3×10^{21} cm^{-3}) and mobility (2.28 cm^2 V^{-1} s^{-1}) compared to the pristine MBI films. Luo *et al*. proposed that triiodide can induce band structure modification in 0D (4-methylpiperidinium)$_3$Bi$_2$I$_9$ perovskite.[80] The triiodide integrated perovskite (4-methylpiperidinium)$_4 \cdot$I$_3 \cdot$BiI$_6$ featured a reduced bandgap of 1.58 eV compared to the pristine (4-methylpiperidinium)$_3$Bi$_2$I$_9$ single crystals (2.02 eV). DFT calculations revealed that the triiodide orbitals contribute to the band edge states of (4-methylpiperidinium)$_4 \cdot$I$_3 \cdot$BiI$_6$ and subsequently lowered the bandgap.

Evans *et al.* integrated tetrathiafulvalene (TTF) as an organic spacer cation in a Bi-based perovskite, considering the extensive π-π stacking ability of TTF.[81] Long-range mixed-valence (TTF$^{\bullet+}$-TTF^0) π-π stacking was observed in the zero-dimensional (TTF)$_4$BiI$_6$, whereas, partially eclipsed π-π stacking of TTF moieties are observed in the one-dimensional (TTF)BiI$_4$. Despite the higher dimensionality of (TTF)BiI$_4$, the zero-dimensional (TTF)$_4$BiI$_6$ perovskite exhibited a higher electrical conductivity (10^{-4} S cm^{-1}) owing to the efficient charge transport across the mixed-valence TTF stacks in the latter. Recently Yao *et al.* reported 0D and 1D Bi-based perovskites with identical organic spacer cation, *N,N'*-dimethylethanediamine (DMEDA), by changing the molar ratio of the organic and inorganic salts.[82] The 1D perovskite, (DMEDA)BiI$_5$, exhibited a narrow optical bandgap (1.87 eV) compared to the 0D perovskite (DMEDA)$_{1.5}$BiI$_6$ (~ 2.1 eV) owing to the weak quantum confinement in the former. Neilson *et al.* reported a charge transfer 1D perovskite material with tropylium as the organic spacer cation ((C$_7$H$_7$)BiI$_4$).[73] The DFT calculations revealed a significant contribution of tropylium atomic orbitals at the CBM, which facilitated charge transfer from the inorganic BiI$_4^-$ chains to the tropylium cations upon photoexcitation. Moreover, the contribution of π^* atomic orbitals of tropylium cations to the band edges of (C$_7$H$_7$)BiI$_4$ resulted in a narrow optical bandgap of 1.83 eV. Robertson *et al.* reported 1D perovskites, (pyridinium)BiI$_4$ and (methylpyridinium)BiI$_4$, consisting of BiI$_4^-$ inorganic chains formed by the edge-sharing of Bi-I octahedrons.[83] Band structure calculations proposed that both the materials are having direct optical bandgap and significant energy level

contribution from the organic cations at the band edges. (methylpyridinium)BiI_4 exhibited higher band edge dispersion compared to (pyridinium)BiI_4 attributed to the superior inter-inorganic chain electronic coupling in the former, and hence it will act as a pseudo-3D perovskite material.

There are 1D perovskites with electronically inactive organic cations where the optoelectronic properties are fully dictated by the inorganic framework. For example, the 1D perovskites (*N,N,N,N*-tetramethyl-1,6-hexanediammonium)$_2$BiBr$_5$ (**Figure 1.9**c) and (tetramethylpiperidinium)$_2$BiI$_5$ does not have any orbital electronic contribution from the wide bandgap organic spacers towards the band edge states.[74,84] Even though the organic cations are electronically inactive in these materials, they exhibited an appreciably long carrier lifetime of 65.58 and 226.9 ns (**Figure 1.9**d), respectively.

1.2.8.2. 2D Bi-based Perovskites
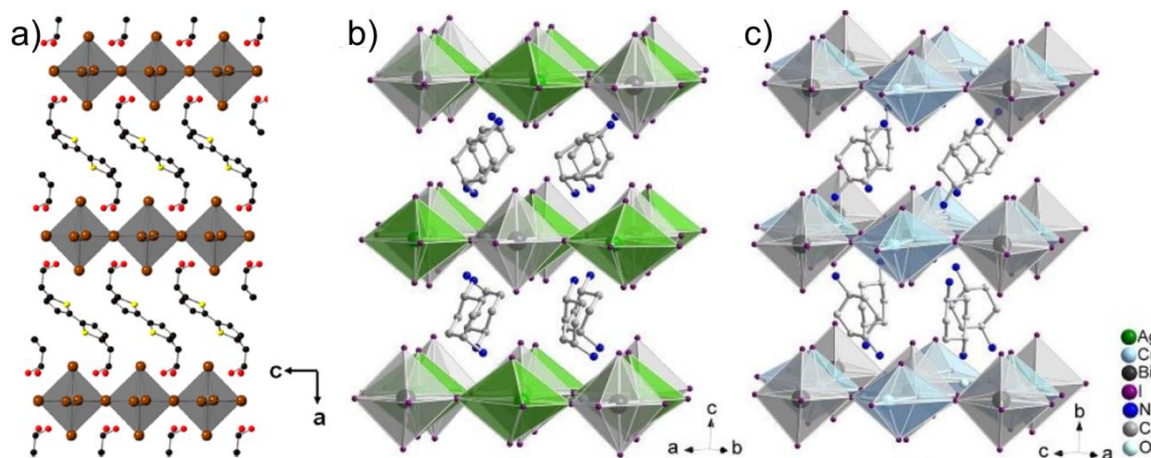
Figure 1.10. a), b) and c) are crystal structures of [AE2T]$_2$AgBiI$_8$ (AE2T= 5,5'-diylbis(aminoethyl)-[2,2'-bithiophene]) , (1,4-cyclohexanediamine)$_2$AgBiI$_8$.H$_2$O, and (1,4-cyclohexanediamine)$_2$CuBiI$_8$.0.5H$_2$O, respectively. Adapted from references 85 and 86.

Karunadasa *et al*. reported two novel 2D hybrid Ag-Bi double perovskites, $(BA)_4AgBiBr_8$ and $(BA)_2CsAgBiBr_7$ (BA = butylammonium) with a mono and bi octahedral thick inorganic layers, respectively.[87] Significant Ag-I octahedral distortion was observed in both these materials, and the distortions are stabilized by the mixing of nd and (n+1)s atomic orbitals of Ag. Even though the inorganic layer thickness was increased from $(BA)_4AgBiBr_8$ to $(BA)_2CsAgBiBr_7$, only a marginal bandgap variation was observed, suggesting isoenergetic electronic transitions in both perovskites. DFT calculations revealed that the identical charge transfer transition from Ag-I orbitals to Bi-I orbitals is responsible for the identical bandgap of these materials. Moreover, the band structure calculations suggested an indirect bandgap for $(BA)_2CsAgBiBr_7$ and a direct bandgap for $(BA)_4AgBiBr_8$. The VBM states of $(BA)_4AgBiBr_8$ are derived from Ag-d and Br-p orbitals, and CBM states are composed of Bi and Br p atomic orbitals. In the case of $(BA)_4AgBiBr_8$, the VBM states have a significant contribution from Ag-d, Bi-s, and Br-p orbitals, whereas the CBM levels are contributed by Ag-s, Bi-p, and Br-p atomic orbitals. Both these materials featured defect-mediated photoluminescence, which is confirmed through excitation intensity-dependent PL measurements. One of the significant drawbacks of these materials is the wide optical bandgap, 2.85 eV and 2.40 eV for $(BA)_4AgBiBr_8$ and $(BA)_2CsAgBiBr_7$, respectively. This is due to the large electronegativity of Br and the presence of a long alkyl chain. Followed by this report, Luo *et al*. synthesized a novel Ruddlesden popper double perovskite, $(C_3H_9NI)_4AgBiI_8$, with 3-iodopropylamine as the organic cation.[88] Due to the short alkyl chain length (3-

iodopropylamine), and lower electronegativity of I compared to Br, this material exhibited the lowest bandgap (1.87 eV) compared to other hybrid double perovskites.

Mitzi *et al*. reported the templating ability of thiophene organic spacer cations in stabilizing the 2D perovskite structure for homovalent Bi-based perovskites and Ag-Bi-based double perovskites.[85] The organic spacer moiety 5,5'''-bis-(aminoethyl)-2,2':5',2'':5'',2'''-quaterthiophene (AEQT) stabilize the formation of a metal-deficient perovskite, $(H_2AEQT)Bi_{2/3}I_4$, where 1/3 of the Bi sites are vacant. Single-crystal XRD analysis revealed that the herringbone arrangement of the quaterthiophene cations and its structural rigidity due to the short terminal alkyl chain is compensating the large formation energy of this unique 2D perovskite. In light of the structure-directing influence of thiophene molecules, Mitzi *et al*. reported a 2D hybrid Ag-Bi double perovskite with 5,5'-diylbis(aminoethyl)-[2,2'-bithiophene] (AE2T) as the spacer cation (**Figure 1.10**a). The perovskite, $[AE2T]_2AgBiI_8$, featured an optical bandgap of 2 eV, and no observable PL was observed from this material. The lack of PL in this material was ascribed to the type-II band alignment of $[AE2T]_2AgBiI_8$; where the VBM and CBM energy levels have characters of organic and inorganic frameworks, respectively. Recently, Zheng *et al*. reported hybrid lead-free 2D perovskites $(1,4-CHD)_2AgBiI_8.H_2O$ (AgBiI) and $(1,4-CHD)_2CuBiI_8.0.5H_2O$ (CuBiI) (CHD: cyclohexanediamine; **Figure 1.10**b and c).[86] AgBiI and CuBiI exhibited bandgaps of 1.93 eV and 1.68 eV, respectively. Moreover, they featured excellent moisture and thermal stability under the conditions of 55% relative humidity and a temperature up to 300 °C, respectively.

Notably, the thin films of AgBiI and CuBiI showed a vertical growth of inorganic layers over the ITO glass substrate, which is beneficial for excellent carrier transport in photovoltaic devices.

1.2.8.3. 3D Bi-based Perovskites
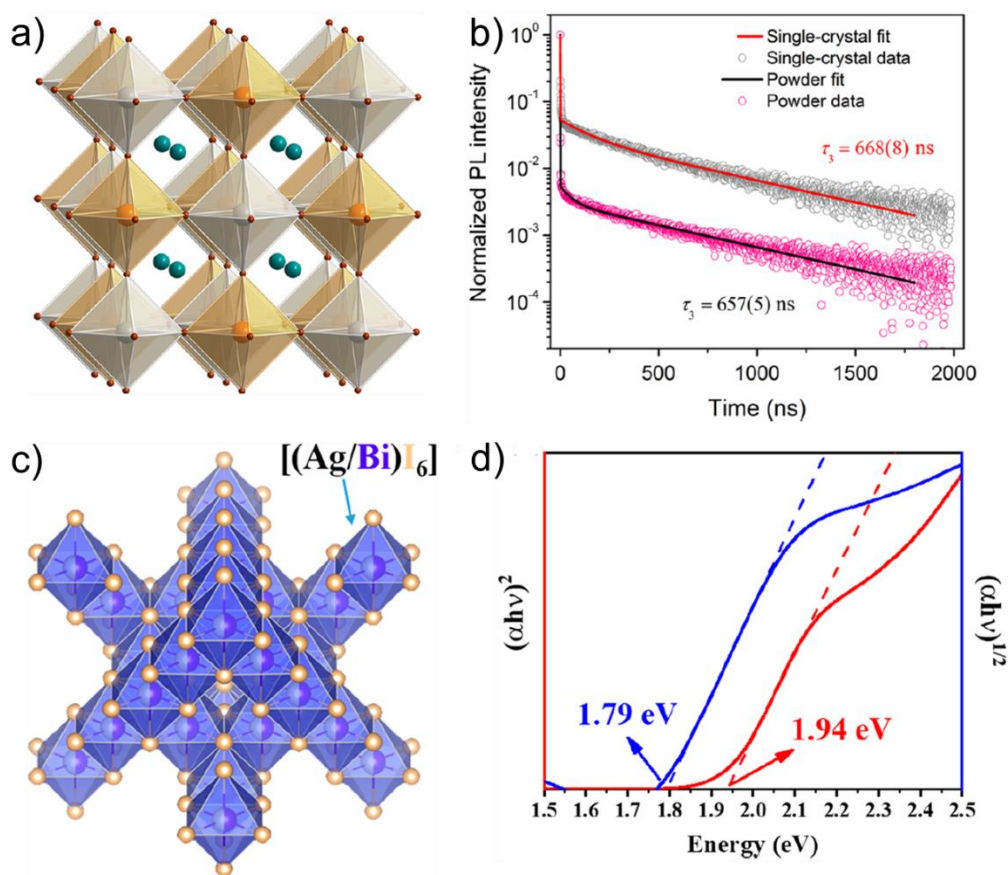
Figure 1.11. a), X-ray crystal structure of $Cs_2AgBiBr_6$. b) Time-resolved photoluminescence decay traces of $Cs_2AgBiBr_6$ single crystals and powder samples. c) X-ray crystal structure of $AgBiI_4$ rudorffite. d) Tauc plot showing direct and indirect bandgaps of $AgBiI_4$. Adapted from references 89 and 90.

Karunadasa and coworkers made a remarkable breakthrough in the material design strategy and synthesized the benchmark 3D lead-free double perovskite, $Cs_2AgBiBr_6$

(**Figure 1.11**a).[89] Its crystal structure consists of corner shared Ag-I and Bi-I octahedrons and forms an octahedral cavity. The Cs^+ cation sits in this cavity and neutralizes the negative charge of the inorganic framework. Interestingly, most charge carriers (85%) in the single crystals of $Cs_2AgBiBr_6$ featured a long carrier lifetime of 660 ns (**Figure 1.11**b). This is an indication of the low defect state density of the material, which is advantageous for photovoltaic application. The carrier lifetime of this material is comparable or even higher than that of the state-of-the-art perovskites such as (MA)PbI$_3$ (736 ns to 1 µs) and (MA)PbBr$_3$ (170 ns) and hence would be an ideal candidate to replace the toxic lead halide perovskites. The material exhibited excellent moisture and light stability under 55% relative humidity and 0.75 Sun illumination conditions, respectively. The thermal stability of this all-inorganic material is significantly higher (stable up to 430 ℃) than the conventional hybrid perovskites. However, it features a wide indirect bandgap of 1.95 eV, which is not suitable for a photoabsorber layer in solar cells. Mitzi *et al*. reported that alloying Sb^{3+} in the $Cs_2AgBiBr_6$ host lattice could reduce the indirect optical bandgap of the host from 2.12 eV to 1.58 eV.[91] Band structure of this alloyed perovskite unraveled the contribution of Sb-5s and 5p orbitals at the VBM and CBM states resulted in the overall bandgap reduction. Gao *et al*. demonstrated that controlling the crystallization rate of $Cs_2AgBiBr_6$ by varying the temperature could modulate the optical bandgap.[92] They have crystallized nearly centimeter-sized single crystals having an optical bandgap of 1.72 eV. DFT calculations proposed that Ag-Bi antisite defect levels at the band edges

of $Cs_2AgBiBr_6$ lowered the bandgap by ~0.26 eV. Karunadasa *et al.* reported that Tl alloying in $Cs_2AgBiBr_6$ could reduce its bandgap by 0.5 eV.[93] DFT calculations revealed that the defect levels created by the Tl- $6s^2$ and $6p^0$ orbitals at the band edge are attributed to the lowering of the bandgap. The alloyed $Cs_2AgBiBr_6$ featured a micro second lifetime in the time-resolved microwave conductivity analysis, which is beneficial for photovoltaic applications.

Another class of perovskite having crystal structures similar to $NaVO_2$ is called rudorffites, named after its discovery by Walter Rudorff. Ag and Bi can form rudorffite structures of general formula $Ag_aBi_bI_{a+3b}$ ($AgBiI_4$, Ag_2BiI_5, $AgBi_2I_7$, etc).[90,94,95] $AgBiI_4$ has a cubic defect spinel structure with a direct and indirect bandgap of 1.94 eV and 1.79 eV, respectively (**Figure 1.11**c and d). Ag_2BiI_5 crystallizes in a hexagonal phase with an optical bandgap of 1.85 eV. $AgBi_2I_7$ has a cubic crystal structure and belongs to *Fd$_3$m* space group having an indirect and direct bandgap of 1.62 eV and 1.87 eV, respectively.

1.2.9. Applications of Bi-based perovskites

1.2.9.1. Photovoltaic Devices

Johansson *et al.* introduced bismuth halide perovskites as a photoabsorber layer in perovskite solar cells in 2015. They have evaluated the photovoltaic performance of three materials, $MA_3Bi_2I_9$, $FA_3Bi_2I_9$, and $Cs_3Bi_2I_9$ (**Figure 1.7**a); the highest solar cell efficiency was obtained for $Cs_3Bi_2I_9$ (1.09%). The poor solar cell performance of these
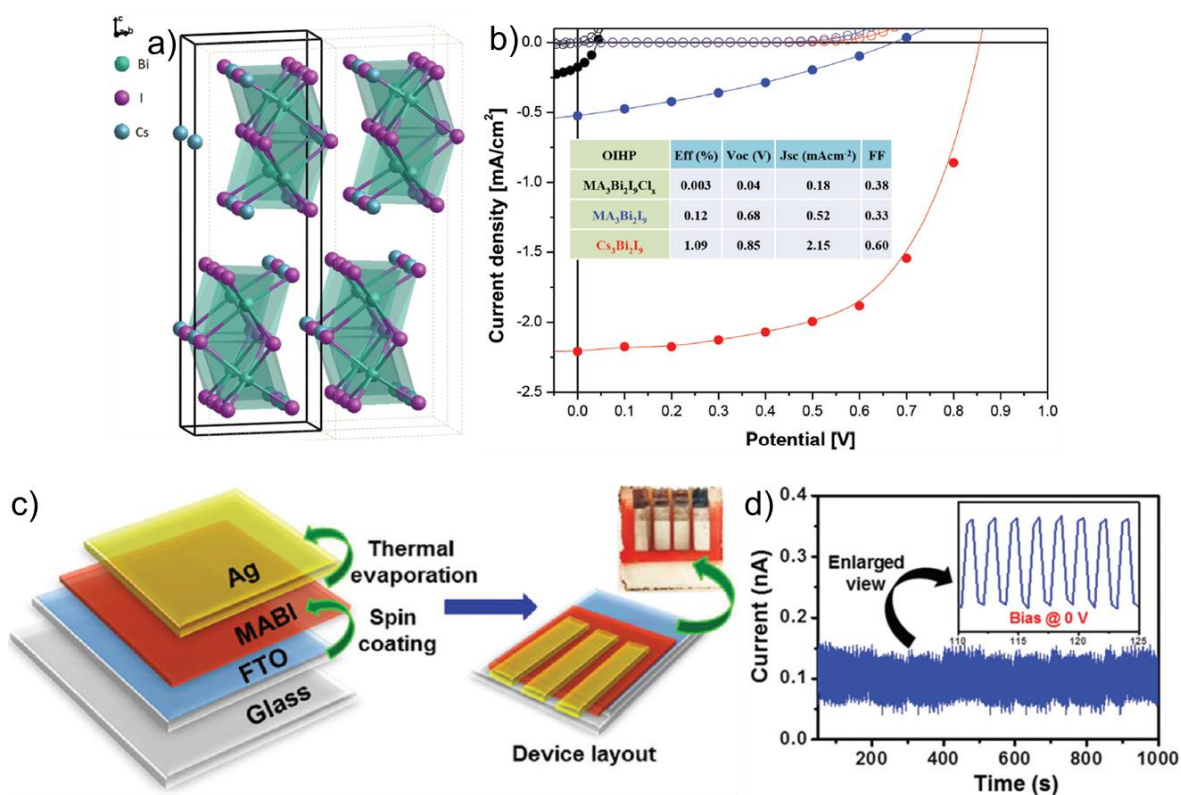
Figure 1.7. a) Crystal structure of $Cs_3Bi_2I_9$ perovskite consisting of isolated $Bi_2I_9^{3-}$ dimer units separated by Cs^+ cations. b) J-V curves of $Cs_3Bi_2I_9$, $MA_3Bi_2I_9$, and $MA_3Bi_2I_{9-x}Cl_x$ based solar cells, respectively. Inset shows the various solar cell parameters of the fabricated solar cells. c) Schematic of the photodetector device fabrication using $MA_3Bi_2I_9$ as the photoactive layer. d) Photoswitching cycles of self-powered $MA_3Bi_2I_9$ based photodetectors. Adapted from references 96 and 97.

materials (**Figure 1.7**b) is due to their inhomogeneous film morphology and wide optical bandgap as a consequence of 0D crystal structure. To further improve the visible light absorption, Malin and coworkers synthesized a 2D perovskite phase, $CsBi_3I_{10}$, via compositional engineering by varying the molar ratio of inorganic precursor salts (CsI and BiI_3).[98] This material featured a narrow optical bandgap (1.77 eV) compared to the state-of-the-art material $Cs_3Bi_2I_9$, owing to the layered crystal structure of the former.

Despite their extended visible light absorption, the solar cells fabricated with this material exhibited a PCE of only 0.4%. Su *et al.* revealed the layered crystal structure of $CsBi_3I_{10}$ with the help of DFT calculations and improved the quality of $CsBi_3I_{10}$ via a solvent annealing technique.[99] The solvent annealed $CsBi_3I_{10}$ perovskite material exhibited a PCE of 1.05%. Malin and coworkers achieved large grain size, extended optical absorption, and preferred crystal orientation in $Cs_3Bi_2I_9$ perovskite via thiourea addition.[100] The solar cell fabricated using the thiourea modified $Cs_3Bi_2I_9$ perovskite layer exhibited a PCE of 1.69%. Considering the inferior solar cell performance of single component $Cs_3Bi_2I_9$ perovskite, Yang *et al.* introduced a bulk heterojunction (BHJ) between $Cs_3Bi_2I_9$ - $Ag_3Bi_2I_9$ in the solar cell configuration.[101] The type-II band alignment of the BHJ resulted in efficient exciton dissociation and excellent carrier transport, which in turn resulted in the highest PCE of 3.6%.

The initial solar cell efficiency of the hybrid bismuth-based perovskite material $(MA)_3Bi_2I_9$ was only 0.12% due to its inferior film quality. To improve the quality of the films, Gao *et al.* adopted a two-step, high-low vacuum deposition technique. The solar cell devices fabricated using these films exhibited a decent PCE and V_{OC} of 1.64% and 0.81 V, respectively.[78] Durrant *et al.* adopted a two-step method known as vapor-assisted solution processing for depositing $(MA)_3Bi_2I_9$ thin-films. In the optimized process, spin-casted BiI_3 film was exposed to CH_3NH_3I vapor for 25 minutes to obtain homogenous perovskite thin films. The solar cell devices fabricated using these films delivered a PCE of 3.17%, which is the highest value reported so far.[102]

Apart from solar cell applications, these low dimensional perovskites are promising for photodetector applications as well. Amreen *et al*. fabricated a self-powered photodiode using $(MA)_3Bi_2I_9$ as the light-absorbing layer (**Figure 1.7**c). The fabricated photodetector (FTO/ $MA_3Bi_2I_9$/ Ag) exhibited stable photoswitching cycles (**Figure 1.7**d), high photosensitivity (10^5), and excellent detectivity (10^{12} Jones). The all-inorganic perovskite ($CsBi_3I_{10}$)-based photodetector yielded a high responsivity (21.8 A W^{-1}) and detectivity (1.93×10^{13} Jones), much higher than the lead halide perovskites.[103]

To improve the dimensionality of Bi-based perovskite materials, the conventional methylammonium organic cations have been substituted with a large variety of different organic cations to access novel higher dimensional perovskite structures. Luo *et al*. showed that 4-methylpiperidinum (AMP) and *N,N,N,N*-tetramethyl-1,6-hexanediammonium (TMHD) cations could form 1D perovskite structures of formula $(AMP)_2BiI_5$ and $(TMHD)BiBr_5$, respectively.[74,84] The semiconducting $(AMP)_2BiI_5$ showed an electrical conductivity of 2.69×10^{-9} S cm^{-1} at room temperature and obvious photoconductivity with a maximum photocurrent of 7.5 nA under AM 1.5 simulated solar light illumination. Since in thin films, charge transport is limited by grain boundaries, inch sized single crystals of $(TMHD)BiBr_5$ were used for the fabrication of photodetectors, and the device exhibited an on-off ratio of 10^3 and a fast photoresponse time ($\tau_{rise} = 8.9$ ms and $\tau_{decay} = 10.2$ ms).

1.2.9.2. X-ray Radiation Detectors

X-ray detectors are devices able to convert X-ray photons to electrical signals under an applied voltage. The materials with a large product of carrier mobility and lifetime ($\mu\tau$), high X-ray absorption coefficient, and low defect state density are highly beneficial for X-ray detector application. Sun *et al*. showed the potential of a lead-free hybrid double perovskite $(BA)_2CsAgBiBr_7$ (BA = butylammonium) as an X-ray detector material.[104] The fabricated $(BA)_2CsAgBiBr_7$ single crystal-based X-ray detector exhibited a sensitivity of 4.2 μC Gy_{air}^{-1} cm^{-2}. The excellent radiation sensitivity of $(BA)_2CsAgBiBr_7$ stems from its large $\mu\tau$ (1.21×10^{-3} cm^2 V^{-1}) and low defect state concentration (4.2×10^{10} cm^{-3}). Followed by this report, Tang and coworkers crystallized a 1D perovskite material featuring BiI_5^{2-} units separated by *N,N'*-dimethylethanediamonium (DMEDA) cation. They have fabricated an X-ray radiation detector using this material ($(DMEDA)BiI_5$) and the device delivered an X-ray sensitivity of 72.5 μC Gy_{air}^{-1} cm^{-2}.[80] The lower dimensionality of $(DMEDA)BiI_5$ single-crystal resulted in a low dark current (600 pA) and helped it to achieve a high X-ray sensitivity. Yang *et al*. employed the layered perovskite single crystals of $(NH_4)_3Bi_2I_9$ for X-ray detection due to its low ionic conductivity and excellent intrinsic stability. The single crystals of $(NH_4)_3Bi_2I_9$ featured anisotropic X-ray response and a low detection limit of 55 nGy_{air} s^{-1}.[105]

1.2.9.3. Photocatalysis

Photocatalysis is a process of utilizing solar energy for chemical transformations (e.g. dye degradation, photopolymerization) and energy conversion (e.g. water splitting, CO_2 reduction). Zhang *et al*. reported the utility of a 3D double perovskite $Cs_2AgBiBr_6$ as a photocatalyst for the degradation of cationic (Rhodamine B, Rhodamine 110), anionic (Methyl orange), and neutral (Methyl red) dyes.[106] The strong adsorption of the cationic dyes over the negatively charged surface of $Cs_2AgBiBr_6$ photocatalyst renders a faster degradation rate for these dyes compared to anionic and neutral dyes. The deposition of metals such as Pt and Au over the surface of $Cs_2AgBiBr_6$ further improved their photocatalytic efficiency due to the enhanced photogenerated electron-hole pair separation and transport at the $Cs_2AgBiBr_6$/metal heterojunction. Electron spin resonance analysis revealed that superoxide radical is the active species involved during the mineralization process of the dyes.

Liu *et al*. demonstrated that $Cs_2AgBiBr_6$ nanoplatelets (NPL's) as a photocatalyst for the CO_2 reduction.[107] The proposed mechanism of CO_2 reduction is through photo-induced electron transfer from $Cs_2AgBiBr_6$ to CO_2. The products of this photochemical reaction are CO and CH_4 (**Figure 1.8**a). Interestingly, they have observed that the photocatalytic production yield of CO and CH_4 was 4 fold higher for NPL morphology compared to their nanocube (NC) counterpart (**Figure 1.8**b). This was ascribed to the anisotropic carrier conductivity, long charge carrier diffusion length, and high density of photoactive metal sites at the surface of NPL's compared to NC's.
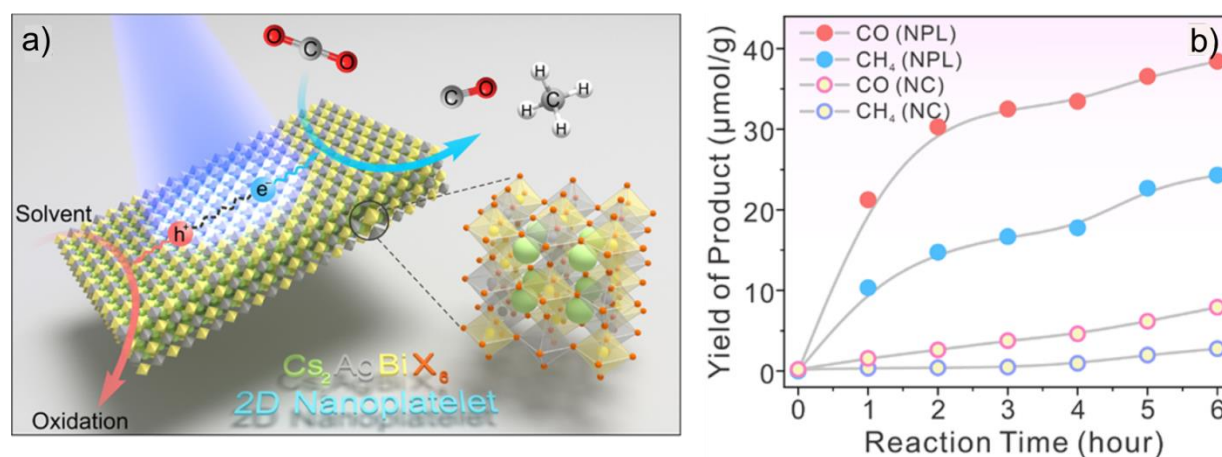
Figure 1.8. a) Schematic of the CO_2 reduction by $Cs_2AgBiBr_6$ nanoplatelets to CO and CH_4. b) Production yield of CO and CH_4 as a function of reaction time for catalysts $Cs_2AgBiBr_6$ NPL's and $Cs_2AgBiBr_6$ nanocubes. Adapted from reference 107.

Zhao *et al*. fabricated a photocatalytic system based on $(CH_3NH_3)_3Bi_2I_9$ perovskite for hydrogen production by the decomposition of hydriodic acid.[108] The photocatalytic rate of hydrogen generation was increased from 12.19 μmol g^{-1} h^{-1} to 169.21 μmol g^{-1} h^{-1} when Pt was used as a cocatalyst. The efficiency of the cocatalyzed hydrogen evolution reaction is 0.48%. Recently, Sillanpää and co-workers employed $Cs_3Bi_2I_9$ as a photocatalyst for Rhodamine B dye degradation.[109] 93% mineralization of the dye was observed after 3 hr continuous visible light illumination in presence of $Cs_3Bi_2I_9$ photocatalyst. Although Bi-perovskite materials have shown great potential in the field of photocatalysis, the poor recycling stability of these materials is yet to be solved.

1.3. Objectives of the present investigation

Bismuth-based perovskites are currently receiving intense research interest for optoelectronic device applications due to less toxicity and better moisture stability compared to lead-based analogues. Recent literature reports suggest that most bismuth halide perovskites consist of electronically inactive and insulating organic spacer cations. Therefore, the optical and electronic properties of these materials are solely dictated by the inorganic framework. The present thesis deals with synthesizing novel bismuth halide perovskite structures incorporating functional organic cations, molecular-level understanding of their photophysics, correlation of structure-property relationships, and exploring their use in various optoelectronic devices. The thesis is organized into four chapters. The **first chapter** gives an overview of halide perovskites, particularly of lead-free materials, and the recent developments in this area. In **Chapter 2**, we introduce a novel, lead-free, zero-dimensional perovskite-like material, (1,3-propanediammonium)$_2$Bi$_2$I$_{10}$.2H$_2$O, for optoelectronic applications. This material exhibited good moisture and thermal stability under ambient conditions. The photodetector device fabricated using it showed an efficient charge separation at low voltage (1 V) due to the good electronic conduction between the Bi$_2$I$_{10}^{4-}$ dimer units. In the second part of this chapter, we have used a straightforward methodology to reduce the dielectric confinement in hybrid A$_3$Bi$_2$I$_9$ type perovskite-like materials (A is an organic cation) to improve the charge-carrier separation efficiency. For that, the electronically inert methylammonium (MA) was replaced with a polarizable

benzylammonium cation in the well-studied $MA_3Bi_2I_9$ (MBI) structure. **Chapter 3** deals with the combined experimental and theoretical investigation on the role of functional organic cations (naphthalimides and biphenyl) in tuning the band alignment, photoconductivity, and optical bandgap of bismuth halide perovskites. In **Chapter 4**, we have fabricated an electrochemical double-layer capacitor using methylammonium bismuth iodide $(CH_3NH_3)_3Bi_2I_9$, a lead-free, zero-dimensional hybrid perovskite. A maximum areal capacitance of 5.5×10^{-3} F cm^{-2} was obtained, and the device retained 84.8% of its initial maximum capacitance even after 10,000 charge-discharge cycles.

1.4. References

1. Q. Chen, N. De Marco, Y. Yang, T. Bin Song, C. C. Chen, H. Zhao, Z. Hong, H. Zhou, Y. Yang, *Nano Today* **2015**, *10*, 355-396.

2. B. Saparov, D. B. Mitzi, *Chem. Rev.* **2016**, *116*, 4558-4596.

3. E. Sandor, W. A. Wooster, *Nature* **1958**, *182*, 1436.

4. D. Weber, *Inst. Anorg. Chem. Univ. Stutt.* **1978**, *33b*, 1443-1445.

5. D. B. Mitzi, D. B. Mitzi, *J. Chem. Soc., Dalton Trans.* **2001**, *1*, 1-12**.**

6. W. Li, Z. Wang, F. Deschler, S. Gao, R. H. Friend, A. K. Cheetham, *Nat. Rev. Mater.* **2017**, *2*, 16099.

7. J. Huang, Y. Yuan, Y. Shao, Y. Yan, *Nat. Rev. Mater.* **2017**, *2*, 17042.

8. J. S. Manser, J. A. Christians, P. V. Kamat, *Chem. Rev.* **2016**, *116*, 12956-13008.

9. Y. Zhao, K. Zhu, *Chem. Soc. Rev.* **2016**, *45*, 655-689.

10. K. Chen, S. Schu, S. Song, H. Tuysuz, *Chem. Soc. Rev.* **2018**, *47*, 7045-7077.

11. A. Kojima, K. Teshima, Y. Shirai, T. Miyasaka, *J. Am. Chem. Soc.* **2009**, *131*, 6050-6051.

12. J.-H. Im, C.-R. Lee, J.-W. Lee, S.-W. Park, N.-G. Park, *Nanoscale* **2011**, *3*, 4088-

4093.

13. H. S. Kim, C. R. Lee, J. H. Im, K. B. Lee, T. Moehl, A. Marchioro, S. J. Moon, R. Humphry-Baker, J. H. Yum, J. E. Moser, M. Gratzel, N.-G. Park, *Sci. Rep.* **2012**, *2*, 591 (1-7).

14. M. M. Lee, J. Teuscher, T. Miyasaka, T. N. Murakami, H. J. Snaith, *Sci. Rep.* **2012,** *338*, 643-648.

15. Y. Zhao, K. Zhu, *Chem. Soc. Rev*. **2016**, *45*, 655-689.

16. B. R. Sutherland, E. H. Sargent, *Nature Photonics* **2016**, 10, 295-302.

17. M. D. Smith, H. I. Karunadasa, Acc. Chem. Res. **2018**, *51*, 619-627.

18. H. Zhang, Z. Zhang, X. Chen, X. Song, Y. Zhang, R. Xiong, *J. Am. Chem. Soc.* **2021**, *143*, 1664-1672.

19. H. Zhang, Z. Zhang, X. Song, X. Chen, R. Xiong, *J. Am. Chem. Soc.* **2020**, *142*, 20208-20215.

20. X. Chen, X. Song, Z. Zhang, H. Zhang, Q. Pan, J. Yao, Y. You, R. Xiong, *J. Am. Chem. Soc.* **2020**, *142*, 10212-10218.

21. H.-Y. Ye, Y. Zhang, D.-W. Fu, R.-G. Xiong, *Angew. Chem. Int. Ed.* **2014**, *53*, 11242-11247.

22. C. Li, H. Wang, F. Wang, T. Li, M. Xu, H. Wang, Z. Wang, X. Zhan, *Light Sci. Appl.* **2020**, *3*, 1-8.

23. H. Huang, B. Pradhan, J. Hofkens, J. A. Steele, *ACS Energy Lett*. **2020**, *5*, 1107-1123.

24. C. Muthu, S. R. Nagamma, V. C. Nair, *RSC Adv*., **2014**, *4*, 55908-55911.

25. Y. Liu, Y. Zhang, X. Zhu, J. Feng, I. Spanopoulos, W. Ke, Y. He, X. Ren, Z. Yang, F. Xiao, K. Zhao, M. Kanatzidis, S. Liu, *Adv. Mater.* **2021**, *33*, *2006010* (1-10).

26. A. Kostopoulou, D. Vernardou, D. Makri, K. Brintakis, *J. Power Sources Adv.* **2020**, *3*, 100015 (1-6).

27. Z. Yi, H. Ladi, X. Shai, H. Li, Y. Shen, M. Wang, *Nanoscale Adv.* **2019**, 1276-1289.

28. A. H. Slavney, T. Hu, A. M. Lindenberg, H. I. Karunadasa, *J. Am. Chem. Soc*. **2016**, *138*, 2138-2141.

29. D. Umeyama, L. Leppert, B. A. Connor, M. A. Manumpil, J. B. Neaton, H. I. Karunadasa, *Angew. Chem. Int. Ed.* **2020**, *59*, 19087-19094.

30. C. Ma, N. Park, *ACS Energy Lett*. **2020**, *5*, 3268−3275.

31. D. Ghosh, A. J. Neukirch, D. Ghosh, C. Katan, *J. Mater. Chem. A*, **2020**, *8*, 21885-22438.

32. J. M. Hoffman, X. Che, S. Sidhik, X. Li, I. Hadar, J.-C. Blancon, H. Yamaguchi, M. Kepenekian, C. Katan, J. Even, C. C. Stoumpos, A. D. Mohite, M. G. Kanatzidis, *J. Am. Chem. Soc.* **2019**, *141*, 10661-10676.

33. J. S. Manser, J. A. Christians, P. V. Kamat, *Chem. Rev.* **2016**, *116*, 12956-13008.

34. T. Leijtens, K. Bush, R. Cheacharoen, R. Beal, A. Bowring, M. D. Mcgehee, *J. Mater. Chem. A,* **2017**, *5*, 11483-11500.

35. R. Nie, R. R. Sumukam, S. H. Reddy, M. Banavoth, S. Il Seok, *Energy Environ. Sci.* **2020**, *13*, 2363-2385.

36. X. Li, J. M. Hoffman, M. G. Kanatzidis, *Chem. Rev.* **2021**, *121*, 2230-2291**.**

37. R. Prasanna, A. Gold-parker, T. Leijtens, B. Conings, A. Babayigit, H. Boyen, M. F. Toney, M. D. Mcgehee, *J. Am. Chem. Soc.* **2017**, *139*, 11117-11124.

38. T. M. Brenner, D. A. Egger, L. Kronik, G. Hodes, D. Cahen, *Nat. Rev. Mater.* **2016**, *1*, 15007 (1-17).

39. A. D. Jodlowski, D. R.-padrón, R. Luque, G. D. Miguel, *Adv. Energy Mater.* **2018**, *8, 1703120* (1-24).

40. G. Xing, N. Mathews, S. S. Lim, Y. M. Lam, S. Mhaisalkar, T. C. Sum, *Science,* **2013**, *342*, 344-347.

41. S. D. Stranks, G. E. Eperon, G. Grancini, C. Menelaou, M. J. P. Alcocer, T. Leijtens, L. M. Herz, A. Petrozza, H. J. Snaith, *Science,* **2013**, *342*, 341-345.

42. Q. Dong, Y. Fang, Y. Shao, P. Mulligan, J. Qiu, L. Cao, J. Huang, *Science*, **2015**, *347*, 967-970.

43. Y. Deng, E. Peng, Y. Shao, Z. Xiao, Q. Dong, J. Huang, *Energy Environ. Sci.* **2015**, 8, 1544-1550.

44. C. Wehrenfennig, G. E. Eperon, M. B. Johnston, H. J. Snaith, L. M. Herz, *Adv. Mater.* **2014**, *26*, 1584-1589.

45. T. Ishihara, J. Takahashi, T. Goto, *Solid State Communications* **1989**, *69*, 933-936.

46. Y. Hsiao, T. Wu, M. Li, Q. Liu, W. Qin, B. Hu, *J. Mater. Chem. A* **2015**, *3*, 15372-15385.

47. B. Cheng, T.-Y. Li, P. Maity, P.-C. Wei, D. Nordlund, K.-T. Ho, D.-H. Lien, C.-H. Lin, R.-Z. Liang, X. Miao, I. A. Ajia, J. Yin, D. Sokaras, A. Javey, I. S. Roqan, O. F. Mohammed, J.-H. He, *Commun. Phys.* **2018**, *1*, 80 (1-8).

48. S. Attique, N. Ali, S. Ali, R. Khatoon, N. Li, A. Khesro, S. Rauf, S. Yang, H. Wu, *Adv. Sci.* **2020**, *7*, 1903143 (1-34).

49. J. Li, H. Cao, W. Jiao, Q. Wang, M. Wei, I. Cantone, J. Lü, A. Abate, *Nat. Commun.* **2020**, *11*, 310 (1-5).

50. A. Babayigit, D. D. Thanh, A. Ethirajan, J. Manca, M. Muller, H.-G. Boyen, B. Conings, *Scientific Reports* **2016**, *6*, 18721 (1–11).

51. A. Babayigit, A. Ethirajan, M. Muller, B. Conings, *Nat. Publ. Gr.* **2016**, *15*, 247–251.

52. S. Wang, Y. Jiang, E. J. Juarez-perez, L. K. Ono, Y. Qi, *Nature Energy* **2016**, *2*, 16195 (1-8).

53. J. M. Frost, K. T. Butler, F. Brivio, C. H. Hendon, M. Van Schilfgaarde, A. Walsh, *Nano Lett.* **2014**, *14*, 2584-2590.

54. J. Yang, B. D. Siempelkamp, D. Liu, T. L. Kelly, *ACS Nano* **2015**, *9*, 1955-1963.

55. F. M. Rombach, S. A. Haque, T. J. Macdonald, *Energy Environ. Sci*., **2021**, *14*, 5161-5190.

56. N. H. Nickel, F. Lang, V. V Brus, O. Shargaieva, J. Rappich, *Adv. Electron. Mater.* **2017**, *3*, 1700158 (1-9).

57. T. Krishnamoorthy, H. Ding, C. Yan, L. Leong, T. Baikie, *J. Mater. Chem. A*,

2015, *3*, 23829-23832.

58. C. C. Stoumpos, L. Fraser, D. J. Clark, Y. S. Kim, H. Sonny, A. J. Freeman, J. B. Ketterson, J. I. Jang, M. G. Kanatzidis, A. J. Freeman, John B. Ketterson, J. I. Jang, M. G. Kanatzidis, *J. Am. Chem. Soc.* **2015**, *137*, 6804-6819.

59. W. Ming, H. Shi, M.-H. Du, *J. Mater. Chem. A*, **2016**, 4, 13852-13858.

60. L.-J. Chen, *RSC Adv.* **2018**, *8*, 18396-18399.

61. C. C. Stoumpos, C. D. Malliakas, M. G. Kanatzidis, *Inorg. Chem.* **2013**, *52*, 9019-9038.

62. L. Ma, F. Hao, C. C. Stoumpos, B. T. Phelan, M. R. Wasielewski, M. G. Kanatzidis, *J. Am. Chem. Soc.* **2016**, *138*, 14750-14755.

63. R. Lin, K. Xiao, Z. Qin, Q. Han, C. Zhang, M. Wei, M. I. Saidaminov, Y. Gao, J. Xu, M. Xiao, A. Li, J. Zhu, E. H. Sargent, H. Tan, *Nat. Energy* **2019**, *4*, 864-873.

64. P. Li, H. Dong, J. Xu, J. Chen, B. Jiao, X. Hou, J. Li, Z. Wu, *ACS Energy Lett.* **2020**, *5*, 2327-2334.

65. P. Li, X. Liu, Y. Zhang, C. Liang, G. Chen, F. Li, M. Su, G. Xing, X. Tao, Y. Song, *Angew. Chem. Int. Ed.* **2020**, *132*, 6976-6981.

66. K. Nishimura, M. A. Kamarudin, D. Hirotani, K. Hamada, Q. Shen, S. Iikubo, T. Minemoto, K. Yoshino, S. Hayase, *Nano Energy* **2020**, *74*, 104858 (1-10).

67. C. Wu, Q. Zhang, G. Liu, Z. Zhang, D. Wang, B. Qu, Z. Chen, L. Xiao, *Adv. Energy Mater.* **2020**, *10*, 1902496 (1-30).

68. S. Attique, N. Ali, S. Ali, R. Khatoon, N. Li, A. Khesro, S. Rauf, S. Yang, H. Wu, *Adv. Sci.* **2020**, *7*, 1903143 (1-34).

69. R. Nie, R. R. Sumukam, S. H. Reddy, M. Banavoth, S. Il Seok, *Energy Environ. Sci.* **2020**, *13*, 2363-2385.

70. E. V. Ushakova, S. A. Cherevkov, V. A. Kuznetsova, A. V. Baranov, *Materials* **2019**, *12*, 3845 (1-27).

71. M. Li, Z. Xia, *Chem. Soc. Rev.* **2021**, *50*, 2626-2662.

72. K. Eckhardt, V. Bon, J. Getzschmann, J. Grothe, F. M. Wisser, S. Kaskel, *Chem.*

Commun. **2016**, *52*, 3058-3060.

73. I. W. H. Oswald, E. M. Mozur, I. P. Moseley, H. Ahn, J. R. Neilson, *Inorg. Chem.* **2019**, *58*, 5818-5826.

74. C. Ji, P. Wang, Z. Wu, Z. Sun, L. Li, J. Zhang, W. Hu, M. Hong, J. Luo, *Adv. Funct. Mater.* **2018**, *28*, 1705467 (1-7).

75. C. Ni, G. Hedley, J. Payne, V. Svrcek, C. McDonald, L. K. Jagadamma, P. Edwards, R. Martin, G. Jain, D. Carolan, D. Mariotti, P. Maguire, I. Samuel, J. Irvine, *Nat. Commun.* **2017**, *8*, 170 (1-7).

76. R. L. Z. Hoye, R. E. Brandt, A. Osherov, V. Stevanovic, S. D. Stranks, M. W. B. Wilson, H. Kim, A. J. Akey, J. D. Perkins, R. C. Kurchin, J. R. Poindexter, E. N. Wang, M. G. Bawendi, V. Bulovic, T. Buonassisi, *Chem. - A Eur. J.* **2016**, *22*, 2605-2610.

77. T. Kawai, S. Shimanuki, *Phy. Stat. Sol.* **1993**, *177*, K43-K45.

78. Z. Zhang, X. Li, X. Xia, Z. Wang, Z. Huang, B. Lei, Y. Gao, *J. Phys. Chem. Lett.* **2017**, *8*, 4300-4307.

79. M. Vigneshwaran, T. Ohta, S. Iikubo, G. Kapil, T. S. Ripolles, Y. Ogomi, T. Ma, S. S. Pandey, Q. Shen, T. Toyoda, K. Yoshino, T. Minemoto, S. Hayase, *Chem. Mater.* **2016**, *28*, 6436-6440.

80. W. Zhang, X. Liu, L. Li, Z. Sun, S. Han, Z. Wu, J. Luo, *Chem. Mater.* **2018**, *30*, 4081-4088.

81. W. Yin, Y. Weng, M. Jiang, S. Yu, Q. Zhu, J. Dai, *Inorg. Chem.* **2020**, *59*, 5161-5169.

82. L. Yao, G. Niu, L. Yin, X. Du, Y. Lin, X. Den, J. Zhang, J. Tang, *J. Mater. Chem. C* **2020**, *8*, 1239-1243.

83. T. Li, Y. Hu, C. A. Morrison, W. Wu, H. Han, N. Robertson, *Sustain. Energy Fuels* **2017**, *1*, 308-316.

84. W. Zhang, K. Tao, C. Ji, Z. Sun, S. Han, J. Zhang, Z. Wu, J. Luo, *Inorg. Chem.* **2018**, *57*, 4239-4243.

85. M. K. Jana, S. M. Janke, D. J. Dirkes, S. Dovletgeldi, C. Liu, X. Qin, K. Gundogdu, W. You, V. Blum, D. B. Mitzi, *J. Am. Chem. Soc.* **2019**, *141*, 7955-7964.

86. L.-Y. Bi, Y.-Q. Hu, M.-Q. Li, T.-L. Hu, H.-L. Zhang, X.-T. Yin, W.-X. Que, M. S. Lassoueda, Y.-Z. Zheng, *J. Mater. Chem. A*, **2019**, *7*, 19662-19667.

87. B. A. Connor, L. Leppert, M. D. Smith, J. B. Neaton, H. I. Karunadasa, *J. Am. Chem. Soc.* **2018**, *140*, 5235-5240.

88. Y. Yao, B. Kou, Y. Peng, Z. Wu, L. Li, S. Wang, X. Zhang, X. Liu, J. Luo, *Chem. Commun.* **2020**, *56*, 3206-3209.

89. A. H. Slavney, T. Hu, A. M. Lindenberg, H. I. Karunadasa, *J. Am. Chem. Soc.* **2016**, *138*, 2138-2141.

90. Q. Zhang, C. Wu, X. Qi, F. Lv, Z. Zhang, Y. Liu, S. Wang, B. Qu, Z. Chen, L. Xiao, *ACS Appl. Energy Mater.* **2019**, *2*, 3651-3656.

91. K. Du, W. Meng, X. Wang, Y. Yan, D. B. Mitzi, *Angew. Chem. Int. Ed.* **2017**, *56*, 8158-8162.

92. F. Ji, J. Klarbring, F. Wang, W. Ning, L. Wang, C. Yin, J. S. M. Figueroa, C. K. Christensen, M. Etter,   T. Ederth, L. Sun, S. I. Simak, I. A. Abrikosov, F. Gao, *Angew. Chemie* **2020**, *132*, 15303-15306.

93. A. H. Slavney, L. Leppert, D. Bartesaghi, A. Gold-Parker, M. F. Toney, T. J. Savenije, J. B. Neaton, H. I. Karunadasa, *J. Am. Chem. Soc.* **2017**, *139*, 5015-5018.

94. K. W. Jung, M. R. Sohn, H. M. Lee, I. S. Yang, S. Do Sung, J. Kim, E. W. Diau, W. I. Lee, *Sustainable Energy Fuels* **2018**, *2*, 294-302.

95. A. Kulkarni, A. K. Jena, M. Ikegami, T. Miyasaka, *Chem. Commun.* **2019**, *55*, 4031-4034**.**

96. B. W. Park, B. Philippe, X. Zhang, H. Rensmo, G. Boschloo, E. M. J. Johansson, *Adv. Mater.* **2015**, *27*, 6806-6813.

97. A. A. Hussain, A. K. Rana, M. Ranjan, *Nanoscale* **2019**, *11*, 1217-1227.

98. M. B. Johansson, H. Zhu, E. M. J. Johansson, *J. Phys. Chem. Lett.* **2016**, *7*, 3467-

3471.

99. G. Liang, X. Chen, Z. Chen, H. Lan, Z. Zheng, P. Fan, X.-Q. Tian, J.-Y. Duan, Y.-D. Wei, Z.-H. Su, *J. Phys. Chem. C* **2019**, *123*, 27423-27428.

100. Q. Jia, C. Li, W. Tian, M. B. Johansson, E. M. J. Johansson, R. Yang, *ACS Appl. Mater. Interfaces* **2020**, *12*, 43876-43884.

101. W. Hu, X. He, Z. Fang, W. Lian, Y. Shang, X. Li, W. Zhou, M. Zhang, T. Chen, Y. Lu, L. Zhang, L. Ding, S. Yang, *Nano Energy* **2020**, *68*, 104362 (1-44).

102. S. M. Jain, D. Phuyal, M. L. Davies, M. Li, B. Philippe, C. De Castro, C. Tsoi, O. Karis, H. Rensmo, T. Edvinsson, J. R. Durrant, *Nano Energy* **2018**, *49*, 614-624.

103. X. Tong, W. Kong, Y. Wang, J. Zhu, L. Luo, Z. Wang, *ACS Appl. Mater. Interfaces* **2017**, *9*, 18977-18985.

104. Z. Xu, X. Liu, Y. Li, X. Liu, T. Yang, C. Ji, S. Han, Y. Xu, J. Luo, Z. Sun, *Angew. Chem.* **2019**, *131*, 15904 -15908.

105. R. Zhuang, X. Wang, W. Ma, Y. Wu, X. Chen, L. Tang, H. Zhu, J. Liu, L. Wu, W. Zhou, X. Liu, Y. (Michael) Yang, *Nat. Photonics* **2019**, *13*, 602-608.

106. Z. Zhanga, Y. Liang, H. Huang, X. Liub, Q. Li, L. Chena, D. Xu, *Angew. Chem. Int. Ed.* **2019**, *58*, 7263-7267.

107. Z. Liu, H. Yang, J. Wang, Y. Yuan, K. H.-Kimball, T. Cai, P. Wang, A. Tang, O. Chen, *Nano Lett*. **2021**, *21*, 1620-1627.

108. Y. Guo, G. Liu, Z. Li, Y. Lou, J. Chen, Y. Zhao, *ACS Sustainable Chem. Eng*. **2019**, *7*, 15080-15085.

109. B.-M. Bresolin, C. Günnemann, D. W. Bahnemann, M. Sillanpää, *Nanomaterials* **2020**, *10*, 763.

Chapter 2

Organic Cations Assisted Reduction of Quantum and Dielectric Confinements in Bismuth Halide Perovskites

2.1. Abstract

Quantum and dielectric confinements have a significant influence on the electronic properties of low-dimensional bismuth-based perovskites. The majority of the bismuth halide perovskites exhibit poor charge carrier separation and transport owing to strong quantum and dielectric confinement effects. In this chapter, we introduce a novel, lead-free, zero-dimensional perovskite material, $(1,3\text{-propanediammonium})_2Bi_2I_{10}\cdot 2H_2O$, with weak quantum confinement. The photodetector device fabricated using this material showed an efficient charge separation at low voltage (1 V) due to its quantum-well structure. In the second work, we have addressed the high dielectric confinement and the associated poor charge-carrier separation in $A_3Bi_2I_9$ (A is an organic cation) type perovskite materials. For that, the electronically inert methylammonium (MA) was replaced with a polarizable benzylammonium (BA) cation in the $MA_3Bi_2I_9$ structure. Flash-photolysis time-resolved microwave conductivity studies revealed about 2.5-fold enhancement of $\phi\Sigma\mu$ (the product of charge-carrier generation quantum yield and the sum of charge-carrier mobilities) for $BA_3Bi_2I_9$ when compared to that of $MA_3Bi_2I_9$, which is attributed to the low dielectric confinement in the former.

2.2. Introduction

The word perovskite was initially used to refer to the mineral $CaTiO_3$ specifically, but nowadays, it represents a class of materials isostructural to $CaTiO_3$. Bi-based hybrid perovskite materials attracted immense research attention in recent years due to their versatile crystal structures and associated tunable optoelectronic properties. The low-dimensional crystal structures and wide bandgap of organic spacer cations imparted strong charge carrier confinements in these materials. Even though in most of the Bi-perovskites, the organic spacer cations are electronically insulating, they could modulate the van der Waals spacing between the inorganic octahedrons and the dielectric environment of the medium surrounding the inorganic framework. Therefore, the rational selection of organic spacer cation is crucial for manipulating the electronic confinements such as quantum and dielectric confinements in these low dimensional perovskites.

2.2.A. Quantum confinement effect

The optical bandgap and exciton binding energy of perovskite materials are strongly influenced by their structural dimensionality and particle size. This phenomenon is observed in other nanomaterials also and is known as quantum confinement. Due to this effect, perovskite nanoparticles have high exciton binding energy and exhibit strong photoluminescence compared to the corresponding bulk material.[1]
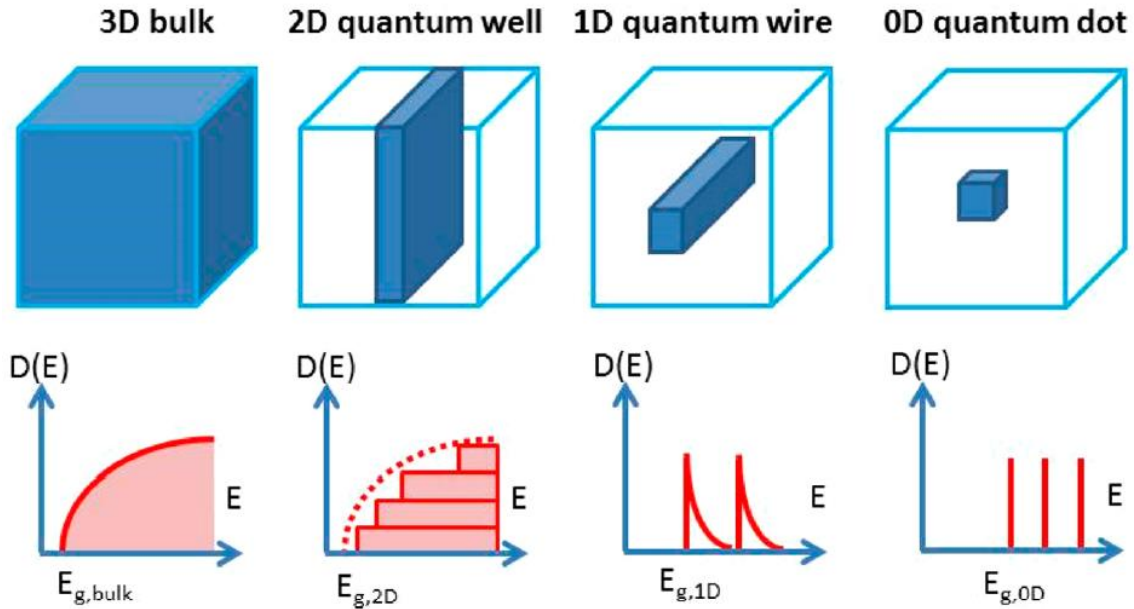
Figure 2.1. Schematic representation of various quantum confinements in perovskites and their corresponding joint density of states plot (Adapted from reference 2).

Quantum confinement will modify the band edge joint density of states from continuum to discrete up on dimensional reduction of the material from 3D to 0D (**Figure 2.1**).[2] As a consequence of this band edge modification, the bandgap and exciton binding energy of perovskites increases from 3D→2D→1D→0D. For layered 2D perovskite, the inorganic layer thickness tunes the quantum confinement effect. When inorganic layer thickness increases, the quantum confinement effect reduces, and thereby the optical bandgap and exciton binding energy will also be altered. Kanatzidis *et al*. prepared thin films of a series of 2D perovskite materials, $(CH_3(CH_2)_3NH_3)_2(CH_3NH_3)_{n-1}Pb_nI_{3n+1}$; inorganic layer thickness (*n*) = 1 to 4, by a single-step solution processing method.[4] The optical bandgap of these materials was
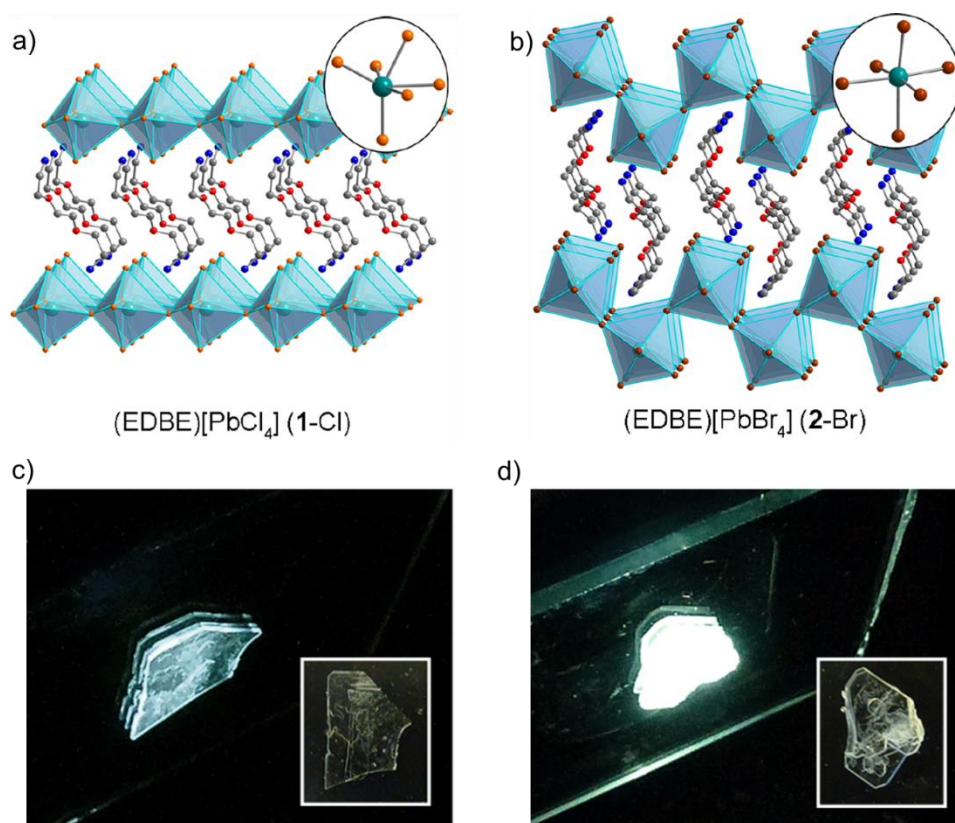
Figure 2.2. a) and b) are the crystals structures of (EDBE)[PbCl$_4$] and (EDBE)[PbBr$_4$] respectively (EDBE= 2,2'- (ethylenedioxy)bis(ethylammonium)). c) and d) are the photographs of (EDBE)[PbCl$_4$] and (EDBE)[PbBr$_4$] single crystals under 310 and 365 nm excitation respectively. Adapted from reference 3.

reduced from 2.24 eV to 1.60 eV when the *n* increased from 1 to 4 due to the reduced quantum confinement effect. Following this optical bandgap narrowing trend, photoluminescence maximum also exhibited a gradual bathochromic shift. Yang *et al*. prepared an atomically thin 2D perovskite material, (C$_4$H$_9$NH$_3$)$_2$PbBr$_4$, by solution processing using a ternary co-solvent method and via the conventional scotch tape exfoliation process.[5] The layered perovskites with inorganic sheet thickness, *n* = 3, 8,

and 22 featured distinct absorption and photoluminescence properties attributed to the quantum confinement effect. The exfoliated perovskites exhibited a wide optical bandgap and blue-shifted emission compared to the bulk crystals owing to the lattice expansion in the former.

Another important feature of the strong quantum confinement effect is the white-light generation from self-trapped excitonic states. The self-trapped excitonic energy levels are transient states generated upon photoexcitation of low-dimensional perovskite structures. The soft ionic nature of the inorganic lattice is vulnerable to structural deformation in the excited state, which leads to an offset in the excited state parabolic potential energy functions with respect to the ground state. This leads to highly Stokes shifted, intense phonon mediated photoluminescence with long carrier lifetime in the microsecond or millisecond time scale. White light-emitting perovskites are promising for solid-state lighting applications due to their high photoluminescence quantum yield, low self-absorption, and high color rendering index. Karunadasa's group reported broad white light emission from ⟨110⟩ corrugated 2D perovskite (N-MEDA)[$PbBr_4$] with a photoluminescence quantum yield (PLQY) of 0.15% and chromaticity coordinate corresponds to "warm" white light.[6] Chloride substituted perovskite derivate, (N-MEDA)[$PbBr_{3.5}Cl_{0.5}$], exhibited improved PLQY of 1.5% and "cold" white light with chromaticity coordinate of (0.31,0.36). Moreover, the CRI index of (N-MEDA)[$PbBr_{3.5}Cl_{0.5}$] is 85, which is much higher than that of conventional fluorescent light sources (~65). Followed by this report, the same group

have reported layered $\langle 100 \rangle$ and $\langle 110 \rangle$ perovskites, (EDBE)[PbBr$_4$] and (EDBE)[PbCl$_4$], respectively (EDBE: 2,2′- (ethylenedioxy)bis(ethylammonium); **Figure 2.2a** and **2.2b**). Both the materials exhibited broad white light emission with a higher PLQY of 9% for (EDBE)[PbBr$_4$] (**Figure 2.2c** and **2.2d**). Excitation intensity-dependent photoluminescence measurement revealed no saturation of photoluminescence intensity at high pump fluence (300 mW/cm^2), which implies that the origin of emission is from self-trapped excitonic states rather than permanent defects. Importantly, the material has retained 100% of its initial PLQY even after 3 months of continuous UV light irradiation. Kanatzidis *et al*. correlated extend of metal halide octahedral distortion (Δd) with self-trapped excitonic emission. They found that Δd is highest for α-(DMEN)PbBr$_4$ (DMEN: 2-(Dimethylamino)ethylamine) compared to (DMAPA)PbBr$_4$ and (DMABA)PbBr$_4$ (DMAPA: 3-(Dimethylamino)-1-propylamine, DMABA: 4-dimethylaminobutylamine) owing to the $\langle 110 \rangle$ corrugated structure of α-(DMEN)PbBr$_4$.[7] Large octahedral distortion in α-(DMEN)PbBr$_4$ is reasoned for its broadest emission (FWHM = 183 nm) and longest average photoluminescence lifetime (1.39 ns) among the three materials. Although strong quantum confinement could bring excellent photoluminescence property in low dimensional perovskites, the localization of charge carriers or high exciton binding energy is not beneficial for optoelectronic applications.

The Quantum confinement effect is very pronounced in Bi halide perovskites because they usually adopt zero-dimensional crystal structures. Wessels *et al*. reported

strong electron-phonon coupling in $Cs_3Bi_2I_9$ perovskite, which leads to lattice deformations or polarons.[8] Irvine *et al.* proposed a quantum dot structure for $MA_3Bi_2I_9$ perovskite due to the insulating nature of methylammonium cations around the $Bi_2I_9{}^{3-}$ clusters.[9] The quantum dot structure of $MA_3Bi_2I_9$ subsequently leads to a short carrier lifetime and high exciton binding energy.

2.2.B. Dielectric confinement effect

2D perovskites have a quantum-well structure with inorganic layers act as semiconducting wells and organic cations as insulating barriers. The dielectric constant mismatch between the inorganic wells and organic barriers leads to an "image charge" effect called dielectric confinement. Image charge is a theoretical terminology representing two charge carriers (electron and hole) residing on either side of the dielectric interface, separating two dielectric mediums of different dielectric constants. Dielectric confinement has a strong influence on the exciton binding energy of perovskites, *i.e.*, the strength of dielectric confinement is directly proportional to the exciton binding energy. Electron-hole pairs generated in the inorganic layers will experience a Coulombic force of attraction, and this force will extend to the organic barriers as well. If the organic cations are highly polarizable, it could effectively screen the electrostatic force of attraction between the charge carriers, and thereby exciton binding energy can be reduced.[10]

Post synthetic I_2 intercalation in a 2D layered perovskite material is an efficient strategy to reduce the dielectric confinement, modulate the optical bandgap (E_g) and exciton binding energy (E_b).[11] The I_2 intercalated perovskite, $(IC_6)_2[PbI_4].2I_2$ (IC_6: 1-iodo hexylammonium), featured a narrow optical bandgap and low exciton binding energy of 2.49 eV and 180 meV respectively compared to the pristine perovskite, $(IC_6)_2[PbI_4]$ (E_g = 2.56 eV and E_b = 230 meV). Ishihara *et al.* reported a 100 meV reduction of the exciton binding energy in a layered perovskite material,
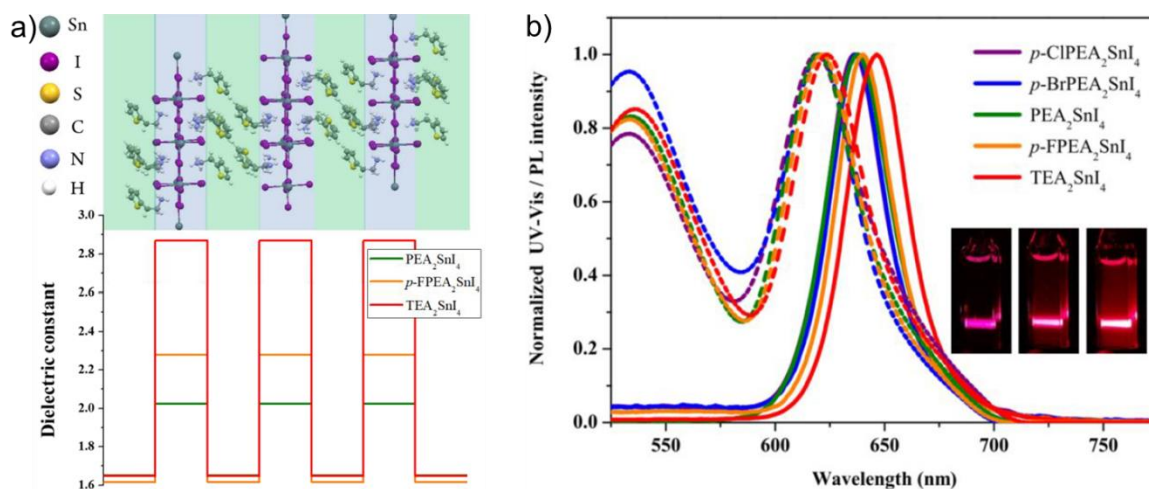
Figure 2.3. a) Schematic representation of 2D Sn halide perovskites and the corresponding dielectric constants of inorganic (SnI_4^{2-}) and organic layers. b) Optical absorption and photoluminescence spectra of *p*-ClPEA$_2$SnI$_4$, *p*-BrPEA$_2$SnI$_4$, PEA$_2$SnI$_4$, *p*-FPEA$_2$SnI$_4$, TEA$_2$SnI$_4$ perovskites. Inset shows the emission photographs of PEA$_2$SnI$_4$ (left), *p*-FPEA$_2$SnI$_4$ (center), and TEA$_2$SnI$_4$ (right) nano-disks. Adapted from reference 13.

(decylammonium)$_2$PbI$_4$ compared to (phenethylammonium)$_2$PbI$_4$.[12] This observation was attributed to the high dielectric constant of aromatic conjugated phenethylammonium cation compared to the aliphatic decylammonium cation. Chiu

et al. demonstrated the tuning of PLQY in 2D Sn halide perovskites by varying the dielectric constant of the organic spacer cations.[13] They have synthesized a homologous series of Sn-based perovskites, *p*-ClPEA$_2$SnI$_4$, *p*-BrPEA$_2$SnI$_4$, PEA$_2$SnI$_4$, *p*-FPEA$_2$SnI$_4$, TEA$_2$SnI$_4$ (PEA: phenylethyl ammonium, TEA: 2-(thiophen-2-yl)ethyl ammonium). DFT calculations suggested a large mismatch in the dielectric constants of SnI$_4^{2-}$ layers and 2-(thiophen-2-yl)ethyl ammonium organic barriers of TEA$_2$SnI$_4$ (**Figure 2.3**a). The strong dielectric confinement in TEA$_2$SnI$_4$ resulted in a higher PLQY (5.8%) compared to the other perovskites in the series. Absorbance and PL spectra exhibited a gradual red shift upon increasing the strength of dielectric confinement (**Figure 2.3**b).
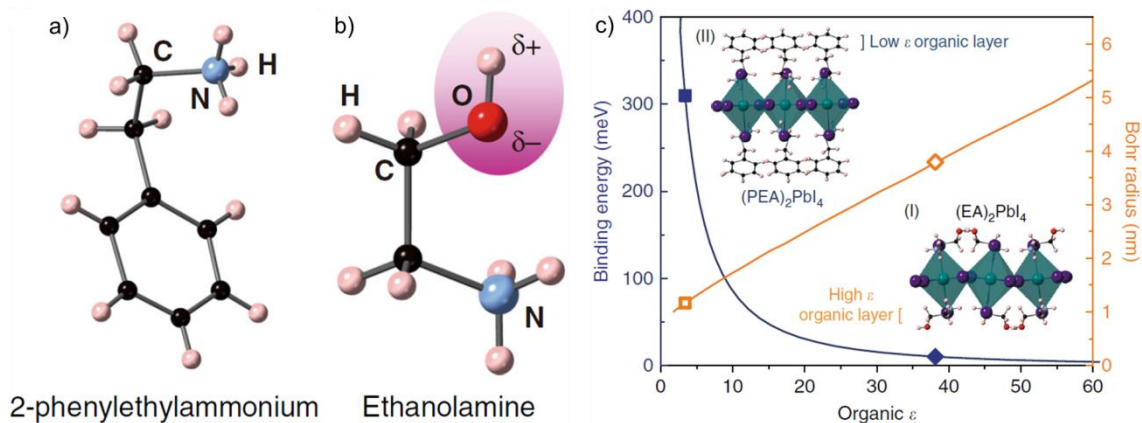
Figure 2.4. a) The chemical structures of organic spacer cations selected for tuning the dielectric confinement of 2D lead halide perovskites. b) Graph showing the variation of exciton binding energy and exciton Bohr radius of the perovskites with respect to the polarizability of organic spacer layers. Adapted from reference 14.

He *et al*. investigated the role of organic spacer cations such as benzylammonium and ethanolammonium in tuning the dielectric confinement of 2D lead halide

perovskites (**Figure 2.4**a).[14] The material $(HOCH_2CH_2NH_3)_2PbI_4$ featured extremely low exciton binding energy (13 meV) compared to (2-phenylethylammonium)PbI_4 (250 meV; **Figure 2.4**b). The low exciton binding energy of this material was attributed to the high dielectric constant of ethanolamine (37), which lowered the dielectric confinement in $(HOCH_2CH_2NH_3)_2PbI_4$ (**Figure 2.4**b). Moreover, the polarized ethanolamine effectively screened the charged defects in the material and subsequently resulted in high electron and hole mobility of 11.1 and 9.5 cm^2 V^{-1} s^{-1}, respectively. Apart from these Pb-based perovskites, most of the Bi-halide perovskite having $A_3Bi_2I_9$ structures reported so far consist of organic spacers with low dielectric constants resulting in high dielectric confinement in the perovskite structure. Coupled with strong quantum confinement, these perovskite structures exhibit poor optoelectronic performances.

2.3. Results and discussion

2.3.A. Quantum-well structure and charge carrier transport

It could be assumed that the creation of zero-dimensional perovskites with a quantum-well structure would exhibit improved electronic properties without compromising the stability aspects. This could be achieved by periodically aligning the inorganic dimer units in one of the three axes without hindering the organic moieties. Keeping this in mind, in the present work, we have synthesized and characterized a novel, lead-free, zero-dimensional perovskite material,

$(PD)_2Bi_2I_{10} \cdot 2H_2O$ (**PDBI**, PD: 1,3-propanediammonium). Single crystals of **PDBI** were prepared by the antisolvent diffusion technique using methanol as the good solvent and chloroform as the poor solvent.
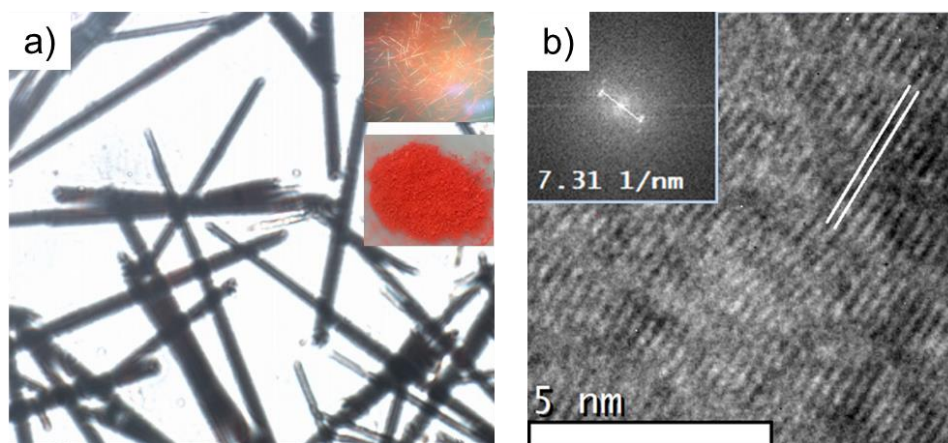
Figure 2.5. a) Optical polarizing microscope image of the crystals of **PDBI**. The inset shows the photograph of the crystals (top) and powder (bottom) samples b) High-resolution transmission electron microscope image of **PDBI**. The corresponding FFT image is shown in the inset.

Needle-like single crystals having several millimeters of lengths were obtained (**Figure 2.5**a). Like most of the Bi-halide perovskites, the single crystals and the powdered form of **PDBI** featured red color owing to its relatively wide optical bandgap than the lead-based analogues (inset of **Figure 2.5**a). The high-resolution transmission electron microscopy image showed a well-defined atomic lattice with a spacing of 1.3 Å (**Figure 2.5**b). Bright diffraction spots in the fast Fourier transform (FFT) image indicated the high crystallinity of the material. Structure characterization of **PDBI** was performed by single-crystal X-ray diffraction (XRD) analysis.

2.3.A1. Single crystal X-ray structural analysis
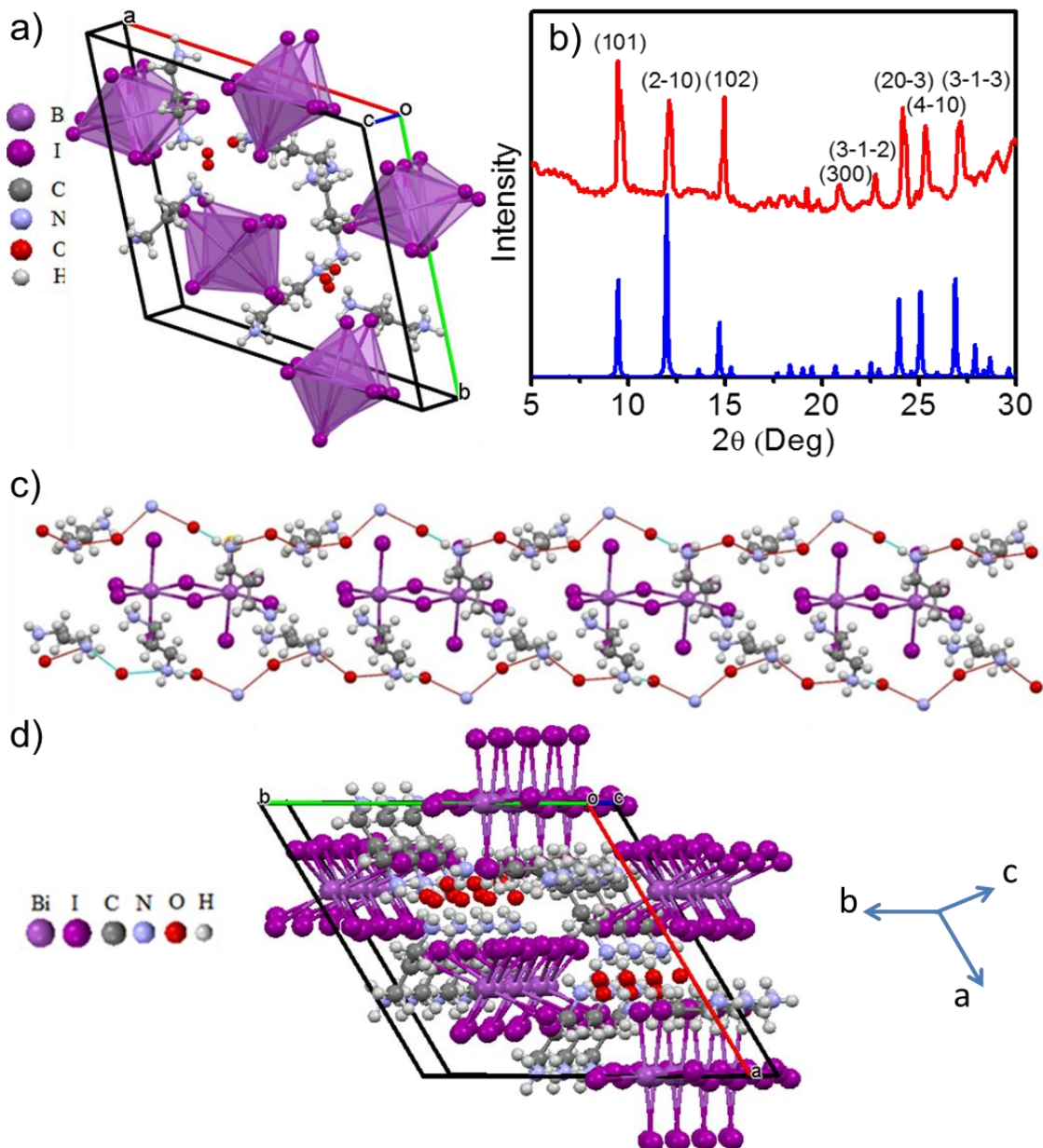
Figure 2.6. (a) The unit cell of **PDBI**, the crystal system is trigonal with the *P3₁21* space group. (b) Simulated (blue line) and experimental (red line) XRD patterns of **PDBI** obtained from the single-crystal sample. (c) $Bi_2I_{10}^{4-}$ dimer layer sandwiched between the organic layers. (d) Crystal growth of **PDBI** along the crystallographic "c" axis. $Bi_2I_{10}^{4-}$ dimers are aligned in this direction without the hindrance of organic cations. The dimer $Bi_2I_{10}^{4-}$ is formed by the edge-sharing of two BiI_6^{3-} octahedrons.

The crystal system was found to be trigonal with the $P3_121$ space group (**Figure 2.6**a). Powder XRD patterns obtained from the powdered single crystals were well matched with the simulated patterns obtained from the single crystal X-ray analysis (**Figure 2.6.**b). The crystals have a preferential growth along the crystallographic *a* and *b* axes showing an intense characteristic peak around $2\theta = 12.5°$, corresponding to the ⟨2-10⟩ plane. Each $Bi_2I_{10}^{4-}$ dimer was formed by the edge-sharing of two tilted BiI_6^{3-} octahedrons with two different bridging I−Bi−I bond lengths (3.19 and 3.25 Å). Previously reported bismuth- and antimony-based zero-dimensional perovskites such as $(CH_3NH_3)_3Bi_2I_9$, $(CH_3NH_3)_3Sb_2I_9$, $(NH_4)_3Bi_2I_9$, and $Cs_3Bi_2I_9$ are formed by the face sharing of octahedra.[15−18] In the present material, the BiI_6^{3-} octahedral units were separated by propane diammonium cations, which are connected through hydrogen bonding from water molecules (**Figure 2.6.**c). Well-aligned inorganic units along the crystallographic *c* axis and the sandwiched organic cation layers on either side result in a quantum-well structure. **Figure 2.6.**d provides the three-dimensional view of the quantum-well structure of **PDBI**.
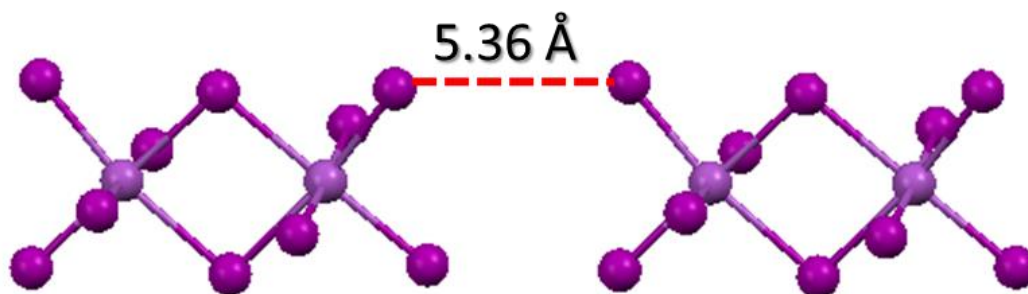
Figure 2.7. Schematic illustration of the inter-cluster ($Bi_2I_{10}^{4-}$) distance in **PDBI**. The separating distance between the adjacent $Bi_2I_{10}^{4-}$ dimer units was calculated using Mercury 3.7 software.

Compared to the distance between the neighboring $Bi_2I_9{}^{3-}$ dimers in $(CH_3NH_3)_3Bi_2I_9$ (14.3 Å), the $Bi_2I_{10}{}^{4-}$ clusters in **PDBI** are separated by a distance of only 5.36 Å (**Figure 2.7**). This is beneficial to improve the electronic communication between the inorganic clusters in **PDBI** than that in the former. Water molecules in the **PDBI** structure are assumed to be trapped during the crystallization process because of the hygroscopic nature of the propane diammonium cation. The presence of water molecules was confirmed from the Fourier transform infrared spectroscopy analysis, which showed a broad O−H stretching frequency at 3500 cm^{-1} (**Figure 2.8**).
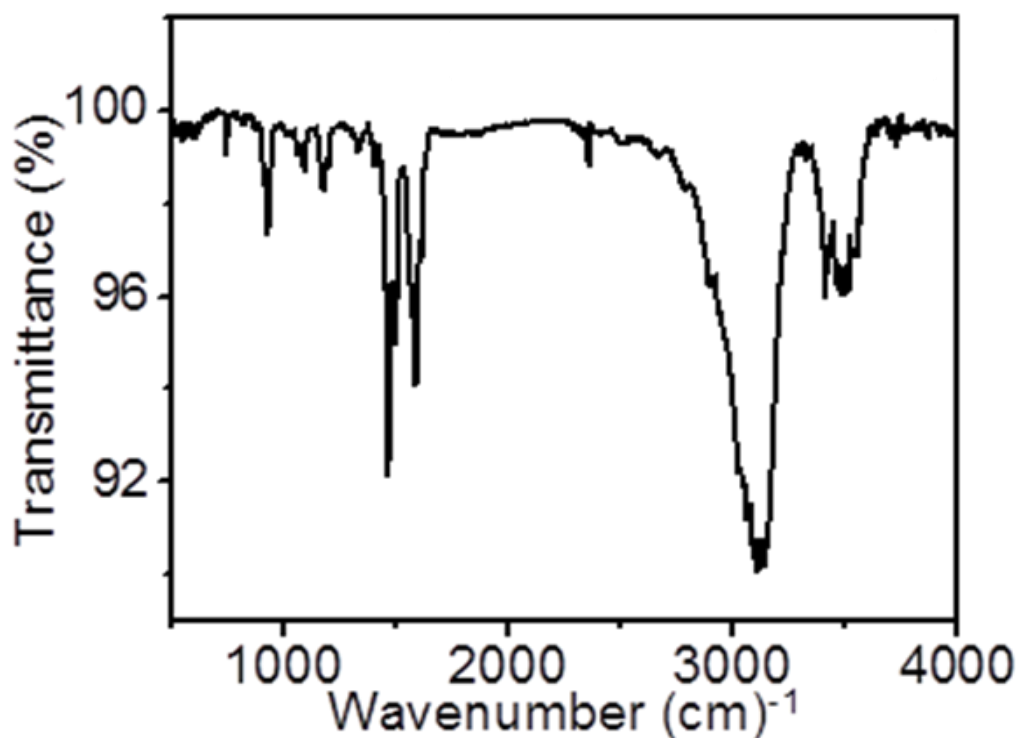
Figure 2.8. Fourier transform infrared spectrum of **PDBI**.

2.3.A2. Optical characterizations
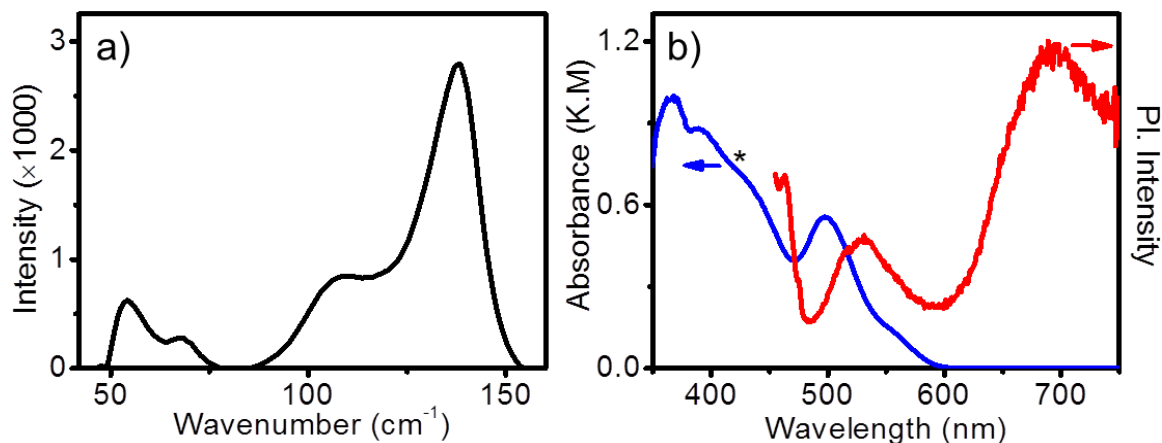
Figure 2.9. a) Raman, b) absorption (blue line) and emission (red line) spectra of **PDBI** on a glass substrate. The samples were excited at 785 nm for the Raman spectrum and 425 nm for the emission spectrum.

Further characterization of the material was carried out by Raman, UV−vis absorption, and fluorescence spectroscopy techniques. Intense Raman signals were observed from it on excitation with a 785 nm laser source (**Figure 2.9.**a). Peaks observed below 100 cm^{-1} correspond to Bi−I bending vibrational modes, whereas peaks close to 100 and 150 cm^{-1} correspond to terminal Bi−I asymmetric and symmetric stretching modes, respectively, in the $Bi_2I_{10}^{4-}$ dimer units.[19] The powder samples exhibited a broad absorption spectrum (**Figure 2.9.**b, left) in the visible region ranging from 350 to 600 nm. A well-defined narrow excitonic peak was observed at 500 nm in the absorption spectrum. The emission spectrum exhibited two peaks centered at 530 and 690 nm (**Figure 2.9.**b, right). Similar emission features were observed for $(CH_3NH_3)_3Bi_2I_9$ also, which was attributed to the existence of direct and indirect bandgaps in the material.[20]

2.3.A3. DFT calculations
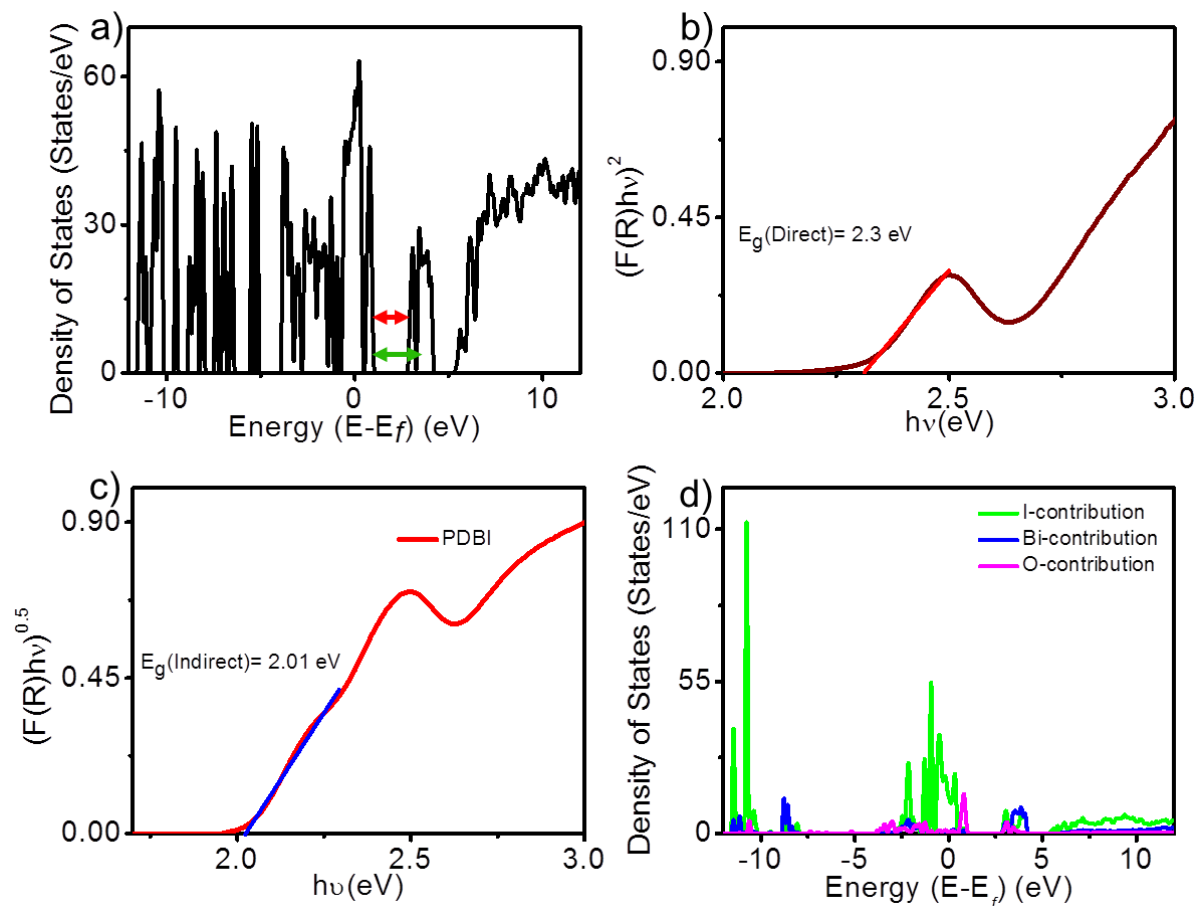
Figure 2.10. a) Total DOSs plot for the calculated band structure of **PDBI** marked with arrows indicating lower (red arrow) and higher (green arrow) energy end of the split conduction band. b) Direct and c) indirect bandgap calculation of **PDBI** from Tauc plot. d) Projected density of states of **PDBI**. The individual contribution of Bi, I, and O to the total density of states are shown as the projected density of states form.

Density functional theory (DFT)-based electronic structure calculations were performed to explore the optical properties of **PDBI**. The computed density of states (DOS) for the experimentally synthesized **PDBI** is shown in **Figure 2.10.**a. DOS calculations revealed the presence of the split conduction band with a higher energy

transition at 2.3 eV and a lower energy transition at 1.8 eV. These values were comparable with the experimentally observed direct and indirect bandgap values deduced from the Tauc plot (**Figure 2.10.**b and c). Hence, the emission at 530 and 690 nm may be originated from the higher and lower energy ends of the split conduction band. The corresponding projected DOS is shown in **Figure 2.10.**d, which reveals the contribution of each atomic species to the total DOS and helps to find out
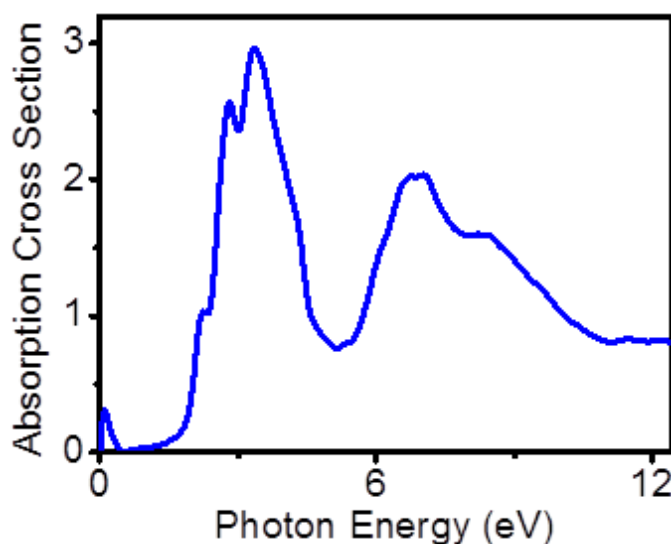
Figure 2.11. Calculated optical absorption spectra of **PDBI** from the single-crystal data. Peaks at 2.47, 2.95, and 3.58 eV correspond to electronic transitions from $^1S_0$ to $^3P_1$, $^3P_2$, and $^1P_1$ states, respectively.[21]

which states are dominant near bandgap. A significant contribution from iodine can be readily observed from the plot. A peak arising because of oxygen is also visible near the VBM. Hybridization between iodine and oxygen is evident at the CBM. The reflection of the DOSs calculations could be observed in the optical absorption spectrum as depicted in **Figure 2.11.** We can observe the first optical peak near the

lower photon energy range, which is corresponding to the water molecules coordinated with the organic layer. Two of the most prominent peaks are observed in the range of 2−4 eV, whereas the second most prominent absorption peak is observed between 6.5 and 7 eV. The nature of the optical absorption spectrum follows the similar trend as observed experimentally, depicted in **Figure 2.9.**b, where one can observe the highest optical response around 250−620 nm.

2.3.A4. Stability studies
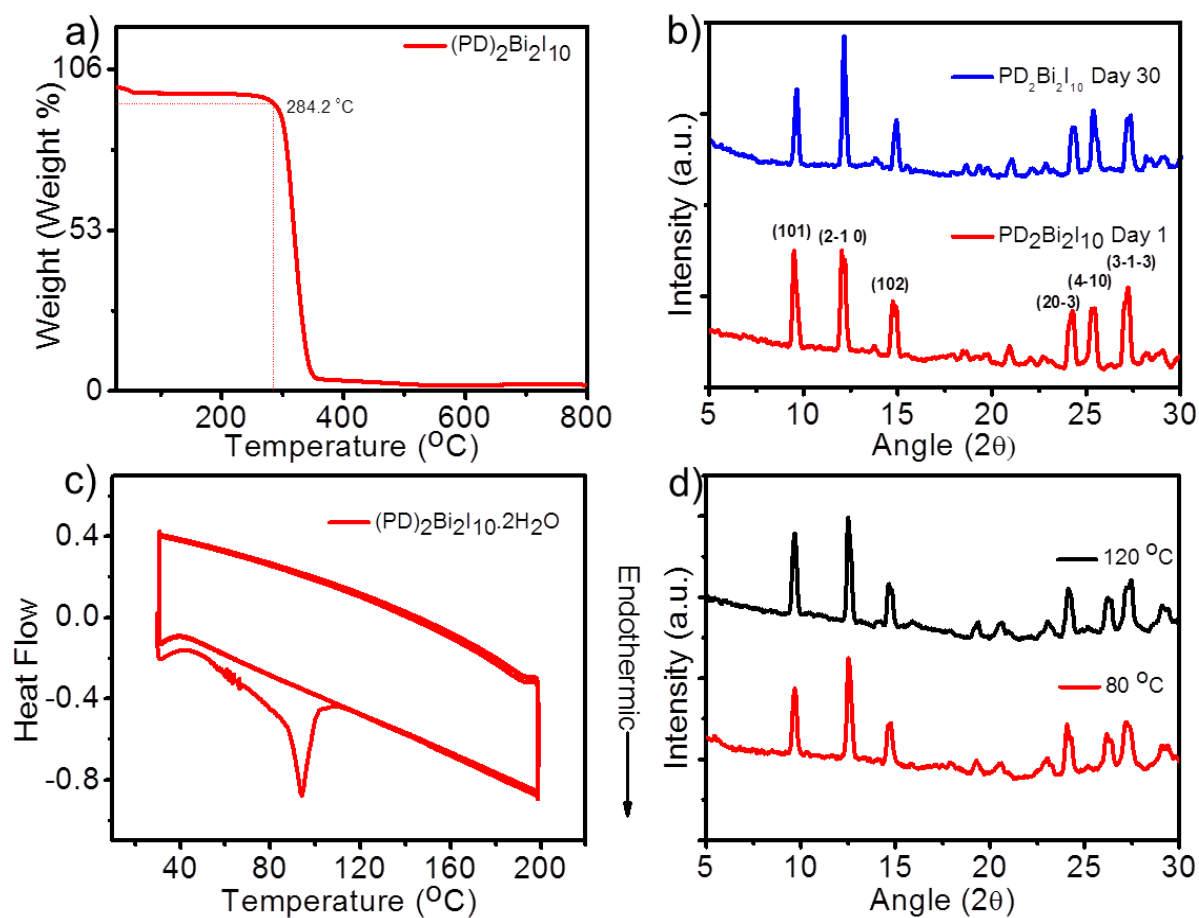
Figure 2.12. a) Thermogravimetric profile, b) X-ray diffraction spectrum, c) DSC profile, and d) temperature-dependent XRD of **PDBI**.

The thermal and moisture stability of perovskites is essential for its practical applications, which were evaluated using thermogravimetric (TGA) and XRD analysis. The TGA revealed that the **PDBI** was thermally stable up to 284 °C; above this temperature, the propane diammonium cation was sublimed and resulted in weight loss (**Figure 2.12.**a). Moisture stability of a perovskite material is related to its structural rigidity; here, the edge-sharing of BiI_6^{3-} octahedra provides rigidity to the perovskite framework, providing better moisture tolerance to the material. XRD measurements were further confirmed that **PDBI** was stable under ambient conditions for weeks (**Figure 2.12.**b). Differential scanning calorimetry (DSC) analysis was performed to evaluate the phase stability of the material. An endothermic peak was observed in the first cycle at 90 °C due to the escape of the adsorbed water molecules from the sample, which was absent in the second and third DSC cycles (**Figure 2.12.**c). XRD analysis at 80 and 120 °C did not exhibit any apparent change in the XRD pattern, implying the excellent phase stability of the material (**Figure 2.12.**d).

2.3.A5. Photodetector device characteristics

Photodetectors that capture incident light (photons) and convert it to electrical signals instantaneously have many critical applications including imaging, optical communication, remote control, chemical/biological sensing, and so on.[33] Very recently, hybrid perovskite materials found special attention for photodetector device application.[34–36] This could be attributed to the ability of hybrid perovskites to

efficiently absorb the incident light even if the thickness of the film is only a few hundred nanometers. In such thin films, the photogenerated charge carriers need to travel only small distances resulting in a fast and efficient photoresponse.
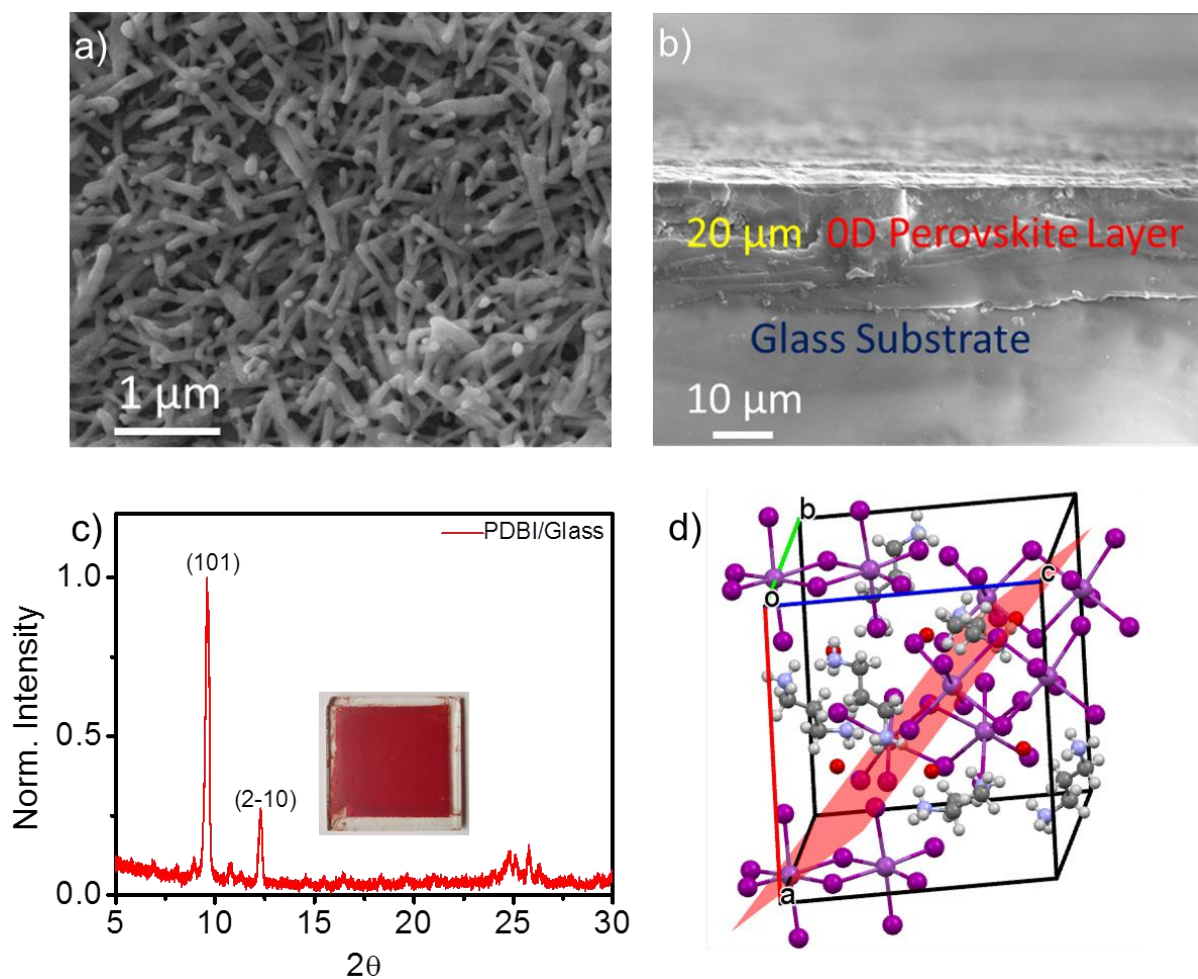
Figure 2.13. a) Topographical SEM image of **PDBI** over a glass substrate. b) Cross-sectional SEM image of a photodetector device fabricated using **PDBI** as the active layer. c) Thin-film XRD of **PDBI** over a glass substrate. d) ⟨101⟩ lattice plane comprises of $Bi_2I_{10}^{4-}$ dimer units.

To evaluate the light-harvesting and charge separation properties of **PDBI**, photodetector devices were fabricated using it as the active layer. For this purpose,

PDBI dissolved in dimethylformamide was spin-coated between the pre-patterned fluorine-doped tin oxide (FTO) electrodes having an electrode separation of 0.5 cm and annealed at 110 °C for 10 min. The crystallites formed during film formation had a rod-like morphology with several micrometers in size as evident from the topological scanning electron microscopy (SEM) image (**Figure 2.13.**a). To avoid pinholes and to ensure the interconnectivity between the crystallites, thicker films were prepared. From the cross-sectional SEM analysis, the thickness of the **PDBI** layer was obtained as 20 μm (**Figure 2.13.**b). The photoconductivity ($I-V$) measurements (dark and light) were carried out by illuminating the fabricated photodetector device with a 365 nm UV lamp (350 μW/cm^2; Spectroline model CM-10A) connected to a Keithley 2450 semiconductor characterization system. On illumination, the photogenerated charge carriers on the surface need to be transported through the **PDBI** crystal grains and injected into the electrodes. Though the **PDBI** microcrystals carry a substantial amount of insulating propane diammonium chains, a lower bias voltage (1 V) was enough to overcome the energetic barrier for charge injection at the electrodes and initiate a charge transfer between adjacent microcrystals compared to the zero-dimensional $(CH_3NH_3)_3Sb_2I_9$ (3 V) and one-dimensional $(C_6H_{14}N_4)_3I_3BiI_6$ (5 V) perovskite-based photodetectors.[36,37] The above-mentioned observation could be explained by the quantum-well structure of **PDBI**, which ensures better electronic dimensionality. In addition to that, the thin-film XRD pattern of **PDBI** over the glass substrate showed a preferential orientation along the

⟨101⟩ crystal plane (**Figure 2.13.**c); this plane is primarily composed of $Bi_2I_{10}^{4-}$

inorganic units which facilitate the interelectronic conduction between the $Bi_2I_{10}^{4-}$

dimers (**Figure 2.13.**d).
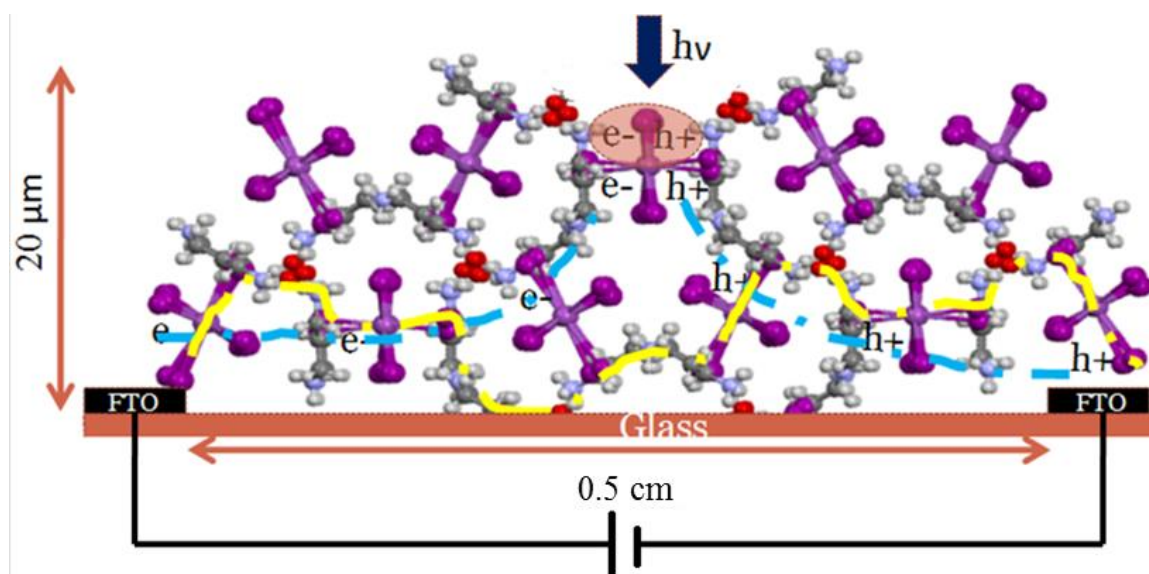
Figure 2.14. The illustrative cross-section in particle-based photodetectors with an average conductor path distance of 0.5 cm and a thickness of ~20 µm. Yellow line: in the dark, the charge transport across grain boundaries occurs between the electrodes with a distance of 0.5 cm due to the electric field of the applied voltage. Blue line: under illumination with light ON/OFF experiments, photogenerated charges at the **PDBI** surface are extracted to the electrodes to generate the signal. Therefore, a constant bias is applied to create a potential, which separates electrons (e-) and holes (h+) to the injecting electrodes.

Under illumination, photogenerated charges at the **PDBI** surface were extracted to

the electrodes to generate the signal. Therefore, a constant bias was applied to create a

potential, which separates electrons (e$^-$) and holes (h$^+$) to the injecting electrodes. In

the dark, the charge transport across grain boundaries occurs between the electrodes

with an average distance of 0.5 cm due to the electric field of the applied voltage

(**Figure 2.14**). In this device, the electronic conduction occurs exclusively through the

PDBI crystallites because of the absence of any other charge-transporting layers.
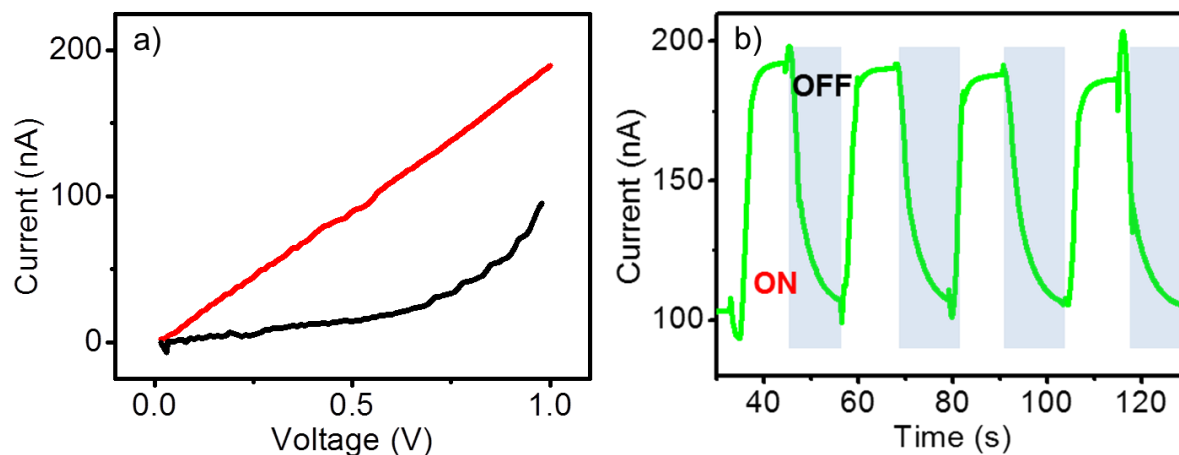
Figure 2.15. a) *I−V* curves of the **PDBI** photodetector measured in the dark (black line) and under illumination (red line). b) Time-dependent photocurrent response of the **PDBI** photodetector under chopped light irradiation (365 nm; 350 µW/ cm^2) at a bias voltage of 1 V, showing no apparent attenuation after multiple cycles.

The device exhibited 194 nA photocurrent and 94 nA dark current, as shown in the

I−V curves (**Figure 2.15.**a). The high dark current in the device is attributed to the

injection of charge carriers from the FTO electrodes because of the absence of

electron-/hole blocking layers.[38] The nonlinear *I−V* curve in the dark implies a

Schottky contact at the FTO/**PDBI** interface.[37] However, the devices exhibited an

Ohmic contact under illumination, which was beneficial for efficient charge collection

at the electrodes. The on/off ratio of the **PDBI** photodetector was calculated from

light (194 nA) and dark current (94 nA) measurements as 2.1, which is comparable

with the on/off ratio of one-dimensional perovskites reported in the literature such as

$(C_6H_{13}N)_2BiI_5$ (on/off ratio of 2.9) and (*N,N,N′,N′*- tetramethyl-piperazine)$_{1.5}$[Bi$_2$I$_7$Cl$_2$]

(on/off ratio of 3).[39,40] The responsivity of the device was obtained as 1.14 mA/W. In addition to the responsivity, other important figures of merits for the photodetector devices are specific detectivity, and the number of electrons probed per incident photon (external quantum efficiency). For **PDBI**, these parameters were estimated to be 1.9×10^6 Jones and 0.4%, respectively. More importantly, the photocurrent was consistent and repeatable over several photoswitching cycles (**Figure 2.15.**b). Properties of **PDBI** described above, and the comparison of that with other lead-free, zero-dimensional perovskite revealed that the former is an excellent candidate for optoelectronic device applications. The study of Irvine *et al.* with $(CH_3NH_3)_3Bi_2I_9$ perovskites is particularly important in this context.[9] Organic cations of this material separate the $Bi_2I_9{}^{3-}$ moiety by a distance of 14.3 Å, which results in a core−shell quantum dot structure. This hinders particle−particle electronic communication resulting in poor optoelectronic performances. On the other hand, the "quantum-well" structure of **PDBI** brings the $Bi_2I_{10}{}^{4-}$ dimer units to close proximity of 5.36 Å enabling better inter-inorganic cluster electronic communication. Excellent photoresponse properties comparable to that of one-dimensional perovskites reiterated this aspect.

2.3.B. Dielectric confinement and exciton binding energy

Polar aromatic organic spacers are good candidates for reducing the exciton binding energy in low-dimensional perovskites by lowering the dielectric confinement. However, the "A" site organic cations have a significant structure-directing ability on bismuth halide $A_3Bi_2I_9$-type perovskites. Hence, it is challenging to incorporate a polarizable organic spacer at that site without distorting the crystal structure. We have achieved this by introducing the aromatic benzylammonium (BA) cations via crystal engineering in the present work. The novel perovskite material we developed has the formula $BA_3Bi_2I_9$ (**BBI**). Both **BBI** and the well-studied methylammonium (MA) analogue, $(CH_3NH_3)_3Bi_2I_9$ (**MBI**), perovskites are isostructural. This enabled us to precisely investigate the role of the benzylammonium cation in the dielectric confinement in **BBI**.

2.3.B1. Structural and optical characterizations of BBI and MBI

The single crystals of **BBI** were synthesized by the solvent layering technique. Briefly, BiI_3 in 57% aq. hydrogen iodide (HI) and benzylammonium iodide in methanol were carefully taken in a glass vial as separate layers, and single crystals were formed by the slow reaction at the sharp interface of the two solutions. Millimeter-sized rod-shaped crystals were formed after several hours (**Figure 2.16.**a, b). The interatomic plane distance of **BBI** was calculated from the high-resolution
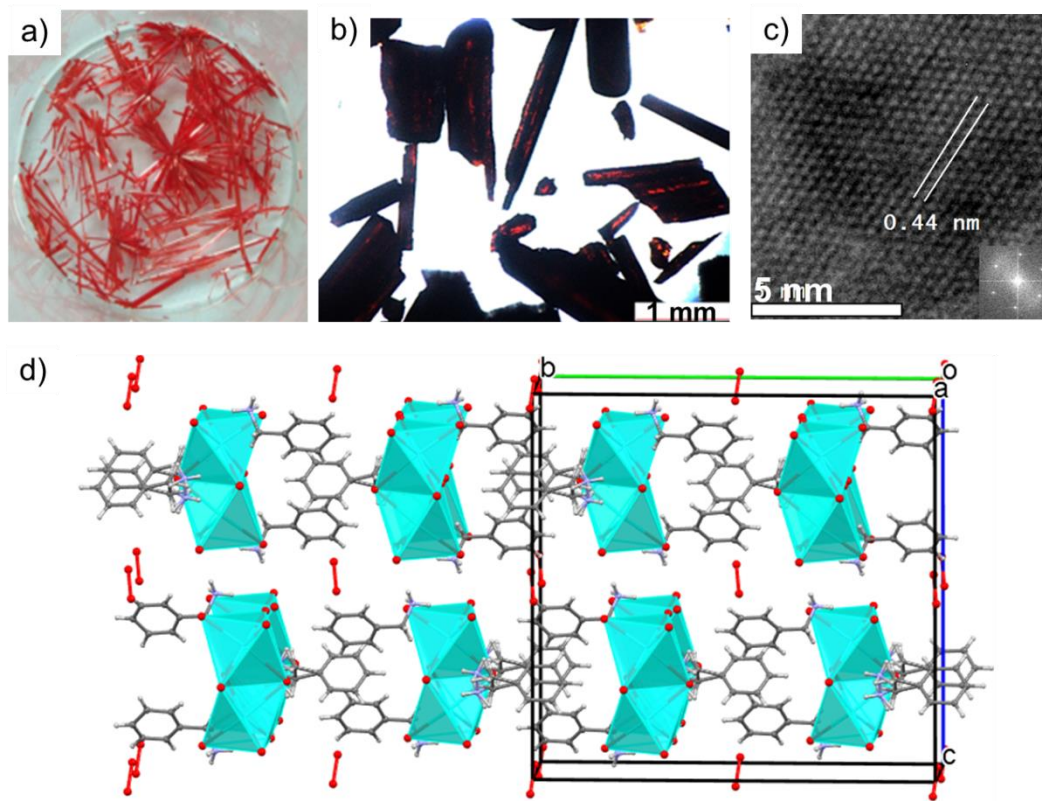
Figure 2.16. a) Photograph and b) optical polarization microscope image of **BBI** single crystals. c) High-resolution transmission electron microscopic image of the **BBI** thin film. The corresponding fast Fourier transform image in the inset. d) Three-dimensional crystallographic packing of **BBI** obtained from single-crystal X-ray diffraction analysis. The unit cell is represented with the crystallographic axes a, b, and c.

transmission electron microscopy (HRTEM) analysis as 0.44 nm (**Figure 2.16.**c). The bright diffraction spots in the fast Fourier transform (FFT) image indicate a high crystallinity. The single-crystal X-ray diffraction (SCXRD) measurement was done at room temperature, but crystal structure refinement was not possible due to the poor electron density in the organic part. Subsequently, the crystal structure was resolved through SCXRD analysis at 180 K. The unit cell of **BBI** represents a monoclinic crystal system with a $C\,2/c$ space group (**Figure 2.16.**d).
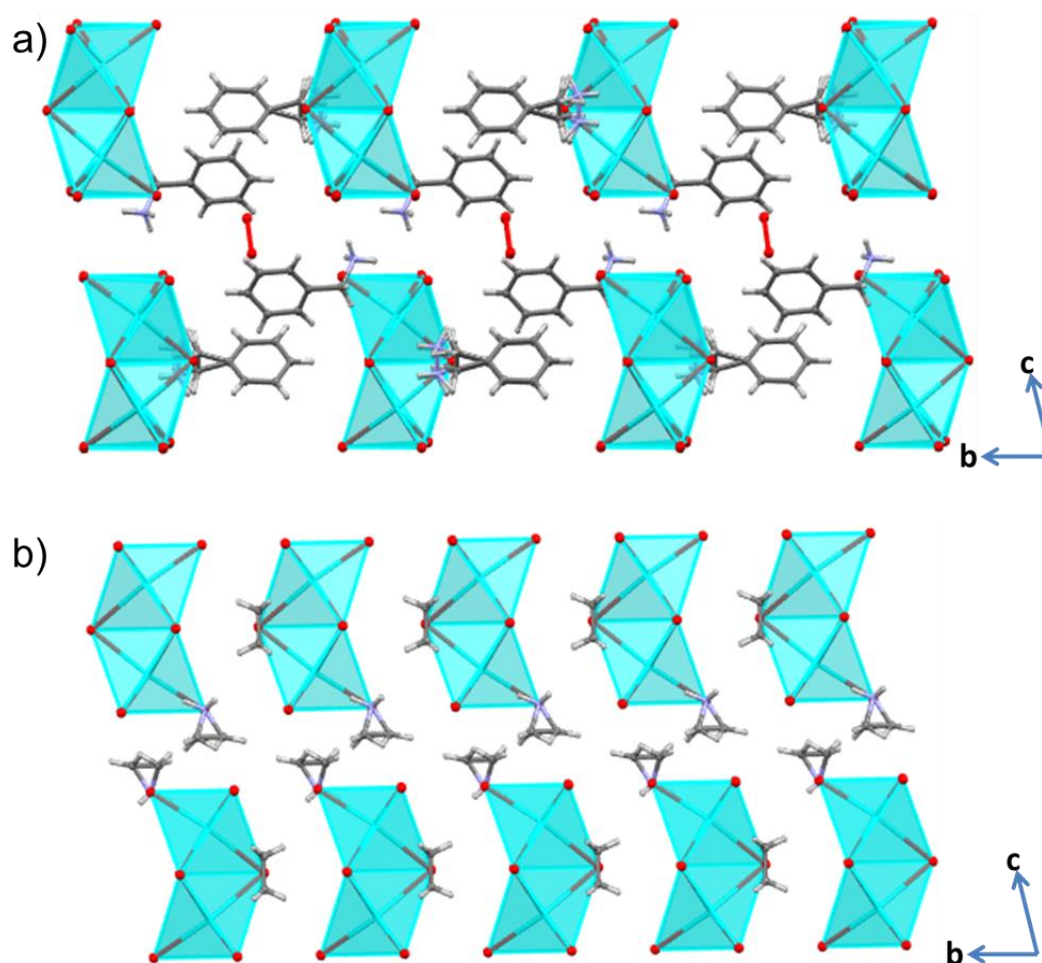
Figure 2.17. Comparison of the crystal packing of a) **BBI** (present work) and b) **MBI** (CCDC 1433118; Previously reported: *Chem. Commun.* **2016**, *52*, 3058-3060).

BBI belongs to the category of zero-dimensional perovskites due to the isolated nature of $Bi_2I_9^{3-}$ bi-octahedra. As the crystal structure shows, these bi-octahedral units are formed by face sharing of two BiI_6^{3-} octahedra. It was also observed that HI molecules are trapped in the crystal structure of **BBI**. SCXRD analysis also proved that **BBI** is isostructural compared with **MBI** (**Figure 2.17.**);[30] Both **BBI** and **MBI** consist of $Bi_2I_9^{3-}$ bi-octahedra surrounded by benzylammonium and

methylammonium cations, respectively. Similar quantum confinement was expected in both materials because the thickness of $Bi_2I_9^{3-}$ inorganic layers is the same in them (*n* = 2 along the "*b*" axis, where "*n*" is the no. of octahedra). In **BBI**, the benzylammonium cations adopted an edge-to-face arrangement making an angle of 71.92° with a minimum separation distance of 3.26 Å. This enables an edge−face
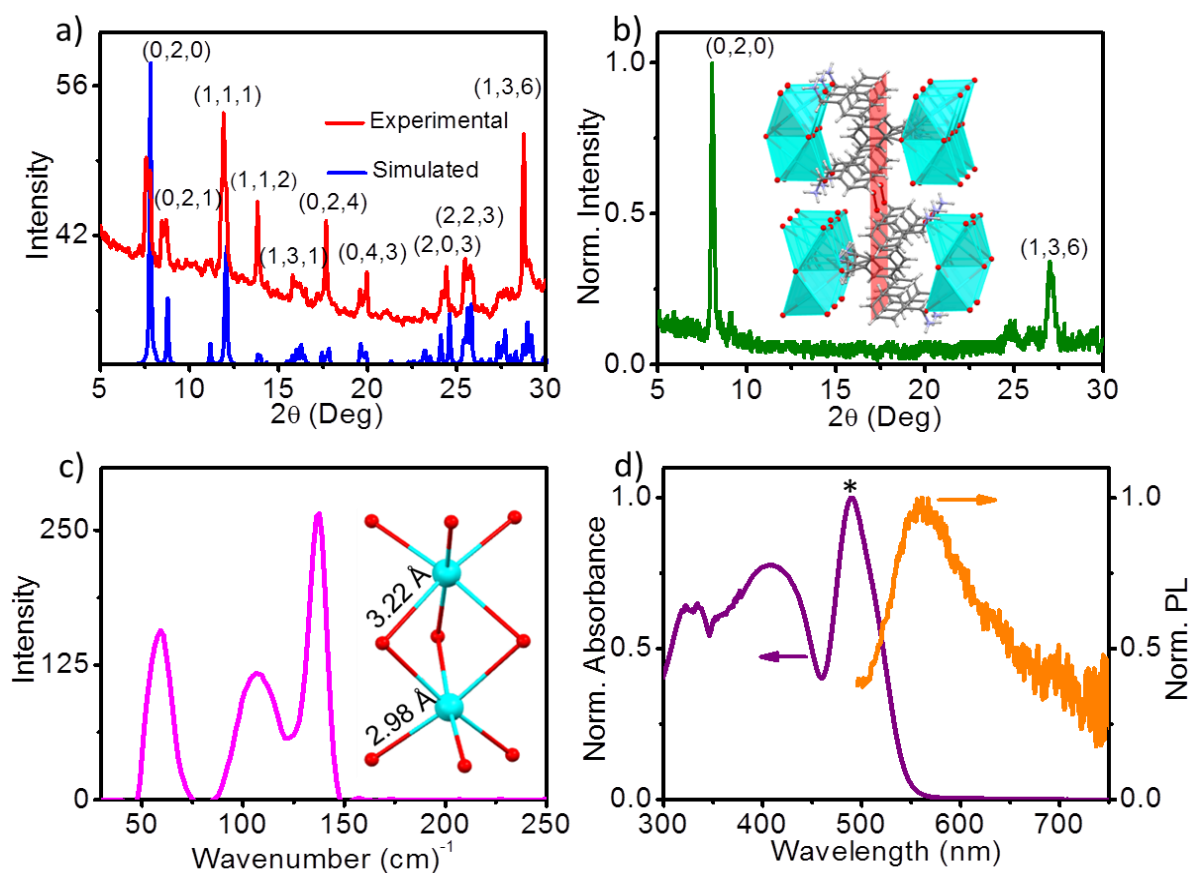
Figure 2.18. a) Comparison of the experimental XRD pattern of crushed **BBI** crystals and simulated XRD patterns obtained from the single-crystal analysis. b) Thin-film XRD of **BBI** coated over the FTO substrate; the inset showing the preferentially oriented ⟨020⟩ plane. c) Raman spectrum of **BBI** crystals upon 785 nm laser excitation. The inset shows the $Bi_2I_9^{3-}$ dimer units labeled with two different Bi−I bond lengths, 2.98 and 3.22 Å. d) Absorption and emission spectra of **BBI** thin films coated over FTO substrates. The asterisk indicates the excitonic peak corresponding to the $^1S_0-^3P_1$ electronic transition.

π−π stacking of benzylammonium cations. This self-assembly of benzylammonium cations in the "*ac*" crystallographic plane brings the $Bi_2I_9{}^{3-}$ bi-octahedra to close proximity of 4.13 Å along the crystallographic "*a*" axis. Notably, the tight packing of inorganic units provides structural rigidity to the **BBI** perovskite framework.

The powder X-ray diffraction (PXRD) pattern of **BBI** is comparable with the simulated one obtained from the SCXRD analysis (**Figure 2.18.**a), which indicates the phase purity of the powder samples. XRD analysis of thin films over fluorine-doped tin oxide (FTO) substrates revealed a preferential orientation of **BBI** crystallites along the ⟨020⟩ crystallographic plane (**Figure 2.18.**b). Interestingly, this crystallographic plane is composed of benzylammonium cations. This observation implies that the organic part is playing a significant role in the assembly of perovskite crystallites. In other words, our observation proved that the growth and orientation of perovskite crystallites could be controlled by the rational selection of organic cations. Further control over the packing could be achieved using organic chromophores with strong π−π stacking abilities. The Raman spectrum of **BBI** crystals was recorded at 785 nm laser excitation (**Figure 2.18.**c). The peak at 50 cm^{-1} corresponds to the bending vibrations of the Bi−I bridging bond, and the peaks close to 100 and 150 cm^{-1} are attributed to the asymmetric and symmetric stretching vibrations of the terminal Bi−I bonds, respectively.[31] The optical properties of **BBI** were studied using UV−visible absorption and fluorescence spectroscopy (**Figure 2.18.**d). The

absorption spectrum spans from the UV region up to 550 nm with a well-defined excitonic peak at 490 nm corresponding to $^1S_0$–$^3P_1$ electronic transition.[32]

2.3.B2. Thin-film morphology analysis
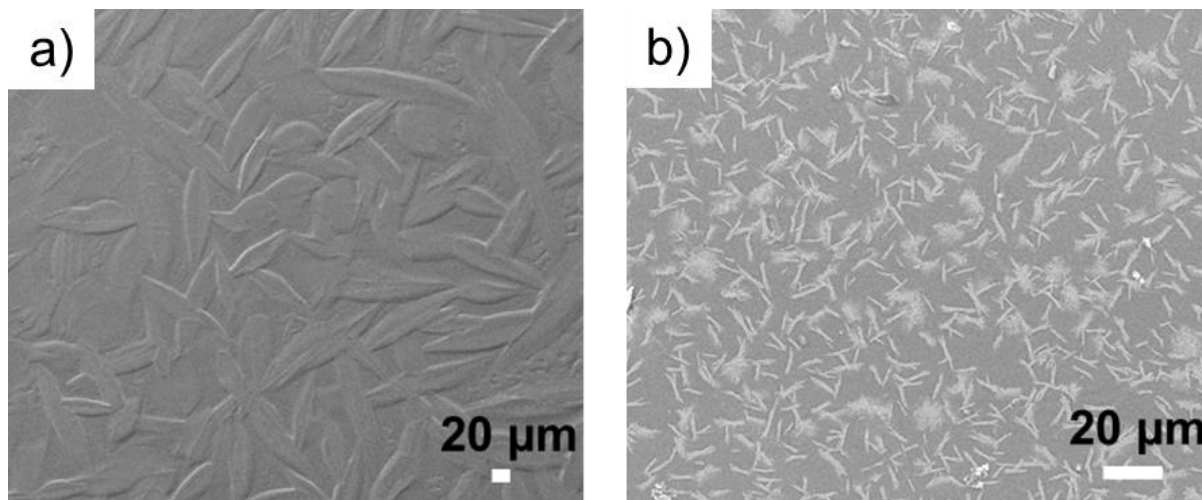
Figure 2.19. SEM images of a) **BBI** and b) **MBI** thin films over FTO substrates. The FTO substrate was fully covered by **BBI** crystallites, whereas a large portion of FTO was exposed in the case of **MBI** crystallites at similar concentrations (35 wt% in DMF).

We also observed that **BBI** thin films obtained via single-step solution processing on FTO substrates exhibited better uniform coverage (**Figure 2.19.**a and b) than **MBI**. This would be beneficial for fabricating devices for optoelectronic applications.

2.3.B3. Thermal stability analysis and optical bandgap estimation

The thermal stability of **BBI** was evaluated using thermogravimetry, which revealed that **BBI** is thermally stable up to 250 °C and further heating resulted in the
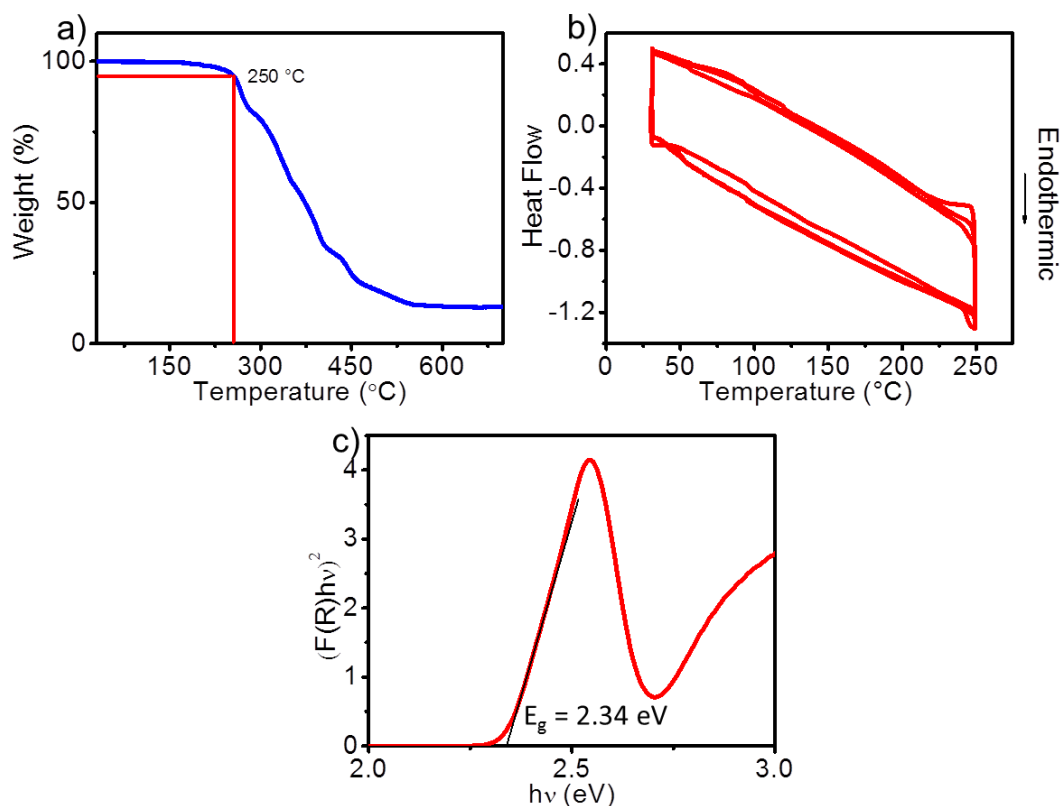
Figure 2.20. a) Thermogram of **BBI**. The T_5 value (the temperature at which the material loses 5% of its initial weight) was found to be 250 °C. b) DSC curve of **BBI**. No endothermic or exothermic peaks were obtained during the heating or cooling cycle indicating the absence of phase changes. c) Direct bandgap calculation of **BBI** from Tauc plot.

sublimation of the organic component (**Figure 2.20.**a). Phase stability of the material was monitored by differential scanning calorimetry analysis. It exhibited excellent phase stability up to 250 °C without showing any endo/exothermic peaks during the temperature scans (**Figure 2.20.**b). The sharp excitonic peak indicates strong quantum confinement in **BBI**. The optical bandgap of the material was calculated from the Tauc plot as 2.34 eV (**Figure 2.20.**c). **BBI** exhibited weak photoluminescence with an emission maximum at 560 nm (2.21 eV). Since the emission maximum is close to the

excitonic absorption peak and from the narrow emission feature, it could be assumed as excitonic emission.[33] The slight Stokes shift between the optical bandgap and emission maximum in **BBI** is a piece of evidence for its low exciton binding energy. Exciton nonlocality effects[34] on the position of the PL maximum of **BBI** could be ruled out due to strong quantum confinement in **BBI** as a result of relatively large inter-inorganic cluster separation (4.13 Å; **Figure 2.21**). From the optical bandgap and PL maximum, the exciton binding energy of **BBI** at room temperature was estimated as 130 meV.
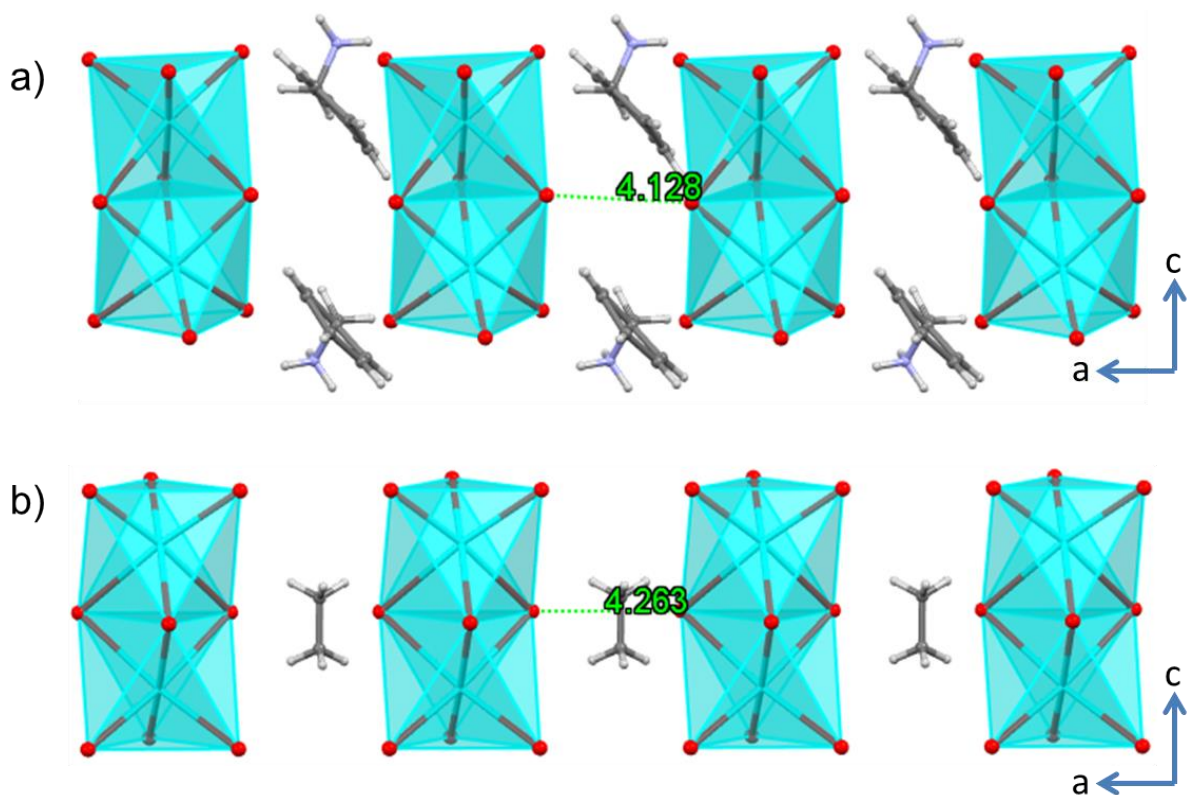
Figure 2.21. Crystal packing of a) **BBI** and b) **MBI** (CCDC 1433118). The inter-inorganic cluster separations in Å of each material are indicated.

2.3.B4. X-ray diffraction and optical characterizations of MBI

To compare the optical properties of **BBI** and **MBI**, we have synthesized the single crystals of **MBI** (**Figure 2.22.**a). Similar to **BBI**, **MBI** also exhibited a well-defined band edge excitonic absorption peak at 490 nm corresponding to the $^1S_0-^3P_1$ electronic transition occurring in their $Bi_2I_9{}^{3-}$ clusters (**Figure 2.22.**b). We have calculated the bandgap of **MBI** as 2.26 eV from the Tauc plot (**Figure 2.22.**c), which is comparable with previous reports.[30,35]
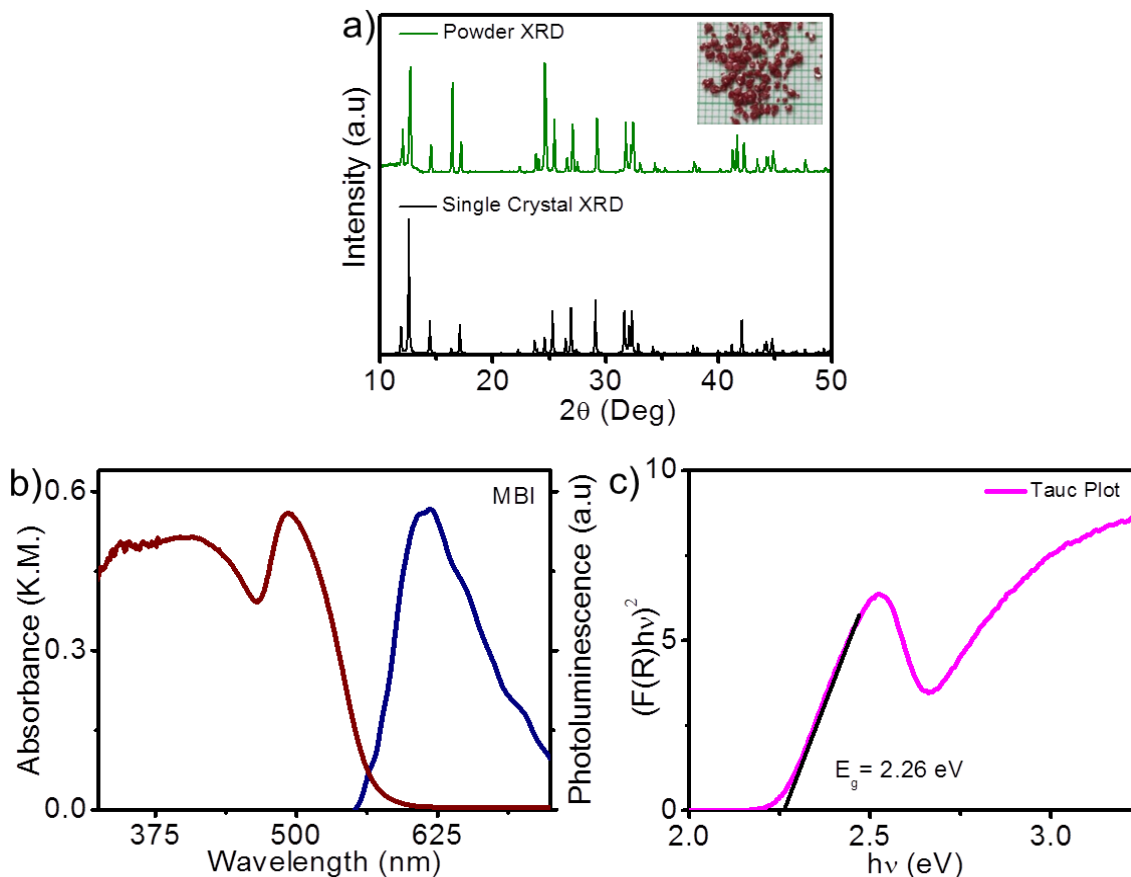
Figure 2.22. a) Single crystal XRD (CCDC 1433118) and powder XRD of **MBI**. Inset shows the photograph of **MBI** single crystals b) absorption and photoluminescence spectrum of **MBI** and c) bandgap calculation of **MBI** from Tauc plot.

The excitonic emission from **MBI** was observed at 620 nm (2 eV; **Figure 2.22.**b). Thus, the exciton binding energy for **MBI** was calculated as 260 meV. This is also comparable with previous reports.[24–26] The lower exciton binding energy of **BBI** compared to that of **MBI** could be attributed to the weak dielectric confinement in the former due to the effective screening of Coulomb's interaction induced by the polarizable organic spacer present in it.[27] This can result in the facile dissociation of excitons into charge carriers. In other words, higher photoconductivity can be expected in **BBI** than that in **MBI**. To validate the above-mentioned point, we have performed flash-photolysis time-resolved microwave conductivity (FPTRMC) analysis.

2.3.B5. Photoconductivity analysis
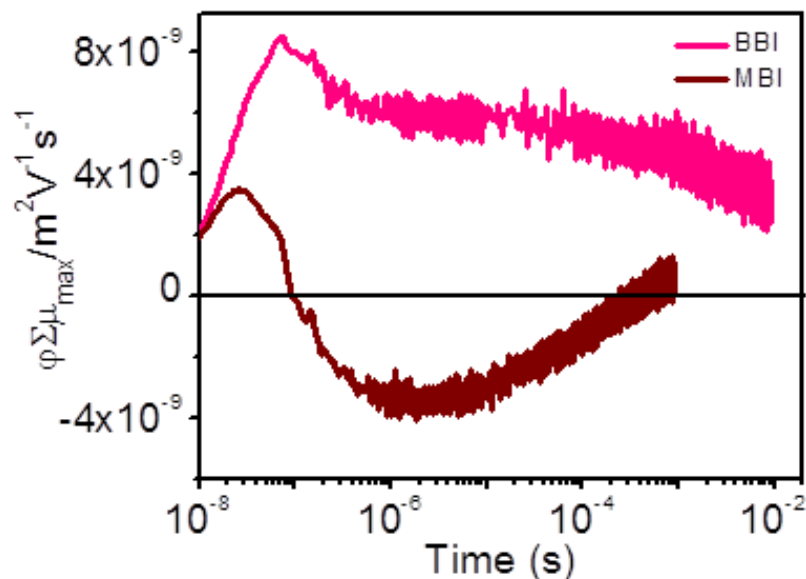
Figure 2.23. Product of TRMC mobility and yield dissociation of free charges as a function of time for **BBI** and **MBI** powder samples.

TRMC measurement is an excellent electrode-less technique to gain insight into the photogenerated charge-carrier mobility and its dynamics of functional materials including perovskites.[39–41] In this technique, microwave radiation is used to probe the radiative and nonradiative recombination of all free mobile charge carriers in the material on photoexcitation. It is based on the interaction between the electric field component of high frequency (GHz) microwave radiations and photoinduced mobile charge carriers. Hence, TRMC analysis could avoid the interfacial effects and undesired chemical reactions between the semiconducting material and electrodes. The absorption of microwave radiation varies with the photoconductivity changes, which is recorded to calculate the product of mobility ($\Sigma\mu$) and dissociation yield of charge carriers (ϕ).

For the TRMC measurements, the powdered single crystals of **BBI** and **MBI** were excited using a 355 nm laser, and transient photoconductivity was probed using microwave radiation. The product of mobility ($\Sigma\mu$) and dissociation yield of charge carriers at the end-of-pulse (ϕ) for **BBI** (8.4×10^{-9} m^2 V^{-1} s^{-1}) was about 2.5-fold higher than that for **MBI** (3.3×10^{-9} m^2 V^{-1} s^{-1}, **Figure 2.23**), which is a direct evidence of a larger charge-carrier mobility and/or the facile dissociation of excitons into free charge carriers in **BBI** compared to **MBI**.[42] The lower $\phi\Sigma\mu$ value of **MBI** could be attributed to the presence of bound excitons, which do not separate into free charge carriers and contribute to the TRMC signal intensity. This was further

supported by the anomalous TRMC signal transition of **MBI** from positive to negative with time. This is due to the decrease in the dielectric permittivity of **MBI** upon photoexcitation. In detail, methylammonium dipoles are disordered in the ground state of **MBI**, which leads to a high dielectric permittivity of 7.94 $\mu C/cm^2$.[43] Upon photoexcitation, the localized excitons will restrict the free rotation of methylammonium cations and subsequently reduce the dielectric permittivity of the material. This dielectric permittivity change resulted in the unusual TRMC signal for **MBI**. A similar strange TRMC signal transition in the case of $MAPb_{1-x}Sn_xX_3$ (x = 0−1, X = I and Br) perovskites was reported recently.[44] In contrast, the higher and long-lived TRMC signal for **BBI** is due to the facile dissociation of excitons into free charge carriers. This could be attributed to the lower dielectric confinement in **BBI**. The C=C bonds in benzylammonium are more polarizable than the C−H bond in methylammonium. As a result, benzylammonium could reduce the dielectric confinement in **BBI** compared with the methylammonium in **MBI**.

2.4. Conclusions

In conclusion, we have synthesized and characterized a novel, lead-free, zero-dimensional perovskite material consisting of $Bi_2I_{10}^{4-}$ dimers formed by the edge sharing of BiI_6^{3-} octahedra. This material exhibited excellent photoabsorption and environmental stability. Experimentally observed optical properties of **PDBI** are in accordance with the DFT calculations. The thin-film photodetector fabricated using

PDBI showed consistent and repeatable photocurrent in several light-on/off cycles under a low bias voltage. We have also successfully synthesized and characterized a novel lead-free zero-dimensional perovskite material (**BBI**) consisting of isolated $Bi_2I_9{}^{3-}$ bi-octahedra separated by benzylammonium cations. Comparable quantum confinement was observed for **BBI** and **MBI** due to their identical structural dimensionality (0D). The polarizable benzylammonium cations in **BBI** reduced the dielectric mismatch between the inorganic $Bi_2I_9{}^{3-}$ clusters and their organic counterpart. From the TRMC studies, the higher product of charge carrier mobility and yield dissociation of charge carriers for **BBI** compared to **MBI** revealed that the benzylammonium cation induced low dielectric confinement in **BBI**. More importantly, we have also proved that it is possible to control the packing orientation of hybrid perovskite materials with the rational choice of organic cations. This would have far-reaching implications on the design and synthesis of tailor-made hybrid perovskites for functional applications. These reports open up new directions in crystal engineering of zero-dimensional, lead-free perovskites to improve their optoelectronic properties for advanced device applications.

2.5. Experimental section

2.5.1. Chemicals: Bismuth (III) iodide (99.9%, Sigma Aldrich), 1,3-diaminopropane (99%, Sigma Aldrich), benzylamine (98%, Spectrochem), hydriodic acid (57 wt.% in H_2O, 99.95%, Sigma Aldrich), dichloromethane (99.0%, Merck), dimethylformamide

(anhydrous 99.8%, Sigma Aldrich), chloroform (99.4%, Spectrochem) and methanol (99.7%, Merck) were used without any further purification.

2.5.2. synthesis of 1,3-propyl diammonium dihydrogen iodide (PDI): 1,3-diaminopropane (3mL, 36 mmol, 1 equiv.) was taken in an RB flask, and hydriodic acid (6 mL, 80 mmol, 2.2 equiv.) was added at 0 °C with constant stirring for 1 hour. The solution was transferred to a petri dish and heated at 110 °C for 1.5 hours and then cooled to room temperature to obtain the crude product. The product was further purified by dissolving in a minimum quantity of ethanol, followed by reprecipitation using diethyl ether. Yield: 98 %; ^{1}H NMR (500 MHz, DMSO-d_6): δ 7.63-7.79 (bs, 6H), 2.84-2.91 (t, 4H), 1.77-1.85 (m, 2H).

2.5.3. Synthesis of PDBI single crystal: Bismuth (III) iodide (589.69 mg, 1 mmol, 1 equiv.) and PDI (330 mg, 1 mmol, 1 equiv.) were dissolved in 0.6 ml of hydroiodic acid (0.6 mL, 4.5 mmol, 4.5 equiv.) and heated at 90 °C for 3 hours and the solution was filtered under hot condition. The filtrate was dried under a vacuum for 8 hours. 100 mg of the filtrate was dissolved in 1 mL methanol taken in a 15 mL glass vial, and the vial was immersed in a 100 mL beaker containing 5 mL chloroform. The mouth of the beaker was covered with parafilm. After several hours, red colored needle-like crystals were formed, which were washed with methanol/chloroform (1:10 v/v) mixture. The crystals were kept in a vacuum oven at 80 °C for 8 hours.

2.5.4. Synthesis of Benzylammonium Iodide: Benzylamine (3 mL, 27.4 mmol, 1 equiv) was taken in an RB flask, and 57% aq hydriodic acid (4.62 mL, 102.9 mmol,

3.75 equiv) was added to it at 0 °C with constant stirring for an hour. A white precipitate of benzylammonium iodide was formed, purified by dissolving in a minimum amount of ethanol, followed by reprecipitation using diethyl ether. Yield: 97 %; ^{1}H NMR (500 MHz, DMSO-d_6): δ 8.09-8.19 (bs, 3H), 7.45-7.49 (d, 2H), 7.39-7.44 (t, 2H), 7.34-7.39 (t, 1H), 4.06 (s, 2H).

2.5.5. Preparation of (BA)$_3$Bi$_2$I$_9$·HI Single Crystals: Single crystals of BA$_3$Bi$_2$I$_9$·HI were prepared by the solvent layering technique using a 57% aqueous hydriodic acid solution of BiI$_3$ (60 mg, 1 mmol, 2 equiv.) and methanol solution of benzylammonium iodide (36 mg, 1.5 mmol, 3 equiv.) in a glass vial. Red, block-shaped crystals were formed at the interface of the two solutions by a slow reaction.

2.5.6. Preparation of (MA)$_3$Bi$_2$I$_9$ Single Crystals: BiI$_3$ (589.69 mg, 1 mmol, 2 equiv) and methylammonium iodide (238 mg, 1.5 mmol, 3 equiv) were dissolved in 1 mL of dimethylformamide (DMF) and immersed in a 100 mL beaker containing chloroform, and the mouth of the beaker was covered with parafilm. Dark, red single crystals of (MA)$_3$Bi$_2$I$_9$ were formed after several days.

2.5.7. Characterization: The diffuse reflectance spectra of **BPBI** and **NDBI** powder samples were recorded in the range of 400-800 nm using Shimadzu UV-2600 UV-vis spectrophotometer. Using the Kubelka-Munk function, the reflectance spectrum was converted into absorbance data. Powder XRD data of the perovskite samples were collected with Xeuss Simultaneous 2D WAXs. The wavelength of X-ray radiations used is 1.5418 Å (Cu-Kα radiation). The single-crystal structure determination is

carried out using Bruker Kappa APEXII diffractometer at 297 K. Softwares such as APEX$_3$, SAINT, and SADABS are used for data collection, data reduction, and absorption correction, respectively. The topological and cross-sectional SEM imaging of the device was performed by subjecting the device to thin gold coating using a JEOL JFC-1200 fine coater. The probe side was inserted into a JEOL JSM-5600 LV scanning electron microscope for imaging. The morphology and electron diffraction pattern of the perovskite material were studied by using an FEI-Tecnai T30 high-resolution transmission electron microscope, at an accelerating voltage of 300 kV. Thermogravimetric data was recorded in the range of 30-800 °C using the instrument TA Q50 under the nitrogen gas atmosphere at a heating rate of 10 °C min^{-1}. Raman spectral characterizations were carried out using WITec Raman microscope (WITec Inc. Germany, alpha 300R). Samples were excited at 633 nm with a laser source of power 5 mW. Vibrational Raman signals were collected using a Peltier cooled CCD detector in the range of 0 to 1800 cm^{-1} with 1 cm^{-1} resolution. WITec Project plus (v2.1) software package was used for data processing. Transient conductivity was measured by the flash-photolysis time-resolved microwave conductivity (FP-TRMC) technique. A resonant cavity was used to obtain a high degree of sensitivity in the measurement. The resonant frequency and the microwave power were set at 9.1 GHz and 3 mW, respectively, so that the electric field of the microwave was sufficiently small not to disturb the motion of charge carriers. The conductivity value was

converted to the product of the quantum yield (ϕ) and the sum of charge carrier mobilities ($\Sigma\mu$), by the following equation.

$$\phi \sum \mu = \frac{1}{e \cdot A \cdot I_0 \cdot F_{light}} \cdot \frac{\Delta P_r}{P_r}$$

Where e, A, I_0, F_{light}, ΔP_r, and P_r are the unit charge of a single electron, a sensitivity factor [(S m^{-1})$^{-1}$], incident photon density of the excitation laser (photons per m^2), a correction (or filling) factor (m^{-1}), a change in reflected microwave power, and a power of the reflected microwave, respectively. The difference in conductivity was equivalent to $\Delta P_r/(AP_r)$. 500 nm laser light with a photon density of 1.3 $\times 10^{16}$ photons/cm^2 was used as the excitation source. The sample was set at the highest electric field in a resonant cavity. The experiments were carried out at room temperature.

2.5.8. Computational Methodology: The projected density of states has been determined while performing systematic electronic structure calculations with the DFT framework in conjunction with PAW formalism as implemented in Vienna Ab-initio Simulation Package (VASP) code. The exchange and correlation energies have been treated within the General Gradient Approximation (GGA) approach as implemented in Predew-Burke-Ernzerhof (PBE) functional. The cut-off energy used throughout the calculation is 500 eV, which has been found after going through the energy conversion criteria. The Brillouin zone has been sampled using 3 x 3 x 3 Monkhorst-Pack k -mesh for the ionic relaxation. Since the system consists of an even

number of atoms, the spin-polarized calculation has not been considered. After getting the minimum energy configuration for the system, we have carried out the calculations for the projected density of states.

2.5.9. Exciton Binding Energy Calculation: The exciton binding energy was estimated using the following equation[45]

$$hv = E_g - E_x$$

where hv is the emitted photon energy (corresponds to the excitonic emission maximum), E_g is the optical bandgap (from Tauc's plot), and E_x is the exciton binding energy.

2.6. References

1. J. Shamsi, A. S. Urban, M. Imran, L. D. Trizio, L. Manna, *Chem. Rev.* **2019**, *119*, 3296-3348.
2. C. Katan, N. Mercier, J. Even, *Chem. Rev.* **2019**, *119*, 3140-3192.
3. E. R. Dohner, A. Jaffe, L. R. Bradshaw, H. I. Karunadasa, *J. Am. Chem. Soc.* **2014**, *136*, 13154-13157.
4. D. H. Cao, C. C. Stoumpos, O. K. Farha, J. T. Hupp, M. G. Kanatzidis, *J. Am. Chem. Soc.* **2015**, *137*, 7843-7850.
5. L. Dou, A. B. Wong, Y. Yu, M. Lai, N. Kornienko, S. W. Eaton, A. Fu, C. G. Bischak, J. Ma, T. Ding, N. S. Ginsberg, L.-W. Wang, A. P. Alivisatos, P. Yang, *Science* **2015**, *349*, 1518-1521.
6. E. R. Dohner, E. T. Hoke, H. I. Karunadasa, *J. Am. Chem. Soc.* **2014**, *136*, 1718-1721.

7. L. Mao, Y. Wu, C. C. Stoumpos, M. R. Wasielewski, M. G. Kanatzidis, *J. Am. Chem. Soc.* **2017**, *139*, 5210-5215.

8. K. M. McCall, C. C. Stoumpos, S. S. Kostina, M. G. Kanatzidis, B. W. Wessels, *Chem. Mater.* **2017**, *29*, 4129-4145.

9. C. Ni, G. Hedley, J. Payne, V. Svrcek, C. McDonald, L. K. Jagadamma, P. Edwards, R. Martin, G. Jain, D. Carolan, D. Mariotti, P. Maguire, I. Samuel, J. Irvine, *Nat.Commun.* **2017**, *8*, 170.

10. R. Chakraborty, A. Nag, *J. Phys. Chem. C* **2020**, *124*, 16177-16185.

11. M. D. Smith, L. Pedesseau, M. Kepenekian, I. C. Smith, C. Katan, J. Even, H. I. Karunadasa, *Chem. Sci.* **2017**, *8*, 1960-1968.

12. X. Hong, T. Ishihara, A. U. Nurmikko, *Phys. Rev. B* **1992**, *45,* 6961-6964.

13. J.-T. Lin, C.-C. Liao, C.-S. Hsu, D.-G. Chen, H. M. Chen, M.-K. Tsai, P.-T. Chou, C.-W. Chiu, *J. Am. Chem. Soc.* **2019**, *141*, 10324-10330.

14. B. Cheng, T.-Y. Li, P. Maity, P.-C. Wei, D. Nordlund, K.-T. Ho, D.-H. Lien, C.-H. Lin, R.-Z. Liang, X. Miao, I. A. Ajia, J. Yin, D. Sokaras, A. Javey, I. S. Roqan, O. F. Mohammed, J.-H. He, *Commun. Phys.* **2018**, *1*, 80.

15. Z. Zhang, X. Li, X. Xia, Z. Wang, Z. Huang, B. Lei, Y. Gao, *J. Phys. Chem. Lett.* **2017**, *8*, 4300-4307.

16. K. M. Boopathi, P. Karuppuswamy, A. Singh, C. Hanmandlu, L. Lin, S. A. Abbas, C. C. Chang, P. C. Wang, G. Li, C. W. Chu, *J. Mater. Chem. A* **2017**, *5*, 20843-20850.

17. S. Sun, S. Tominaka, J. H. Lee, F. Xie, P. D. Bristowe, A. K. Cheetham, *APL Mater.* **2016**, *4*, 031101.

18. B.-W. Park, B. Philippe, X. Zhang, H. Rensmo, G. Boschloo, E. M. J. Johansson, *Adv. Mater.* **2015**, *27*, 6806-6813.

19. K. M. McCall, C. C. Stoumpos, S. S. Kostina, M. G. Kanatzidi, B. W. Wessels, *Chem. Mater.* **2017**, *29*, 4129-4145.

20. R. L. Z. Hoye, R. E. Brandt, A. Osherov, V. Stevanovic, S. D. Stranks, M. W. B. Wilson, H. Kim, A. J. Akey, J. D. Perkins, R. C. Kurchin, *Chem. Eur. J.* **2016**, *22*, 2605-2610.

21. C. Ran, Z. Wu, J. Xi, F. Yuan, H. Dong, T. Lei, X. He, X. Hou, *J. Phys. Chem. Lett.* **2017**, *8*, 394-400.

22. F. P. García de Arquer, A. Armin, P. Meredith, E. H. Sargent, *Nat. Mater.* **2017**, *2*, 16100.

23. X.-W. Tong, W.-Y. Kong, Y.-Y. Wang, J.-M. Zhu, L.-B. Luo, Z.-H. Wang, *ACS Appl. Mater. Interfaces* **2017**, *9*, 18977-18985.

24. C. Ji, P. Wang, Z. Wu, Z. Sun, L. Li, J. Zhang, W. Hu, M. Hong, J. Luo, *Adv. Funct. Mater.* **2018**, *28*, 1705467.

25. W. Zhang, X. Liu, L. Li, Z. Sun, S. Han, Z. Wu, J. Luo, *Chem. Mater.* **2018**, *30*, 4081-4088.

26. B. Yang, Y. J. Li, Y. X. Tang, X. Mao, C. Luo, M. S. Wang, W. Q. Deng, K. L. Han, *J. Phys. Chem. Lett.* **2018**, *9*, 3087-3092.

27. H. Wang, D. H. Kim, *Chem. Soc. Rev.* **2017**, *46*, 5204-5236.

28. W. Zhang, K. Tao, C. Ji, Z. Sun, S. Han, J. Zhang, Z. Wu, J. Luo, *Inorg. Chem.* **2018**, *57*, 4239-4243.

29. M.-Q. Li, Y.-Q. Hu, L.-Y. Bi, H.-L. Zhang, Y. Wang, Y.-Z. Zheng, *Chem. Mater.* **2017**, *29*, 5463-5467.

30. M. Abulikemu, S. Ould-Chikh, X. Miao, E. Alarousu, B. Murali, G. O. Ngongang Ndjawa, J. Barbé, A. E Labban, A. Amassian, S. De Gobbo, *J. Mater. Chem. A* **2016**, *4*, 12504-12515.

31. J. Laane, P. W. Jagodzinski, *Inorg. Chem.* **1980**, *19*, 44-49.

32. C. Ran, Z. Wu, J. Xi, F. Yuan, H. Dong, T. Lei, X. He, X. Hou, *J. Phys. Chem. Lett.* **2017**, *8*, 394-400.

33. R. Zhang, X. Mao, Y. Yang, S. Yang, W. Zhao, T. Wumaier, D. Wei, W. Deng, K. Han, *Angew. Chem., Int. Ed.* **2019**, *58*, 2725-2729.

34. A. S. Berestennikov, Y. Li, I. V. Iorsh, A. A. Zakhidov, A. L. Rogach, S. V. Makarov, *Nanoscale* **2019**, *11*, 6747-6754.

35. Z. Zhang, X. Li, X. Xia, Z. Wang, Z. Huang, B. Lei, Y. Gao, *J. Phys. Chem. Lett.* **2017**, *8*, 4300-4307.

36. T. Kawai, A. Ishii, T. Kitamura, S. Shimanuki, M. Iwata, Y. Ishibashi, *J. Phys. Soc. Jpn.* **1996**, *65*, 1464-1468.

37. C. Ni, G. Hedley, J. Payne, V. Svrcek, C. McDonald, L. K. Jagadamma, P. Edwards, R. Martin, G. Jain, D. Carolan, D. Mariotti, P. Maguire, I. Samuel, J. Irvine, *Nat. Commun.* **2017**, *8*, No. 170.

38. S. M. Jain, D. Phuyal, M. L. Davies, M. Li, B. Philippe, C. De Castro, C. Tsoi, O. Karis, H. Rensmo, T. Edvinsson, *Nano Energy* **2018**, *49*, 614-624.

39. H. Oga, A. Saeki, Y. Ogomi, S. Hayase, S. Seki, *J. Am. Chem. Soc.* **2014**, *136*, 13818-13825.

40. T. Ghosh, A. Gopal, S. Nagasawa, N. Mohan, A. Saeki, V. C. Nair, *ACS Appl. Mater. Interfaces* **2016**, *8*, 25396-25404.

41. J. Peng, Y. Chen, K. Zheng, T. Pullerits, Z. Liang, *Chem. Soc. Rev.* **2017**, *46*, 5714-5729.

42. N. T. P. Hartono, S. Sun, M. C. Gélvez-Rueda, P. J. Pierone, M. P. Erodici, J. Yoo, F. Wei, M. Bawendi, F. C. Grozema, M. Sher, T. Buonassisi, J.-P. Correa-Baena, *J. Mater. Chem. A* **2019**, *7*, 23949-23957.

43. M. E. Kamminga, A. Stroppa, S. Picozzi, M. Chislov, I. A. Zvereva, J. Baas, A. Meetsma, G. R. Blake, T. T. M. Palstra, *Inorg. Chem.* **2017**, *56*, 33-41.

44. K. Yamada, R. Nishikubo, H. Oga, Y. Ogomi, S. Hayase, S. Kanno, Y. Imamura, M. Hada, A. Saeki, *ACS Photonics* **2018**, *5*, 3189-3197.

45. J.-C. Blancon, A. V. Stier, H. Tsai, W. Nie, C. C. Stoumpos, B. Traoré, L. Pedesseau, M. Kepenekian, F. Katsutani, G. T. Noe, J. Kono, S. Tretiak, S. A. Crooker, C. Katan, M. G. Kanatzidis, J. J. Crochet, J. Even, A. D. Mohite, *Nat. Commun.* **2018**, *9*, No. 2254.

Chapter 3

Organic Cations Assisted Improvement of Optoelectronic Properties of Bismuth Halide Perovskites

3.1. Abstract

*Bismuth halide perovskites exhibit poor charge carrier separation efficiency due to the presence of insulating organic barriers in their crystal structure. To address this issue, we have integrated an electronically active organic cation, naphthalimide ethylammonium, between the $[BiI_5^{2-}]_n$ chains via crystal engineering to form a novel perovskite material, (naphthalimide ethylammonium)$_2$BiI$_5$ (**NBI**). It exhibited anisotropic photoconductivity and long-lived charge carriers with milliseconds lifetime, which is higher than that of CH$_3$NH$_3$PbI$_3$. Density functional theory calculations confirmed type-IIa band alignment between the organic cations and inorganic chains, allowing the former to electronically contribute to the overall charge transport properties of the material. Further, we have synthesized similar structures such as biphenyl bis(methylammonium)$_{1.5}$BiI$_6$ (**BPBI**) and naphthalene diimide bis(ethylammonium)$_{1.5}$BiI$_6$ (**NDBI**), investigated the role of organic cations in the formation of type-IIa band alignment and modulating the visible light absorption and photoconductivity. UV-vis absorption spectroscopic analysis indicated a narrow bandgap for **NDBI** (1.82 eV) compared to **BPBI** (2.06 eV). Flash photolysis time-resolved microwave conductivity analysis unraveled about 3.7 fold higher photoconductivity for the former compared to the latter.*

3.2. Introduction

The traditional 3D lead halide perovskites suffer from poor intrinsic stability under moisture, thermal, and light conditions. In contrast, the low dimensional (2D, 1D, and 0D) perovskite analogues exhibited much-improved stability owing to the hydrophobic insulation provided by the bulkier organic spacer cations.[1-3] Although low dimensional perovskites are stable under ambient conditions, the insulating nature of the organic layers and poor electronic coupling between the inorganic framework resulted in a wide optical bandgap and high effective mass of charge carriers. Consequently, the optoelectronic performances of low dimensional perovskites are far inferior to that of the corresponding 3D perovskites. However, the structural diversity of low-dimensional perovskites owing to the capability of the inorganic framework to accommodate a variety of organic spacer cations enabled the fine-tuning of their optoelectronic properties for specific tailor-made applications. The current research is focused on improving the visible light absorption and photoconductivity of these low-dimensional perovskites for further enhancing their optoelectronic device performances. The majority of the reported materials consist of electronically inactive organic cations, which do not have any orbital contribution to the band structure of perovskites. Recently, many theoretical and experimental studies on incorporating functional organic cations for overcoming the charge carrier separation and transport bottleneck in low-dimensional perovskites have been reported.

Stupp *et al.* proposed that the incorporation of tetrachloro-1,2-benzoquinone (TCBQ) into the layered perovskite $(H–Nap–O–Pr–NH_3^+)_2PbI_4$ could effectively screen the Coulombic force of attraction between the electron-hole pair and significantly reduce the exciton binding energy (**Figure 3.1**a).[4] They have selected a series of naphthalene derivatives as the donor moieties and found that only herringbone-arranged naphthalene donors can form charge transfer (CT) complex with TCBQ in the perovskite structures. The perovskites with strong π-π stacked naphthalene donors are incapable of providing space for the occupancy of TCBQ acceptors, and hence no CT complexes are formed in the organic framework. Upon increasing the doping concentration of TCBQ, gradual exciton binding energy reduction was observed from the low-temperature absorption spectra (**Figure 3.1**b).
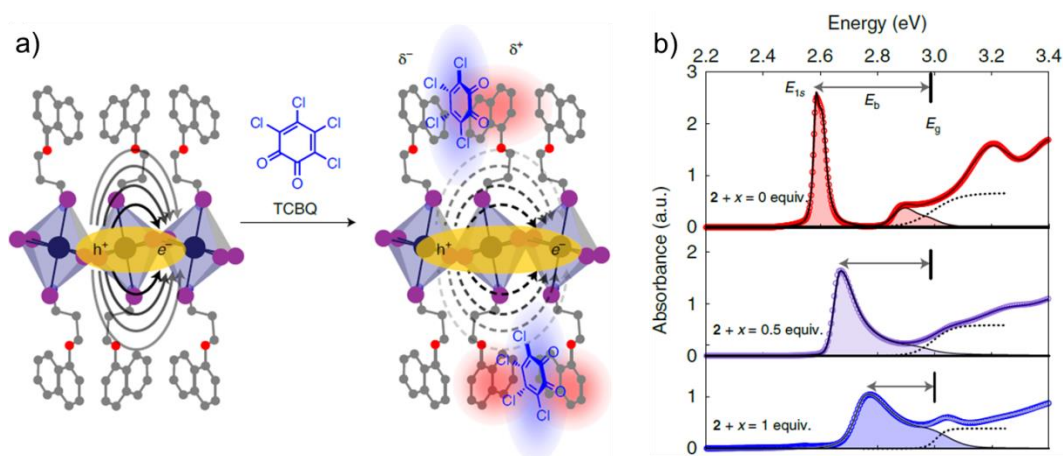
Figure 3.1. a) Schematic of exciton binding energy lowering in $(H–Nap–O–Pr–NH_3^+)_2PbI_4$ perovskite upon addition of TCBQ. b) Low-temperature (78 K) absorption spectra of $(H–Nap–O–Pr–NH_3^+)_2PbI_4$ perovskite showing shift in the exciton band and continuum of absorption at different TCBQ doping levels. Adapted from reference 4.

Grozema *et al*. fabricated thin films of 2D lead halide perovskites integrated with pyrene-tetracyanoquinodimethane (pyrene:TCNQ) CT complex.[5] The thin-films of (pyrene:TCNQ)$_2$PbI$_4$ featured CT bands centered at 600 nm and 850 nm, respectively. They have probed the exciton generation in the inorganic PbI$_4$ layer upon exciting the CT band using femtosecond transient absorption spectroscopy. The time-resolved microwave photoconductivity (TRMC) of the material exhibited a higher photoconductivity signal (200×10^{-6} cm^2 V^{-1} s^{-1}) compared to the pyrene-TCNQ CT complex (50×10^{-6} cm^2 V^{-1} s^{-1}), owing to the efficient exciton dissociation in the material. The energy level alignments suggest that excited electrons will reside in the TCNQ orbitals, whereas the holes will be delocalized in the PbI$_4^{2-}$ framework. This band alignment resulted in a long carrier lifetime of 1-4 μs. Followed by this work, Beljonne and coworkers successfully crystallized a one-dimensional CT perovskite (PyrC$_4$NH$_3$)PbI$_3$·(TCNQ), consisting of [PbI$_3^-$]$_n$ 1D chains formed by the face-sharing of PbI$_6^{3-}$ octahedrons partitioned by pyrene-TCNQ CT complex (**Figure 3.2**a).[6] The material featured a narrow optical bandgap (~1 eV) owing to the absorption contribution from the CT complex in the hybrid structure. DFT calculations and TRMC analysis (**Figure 3.2**b) suggested that the efficient hybridization between the 1D [PbI$_3^-$]$_n$ chains and CT complex of (PyrC$_4$NH$_3$)PbI$_3$·(TCNQ) results in hole localization in the inorganic lattice and electron will reside in the organic framework, which subsequently leads to facile free charge carrier generation.
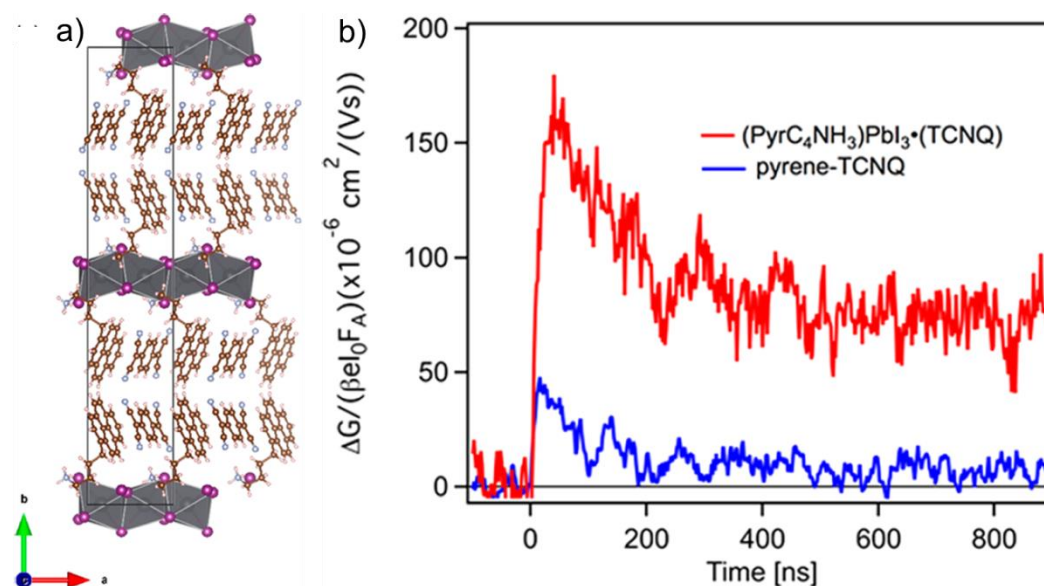
Figure 3.2. a) Crystal packing of (pyrC$_4$NH$_3$)PbI$_3$(TCNQ) consisting of 1D [PbI$_3^-$]$_n$ chains formed by the face sharing of PbI$_6^{3-}$ octahedrons. b) TRMC traces of (pyrC$_4$NH$_3$)PbI$_3$.(TCNQ) and pyrene-TCNQ CT complex. Adapted from reference 6.

Recently, Marder and coworkers have reported a set of lead-based perovskite single-crystals incorporating electron acceptor naphthalene diimide moiety by changing the crystallization conditions. The obtained materials have the formula [(NDIC2)$_2$Pb$_5$I$_{14}$(DMF)$_2$]·4DMF (1), [(NDIC2)$_3$Pb$_5$I$_{16}$]·6NMP (2), [(NDIC2)Pb$_4$I$_{10}$]·4DMF (3), [(NDIC2)Pb$_2$I$_6$]·4NMP (4), and [(NDIC2)Pb$_2$I$_6$]·2H$_2$O (5) (NDIC2: 2,2′-[naphthalene-1,8:4,5-bis(dicarboximide)-N,N′-diyl]-bis-(ethylammonium)).[7] Except compound 2, which is a 0D perovskite, all others are 1D perovskites. Perovskites 4 and 5 have an isostructural 1D inorganic framework formed by the face sharing of Pb-I octahedrons. Extensive π-π stacking of NDIC2 cations was observed in compound 1, which facilitated charge transfer interaction

between the inorganic framework and NDIC2 moiety. The optical absorption of materials 1, 4, and 5 are similar with an absorption onset of ~1 eV.

Etgar *et al*. studied the role of organic spacer cations such as benzylammonium (BA), phenylethylammonium (PEA), and propylphenylammonium (PPA) in 2D lead halide perovskites.[8] The optical bandgap of the perovskites $(BA)_2PbBr_4$, $(PEA)_2PbBr_4$, and $(PPA)_2PbBr_4$ are identical, suggesting that the organic cations do not have any contribution to the band edges of the perovskite materials. The charge density mapping proved that the electron and hole density is delocalized over the entire BA molecule. In contrast, the charge carriers are confined in the phenyl ring of PEA and PPA. This leads to better electronic conductivity in $(BA)_2PbBr_4$ compared to $(PEA)_2PbBr_4$ and $(PPA)_2PbBr_4$. In accordance with the above observation, solar cells fabricated using $(BA)_2PbBr_4$ exhibited a higher power conversion efficiency (7.3%) compared to $(PEA)_2PbBr_4$ (5.8%) and $(PPA)_2PbBr_4$ (4.7%).

Zeng *et al*. theoretically predicted that by varying the inorganic layer thickness and the π-conjugation of organic spacer cations, the band alignment could be tuned between type-I and type-II.[9] In type-I band alignment, only one type of atomic orbitals (organic or inorganic) will participate in band edge contribution. In contrast, both organic and inorganic molecular orbitals hybridize at the band edge states in type-II band alignment. The type-II band alignment favors efficient exciton dissociation into free charge carriers, which is beneficial for optoelectronic applications.
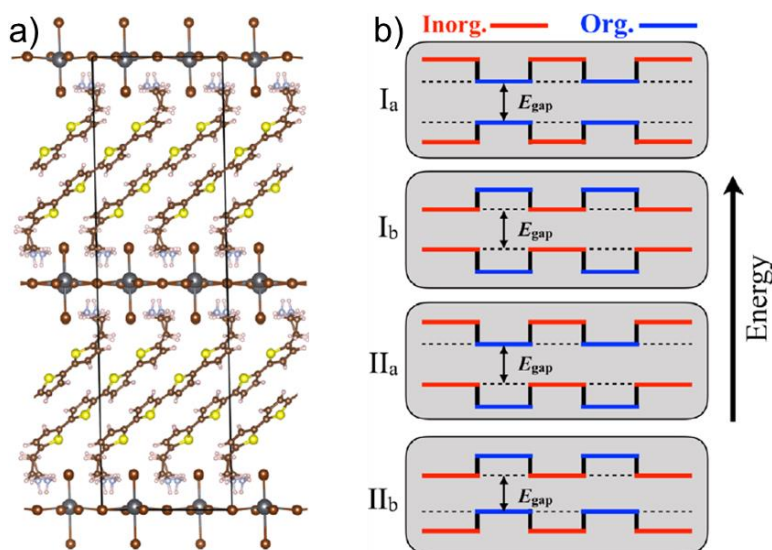
Figure 3.3. a) X-ray crystal structure of (bis(aminoethyl)-quaterthiophene)PbBr$_4$ consisting of alternate layers of bis(aminoethyl)-quaterthiophene and PbI$_4^{2-}$. b) Various band alignments possible in layered 2D perovskites based on the energy level alignment between organic and inorganic components. Adapted from reference 10.

Blum *et al*. theoretically investigated the band structure of a 2D layered perovskite (bis(aminoethyl)-quaterthiophene)PbBr$_4$ (**Figure 3.3**a) using DFT calculations.[10] The band-edge states of this material is composed of inorganic atomic orbitals and classified as a type-Ib semiconductor (**Figure 3.3**b). Grozema *et al*. performed computational calculations to predict the band structure of 2D perovskites incorporating electron-donating and accepting organic chromophores.[11] The functional organic spacer cations selected for the study are 2,7-dibutylammonium[1]benzothieno[3,2-b][1]benzothiophene (BTBT), *N,N*-Bis(n-butylammonium)perylene-3,4,9,10-tetracarboxylic diimide (PDI) and *N,N*-Bis(n-butylammonium)naphthalene-1,4,5,8-tetracarboxylic diimide (NDI). For BTBT-PbI$_4$ perovskite, the VBM states are composed of aromatic π-core of BTBT, and CBM

energy levels are derived from lead iodide inorganic slabs. In contrast, for PDI-PbI$_4$ and NDI-PbI$_4$ perovskites, the organic cation atomic orbitals significantly contribute to the CBM energy levels, whereas the VBM states are constructed from the lead iodide inorganic layers. Compared to the conventional lead-based 2D perovskites, these functional organic cations integrated perovskites featured a narrow optical bandgap. For instance, the optical bandgap for BTBT-PbI$_4$, NDI-PbI$_4$ and PDI-PbI$_4$ are 1.66 eV, 0.11 eV and 0.32 eV, respectively. The effective mass for electrons and holes for all three materials are lower along the inorganic layers compared to the perpendicular direction. This was ascribed to the efficient carrier transport through the inorganic sheets, whereas the charge transport in the organic layers relies on the π-π stacking.

Stupp *et al.* reported the role of π-conjugated organic spacer cations based on naphthalene, pyrene, and perylene on the conductivity properties of layered perovskites.[12] Perylene containing perovskite featured the highest out-of-plane conductivity due to the proper energy level alignment between the perylene and inorganic moieties. Importantly, they have observed that edge-face orientation of naphthalene and pyrene in the perovskite structures exhibited improved out of plane conductivity compared to their edge-edge alignment. Sun *et al.* reported ambipolar charge transport in a layered 2D perovskite, (NDIA)$_4$Pb$_3$I$_{10}$ (NDIA: naphthalene diimide ammonium) with electron and hole mobility of 5.44×10^{-3} cm^2 V^{-1} s^{-1}, and 5.83×10^{-3} cm^2 V^{-1} s^{-1}, respectively.[13] The optical absorption spectrum revealed a

narrow optical bandgap of 1.45 eV for $(NDIA)_4Pb_3I_{10}$ owing to the charge transfer interaction between the NDIA organic layers and Pb-I inorganic lattice. The authors reasoned that the NDIA would be acting as an electron acceptor and the Pb-I framework as electron donors. This synergistic electronic interaction is responsible for the ambipolar charge transport of $(NDIA)_4Pb_3I_{10}$. The above reports suggest that the electron acceptor/donor organic cations could improve overall exciton dissociation efficiency and charge carrier transport in low-dimensional perovskites. A similar approach was adopted in lead-free 1D perovskites such as $(C_7H_7)SbI_4$ and $(C_7H_7)BiI_4$, which are reported to form charge-separated states by the photoinduced electron transfer from inorganic layers to the π-π stacked tropilium cations.[14] A charge-transfer semiconductor was formed consisting of conduction and valence bands composed of tropylium cations and inorganic chains, respectively. In addition to the improved conductivity induced by aromatic organic cations, the polarizability of these moieties could lower the exciton binding energy by reducing the dielectric confinement.

3.3. Results and discussion

3.3.A. Semiconducting spacer cation enabled type-II band alignment and anisotropic photoconductivity in 1D Bi-perovskite

In this section, we report the use of naphthalene monoimide to overcome the charge carrier transfer bottleneck in low-dimensional bismuth-halide perovskites. For that, we have interdigitated naphthalene monoimide derived ligands between the

inorganic $[BiI_5^{2-}]_n$ chains to form a perovskite material (naphthalimide ethylammonium)$_2$BiI$_5$ (**NBI**). The single crystals of **NBI** were synthesized from the aqueous hydrogen iodide (HI) solution containing a 1:1 molar ratio of naphthalimide ethylammonium iodide and BiI$_3$. Red needle-like single crystals having several millimeters in length were harvested from the HI solution after 24 h.

3.3.A1. Crystal structure analysis of NBI

The X-ray diffraction (XRD) analysis of the crystals at 297 K revealed that **NBI** has a monoclinic crystal structure and belongs to the *P*2$_1$/*c* space group (**Figure 3.4**a). It also revealed that **NBI** has a 1D perovskite structure consisting of inorganic $[BiI_5^{2-}]_n$ chains formed by the corner-sharing of BiI$_6^{3-}$ octahedra. The organic counterpart, naphthalene monoimides, adopted a face-on π−π stacking arrangement with an average distance of 3.5 Å, which hinted at a potential charge transport pathway. On the other hand, the inorganic chains are stacked one above the other with zero octahedral unit displacement along the crystallographic *b* axis. These chains are separated by bilayers of monovalent naphthalimide cations resulting in a multiple-quantum-well (MQW) structure at the molecular level. In this structure, inorganic chains will act as conducting wells and the organic molecules as screening layers for inter-well charge hopping. This is the first perovskite material exhibiting an eclipsed packing of zig-zag $[BiI_5^{2-}]$n chains separated by organic monocations to the best of our knowledge.
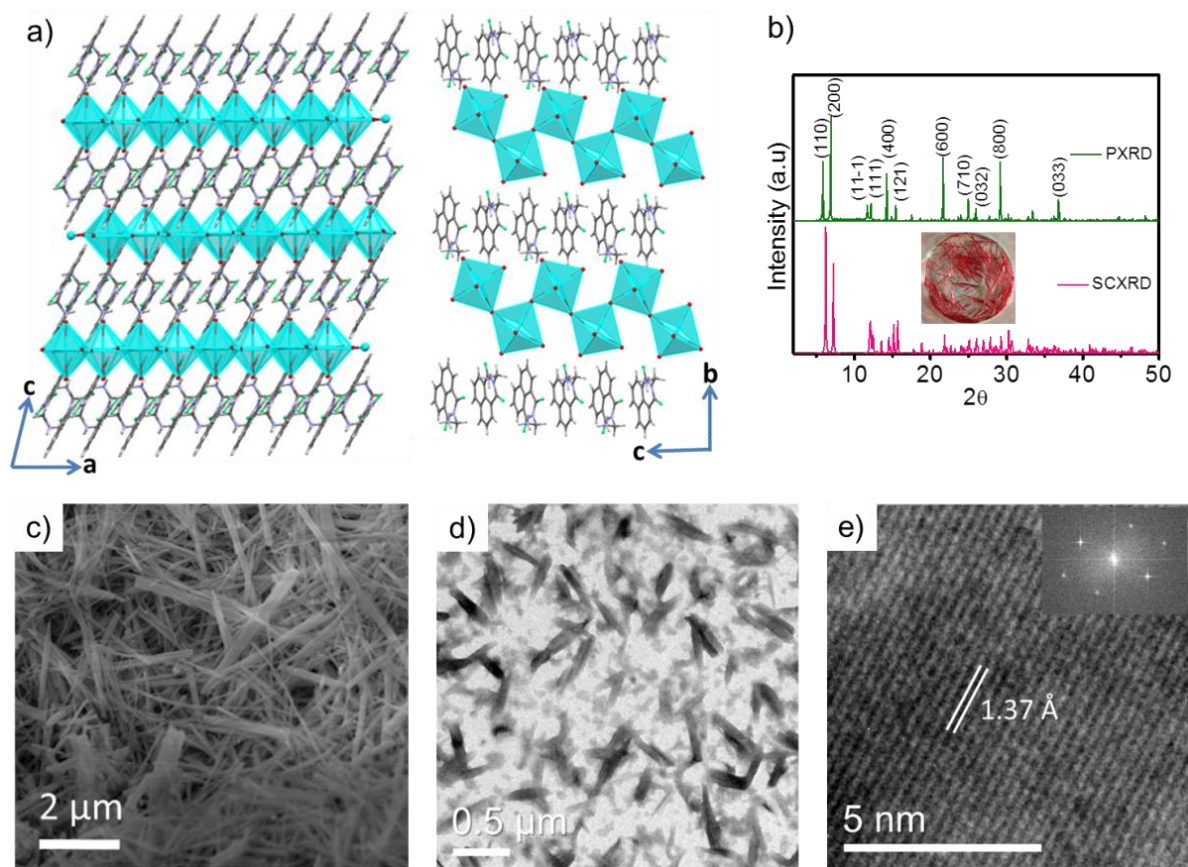
Figure 3.4. (a) Lateral (along b-axis) and top view (along a-axis) of the crystal packing of **NBI** showing a multiple-quantum-well structure. (b) Powder and single-crystal X-ray diffraction patterns of **NBI**. Inset shows the photograph of the needle-shaped single crystals. (c) Scanning electron microscope and (d) transmission electron microscope images of an **NBI** thin-film sample. (e) A high-resolution transmission electron microscope image of **NBI** shows a lattice spacing of 1.37 Å. Inset shows the fast Fourier transform image with bright diffraction spots arranged in a distorted hexagonal shape.

Single-crystal XRD analysis revealed that the aromatic face-on π−π interactions between the rigid organic spacers stabilize the unique crystal packing in **NBI**. Powder and single-crystal XRD patterns match well without any secondary phase peaks, suggesting the phase purity of the crystals (**Figure 3.4**b). The zig-zag connectivity of BiI_6^{3-} octahedras in the $[BiI_5^{2-}]_n$ chains imparted a layered structure to **NBI**, which

was in good agreement with the observed intense ⟨110⟩ plane reflection in the single crystal XRD pattern. Equidistant ⟨100⟩ reflections in the powder XRD pattern confirmed that the inorganic layers are arranged one above the other separated by the organic spacers. The scanning electron microscope and transmission electron microscope analysis showed a needle-like 1D growth morphology similar to the bulk single crystals (**Figure 3.4**c and d, respectively). The high-resolution TEM image showed a well-defined atomic lattice with a lattice separation of 1.37 Å corresponding to a ⟨61-2⟩ plane (**Figure 3.4**e). Bright diffraction spots in the fast Fourier transformation image are attributed to the highly crystalline nature of **NBI**.

3.3.A2. Optical characterizations and thermal stability studies
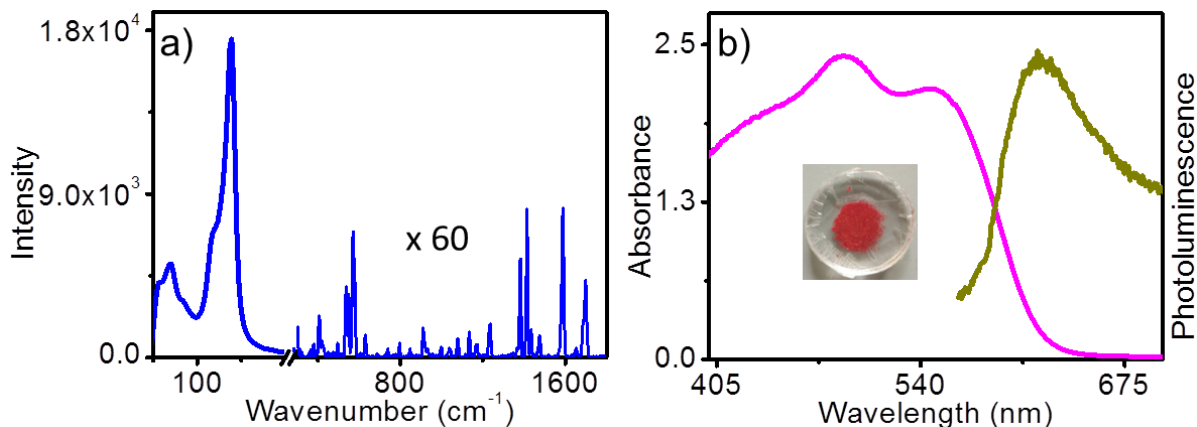
Figure 3.5. a) Raman spectrum of **NBI** single crystals upon 785 nm laser excitation. The region corresponding to the vibrational modes of naphthalimide cations (300−1800 cm⁻¹) is enhanced by 60× for visibility. b) Absorption and emission spectra of the **NBI** powder sample. The inset shows the photograph of the powder sample.

Raman spectrum provides direct evidence for electron-phonon coupling in perovskites. Generally, intense Raman active vibrational modes imply a strong electron-phonon coupling.[15,16] The Raman spectrum of **NBI** at 785 nm laser excitation showed two prominent peaks corresponding to Bi−I bond bending, and symmetric stretching vibrations at 69 and 138 cm^{-1}, respectively (**Figure 3.5**a).[16] In addition to this, vibrational modes of naphthalimide cations were observed between 300 and 1800 cm^{-1}. This implies that the excited electrons are coupled with the vibrational modes of both organic and inorganic moieties. In other words, the naphthalimide cations are contributing to the electronic properties of **NBI**. The intensity of the peaks corresponding to the vibrational modes of BiI_5^{2-} units were remarkably high compared to the naphthalimide cations. This indicates that the vibrational modes of inorganic units are more strongly coupled to the excited electrons than the organic units. The optical absorption spectrum of **NBI** spans from 400 to 600 nm with a well-defined excitonic absorption peak at 548 nm and an additional peak at 490 nm (**Figure 3.5**b). The peaks at 548 and 490 nm could be attributed to the $^1S_0-^3P_1$ and $^1S_0-^3P_2$ electronic transitions of the Bi^{3+} ions in the BiI_5^{2-} units, respectively.[17−19] This indicates that the ground-state electronic transitions are occurring within the BiI_6^{3-} inorganic units. **NBI** showed weak photoluminescence upon 500 nm excitation with a PL maximum at 619 nm. Since the emission peak is narrow and close to the absorption continuum, it is likely originated from excitonic radiative recombination (**Figure 3.5**b).
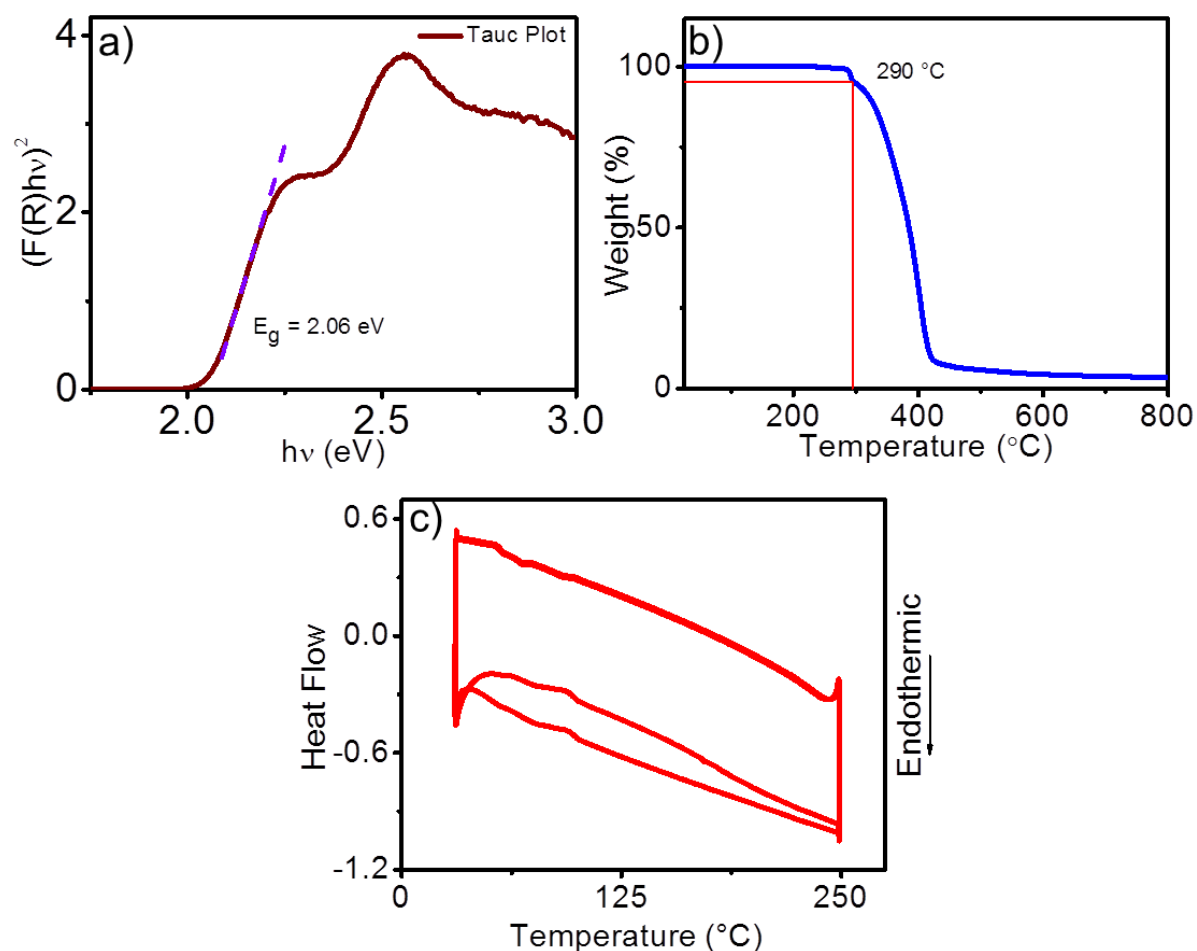
Figure 3.6. a) Optical bandgap calculation of **NBI** from the Tauc plot. b) Thermogram of **NBI**. The T_5 value (the temperature at which the material loses 5% of its initial weight) was 290 °C. c) DSC curve of **NBI**.

The optical bandgap of **NBI** was estimated from the Tauc plot as 2.06 eV (**Figure 3.6**a). Thermal and phase stability of **NBI** were confirmed using thermogravimetry (TG, **Figure 3.6**b) and differential scanning calorimetry (**Figure 3.6**c) analyses. TG profile showed 5% initial weight loss at 290 °C, corresponding to the decomposition of organic component. Neither endothermic nor exothermic peaks were observed in the DSC profile proving the phase stability of **NBI** in the measured temperature range.

3.3.A3. Photoconductivity analysis
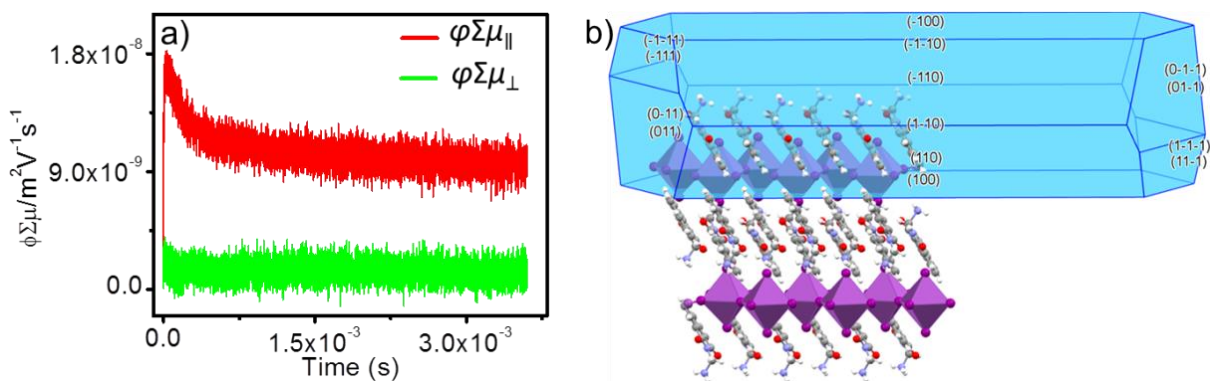
Figure 3.7. a) FP-TRMC kinetics of **NBI** single crystals measured parallel ($\phi\Sigma\mu_\parallel$) and perpendicular ($\phi\Sigma\mu_\perp$) to the crystal long-axis (500 nm laser source was used as the excitation source). b) Crystal shape and packing of **NBI** simulated using Bravais-Friedel-Donnay-Harker method by the Mercury software.[20]

FP-TRMC analysis was performed to evaluate the photoconductivity properties of **NBI**. Since **NBI** crystals have needle shape, the measurement was performed parallel ($\phi\Sigma\mu_\parallel$) and perpendicular ($\phi\Sigma\mu_\perp$) to the crystal long-axis. It was observed that $\phi\Sigma\mu_\parallel$ (1.64×10^{-8} m^2 V^{-1} s^{-1}) was 8.2-fold higher than $\phi\Sigma\mu_\perp$ (2×10^{-9} m^2 V^{-1} s^{-1}; **Figure 3.7**a). High anisotropic photoconductivity in **NBI** suggests that it would be a promising candidate for field-effect transistor and photodetector applications. To get a better understanding of the anisotropic conductivity, the crystal shape and packing direction were simulated using the Bravais-Friedel-Donnay- Harker (BFDH) method. It revealed that the inorganic [BiI$_5^{2-}$]$_n$ chains and stacked naphthalimide cations are arranged along the crystal long-axis, resembling one-dimensional conductor structures for both of them (**Figure 3.7**b). This arrangement provides a facile route for the

charge carriers to move along the crystal long-axis yielding a higher $\phi\Sigma\mu_{\parallel}$. On the other hand, along the perpendicular direction, the charge carriers have to hop from inorganic chains to organic stacks sequentially. Since the latter is a poor conductor compared to the former, such hoping is not favored, resulting in a lower $\phi\Sigma\mu_{\perp}$.
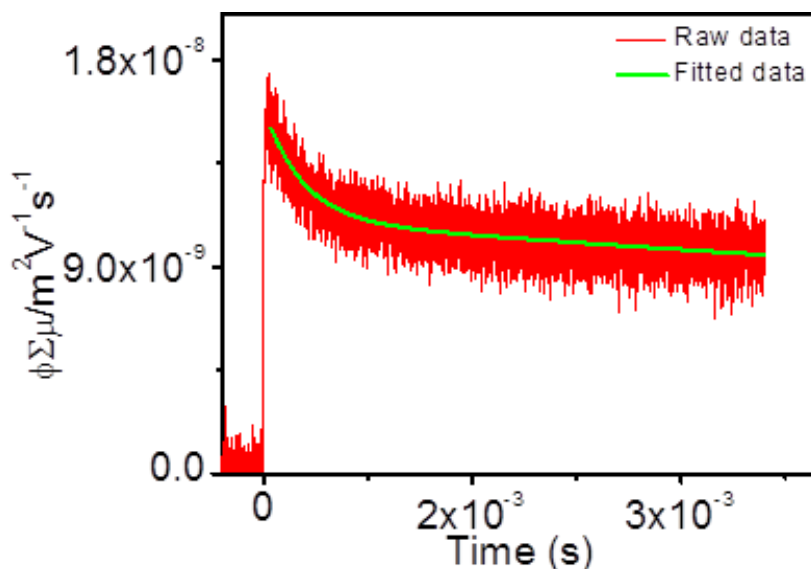
Figure 3.8. TRMC fitting curve of **NBI**.

The $\phi\Sigma\mu_{\parallel}$ signal is fitted using the double exponential function: $A_1\exp(-k_1t) + A_2\exp(-k_2t)$ (**Figure 3.8**). The effective lifetime ($\tau = 18$ ms) was calculated by $(A_1/k_1 + A_2/k_2)/(A_1 + A_2)$, which is significantly higher than the TRMC lifetimes reported for 3D perovskites such as $MAPbI_3$, $Cs_2AgBiBr_6$, and $Cs_2AgBiTlBr_6$.[21,22] The long carrier lifetime of **NBI** implies a critical aspect that the organic moieties are taking part in the charge transport along with the inorganic chains. In other words, the holes move through the one-dimensional $[BiI_5^{2-}]_n$ chains, whereas electrons travel through $\pi-\pi$

stacked naphthalimide moieties. It has been theoretically proven that perylene and naphthalene-based organic cations could provide potential charge transport pathways for electrons in hybrid perovskites.[11] The observation of long-lived carriers in **NBI** is an experimental proof for this theoretical prediction. In most of the 1D bismuth-based perovskites, only the inorganic moieties involved in the charge transport and the organic cations remain electronically inactive.[23–26] Making the organic cations contribute to the electronic properties of perovskites has tremendous implications in the performance of corresponding optoelectronic devices. More importantly, it also opens up an avenue for developing perovskites with tailor-made features for specific applications.

3.3.A4. DFT calculations

To understand the role of the organic cations and the inorganic elements in the electronic properties of **NBI**, density functional theory calculations were performed. After getting the minimum energy configurations, the corresponding projected density of states (PDOS) was estimated for a profound understanding of the electronic structure of **NBI** (**Figure 3.8**). From the PDOS, it is clear that the valence band maximum is composed of bismuth orbitals, whereas, at the conduction band, a dominant hybridization between bismuth and iodine orbitals is observed in addition to the orbital contributions from the naphthalimide cations. The stronger hybridization of bismuth and iodine orbitals led to the stability of BiI_6^{3-} octahedra. The lowest energy
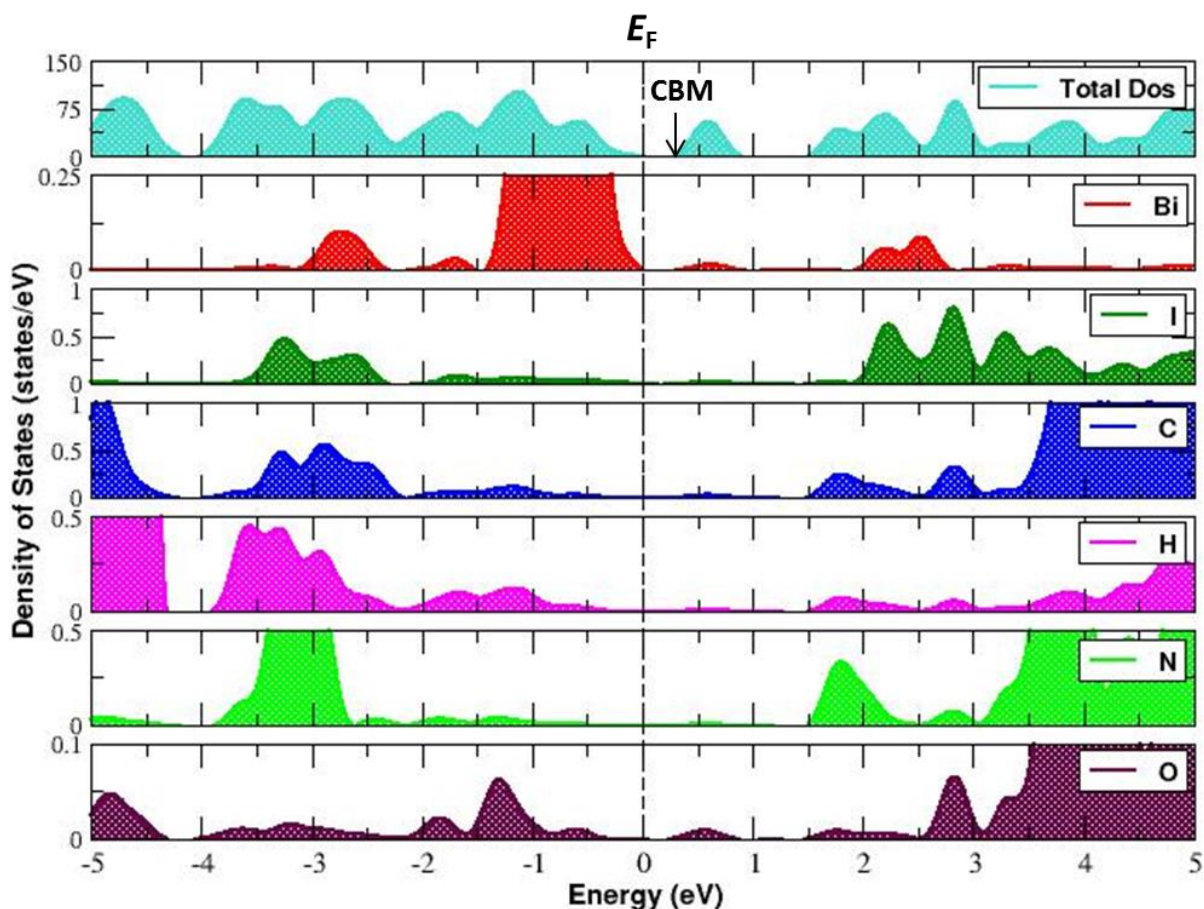
Figure 3.8. The total density of states plot for the calculated band structure of **NBI** and the corresponding partial density of state contribution from the organic and inorganic counterparts. E_F (Fermi energy level) has been considered as the VBM, while the CBM has been indicated with an arrow in the panel of total density of states.

electronic transition in BiI_6^{3-} units occurs at 2 eV, consistent with the observed absorption near the band edges (2.06 eV). In the conduction band, strong hybridization between C, H, N, and O elements of naphthalimide cation is observed at a lower energy (1.8 eV) compared to the BiI_6^{3-} units. One of the prime observations that we can make from this is to relate the electronic structure of **NBI** to the type-IIa band alignment.[27] For the type-IIa alignment, the contribution of the inorganic

elements has prevailed in the vicinity of valence band maxima, whereas organic cations contribute to the deeper electronic levels of the valence bands. The scenario changes in the case of the conduction band regime, where the organic contributions have prevailed nearer to the Fermi level compared to the inorganic counterpart. In other words, the valence band maximum and conduction band minimum states are derived from the BiI_6^{3-} and naphthalimide units, respectively. This band alignment promotes the photoinduced electron transfer from the inorganic Bi−I lattice to the unoccupied frontier molecular orbitals of naphthalimide moieties. In contrast, the holes will reside in the inorganic framework leading to the observed long-lived charge carriers.

3.3.B. Self-assembled spacer cation enabled tuning of optical bandgap and photoconductivity in 0D Bi-perovskites

In the second part of the Chapter, we describe the synthesis and study of two novel bismuth halide perovskite materials; biphenyl bis(methylammonium)$_{1.5}$BiI$_6$.2H$_2$O (**BPBI**) and naphthalene diimide bis(ethylammonium)$_{1.5}$BiI$_6$.2H$_2$O (**NDBI**). Herein, we combined experimental techniques and density functional theory calculations to analyze the structural, electronic, and optical properties of the materials. The title compounds were prepared by the inverse temperature crystallization method from the corresponding precursor solutions in 57% aq. HI.

3.3.B1. X-ray structural and stability analyses
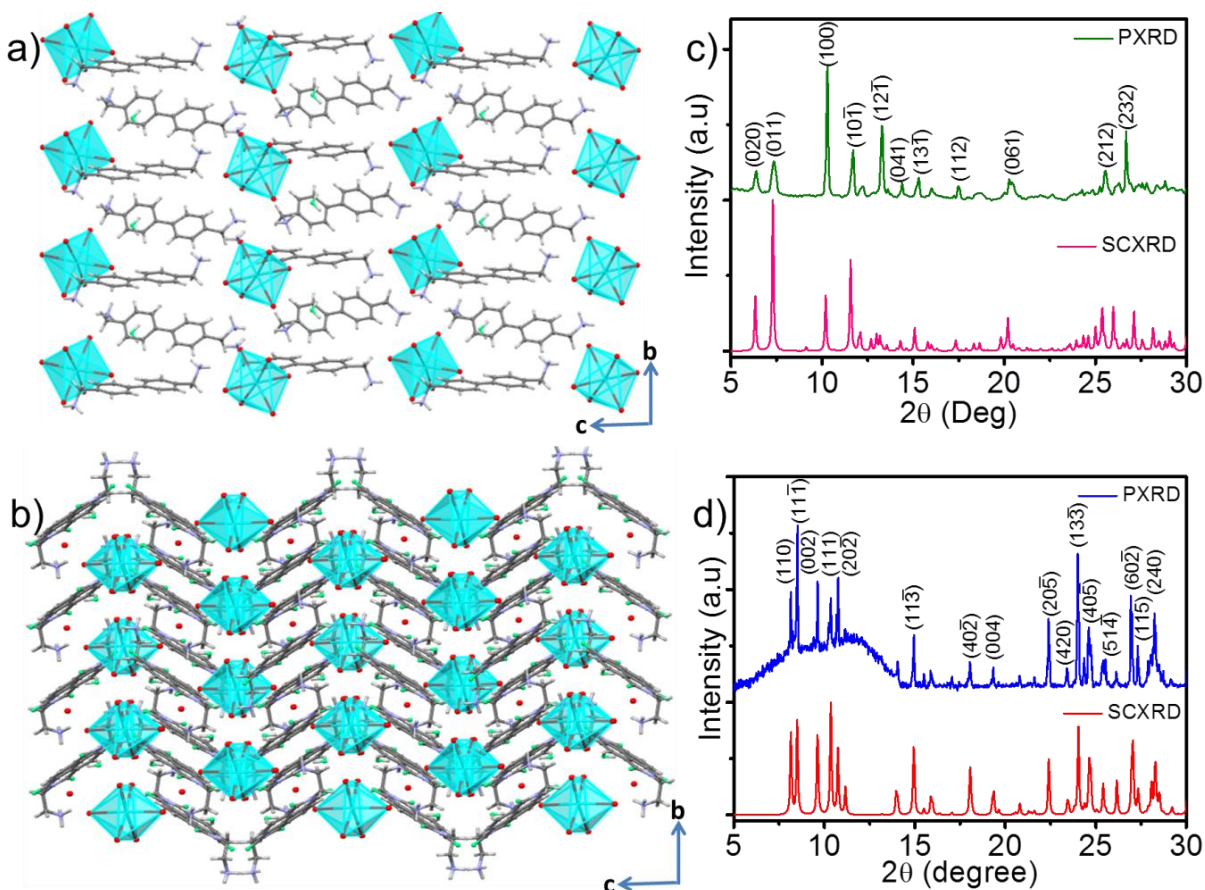
Figure 3.9. Crystal packing along the "*b*" and "*c*" crystallographic axes of a) **BPBI** and b) **NDBI** single crystals. Comparison of the powder and single-crystal X-ray diffraction patterns of c) **BPBI** and d) **NDBI**. All the intense powder X-ray diffraction peaks were indexed using Mercury software.

Room temperature single-crystal X-ray diffraction (SCXRD) analysis revealed the zero-dimensional (0D) crystal structures of **BPBI** and **NDBI** (**Figure 3.9**a and b). Former belongs to *P 2₁/c* space group, whereas the latter belongs to the *C 2/c* space group. **BPBI** and **NDBI** consist of isolated BiI_6^{3-} octahedral units surrounded by biphenyl bis(methylammonium) and naphthalene diimide bis(ethylammonium)

cations, respectively. It may be noted that only a few Bi-I perovskites with completely isolated octahedral units were reported to date to the best of our knowledge.[28, 29] Most of the bismuth perovskite structures exist as dimers or 1D chains ($Bi_2I_9^{3-}$, BiI_4^-, and BiI_5^{2-}) with face, edge, and corner-sharing connectivity of octahedrons. [30-34] They do not fall under the classical "perovskite structure" classification and are called perovskite-like or perovskitoid materials.[35] The formation of completely isolated inorganic octahedrons (BiI_6^{3-}) in the materials under study could be attributed to the large geometrical strain imposed by the bulkier biphenyl and naphthalimide cations.
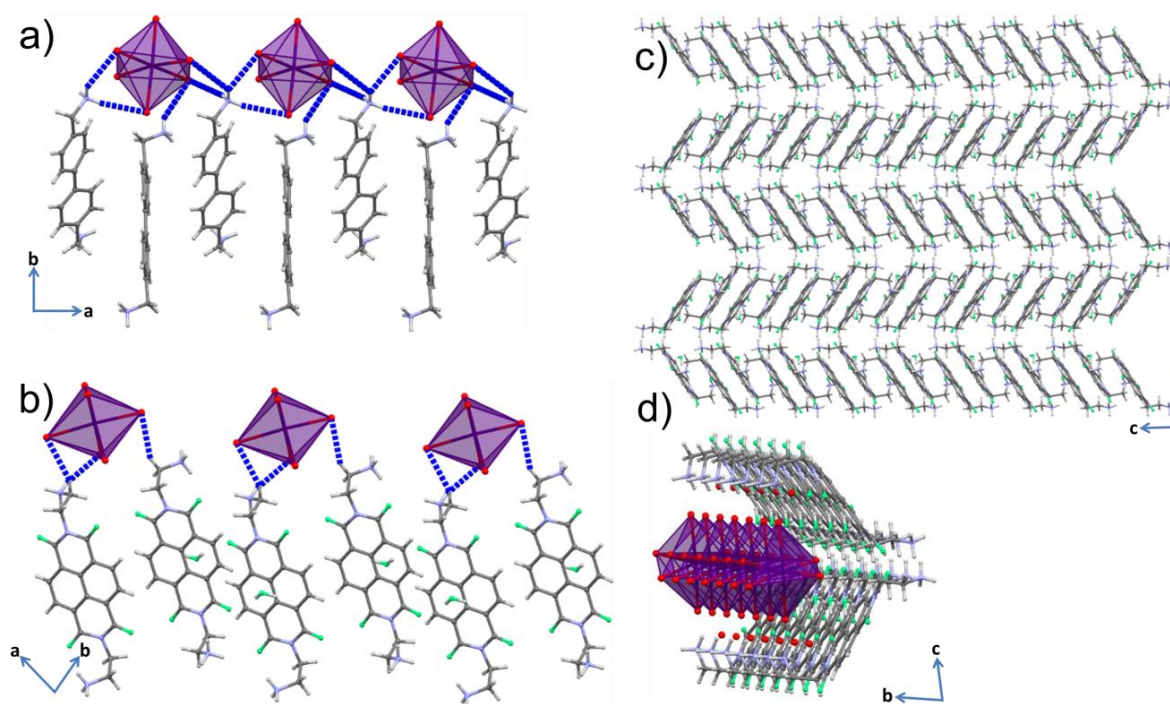
Figure 3.10. a) and b) are showing the intermolecular H-bonding interactions (blue dotted lines) in **BPBI** and **NDBI** perovskite materials, respectively. The adjacent biphenyl cations in **BPBI** are orthogonally stacked, whereas the naphthalimide cations in **NDBI** are arranged in a partially eclipsed fashion. c) Herringbone packing of naphthalene diimide cations in **NDBI**. The inorganic octahedrons are omitted for clarity. d) Picket-fence model arrangement of naphthalene diimide cations around the inorganic framework.

Powder XRD patterns of both materials are in good agreement with their respective SCXRD patterns suggesting the phase purity of the synthesized perovskite single crystals (**Figure 3.9.**c and d).

Biphenyl cations in **BPBI** exhibited strong hydrogen-bonding interactions with the iodine atoms of BiI_6^{3-} octahedral units (**Figure 3.10.**a). However, they are arranged in a disordered manner because of the lack of π-π stacking interaction between the adjacent biphenyl moieties. In **NDBI**, hydrogen-bonding between the naphthalene diimide and inorganic units was observed in the form of HCH...I and $H_2NH...I$ interactions (**Figure 3.10.**b). Moreover, the naphthalimide cations are self-assembled in a tilted-T fashion or otherwise called the herringbone arrangement (**Figure 3.10.**c).[36] The stacking of naphthalimide cations resembles the "picket fence" arrangement of terphenyl moiety in poly(3-"fenced"-thiophene) (**Figure 3.10.**d).[37]

The X-ray photoelectron spectroscopic (XPS) analysis of the title compounds exhibited a similar pattern, with two prominent peaks at 158 and 163 eV ascribed to the binding energies of Bi^{3+} $4f_{7/2}$ and Bi^{3+} $4f_{5/2}$ states, respectively (**Figure 3.11.**a and **3.11.**b).[38] The absence of signals corresponding to the metallic bismuth (Bi^0) in the XPS spectra further confirms the phase purity of the samples. The thermal stability of the materials was evaluated using thermogravimetry analysis. The initial 5% weight loss for **BPBI** and **NDBI** was observed at 273 and 291 °C, respectively (**Figure 3.11.**c and **3.11.**d). The higher thermal stability of **NDBI** could be attributed to the rigidity and strong intermolecular interactions of the interdigitated naphthalimide cations
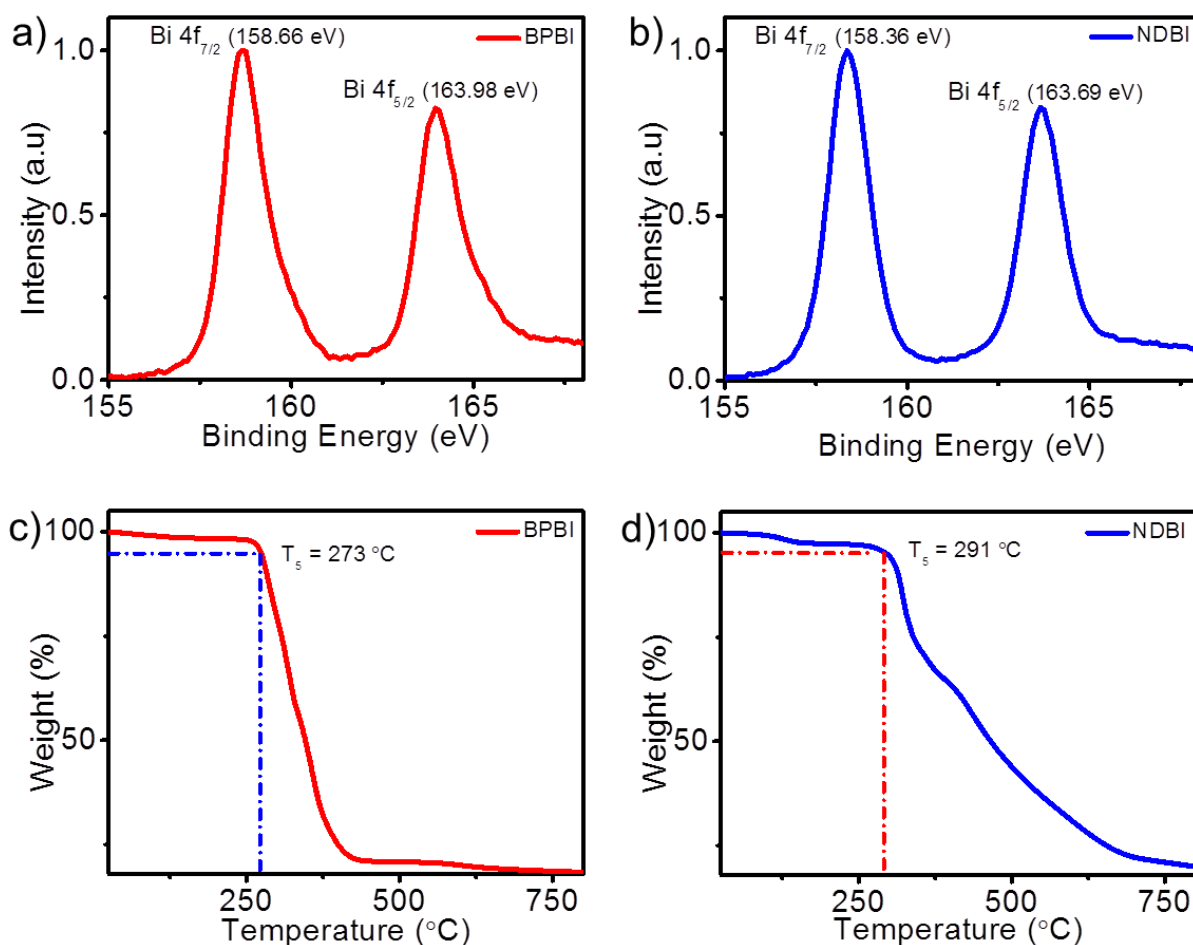
Figure 3.11. a) and b) are XPS spectra of **BPBI** and **NDBI** materials, respectively. Two prominent XPS signals corresponding to the binding energy of the Bi^{3+} state are labeled in the inset. c) and d) are thermograms of **BPBI** and **NDBI,** respectively. The dotted line marks the temperature corresponding to the initial 5% weight loss (T_5) for both materials.

3.3.B2. Optical characterizations

The isostructural feature of the inorganic moieties (BiI_6^{3-}) in these two perovskites enabled us to precisely investigate the role of organic cations in their optical and electronic properties. Both **BPBI** and **NDBI** featured broad visible light absorption across 400-600 nm and 400-680 nm, respectively (**Figure 3.12.**a). The steep
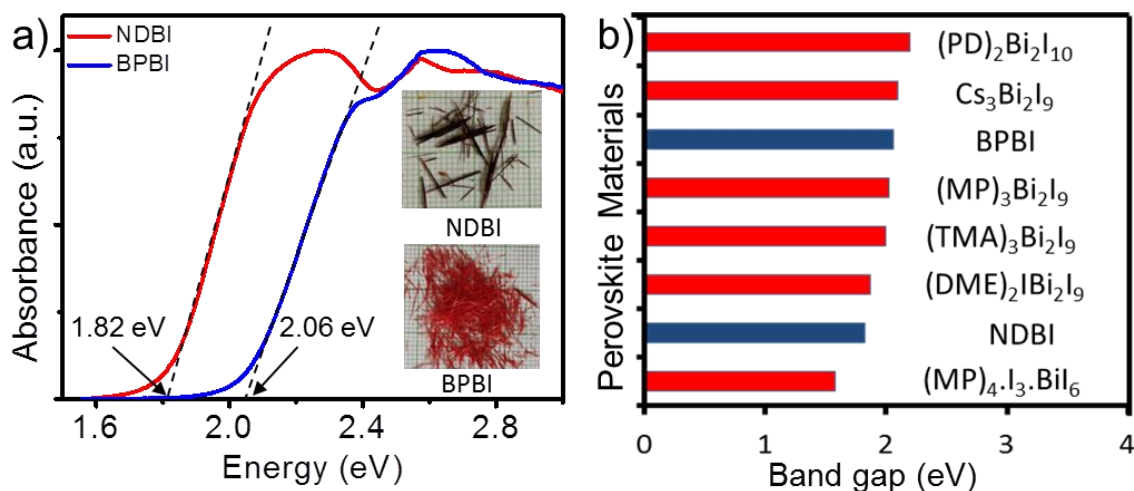
Figure 3.12. a) Absorption spectra of **BPBI** and **NDBI** powder samples derived from diffuse reflectance spectra using the Kubelka-Munk function. The optical bandgap was calculated by extrapolating the steep absorption feature of both materials. Inset shows the photograph of millimeter-sized **BPBI** and **NDBI** single crystals. b) A bandgap comparison plot showing the optical bandgap of various 0D bismuth-based perovskite materials, including **BPBI** and **NDBI** of this study. The abbreviations are PD: 1,3-propane diammonium; MP: 4-methylpiperidinium; TMA: trimethylammonium; DME: bis-(2-dimethylaminoethyl)ether.[30, 31, 39-41]

absorption onset and sharp excitonic features in the optical absorption spectrum indicate the direct bandgap nature of these materials. The optical bandgap of **BPBI** ($E_{g, BPBI}$) and **NDBI** ($E_{g, NDBI}$) were estimated from the absorption onset as 2.06 eV and 1.82 eV, respectively. The significant difference in the optical bandgaps was reflected in the color of their crystals: red for BPBI and blackish red for NDBI (inset of **Figure 3.12.**a). The optical bandgap of these materials compared with that of the 0D bismuth halide perovskite reported in the literature is shown in **Figure 3.12.**b. The lower bandgap of **NDBI** than most reported materials implies its capability of efficient visible light absorption and potential for photovoltaic and photodetector device applications.

Recent reports suggest that metal-halide bond length and distortion of inorganic octahedrons are highly influential in tuning the optical bandgap of perovskites. If the average Bi-I bond length is shorter, the BiI_6^{3-} octahedron will experience a less negative chemical pressure and subsequently leads to a narrow bandgap.[42] The average Bi-I bond length in **BPBI** and **NDBI** is 3.075 Å and 3.081 Å, respectively. Because the mean Bi-I bond length difference is marginal, it could not be correlated to the observed optical bandgap variation in these materials. Another parameter influencing the optical bandgap is the octahedral distortion (Δd), which is calculated using the equation, $\Delta d = \left(\frac{1}{6}\right) \sum (d_i - d)^2 / d^2$ (where d_i denotes the six individual Bi–I bond lengths and d is the average Bi–I bond length). The tilting of inorganic octahedrons leads to poor metal and halide orbital mixing, which will decrease the bandwidth and results in the widening of the optical bandgap.[43] The Δd values for **BPBI** and **NDBI** were calculated as 2.94×10^{-4} and 6.35×10^{-4}, respectively. The calculated Δd values contradict the observed difference in the optical bandgaps of **BPBI** ($E_{g,\text{BPBI}} = 2.06$ eV) and **NDBI** ($E_{g,\text{NDBI}} = 1.82$ eV) materials. Therefore, it is likely that the optical bandgap variation in both the materials arises from reasons other than the slight differences in their inorganic BiI_6^{3-} anion frameworks. Electronic effects such as quantum and dielectric confinements also could modulate the optical bandgap of halide perovskites. The quantum confinement effect varies with structural dimensionality or inorganic layer thickness. Because **BPBI** and **NDBI** have identical

structural dimensionality (i.e., 0D), their quantum confinement effect on optical properties is expected to be similar. Another electronic confinement called dielectric confinement arises from the mismatch in the dielectric constants of inorganic units and the surrounding organic cations. Because both perovskites are composed of aromatic π-conjugated spacer cations, the dielectric environment provided by the organic medium would be comparable.
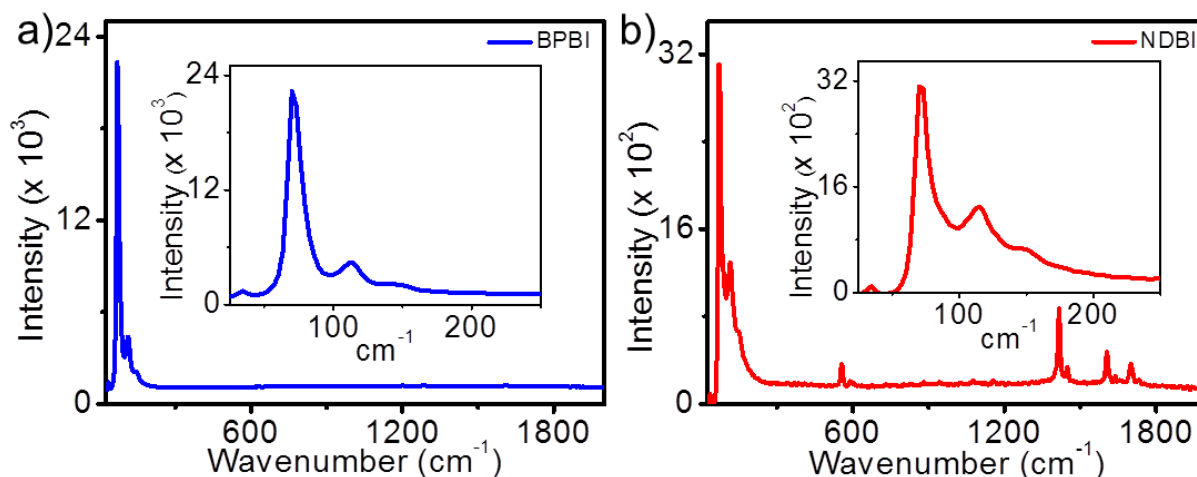
Figure 3.13. Raman spectra of the single crystals of a) **BPBI** and b) **NDBI**. The crystals were excited with a 633 nm laser source. Inset shows zoomed low energy vibrational modes originating from the inorganic octahedrons. The intense Raman peaks at 70 and 113 cm^{-1} for both the materials are attributed to the Bi-I bond bending and stretching vibrational modes, respectively.

By ruling out these electronic possibilities, we hypothesized that the observed substantial red-shift (~80 nm) in the absorption spectrum (and hence a better coverage of the visible region) of **NDBI** compared to that of **BPBI** might originated from the differences in the organic molecular orbital contribution to the overall band structure of these materials. It is well-established that the coupling of electronic excitations

with the vibrational modes of the organic cations in hybrid perovskites could be monitored using Raman spectroscopy.[44] This analysis could reveal the involvement of organic spacer cations in the electronic transitions of **BPBI** and **NDBI**. Single crystals of the respective materials were used for this study. A 633 nm laser, which is very close to the optical band-to-band electronic transition energy of the materials, was used as the excitation source. At this near band edge excitation, both materials showed intense Raman signals between 50-200 cm^{-1} corresponding to the Bi-I bond vibrations (**Figure 3.13.**a and b).[30,31,41] The low energies of inorganic vibrational modes are due to their high reduced mass. Interestingly, the vibrational signatures of naphthalimide cations in the range of 500-1800 cm^{-1} were observed in the Raman spectrum of **NDBI**. This observation implies that the molecular orbitals of both naphthalimide and bismuth-iodide moieties are involved in the absorption of **NDBI**. On the other hand, similar signatures of biphenyl cations were not visible in the Raman spectrum of **BPBI**, indicating the absence of contribution from the organic cations in the overall electronic properties of **BPBI**.

3.3.B3. DFT calculations

Density functional theory (DFT) calculations were performed to understand the influence of organic cations on electronic bandgap of **BPBI** and **NDBI**. The electronic bandgap values calculated from the total density of states plots (**Figure 3.14**.a and b) for **BPBI** and **NDBI** were 2.6 eV (E_g, **BPBI**) and 0.8 eV (E_g, **NDBI**), respectively.
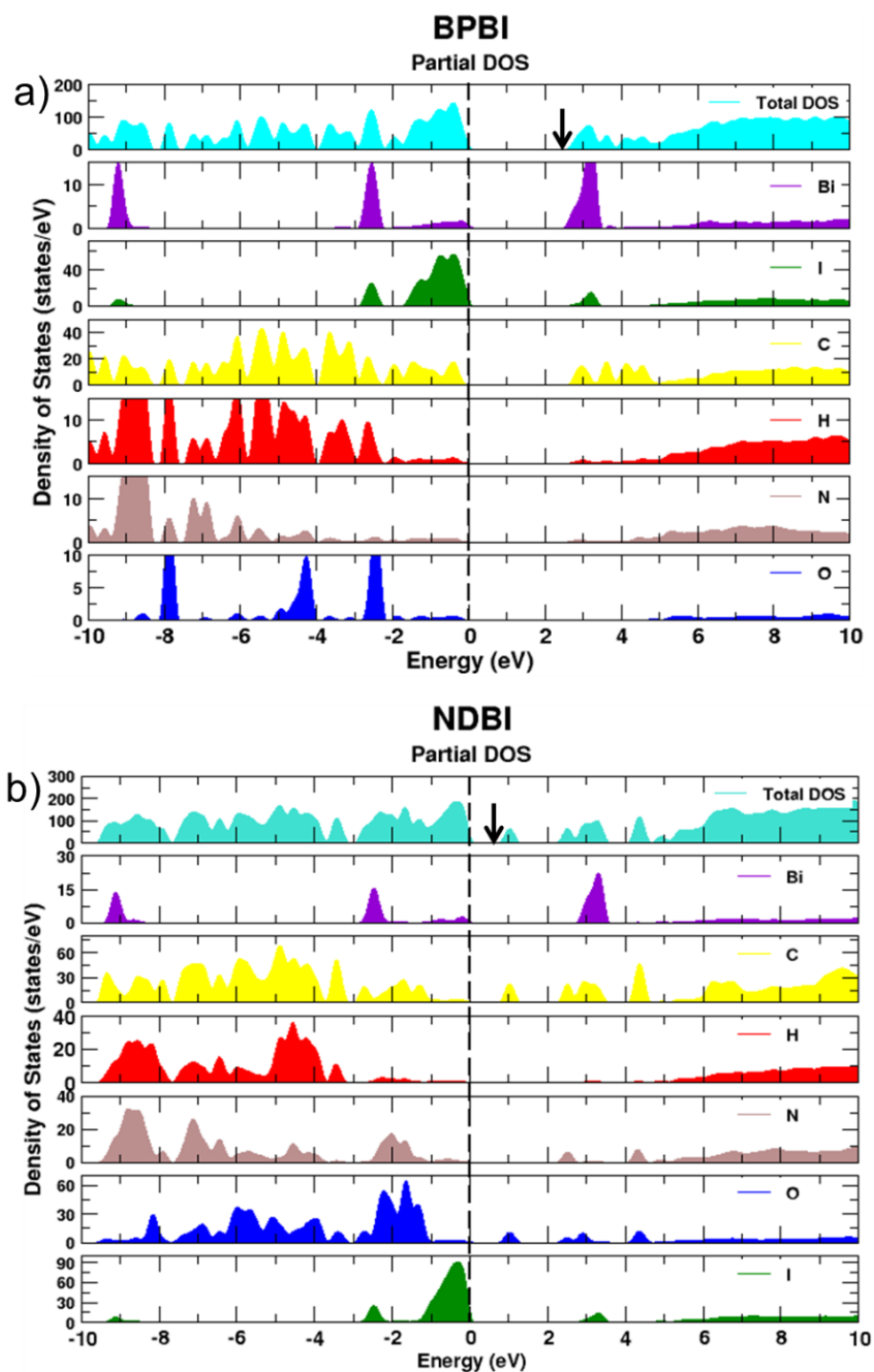
Figure 3.14. The computed partial density of states for a) **BPBI** and b) **NDBI**. The upper panel in both figures shows total density of states of the respective materials. The dotted line indicates the Fermi energy level or valence band maximum. The conduction band minimum is indicated with an arrow in total density of states plot.
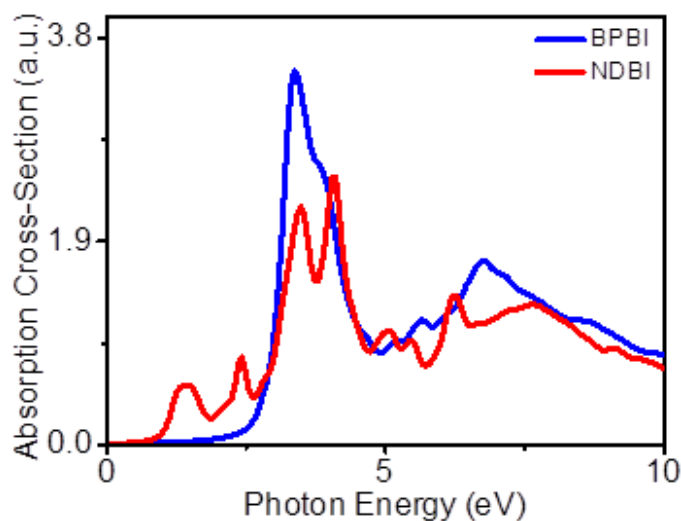
Figure 3.15. Computed optical absorption spectra of **BPBI** and **NDBI** materials.

The computed optical absorption spectra of these materials exhibited absorption onset identical to their calculated electronic bandgaps (**Figure 3.15**). Moreover, the electronic bandgaps estimated from the DFT calculations showed a trend similar to that of experimentally observed optical bandgap with $E_{g, BPBI} > E_{g, NDBI}$. The observed difference in the experimental and theoretical bandgap is due to the limitation of the generalized gradient approximation (GGA) based exchange-correlation functional used in DFT calculations, which could not effectively correct the self-interaction errors.[45] Most importantly, The partial density of states analyses revealed a type-Ib band alignment for **BPBI** and type-IIa band alignment for **NDBI**.[46] In type-Ib band alignment, both valence band maximum (VBM) and conduction band minimum (CBM) density of states is composed of inorganic atomic orbitals (**Figure 3.16.**a). In contrast, for type-IIa band alignment, VBM and CBM energy levels are contributed
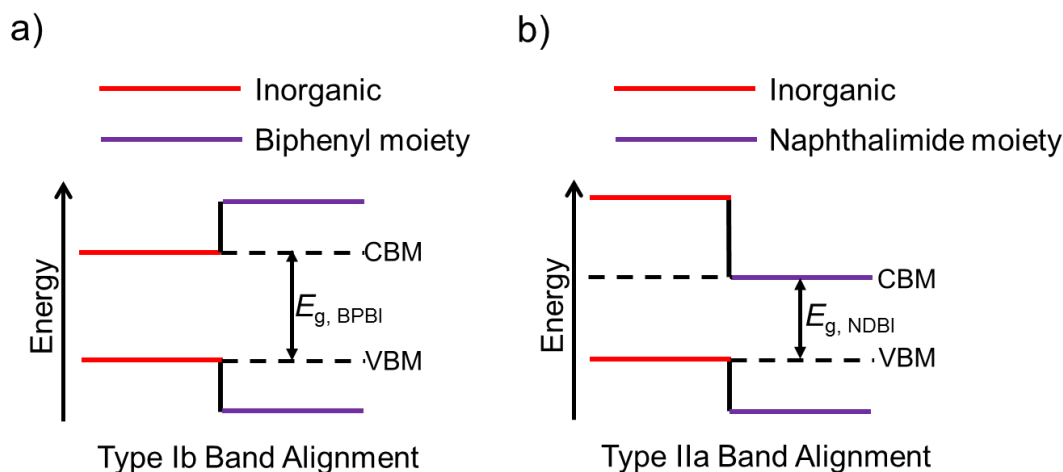
Figure 3.16. Schematic representations of a) type-Ib and b) type-IIa band alignments.

by inorganic and organic atomic orbitals, respectively (**Figure 3.16.**b). In other words, the band edge states are exclusively constructed of inorganic orbitals in **BPBI**, and the biphenyl atomic orbitals have contributions only above the bandgap. This implies that the lower energy electron-hole pairs will reside in the highly confined BiI_6^{3-} clusters. In contrast, for **NDBI**, the VBM energy levels are derived from the inorganic framework, and the CBM states have a major contribution from naphthalimide molecular orbitals. Given these observations, it could be concluded that the observed narrow bandgap for **NDBI** compared to **BPBI** is due to the additional contribution from naphthalimide cations to the density of states at the band edges of the former. Notably, the type-IIa band alignment in **NDBI** will enable a facile dissociation of excitons into free charge carriers at the organic-inorganic interface due to the presence of lower energy electron acceptor levels.

3.3.B4. Photoconductivity analysis
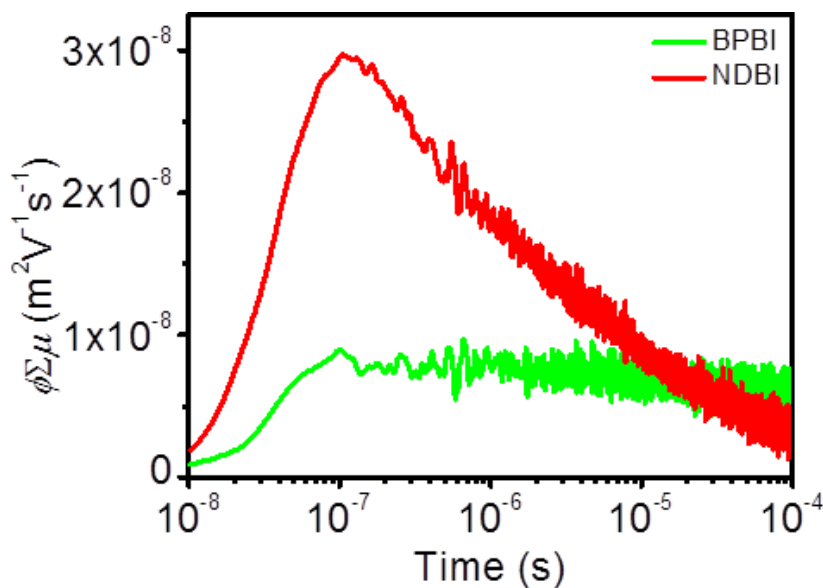
Figure 3.17. Product of charge carrier mobility (electron and hole) and dissociation yield of free charges as a function of time measured along the long crystal axis of **BPBI** and **NDBI** single crystals.

The photoconductivity of **BPBI** and **NDBI** single crystals was evaluated using FP-TRMC analysis. To assess the potential of the materials for optoelectronic applications, we have measured the product of the mobility and charge separation efficiency ($\phi\Sigma\mu$) of **BPBI** and **NDBI** single crystals (**Figure 3.17**). The measurement was done along the long axis of the crystals because the intermolecular interaction is stronger in this direction.

Both materials exhibited intense TRMC signals with a $\phi\Sigma\mu_{max}$ of 8×10^{-9} m^2 V^{-1} s^{-1} for **BPBI** and 2.95×10^{-8} m^2 V^{-1} s^{-1} for **NDBI**. The signal intensity was about one order higher when compared to that of most of the 0D bismuth-based perovskite materials reported in the literature, including (CH$_3$NH$_3$)$_3$Bi$_2$I$_9$ (3.3×10^{-9} m^2 V^{-1} s^{-1}).[30]

The observed 3.7-fold higher TRMC signal for **NDBI** compared to that of **BPBI** stems from the type-IIa band alignment in the former. The energy level landscape at the interface of BiI_6^{3-} octahedron and naphthalimide moiety provides the driving force for the dissociation of excitons into free charge carriers. In the contrast, the excitons generated in **BPBI** are strongly confined in the isolated BiI_6^{3-} octahedrons and subsequently resulted in a weak TRMC signal. There are several reports of using zero-dimensional bismuth halide perovskites as a light-absorbing layer in photovoltaic devices.[47-49] Our materials may also be suitable for such devices, particularly NDBI, which has a relatively low bandgap. Further, these materials may be employed as a top cell light absorber in tandem solar cells consisting of c-Si or CIGS as the bottom cells to improve the overall efficiencies. Moreover, similar materials are being reported as suitable for photodetector applications owing to their high photoconductivity, strong visible light absorption, good thermal stability, and low toxicity.[50-52]

3.4. Conclusions

In summary, we have synthesized a novel lead-free 1D perovskite-like material with a quantum-well structure having the inorganic chains separated by π−π stacked, face-on oriented organic cations. The material exhibited excellent conductivity parallel to the crystal long axis and long charge carrier lifetime. The latter is ascribed to the charge carrier's separation at the naphthalimide−$[BiI_5^{2-}]$n chain interface followed by their transport through the organic and inorganic semiconducting

channels. This was confirmed by DFT calculations, which unraveled a type-IIa band alignment at the organic−inorganic heterojunction. We have also designed and synthesized two novel bismuth halide zero-dimensional perovskite materials, **BPBI** and **NDBI**, consisting of isolated BiI_6^{3-} octahedrons template by biphenyl and naphthalimide-based organic cations. We have precisely investigated the influence of the self-assembly of the organic cations within the perovskite structure in modulating the optical bandgap and electronic properties of the resultant materials. Raman spectroscopy analysis revealed the involvement of both organic and inorganic molecular orbitals in the electronic transitions of naphthalimide-containing perovskite. DFT calculations have confirmed that the orbital contribution from naphthalimide cations at the CBM states of **NDBI** is responsible for its narrow optical bandgap compared to that of BPBI. Further, we found that naphthalimide cations form a type-IIa heterojunction with inorganic units (BiI_6^{3-}), whereas the biphenyl cations form type-Ib band alignment with inorganic clusters. **NDBI** exhibited a 3.7-fold higher photoconductivity signal than BPBI, which could be ascribed to the type-IIa band alignment in the former, which offered an energy level offset at the organic−inorganic interface that facilitated efficient exciton dissociation into free charge carriers. Our studies on the structure−property relationships of these materials open a new avenue of material design strategy to precisely control the optical bandgap and photoconductivity of zero-dimensional bismuth halide perovskites for optoelectronic applications.

3. 5. Experimental section

3.5.1. Chemicals: Bismuth (III) iodide (99.9%, Sigma Aldrich), 1,8-naphthalic anhydride (98%, Spectrochem), 1,4,5,8-naphthalenetetracarboxylic dianhydride (98%, Spectrochem), 4,4′-bis(chloromethyl)-1,1′-biphenyl (95%, TCI), *N*-(*tert*-butoxycarbonyl)-1,2-diaminoethane (>97%, TCI), hydriodic acid (57 wt. % in H_2O, 99.95%, Sigma Aldrich) were used as received.

3.5.2. Synthesis of 1,8-naphthalimide-N-ethylammonium iodide: The quaternary ammonium salt was synthesized by a reported procedure.[1] *N*-(*tert*-butoxycarbonyl)-1,2-diaminoethane (1.60 g, 10 mmol) was mixed with naphthalic anhydride (1.98 g, 10 mmol) in 50 ml of ethanol, and heated to reflux for 2 hours. The mixture was cooled, evaporated to dryness and recrystallized from ethanol to give *N*-(2-ethyl-NH-*(tert*-butoxycarbonyl))-naphthalimide. The filtered crystals were dried in vacuum oven at 80 °C 290 for 24h.Then, *N*-(2-ethyl-NH-*(tert*-butoxycarbonyl))-naphthalimide (340 mg, 1 mmol) in dichloromethane was reacted with 0.8 ml of HI aqueous solution (57 wt. %) at room temperature for 4 hours. During the process of reaction, more and more powder deposits were precipitated out. The powders were filtered, washed with acetone, and dried in the vacuum oven at 60 °C for 24 h to give the corresponding yellowish ammonium salt in a yield of 90 %. ^{1}H NMR (500 MHz, DMSO-d_6): δ 8.48-8.56 (t, 4H), 7.89-7.94 (t, 2H), 7.71-7.83 (bs, 3H), 4.30-4.36 (t, 2H), 3.14-3.19 (m, 2H).

3.5.3. Synthesis of NBI single crystal: Single crystals of **NBI** was prepared by dissolving BiI$_3$ (60 mg, 0.1 mmol, 1 equiv.) and 1,8-naphthalimide-N-ethylammonium iodide (36.8 mg, 0.1 mmol, 1 equiv.) in a solvent mixture of aq. HI, glacial acetic acid and water at 120 °C. Slow cooling of the above solution to room temperature resulted in the formation of red needle shaped crystals.

3.5.4. Synthesis of 2,2′-[naphthalene-1,8:4,5-bis(dicarboximide)-*N,N*′-diyl]-bis(ethylammonium iodide): *N,N*'-bis(2-ethyl-NH-(*tert*-butoxycarbonyl))-naphthalenediimide was synthesized according to a previous report.[1] Then, 2,2′-[Naphthalene-1,8:4,5-bis(dicarboximide)-*N,N*′-diyl]-bis(ethylammonium iodide) was prepared by reacting stoichiometric amounts of *N,N*'-bis(2-ethyl-NH-(*tert*-butoxycarbonyl))-naphthalenediimide and hydriodic acid (57 wt. % in H$_2$O) in dichloromethane at room temperature. The reaction mixture is stirred for 1 hour, during the process of reaction, more and more yellowish powder deposits were precipitated out. The powder was filtered, washed with acetone, and dried in the vacuum oven at 60 °C for 24 h to give the corresponding yellowish ammonium salt. ^{1}H NMR (500 MHz, DMSO-*d$_6$*): δ 8.7 (s, 4H), 7.8 (s, 6H), 4.3 (t, 4H), 3.5 (m, 4H).

3.5.5. Synthesis of [1,1′-biphenyl]- 4,4′-diyldimethanaminium iodide: 4,4′-bis(aminomethyl)-1,1′-biphenyl was synthesized according to a previous report.[2] Then, [1,1′-biphenyl]- 4,4′-diyldimethanaminium iodide was prepared by slowly mixing 4,4′-bis(aminomethyl)-1,1′-biphenyl with stoichiometric amounts of hydroiodic acid in ethanol at 0 °C. After stirring the solution for 1 hour, the solvents

were removed using a rotary evaporator. The solids obtained were washed with copious diethyl ether and dried under vacuum at 50 °C overnight to afford the desired ammonium salts in a yield of 90 %. ^{1}H NMR (500 MHz, DMSO-d_6): δ 8.1 (s, 6H), 7.7 (d, 4H), 7.5 (d, 4H), 4.1 (m, 4H).

3.5.6. Synthesis of (2,2′-[naphthalene-1,8:4,5-bis(dicarboximide)-*N,N′*-diyl]-bis(ethylammonium))$_{1.5}$BiI$_6$.2H$_2$O (NDBI) single crystals: Single crystals of **NDBI** was prepared by dissolving BiI$_3$ (196 mg, 0.33 mmol, 1 equiv.) and 2,2′-[naphthalene-1,8:4,5-bis(dicarboximide)-*N,N′*-diyl]-bis(ethylammonium iodide) (400 mg, 0.66 mmol, 2 equiv.) in 42.5 ml 57% aq. HI at 120 °C. Slow cooling of the above solution to room temperature resulted in the formation of brownish red needle shaped crystals.

3.5.7. Preparation of ([1,1′-biphenyl]- 4,4′-diyldimethanaminium)$_{1.5}$BiI$_6$.2H$_2$O (BPBI) single crystals: Single crystals of **BPBI** was prepared by dissolving [1,1′-biphenyl]- 4,4′-diyldimethanaminium iodide (11.5 mg, 0.025 mmol, 1 equiv.) in 3ml distilled water and add 0.5 ml 57% aq. HI containing BiI$_3$ (60 mg, 0.1 mmol, 4 equiv.). The resultant red precipitate is heated to 180 °C and then adds 1 ml of 57% aq. HI to completely dissolve the precipitate. Slow cooling of the above solution to room temperature resulted in the formation of red needle shaped crystals.

3.6. References

1. C. Ma, N.-G. Park, *ACS Energy Lett.* **2020**, *5*, 3268-3275.
2. H. Lin, C. Zhou, Y. Tian, T. Siegrist, B. Ma, *ACS Energy Lett.* **2018**, *3*, 54-62

3. R. Bakthavatsalam, M. P. U. Haris, S. R. Shaikh, A. Lohar, A. Mohanty, D. Moghe, S. Sharma, C. Biswas, S. S. K. Raavi, R. G. Gonnade, J. Kundu, *J. Phys. Chem. C* **2020**, *124*, 1888-1897.

4. J. V. Passarelli, C. M. Mauck, S. W. Winslow, C. F. Perkinson, J. C. Bard, H. Sai, K. W. Williams, A. Narayanan, D. J. Fairfield, M. P. Hendricks, W. A. Tisdale, S. I. Stupp, *Nat. Chem*. **2020**, *12*, 672-682.

5. M. C. G.-Rueda, W. T. M. V. Gompel, R. Herckens, L. Lutsen, D. Vanderzande, F. C. Grozema, *J. Phys. Chem. Lett*. **2020**, *11*, 824-830.

6. N. Marchal, W. V. Gompel, M. C. G.-Rueda, Koen Vandewal, K. V. Hecke, H.-G. Boyen, B. Conings, R. Herckens, S. Maheshwari, L. Lutsen, C. Quarti, F. C. Grozema, D. Vanderzande, D. Beljonne, *Chem. Mater.* **2019**, *31*, 6880-6888.

7. M.-H. Tremblay, A. M. Zeidell, S. Rigin, C. Tyznik, J. Bacsa, Y. Zhang, K. A. Kurdi, O. D. Jurchescu, T. V. Timofeeva, S. Barlow, S. R. Marder, *Inorg. Chem*. **2020**, *59*, 8070-8080.

8. B.-E. Cohen, M. Wierzbowska, L. Etgar, *Sustainable Energy Fuels* **2017**, *1*, 1935-1943.

9. M.-G. Ju, J. Dai, L. Ma, Y. Zhou, W. Liang, X. C. Zeng, *J. Mater. Chem. A*, **2019**, *7*, 16742-16747.

10. C. Liu, W. Huhn, K.-Z. Du, A. V.-Mayagoitia, D. Dirkes, W. You, Y. Kanai, D. B. Mitzi, V. Blum, *Phys. Rev. Lett*. **2018**, *121*, 146401.

11. S. Maheshwari, T. J. Savenije, N. Renaud, F. C. Grozema, *J. Phys. Chem. C* **2018**, *122*, 17118-17122.

12. J. V. Passarelli, D. J. Fairfield, N. A. Sather, M. P. Hendricks, H. Sai, C. L. Stern, S. I. Stupp, *J. Am. Chem. Soc*. **2018**, *140*, 7313-7323.

13. X. Li, J. Yang, Z. Song, R. Chen, L. Ma, H. Li, J. Jia, J. Meng, X. Li, M. Yi, X. Sun, *ACS Appl. Energy Mater*. **2018**, *1*, 4467-4472.

14. I. W. H. Oswald, E. M. Mozur, I. P. Moseley, H. Ahn, J. R. Neilson, *Inorg. Chem*. **2019**, *58*, 5818-5826.

15. X. Gong, O. Voznyy, A. Jain, W. Liu, R. Sabatini, Z. Piontkowski, G. Walters, G. Bappi, S. Nokhrin, O. Bushuyev, M. Yuan, R. Comin, D. McCamant, S. O. Kelley, E. H. Sargent, *Nat. Mater*. **2018**, *17*, 550-556.

16. K. M. McCall, C. C. Stoumpos, S. S. Kostina, M. G. Kanatzidis, B. W. Wessels, $A_3M_2I_9$ (A = Cs, Rb; M = Bi, Sb). *Chem. Mater*. **2017**, *29*, 4129-4145.

17. T. Kawai, A. Ishii, T. Kitamura, S. Shimanuki, M. Iwata, Y. Ishibashi, *J. Phys. Soc. Jpn*. **1996**, *65*, 1464-1468.

18. M. Abulikemu, S. Ould-Chikh, X. Miao, E. Alarousu, B. Murali, N. G. O. Ngongang, J. Barbé, A. E. Labban, A. Amassian,; S. D. Gobbo, *J. Mater. Chem. A* **2016**, *4*, 12504-12515.

19. C. Ran, Z. Wu, J. Xi, F. Yuan, H. Dong, T. Lei, X. He, X. Hou, *J. Phys. Chem. Lett*. **2017**, *8*, 394-400.

20. C. F. Macrae, P. R. Edgington, P. Mccabe, E. Pidcock, G. P. Shields, R. Taylor, M. Towler, J. V. D. Streek, *J. Appl. Crystallogr.* **2006**, *39*, 453-457.

21. Y. Bi, E. M. Hutter, Y. Fang, Q. Dong, J. Huang, T. J. Savenije, *J. Phys. Chem. Lett*. **2016**, *7*, 923-928.

22. A. H. Slavney, L. Leppert, D. Bartesaghi, A. G.-Parker, M. F. Toney, T. J. Savenije, J. B. Neaton, H. I. Karunadasa, *J. Am. Chem. Soc*. **2017**, *139*, 5015-5018.

23. M.-Q. Li, Y.-Q. Hu, L.-Y. Bi, H.-L. Zhang, Y. Wang, Y.-Z. Zheng, *Chem. Mater*. **2017**, *29*, 5463-5467.

24. K. Tao, Y. Li, C. Ji, X. Liu, Z. Wu, S. Han, Z. Sun, J. Luo, *Chem. Mater*. **2019**, *31*, 5927-5932.

25. W. Zhang, K. Tao, C. Ji, Z. Sun, S. Han, J. Zhang, Z. Wu, J. Luo, *Inorg. Chem*. **2018**, *57*, 4239-4243.

26. L. Yao, G. Niu, L. Yin, X. Du, Y. Lin, X. Den, J. Zhang, J. Tang, *J. Mater. Chem. C* **2020**, *8*, 1239-1243.

27. C. Liu, W. Huhn, K.-Z. Du, A. V. Mayagoitia, D. Dirkes, W. You, Y. Kanai, D. B. Mitzi, V. Blum, *Phys. Rev. Lett*. **2018**, *121*, 146401.

28. L. Yao, G. Niu, L. Yin, X. Du, Y. Lin, X. Den, J. Zhang, J. Tang, *J. Mater. Chem. C* **2020**, *8*, 1239-1243.

29. H. A. Evans, J. G. Labram, S. R. Smock, G. Wu, M. L. Chabinyc, R. Seshadri, F. Wudl, *Inorg. Chem.* **2017**, *56*, 395-401.

30. B.-W. Park, B. Philippe, X. Zhang, H. Rensmo, G. Boschloo, E. M. J. Johansson, *Adv. Mater.* **2015**, *27*, 6806-6813.

31. W. Zhang, X. Liu, L. Li, Z. Sun, S. Han, Z. Wu, J. Luo, *Chem. Mater.* **2018**, *30*, 4081-4088.

32. I. W. H. Oswald, E. M. Mozur, I. P. Moseley, H. Ahn, J. R. Neilson, *Inorg. Chem.* **2019**, *58*, 5818-5826.

33. J. K. Pious, C. Muthu, S. Dani, A. Saeki, V. C. Nair, *Chem. Mater.* **2020**, *32*, 2647-2652.

34. J. K. Pious, M. G. Basavarajappa, C. Muthu, N. Krishna, R. Nishikubo, A. Saeki, S. Chakraborty, V. C. Nair, *J. Phys. Chem. Lett.* **2020**, *11*, 6757-6762.

35. J. M. Hoffman, X. Che, S. Sidhik, X. Li, I. Hadar, J.-C. Blancon, H. Yamaguchi, M. Kepenekian, C. Katan, J. Even, C. C. Stoumpos, A. D. Mohite, M. G. Kanatzidis, *J. Am. Chem. Soc.* **2019**, *141*, 10661-10676.

36. M. K. Jana, C. Liu, S. Lidin, D. J. Dirkes, W. You, V. Blum, D. B. Mitzi, *Chem. Mater.* **2019**, *31*, 8523-8532.

37. C. Pan, K. Sugiyasu, J. Aimi, A. Sato, M. Takeuchi, *Angew. Chem. Int. Ed.* **2014**, *53*, 8870-8875.

38. T. Li, Y. Hu, C. A. Morrison, W. Wu, H. Hana, N. Robertson, *Sustainable Energy Fuels*, **2017**, *1*, 308-316.

39. J. K. Pious, A. Katre, C. Muthu, S. Chakraborty, S. Krishna, V. C. Nair, *Chem. Mater.* **2019**, *31*, 1941-1945.

40. J. Zhang, S. Han, C. Ji, W. Zhang, Y. Wang, K. Tao, Z. Sun, J. Luo, *Chem. Eur. J.* **2017**, *23*, 17304-17310.

41. B. Kou, W. Zhang, C. Ji, Z. Wu, S. Zhang, X. Liu, J. Luo, *Chem. Commun*. **2019**, 55, 14174-14177.

42. X. Li, Y. Fu, L. Pedesseau, P. Guo, S. Cuthriell, I. Hadar, J. Even, C. Katan, C. C. Stoumpos, R. D. Schaller, E. Harel, M. G. Kanatzidis, *J. Am. Chem. Soc*. **2020**, *142*, 11486-11496.

43. L. Mao, P. Guo, M. Kepenekian, I. Spanopoulos, Y. He, C. Katan, J. Even, R. D. Schaller, R. Seshadri, C. C. Stoumpos, M. G. Kanatzidis, *J. Am. Chem. Soc*. **2020**, *142*, 8342-8351.

44. X. Gong, O. Voznyy, A. Jain, W. Liu, R. Sabatini, Z. Piontkowski, G. Walters, G. Bappi, S. Nokhrin, O. Bushuyev, M. Yuan, R. Comin, D. McCamant, S. O. Kelley, E. H. Sargent, *Nat. Mater*. **2018**, *17*, 550-556.

45. M.-H. Du, *J. Phys. Chem. Lett*. **2015**, *6*, 1461-1466.

46. C. Liu, W. Huhn, K.-Z. Du, A. V. Mayagoitia, D. Dirkes, W. You, Y. Kanai, D. B. Mitzi, V. Blum, *Phys. Rev. Lett*. **2018**, *121*, 146401.

47. Z. Zhang, X. Li, X. Xia, Z. Wang, Z. Huang, B. Lei, Y. Gao, *J. Phys. Chem. Lett*. **2017**, *8*, 4300-4307.

48. S. M. Jain, D. Phuyal, M. L. Davies, M. Li, B. Philippe, C. D. Castro, Z. Qiu, J. Kim, T. Watson, W. C. Tsoi, O. Karis, H. Rensmo, G. Boschloo, T. Edvinsson, J. R. Durrant, *Nano Energy* **2018**, *49*, 614-624.

49. Q. Jia, C. Li, W. Tian, M. B. Johansson, E. M. J. Johansson, R. Yang, *ACS Appl. Mater. Interfaces* **2020**, *12*, 43876-43884.

50. A. A. Hussain, *ACS Appl. Mater. Interfaces* **2020**, *12*, 46317-46329.

51. A. A. Hussain, A. K. Rana, M. Ranjan, *Nanoscale* **2019**, *11*, 1217-1227.

52. W.-G. Li, X.-D. Wang, J.-F. Liao, Y. Jiang, D.-B. Kuang, *Adv. Funct. Mater*. **2020**, *30*, 1909701.

Chapter 4

Zero-Dimensional Bismuth Halide Perovskite for Energy Storage Application

4.1. Abstract

Symmetrical electrochemical capacitors are attracting immense attention because of their fast charging−discharging ability, high energy density, and low cost of production. The current research in this area is mainly focused on exploring novel low-cost electrode materials with higher energy and power densities. In the present work, we fabricated an electrochemical double-layer capacitor using methylammonium bismuth iodide $(CH_3NH_3)_3Bi_2I_9$, a lead-free, zero-dimensional hybrid perovskite material. A maximum areal capacitance of 5.5 mF cm^{-2} was obtained, and the device retained 84.8% of its initial maximum capacitance even after 10,000 charge−discharge cycles. Furthermore, impedance spectroscopy measurements revealed that the active layer provides a high surface area for the electrolyte to access. As a result, the charge transport resistance is reasonably low, which is advantageous for delivering excellent performance.

4.2. Introduction

The storage of energy is as necessary as its production. The development of novel, environment-friendly, sustainable energy storage devices has attracted considerable research attention in modern times because of the rapid depletion of unsustainable fossil fuels and environmental deterioration, which are also necessary to satisfy the demands of the fast-growing electronic industry.[1-6] Moreover, renewable energy sources are intermittent and regionally dependent. Therefore, the need for energy storage technology is increased to provide an uninterrupted power supply, particularly to portable electronic gadgets. In this context, electrochemical capacitors with a long life span, high power density, and fast charge−discharge characteristics are regarded as excellent energy storage devices, as they have the potential to complement or even replace batteries in numerous applications.[7-13]

Electrochemical capacitors can be classified into electric double-layer capacitors (EDLC's) and pseudocapacitors. The charge storage mechanism for EDLC is through electrostatic adsorption of ions on the electrode surface (**Figure 4.1**a). Supercapacitor electrodes such as carbon nanotubes, activated carbon, graphene, etc., store charge via an electric double-layer mechanism. In pseudocapacitors, the charge is stored through Faradaic redox reaction and intercalation mechanisms (**Figure 4.1**b and c). Electrode materials such as metal oxides (MnO_2, RuO_2, VO_2, $Ni(OH)_2$), transition metal chalcogenides (MoS_2, WS_2, CdS), and conducting polymers are pseudocapacitive materials. The energy density of pseudocapacitors is much higher than that of

EDLC's because a large number of ions can be stored in pseudocapacitors due to redox reactions at the electrode surface.[14-21]
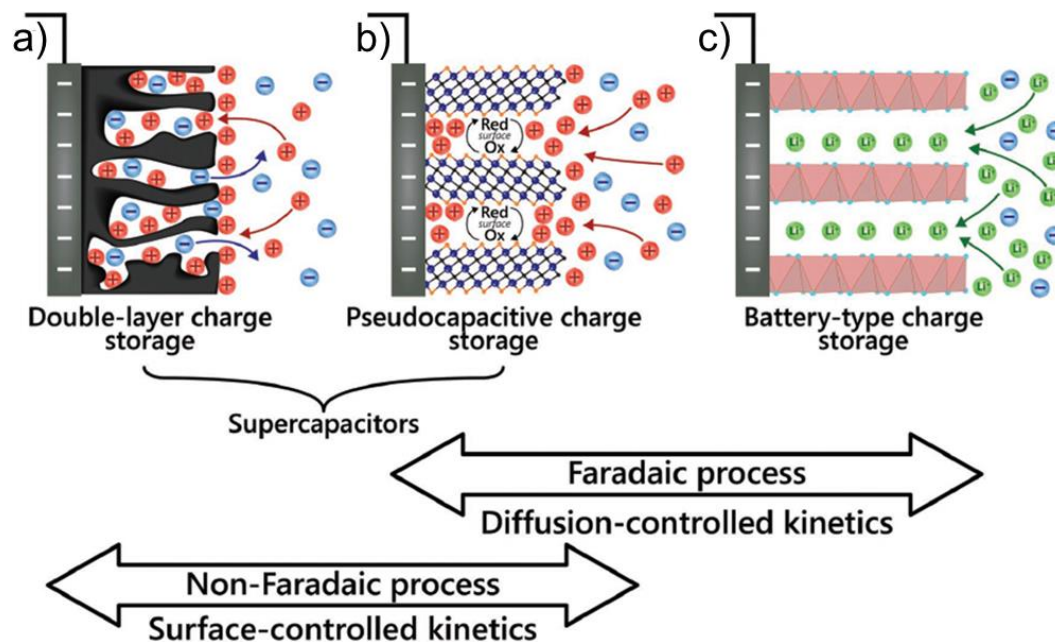
Figure 4.1. The schematic representation of a) electric double-layer, b) Faradaic redox, and c) intercalation charge storage mechanisms. Adapted from reference 14.

However, the cycling stability of pseudocapacitors is lower than that of EDLC's due to the chemical or structural modification of the electrode during charging and discharging. Compared to batteries, the energy density of capacitors is much lower (< 50 W h Kg^{-1}), which limited their widespread practical applications. The energy density (E) of supercapacitors relies on the capacitance (C) and voltage (V) by the relation $E = \frac{1}{2}CV^2$. The energy density of supercapacitors could be improved by increasing the capacitance of electrode materials or using electrolytes with wide operational voltage windows such as organic or ionic liquid electrolytes.[22] Although

supercapacitors have a low energy density, the power density and cycling stability of supercapacitors are higher than that of batteries owing to the fast surface-sensitive charge-discharge mechanism in the former. Hence, the current research in electrochemical capacitors is mainly focused on exploring novel low-cost electrode materials with higher energy and power densities.
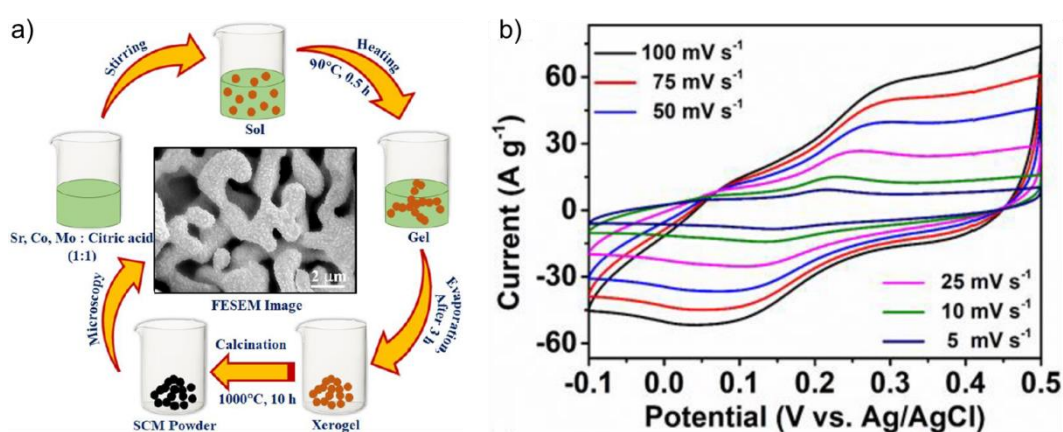
Figure 4.2. a) Synthetic scheme for the preparation of $SrCo_{0.9}Mo_{0.1}O_{3-\delta}$ perovskite. b) Current density-voltage curves of assembled supercapacitor devices at different scan rates. Adapted from reference 23.

Metal oxide perovskites are well-known electrode materials for supercapacitor applications owing to their excellent thermal stability, high electrical conductivity, and unique redox properties. Su *et al*. fabricated a supercapacitor device using $LaFeO_3$ perovskite nanorods as the electrode material.[24] They have observed that the calcination temperature and time significantly influence the morphology and nanostructure of $LaFeO_3$. The optimized reaction conditions (calcination at 700 °C for 3 h) yielded $LaFeO_3$ perovskite nanorods with a large surface area of 45.09 m^2g^{-1} and

a total pore volume of 0.111 cm^3g^{-1}. The asymmetric O 1s peak in the XPS spectrum revealed the existence of oxygen vacancy in $LaFeO_3$ nanorods. Electrochemical analyses suggested both electric double layer and Faradaic redox mechanisms are involved in the charge-storage process. The supercapacitor devices featured a maximum specific capacitance of 313.21 F g^{-1} and retained 86.1% of its initial capacitance even after 5,000 charge-discharge cycles.

Sharma *et al*. reported that Mo doping at the Co site of $SrCoO_3$ is an efficient strategy to stabilize its cubic perovskite structure, maintaining the inherent oxygen vacancy (**Figure 4.2**a).[23] The Mo doped perovskite $SrCo_{0.9}Mo_{0.1}O_{3-\delta}$ featured a high electrical conductivity of 14 S m^{-1} and low equivalent series resistance of 3.1 Ω, beneficial for efficient capacitive performance. The assembled supercapacitor device using $SrCo_{0.9}Mo_{0.1}O_{3-\delta}$ provided a maximum specific capacitance of 1,223.34 F g^{-1} (**Figure 4.2**b) and retained 93.52% of the original capacitance even after 5,000 galvanostatic charge-discharge cycles. Moreover, they have fabricated a hybrid supercapacitor device using the same compound as the cathode electrode material and lacey-reduced graphene oxide (LRGO) as anode material. The assembled hybrid supercapacitor delivered an energy density of 74.8 Wh Kg^{-1}.

Stevenson *et al*. first reported an anion intercalation mechanism of charge storage in $LaMnO_3$ perovskite (**Figure 4.3**a).[25] They have synthesized oxygen-excess and oxygen-deficient perovskites, $LaMnO_{3.09}$ and $LaMnO_{2.91}$, respectively. Both materials exhibited an oxygen intercalation mechanism owing to the presence of inherent
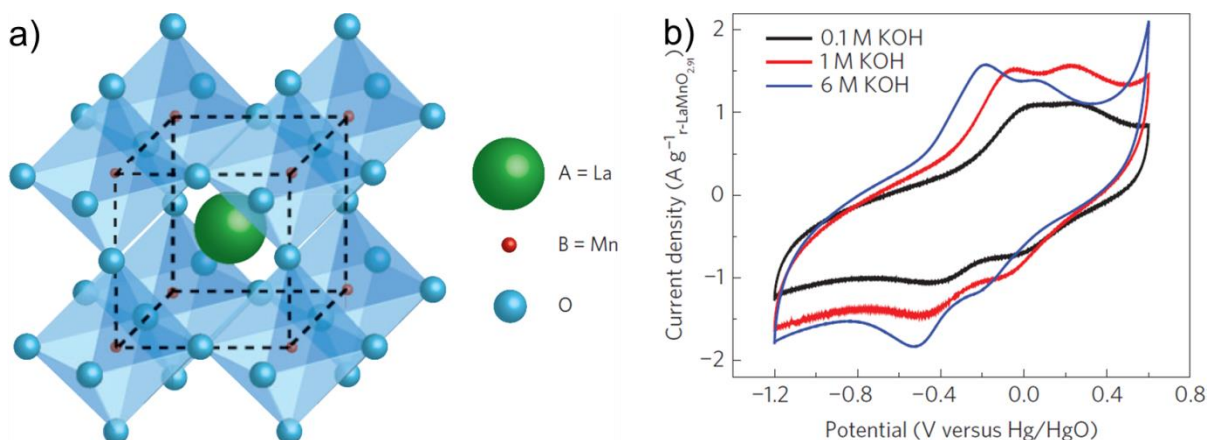
Figure 4.3. a) Crystal structure of $LaMnO_3$ perovskite. b) Current density-voltage curves of assembled supercapacitor devices using oxygen-deficient $LaMnO_{2.91}$ at different scan rates. Adapted from reference 25.

oxygen vacancies in them. Electrochemical studies proved that the oxygen from the electrolyte (KOH) is directly intercalated into the oxygen vacant sites and subsequently resulted in the oxidation of $Mn^{2+} \rightarrow Mn^{3+}$ at low electrolyte concentration and $Mn^{3+} \rightarrow Mn^{4+}$ at excess oxygen condition. $LaMnO_{3.09}$ and $LaMnO_{2.91}$ electrodes exhibited a maximum specific capacitance of 586.7 F g^{-1} and 609.8 F $g^{-1,}$ respectively, at low scan rates (**Figure 4.3**b).

Even though the metal oxide perovskites delivered excellent supercapacitor device performances, the high cost of the starting materials, elevated processing temperature, and long hours of complex synthetic protocols limited their widespread applications. Hence, the current research in electrochemical capacitors is mainly focused on exploring novel low-cost electrode materials with higher energy and power densities. In this context, hybrid perovskite materials are promising because of their low-temperature solution processability and high ionic conductivity; a recent study

suggests that the ionic conductivity of methylammonium lead iodide ($MAPbI_3$) is higher than its electronic conductivity. By exploring this property, Zhao *et al*. have reported a $MAPbI_3$-based thin-film EDLC.[26]
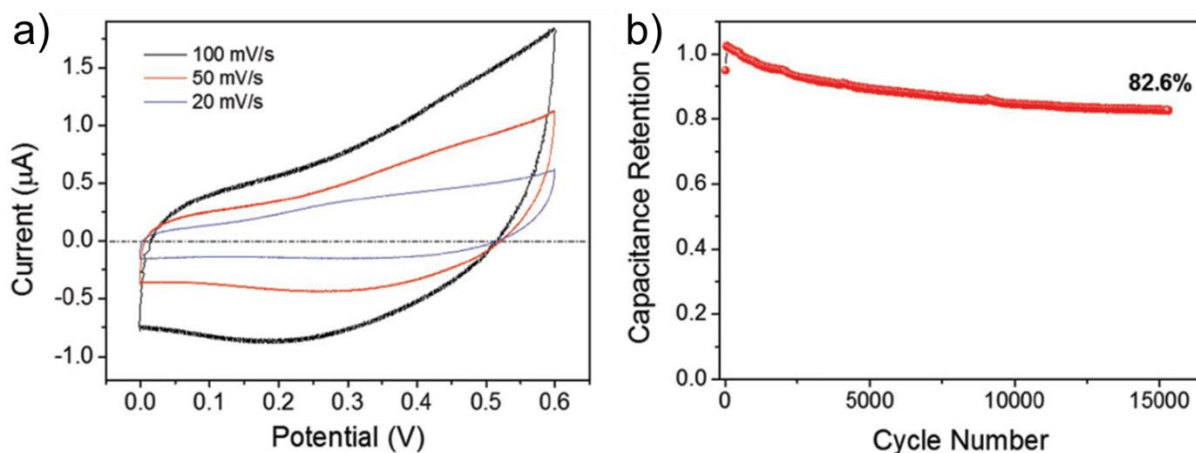
Figure 4.4. a) CV profiles of MAPbI$_3$ EDLC at various scan rates. b) Plot of capacitance retention versus galvanostatic charge-discharge cycle number. Adapted from reference 26.

The quasi rectangular shape and absence of redox peaks in the CV profile at various scan rates confirmed electrochemical double layer formation as the charge storage mechanism (**Figure 4.4**a). The areal capacitance obtained was 5.89 μF cm^{-2} and retained 82.6% of its original capacitance even after 15,000 galvanostatic charge-discharge cycles (**Figure 4.4**a), which proved that hybrid perovskite materials are good candidates for capacitor applications. Followed by this report, Popoola *et al*. replaced the liquid electrolyte with a quasi-solid electrolyte and enhanced the capacitive performance of $MAPbI_3$.[27] They have used different quasi-solid electrolyte systems such as $CHCl_3$/polyvinyl alcohol/KOH and $CHCl_3$/polyvinyl

alcohol/KOH/CH$_3$NH$_3$I for this study. The latter electrolyte exhibited a higher ionic conductivity (3.4 x 10^{-3} S cm^{-1}) compared to the former (1.3 x 10^{-3} S cm^{-1}). The supercapacitor device fabricated using this modified electrolyte featured an areal capacitance of 21.50 µF cm^{-2} and a power density of 5.05 W cm^{-2}.

In another report, bilayer electrodes such as CdS QD's/MAPbI$_3$ and CdS QD's/MA$_3$Bi$_2$I$_9$ have been employed for supercapacitor device assembly.[28] In this electrode architecture, the perovskite layer serves as both electrodes as well as solid electrolyte owing to its mixed electric-ionic conductivity. CdS QD/MAPbI$_3$ exhibited a higher capacitance value (141 µF cm^{-2}) compared to CdS QD/MA$_3$Bi$_2$I$_9$ (95.3 µF cm^{-2}). The relatively lower capacitance of CdS QD/MA$_3$Bi$_2$I$_9$ bilayer electrode is due to the reduced contact surface area between CdS QD and electrolyte were owing to the presence of micrometer-sized MA$_3$Bi$_2$I$_9$ crystallite in the top layer. CdS QD/MAPbI$_3$ and CdS QD/MA$_3$Bi$_2$I$_9$ EDLCs retained 87.7% and 94% of their initial capacitance, respectively, after 4000 cyclic voltammetry cycles.

The toxicity of lead is a significant factor of concern here also. Considering the toxicity issue, lead-free bismuth-based perovskite materials are garnering substantial research interest as electrode materials. Low-dimensional crystal structure, good electrical conductivity, low-temperature solution processability, and high intrinsic stability of bismuth halide perovskites made them attractive candidates for energy storage applications such as supercapacitors and Li-ion batteries.
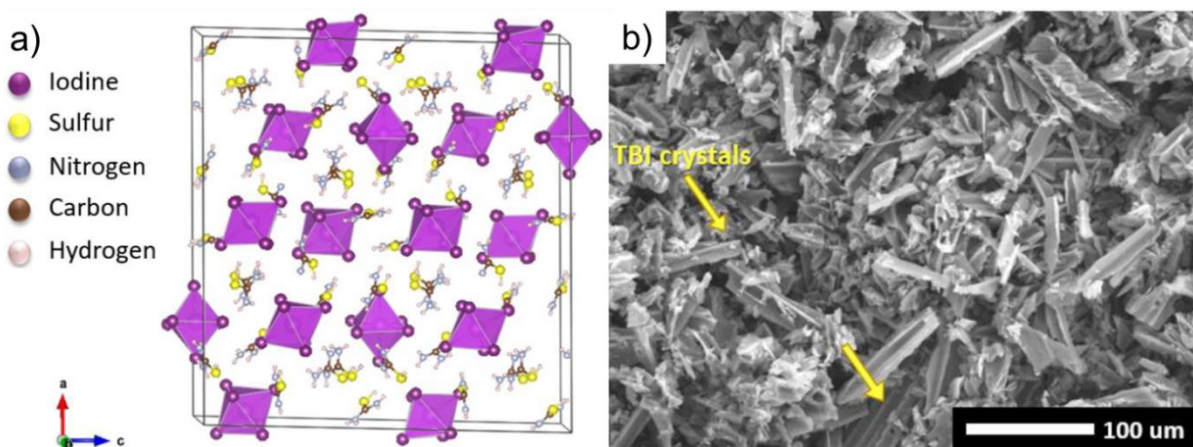
Figure 4.5. a) 3D crystal packing of $(CN_2SH_5)_3BiI_6$ perovskite material consisting of discrete BiI_6^{3-} octahedrons separated by thiourea spacer cations. b) SEM image of the supercapacitor electrode fabricated by drop-casting $(CN_2SH_5)_3BiI_6$ over carbon cloth substrate. Adapted from reference 29.

Neilson *et al*. employed a layered perovskite $(Cs_3Bi_2I_9)$ as an electrode material for supercapacitor application.[30] The capacitor fabricated with this material using $NaClO_4$ as the electrolyte delivered a maximum areal capacitance of 2.4 F cm^{-2}. The device retained 88% of its initial capacitance even after 5,000 charge-discharge cycles. The charge storage mechanism is Faradaic intercalation at lower potentials and electric double-layer formation at higher potentials. A thiourea-based 0D perovskite, $(CN_2SH_5)_3BiI_6$ (TBI; **Figure 4.5**a), featured a much-improved supercapacitor performance owing to its large electroactive surface area.[29] The solution-processed TBI thin-film exhibited a uniform coverage over the carbon cloth substrate (**Figure 4.5**b). The TBI-based electric double-layer capacitor exhibited an areal capacitance of 3.32 F cm^{-2}. In addition, the device showed capacitance retention of almost 100% of its original value after 5,000 charge-discharge cycles.
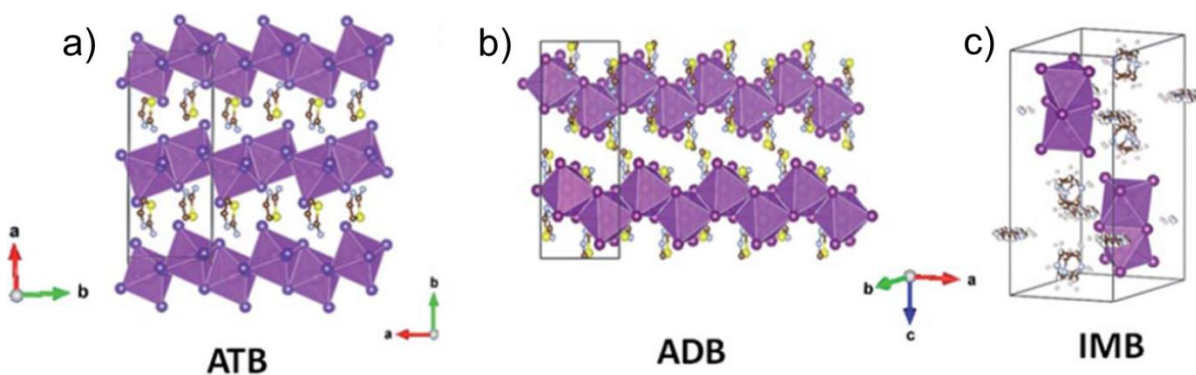
Figure 4.6. a), b), and c) are the crystal structures of the perovskite materials [imidazolium]$_3$[Bi$_2$I$_9$], [2-amino-1,3,4-dithiazolium][BiI$_4$], and [2-aminothiazolium][BiI$_4$], respectively. Adapted from reference 31.

Recently, Ogale and coworkers introduced three bismuth perovskites, [imidazolium]$_3$[Bi$_2$I$_9$] (IMB), [2-amino-1,3,4-dithiazolium][BiI$_4$] (ADB), and [2-aminothiazolium][BiI$_4$] (ATB), as anode materials for Li-ion battery application.[31] ATB and ADB are one-dimensional perovskites with BiI$_4^-$ chains formed by the edge-sharing of Bi-I octahedrons (**Figure 4.6**a and b). In contrast, IMB is a zero-dimensional perovskite with isolated Bi$_2$I$_9^{3-}$ dimer units (**Figure 4.6**c). ADB, IMB, and ATB-based Li-ion batteries showed a reversible capacity of 520 mA h g^{-1}, 450 mA h g^{-1}, and 230 mA h g^{-1}, respectively. The mechanism of charge storage is via the Li$_3$Bi alloy formation and the interaction between the lone pair of nitrogen in the organic cations with Li-ions. These literature reports suggest that lead-free perovskites have a great future in the field of energy storage applications.

4.3. Results and discussion

In this work, we have explored the potential of methylammonium bismuth iodide (**MBI**), which is a lead-free, zero-dimensional perovskite having a unit cell formula of $(CH_3NH_3)_3Bi_2I_9$, for energy storage applications. This bismuth halide perovskite is an environment-friendly alternative with better atmospheric stability than that of the corresponding lead-based perovskites for such applications.

4.3.1. Structural and optical characterizations of MBI
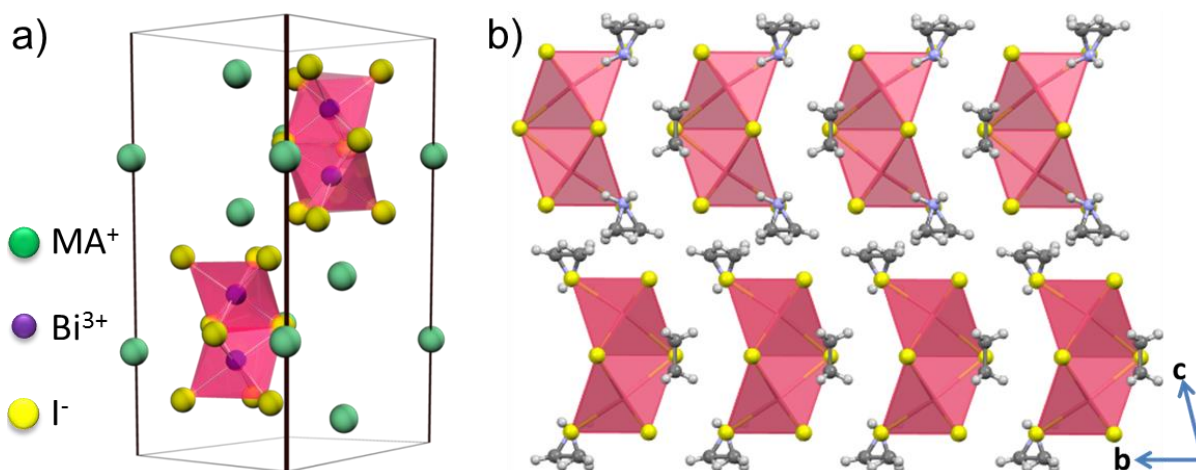
Figure 4.7. a) Unit cell representation of **MBI**. b) Crystal packing of **MBI** along 'bc' crystallographic plane.

The unit cell of **MBI** consists of isolated $Bi_2I_9^{3-}$ units surrounded by methylammonium cations (**Figure 4.7**a). $Bi_2I_9^{3-}$ is formed through face sharing of two BiI_6^{3-} octahedral units and stacked along the crystallographic '*bc*'-plane (**Figure 4.7.**b). We have hypothesized that the isolated $Bi_2I_9^{3-}$ bi-octahedra can supply vacant spaces and large surface area so that the electrolyte can easily access the active

material, resulting in enhanced ionic charge transport. This would lead to capacitors having high energy density. To prove this, we have fabricated capacitor devices with **MBI** and analyzed them using cyclic voltammetry (CV), galvanostatic charge−discharge, and electrochemical impedance spectroscopy (EIS) techniques. The charge transport resistance obtained from the impedance measurement was small, which was in agreement with the large surface area provided by the material.
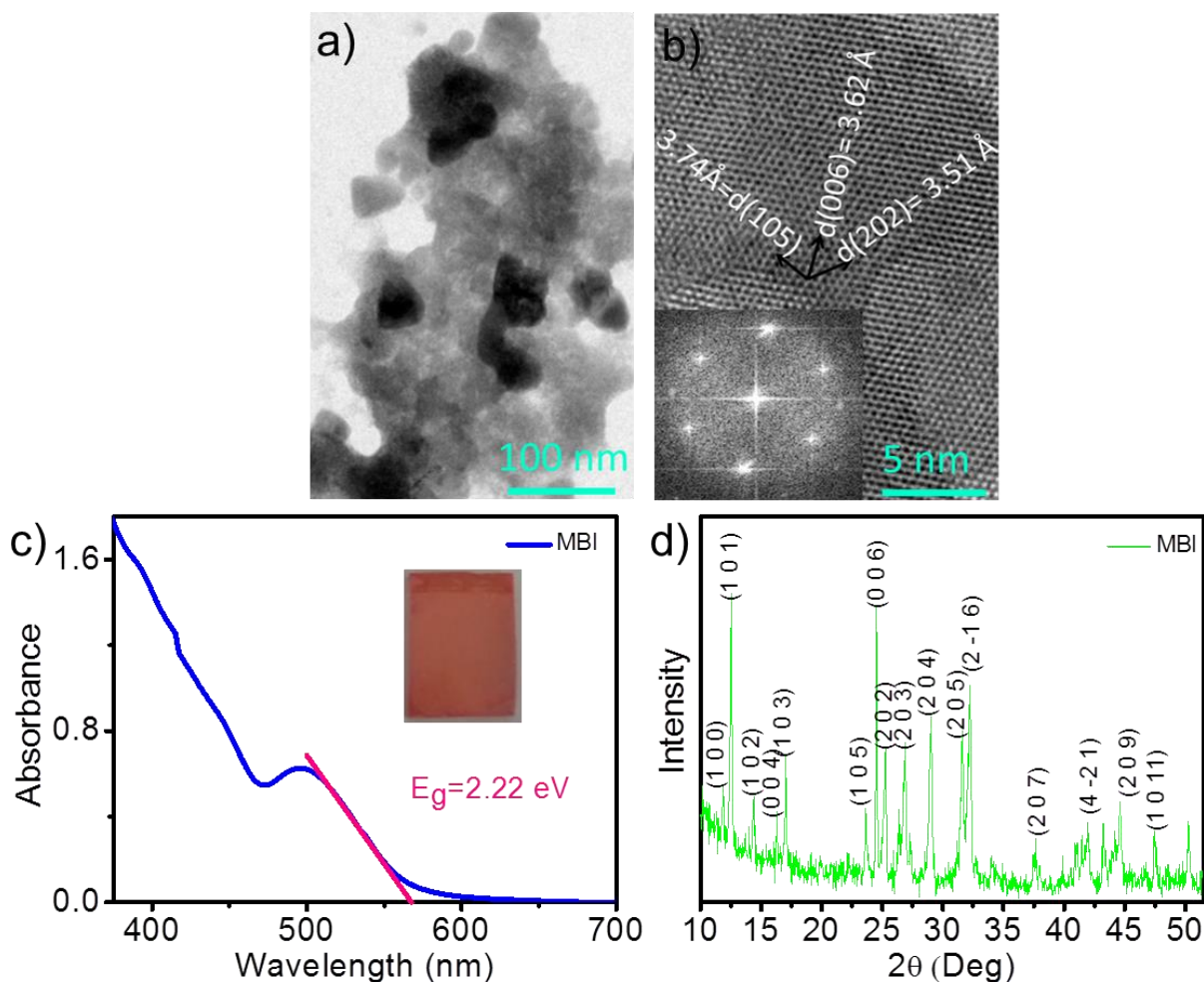
Figure 4.8. a) TEM image of the **MBI** film. b) HR-TEM image of **MBI**, with a fast Fourier transform image in the inset. c) Absorption spectra of **MBI** in the film state. d) Powder XRD of **MBI**.

MBI was characterized using transmission electron microscopy (TEM), ultraviolet−visible (UV−vis) absorption, and X-ray diffraction (XRD) spectroscopy. The TEM image of **MBI** is shown in **Figure 4.8.**a, which indicates that the material forms a thin-film of interconnected **MBI** crystals. The high-resolution transmission electron microscopy (HR-TEM) image of the material is shown in **Figure 4.8.**b, and the corresponding electron diffraction pattern is shown in the inset. The diffraction pattern shows lattice distances of 3.51, 3.62, and 3.74 Å, corresponding to the ⟨202⟩, ⟨006⟩, and ⟨105⟩ lattice planes, respectively. Clear visibility of the lattice planes and the hexagonal array of bright spots indicate that the material is highly crystalline. **MBI** exhibited a broad absorption ranging from 300 to 600 nm in the UV−vis absorption spectrum (**Figure 4.8.**c). The optical band gap of **MBI** calculated from the onset of the absorption was 2.22 eV. XRD patterns obtained from powdered samples, which are in good agreement with the previous reports,[32] revealed the hexagonal crystal structure of the material, with the characteristic perovskite doublet peak at 2θ = ∼12° (**Figure 4.8**d). The XRD profile of the material was studied for one month (**Figure 4.9**). No variation in peak position or intensity was observed, which indicated the good stability of the material under ambient conditions.
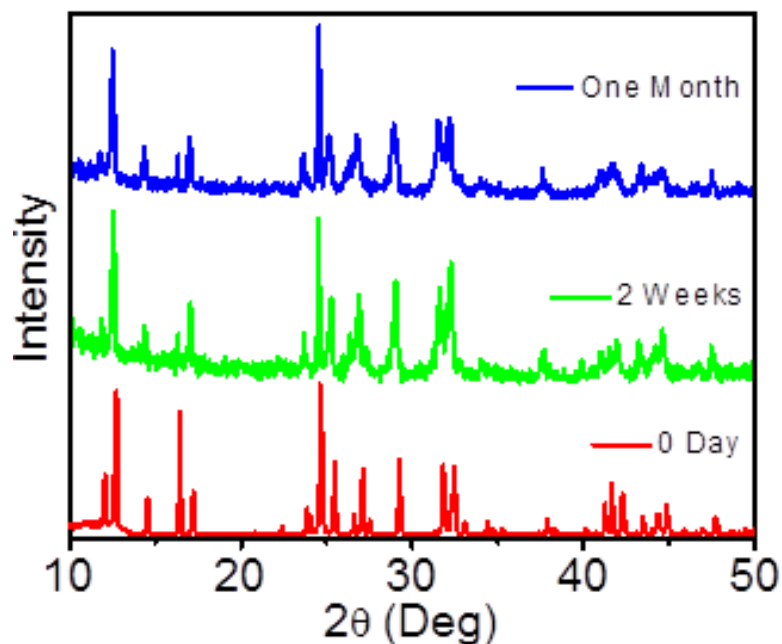
Figure 4.9. Powder X-ray diffraction pattern of MBI for one month. The sample was kept at ambient conditions. No change in peak intensity and position indicates the excellent stability of the material.

4.3.2. Supercapacitor device characterizations

To analyze the electrochemical energy storage performance, **MBI** was coated on a carbon cloth substrate with an area of 1 cm^2, which was used as the electrode. A polymer separator soaked in an electrolytic solution (30 mg mL^{-1} of methylammonium iodide in butanol) was sandwiched between the **MBI**-containing electrodes to form a symmetric capacitor. Additives (5 wt%) such as polytetrafluoroethylene (PTFE) and activated carbon were added during the preparation of the electrode for proper binding of the perovskite material onto the carbon substrate and for improving the conductivity of the active layer.
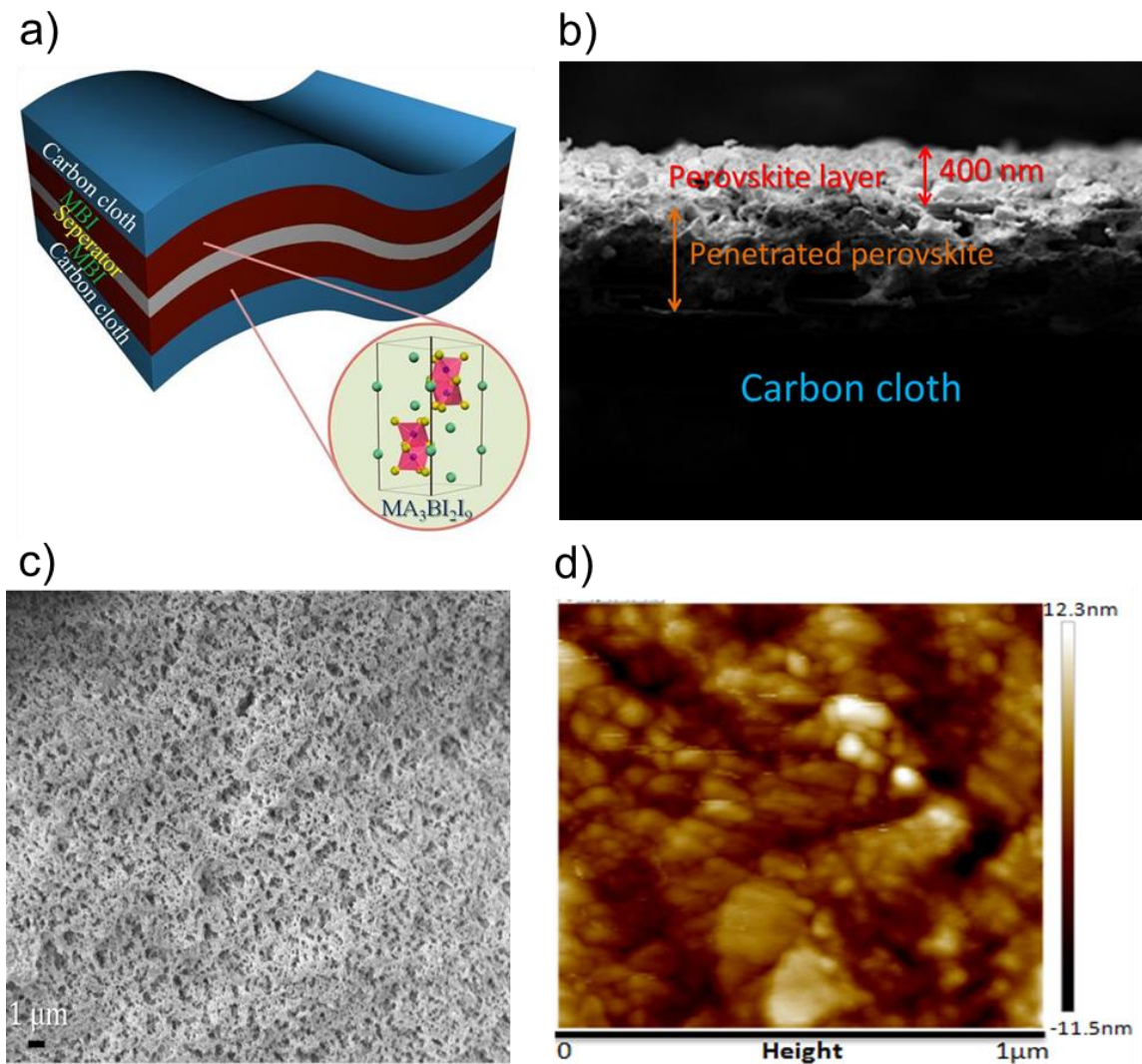
Figure 4.10. a) Schematic representation of the **MBI**-based double-layer capacitor device. b) Cross-sectional SEM image of the capacitor electrode. c) Topological SEM image and d) AFM height image of the **MBI** film.

A simplified schematic representation of the device is shown in **Figure 4.10.**a. The thickness of the active film was about 400 nm as measured from the cross-sectional SEM image, as shown in **Figure 4.10.**b. The perovskite material was uniformly coated over the carbon cloth substrate, as shown in the topological SEM image (**Figure 4.10.**c). The root-mean-square roughness of the film obtained from the

AFM height image (**Figure 4.10.**d) was 16.7 nm, which means that the surface roughness of the film was reasonably high. Such a high surface roughness is suitable for energy storage applications because the electrolyte can strongly interact with the active layer. The high surface roughness of the film is in good agreement with the topological SEM image, which showed relatively large **MBI** crystals (**Figure 4.7.**c).

4.3.3. Electrochemical and impedance analyses
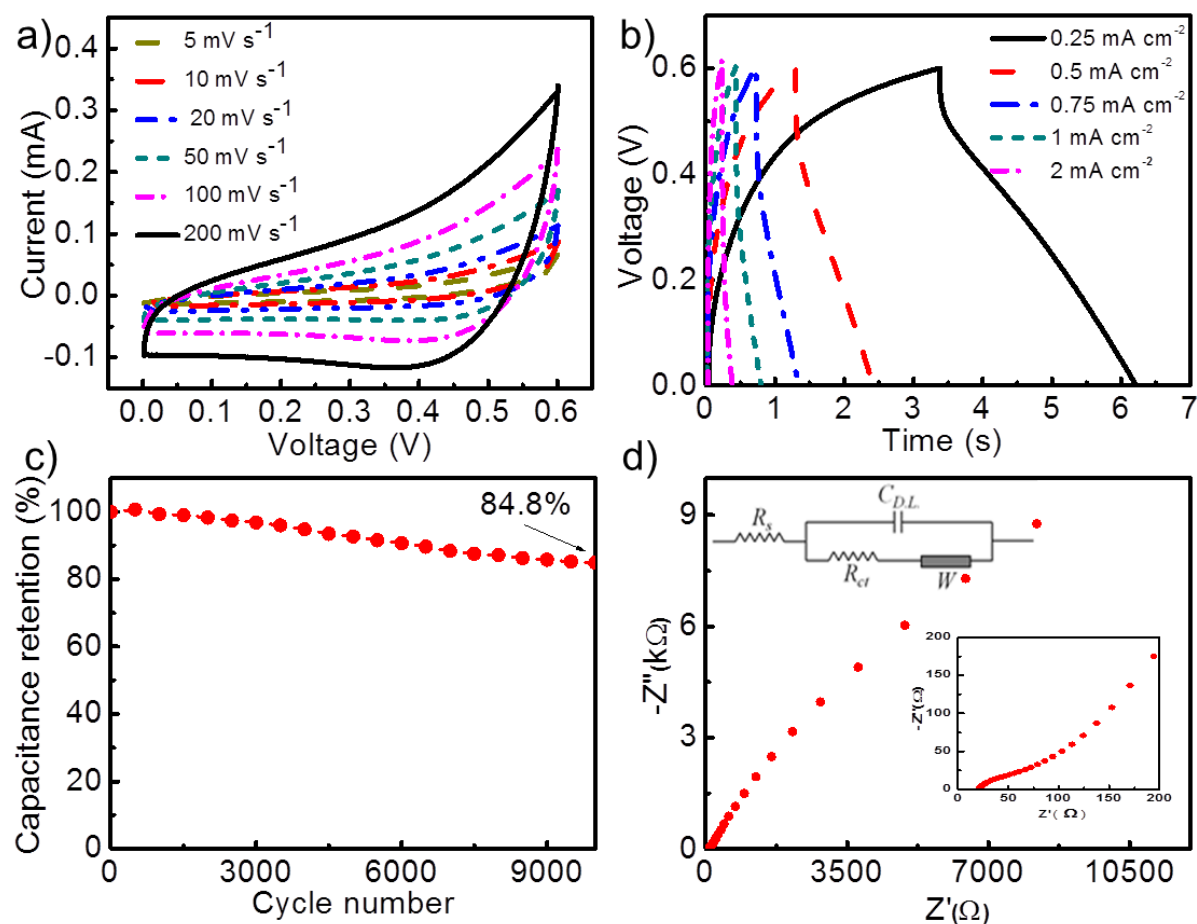
Figure 4.11. a) CV measurements of **MBI**-based capacitor device. b) The galvanostatic charge−discharge curves. c) Capacitance retention as a function of the number of cycles. d) Nyquist plot with equivalent circuit diagram as an inset.

The symmetric EDLC assembly was then sandwiched in a standard electrochemical cell (ECC-std, EL-CELL GmbH), and the capacitive performance was evaluated by CV, galvanostatic charge−discharge, and EIS techniques. The CV loops did not show any peaks during forward and reverse scans, indicating that the electrodes are charged and discharged at a constant rate during a complete voltammetric cycle (**Figure 4.11.**a). The galvanostatic charge−discharge curve was symmetrical, which is a characteristic of an ideal EDLC behavior (**Figure 4.11.**b).[33] The results obtained from the charge-discharge measurements were in good agreement with those from CV measurements, indicating that no surface redox reactions are happening in the device in the given voltage range. The long-term cycling stability of the capacitor device was evaluated from repetitive galvanostatic charge−discharge measurements for 10,000 cycles at a current density of 2 mA cm^{-2}. The capacitor retained 84.8% capacitance of its initial value even after 10,000 cycles (**Figure 4.11.**c).

The Nyquist plot and the equivalent circuit diagram are shown in **Figure 4.11.**d. In the equivalent circuit diagram, the electrolyte solution resistance (R_S) was connected in series to the double-layer capacitance (C_{DL}). R_{CT} is the charge-transfer resistance of the electroactive material, and W is the Warburg impedance associated with ion
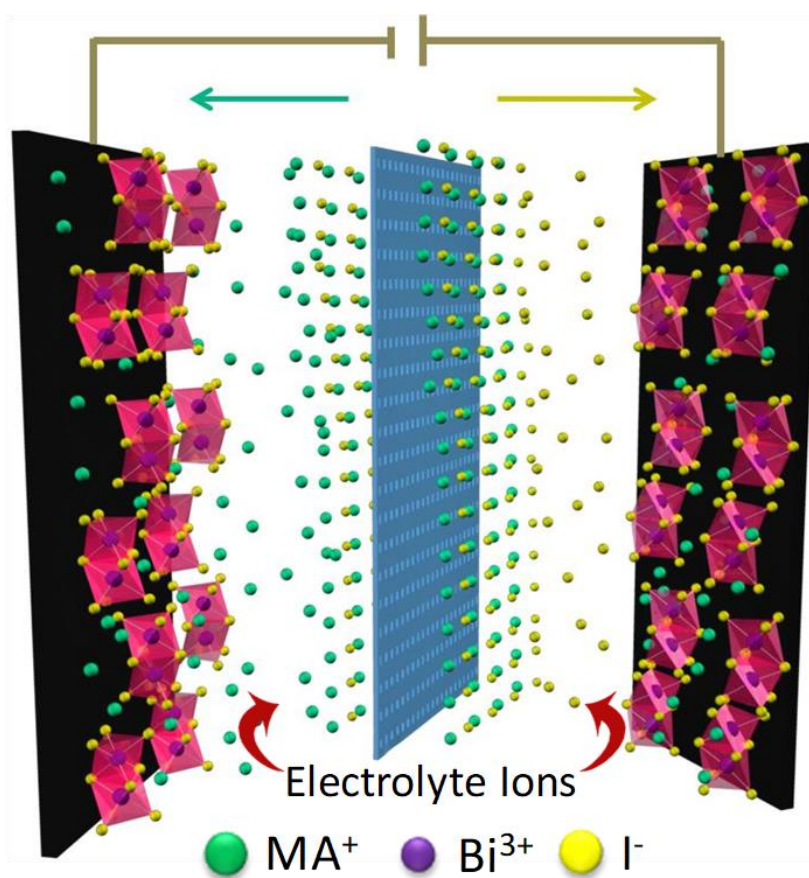
Figure 4.12. Schematic of the charge storage mechanism in the **MBI** based EDLC device.

diffusion in the electrolyte. The charge-transfer resistance (R_{CT}) of the electroactive perovskite material was calculated from the diameter of the semicircle in the higher frequency range of the Nyquist plot and was found to be 50 Ω. The X-intercept of the semicircle arc in the Nyquist plot gives the value of R_S, which is also known as the equivalent series resistance. The lower R_S value (21 Ω) is due to the large electrolyte-accessible surface area provided by the zero-dimensional **MBI**. This implies that during the charging process, MA$^+$ and I$^-$ ions from the electrolyte can easily access the active perovskite material (**Figure 4.12**), and in the discharge process, these ions

move toward the electrolyte. The straight line in the low-frequency region of the Nyquist plot making an angle of 45° with the X-axis represents the Warburg impedance associated with the ion diffusion in the electrolyte.[34] On the other hand, during the discharging process, MA^+ and I^- ions accumulated at the perovskite/ electrolyte interface move toward the electrolyte. Since the $Bi_2I_9{}^{3-}$ octahedra are rigid, the ionic contribution from the perovskite layer will be negligibly small, and thus the perovskite layer acts as an electrode.
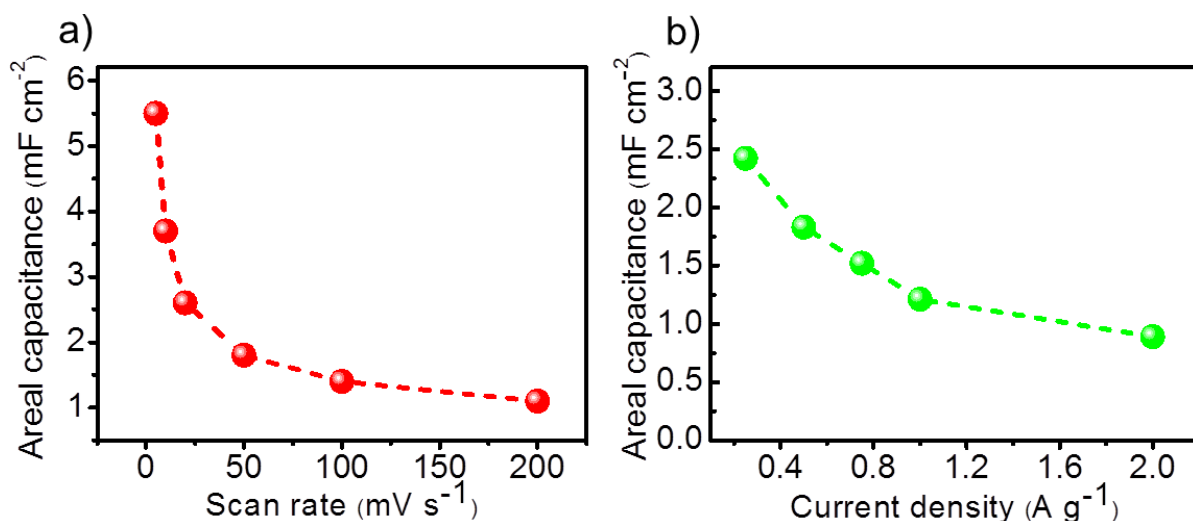
Figure 4.13. Variation of areal capacitance with a) scan rate and b) areal current density.

It was found that the areal capacitance value was decreasing with an increase in applied scan rate or current density (**Figure 4.13**). This property implies the EDLC behavior of the device, which means that at lower scan rates, ions are getting enough time to occupy the vacant spaces supplied by the **MBI** perovskite film, and at higher scan rates, the charge accumulation happens only at the electrode surface. The

MAPbI$_3$ perovskite-based electrochemical capacitor reported by Zhao et al. exhibited a capacitance of 5.89 μF cm^{-2}. On the other hand, our material has a capacitance of 5.5 mF cm^{-2}, which is almost 1000 times higher than that of the above-mentioned material. It should also be noted that the toxicity and moisture instability of MAPbI$_3$ may prevent its practical applications. The lead-free Bi-based hybrid perovskite used in the present work was stable for several months under ambient conditions. The performance of the capacitor devices can be further enhanced by engineering the perovskite material by varying metal ions, organic cations, and electrolytes in addition to the device architecture.

4.4. Conclusion

In summary, for the first time, we have demonstrated the potential of a 0D Bi-halide perovskite material (MBI) for EDLC application. The metal site vacancy ordered perovskite endowed dense ion intercalation sites compared to the conventional 3D MAPbI$_3$ perovskite. The symmetric EDLC devices fabricated using MBI as the electrode material delivered a maximum areal capacitance of 5.5 mF cm^{-2} at a scan rate of 5 mV s^{-1}. This was the highest value of capacitance reported then for a hybrid perovskite material. Moreover, the inherent structural robustness of the core-shell structured MBI offered 84.8% capacitance retention to the EDLC devices after 10,000 charge-discharge cycles. We believe this work has opened up a new research direction for low-dimensional Bi-based perovskites for energy storage applications.

4.5. Experimental section

4.5.1. Chemicals: Bismuth(III) iodide (99.9%, Sigma-Aldrich), methylammonium iodide (98%, TCI Chemicals), and N, N-dimethyl formamide (99.8%, Sigma-Aldrich) were used without any further purification.

4.5.2. Synthesis of a Powder (CH₃NH₃)₃Bi₂I₉ (MBI) Material: Bismuth(III) iodide (0.9729 g) (1.649 mM, 1 equiv) and 0.3934 g of methylammonium iodide (2.474 mM, 1.5 equiv) were dissolved in 1 mL of dimethylformamide (DMF) and heated at 70 °C on a hot plate with constant stirring overnight for complete dissolution. Then, the solution was transferred into a Petri dish and heated to 100 °C for about 4 h for the complete removal of DMF. The obtained powder perovskite material was used for further studies.

4.5.3. Characterization: AFM image was recorded under ambient conditions using an NTEGRA (NT-MDT) operated in the tapping mode regime. Microfabricated thin cantilever tips (NSG 10) with a resonance frequency of 299 kHz and a spring constant of 20−80 N m^{-1} were used.

4.5.4. Preparation of Electrodes: The presynthesized **MBI** was mixed with a PTFE binder and activated charcoal in a weight ratio of 85:10:5 and dispersed in ethanol. The resulting mixture was homogenized by ultrasonication and coated onto a conductive carbon cloth (ELAT, NuVant Systems Inc.) substrate, having an area of 1 cm^2, via a drop-casting method, which was followed by drying at 60 °C for 12 h in a vacuum oven. The two electrodes were separated by a thin polymer separator

(Celgard 3501) in a 30 mg mL^{-1} methylammonium iodide/butanol electrolyte and were sandwiched in a capacitor test cell (ECC-std, EL-CELL GmbH).

4.5.5. Electrochemical Measurements: The electrochemical properties of the capacitor electrodes were studied by symmetric assemblies of the material in a two-electrode configuration by CV, galvanostatic charge−discharge, and EIS using a VMP3 BioLogic electrochemical workstation. The twoelectrode configuration is preferred as it provides the most reliable results of the performance of a material for electrochemical capacitors. The cell capacitance (C in F) was then calculated from the CV curves according to eq 1 or from the charge−discharge curves according to eq 2

$$C = \frac{i}{s} \qquad (1)$$

where 'i' is average cathodic current of CV loop and 's' is the scan rate.

$$C = \frac{I}{\left(\frac{\Delta V}{\Delta t}\right)} \qquad (2)$$

where 'I' is the constant current for charge-discharge, $\frac{\Delta V}{\Delta t}$ is slope of the discharge curve. The areal capacitance (C_{areal} in F cm^{-2}) was then calculated as

$$C_{areal} = \frac{2C}{A} \qquad (3)$$

where 'A' is the area of each electrode.

4.6. References

1. J. P. B. Silva, K. C. Sekhar, H. Pan, J. L. MacManus-Driscoll, M. Pereira, *ACS Energy Lett.* **2021**, *6*, 2208-2217.

2. M. Armand, J. M. Tarascon, *Nature*, **2008**, *451*, 652.

3. Q. Guo, Y. Han, N. Chen, L. Qu, *ACS Energy Lett.* **2021**, *6*, 1786-1794.

4. J. M. Tarascon. M. Armand, *Nature*, **2001**, *414*, 359-367.

5. H. Qiu, H. Cheng, J. Meng, G. Wu, S. Chen, *Angew. Chem. Int. Ed.* **2020**, *59*, 7934-7943.

6. P. Simon, Y. Gogotsi, *Nat. Mater.*, **2008**, *7*, 845.

7. R. B. Rakhi, W. Chen, D. Cha, H. N. Alshareef, *Adv. Energy Mater*. **2012**, *2*, 381-389.

8. T. Liu, R. Yan, H. Huang, L. Pan, X. Cao, A. deMello, M. Niederberger, *Adv. Funct. Mater.* **2020**, *30*, 2004410.

9. L. Sheng, J. Chang, L. Jiang, Z. Jiang, Z. Liu, T. Wei, Z. Fan, *Adv. Funct. Mater*. **2018**, *28*, 1800597.

10. C. Zhao, X. Jia, K. Shu, C. Yu, G. G. Wallace, C. Wang, *J. Mater. Chem. A*, **2020**, *8*, 4677-4699.

11. V. Augustyn, P. Simon, B. Dunn, *Energy Environ. Sci*. **2014**, *7*, 1597-1614.

12. H. Li, C. Qi, Y. Tao, H. Liu, D. W. Wang, F. Li, Q. H. Yang, H. M. Cheng, *Adv. Energy Mater*. **2019**, *9*, 1900079.

13. F. Wang, X. Wu, X. Yuan, Z. Liu, Y. Zhang, L. Fu, Y. Zhu, Q. Zhou, Y. Wu, W. Huang, *Chem. Soc.Rev*. **2017**, *46*, 6816-6854.

14. T. S. Mathis, N. Kurra, X. Wang, D. Pinto, P. Simon, Y. Gogotsi, *Adv. Energy Mater*. **2019**, *9*, 1902007.

15. W. J. Dong, W. S. Cho, J.-L. Lee, *ACS Appl. Mater. Interfaces* **2021**, *13*, 22676-22683.

16. Z. Luo, L. Liu, X. Yang, X. Luo, P. Bi, Z. Fu, A. Pang, W. Li, Y. Yi, *ACS Appl. Mater. Interfaces* **2020**, *12*, 39098-39107.

17. G. Zhang, X. Xiao, B. Li, P. Gu, H. Xue, H. Pang, *J. Mater. Chem. A*, **2017**, *5*, 8155-8186.

18. M. Manuraj, S. Jyothilakshmi, K. N. Narayanan Unni, R. B. Rakhi, *J Mater Sci: Mater Electron*, **2020**, *31*, 20571-20577.

19. F. Lu, M. Zhou, K. Su, T. Ye, Y. Yang, T. D. Lam, Y. Bando, X. Wang, *ACS Appl. Mater. Interfaces* **2019**, *11*, 2082-2092.

20. Y, Cao, J. Liang, X. Li, L. Yue, Q. Liu, S. Lu, A. M. Asiri, J. Hu, Y. Luo, X. Sun, *Chem. Commun.*, **2021**, *57*, 2343-2355.

21. M. A. Memon, W. Bai, J. Sun, M. Imran, S. N. Phulpoto, S. Yan, Y. Huang, J. Geng, *ACS Appl. Mater. Interfaces* **2016**, *8*, 11711-11719.

22. C. Zhong, Y. Deng, W. Hu, J. Qiao, L. Zhang, J. Zhang, *Chem. Soc. Rev*. **2015**, *44*, 7484-7539.

23. A. K. Tomar, G. Singh, R. K. Sharma, *ChemSusChem* **2018**, *11*, 4123-4130.

24. Z. Li, W. Zhang, C. Yuan, Y. Su, *RSC Adv*. **2017**, *7*, 12931-12937.

25. J. T. Mefford, W. G. Hardin, S. Dai, K. P. Johnston, K. J. Stevenson, *Nature Materials* **2014**, *13*, 726-732.

26. S. Zhou, L. Li, H. Yu, J. Chen, C.-P. Wong, N. Zhao, *Adv. Electron. Mater*. **2016**, *2*, 1600114.

27. I. Popoola, M. Gondal, L. Oloore, AJ. Popoola, J. AlGhamdi, *Electrochim. Acta* **2020**, *332*, 135536.

28. L. E. Oloore, M. A. Gondal, I. K. Popoola, AJ. Popoola, *ChemElectroChem* **2020**, *7*, 486-492.

29. T. Li, J. Mallows, K. Adams, G. S. Nichol, J. H. J. Thijssen, N. Robertson, *Batter. Supercaps* **2019**, *2*, 568-575.

30. K. Adams, J. Mallows, T. Li, D. Kampouris, J. H. J. Thijssen, *J. Phys. Energy* **2019**, *1*, 034001.

31. K. Roy, T. Li, S. Ogale, N. Robertson, *J. Mater. Chem. A* **2021**, *9*, 2689-2693.

32. K. Eckhardt, V. Bon, J. Getzschmann, J. Grothe, F. M. Wisser, S. Kaskel, *Chem. Commun*. **2016**, *52*, 3058-3060.

33. W. Chen, R. B. Rakhi, L. Hu, X. Xie, Y. Cui, H. N. Alshareef, *Nano Lett*. **2011**, *11*, 5165-5172.

34. A. N. Naveen, S. Selladurai, *RSC Adv*. **2015**, *5*, 65139-65152.

ABSTRACT

Name of the Student: **Mr. Johnpaul K. P.**

Faculty of Study: Chemical Sciences

AcSIR academic centre/CSIR Lab: CSIR-National
Institute for Interdisciplinary Science
and Technology (CSIR-NIIST)

Registration No.: 10CC16A39003

Year of Submission: 2021

Name of the Supervisor: Dr. Vijayakumar C.

Title of the thesis: **Bismuth Halide Perovskites: Tuning the Optoelectronic Properties Using Functional Organic Cations**

The first chapter gives an overview of hybrid perovskites, particularly lead-free materials, and the recent developments in this area. **In Chapter 2**, we introduce a novel, lead-free, zero-dimensional perovskite-like material, $(1,3\text{-propanediammonium})_2Bi_2I_{10} \cdot 2H_2O$, for optoelectronic applications. The photodetector device fabricated using this material showed an efficient charge separation at low voltage (1 V) due to the good electronic conduction between the $Bi_2I_{10}^{4-}$ dimer units. In the next part of this chapter, we have used a simple methodology to reduce the dielectric confinement in hybrid $A_3Bi_2I_9$ type perovskite-like materials (A is an organic cation) to improve the charge-carrier separation efficiency. For that, the electronically inert methylammonium (MA) was replaced with a polarizable benzylammonium cation in the well-studied $MA_3Bi_2I_9$ (MBI) structure. The single-crystal X-ray diffraction (XRD) and ultraviolet-visible (UV–vis) absorption spectroscopy analyses suggested similar quantum confinement in both $(BA)_3Bi_2I_9$ (BBI) and MBI materials. Flash-photolysis time-resolved microwave conductivity studies revealed about 2.5-fold enhancement of $\varphi\sum\mu$ (the product of charge-carrier generation quantum yield and the sum of charge-carrier mobilities) for BBI when compared to that of MBI, which is attributed to the low dielectric confinement in the former.

In Chapter 3, we have integrated an electronically active organic cation, naphthalimide ethylammonium, between the $[BiI_5^{2-}]_n$ chains via crystal engineering to form a novel perovskite-like material (naphthalimide ethylammonium)$_2BiI_5$ (NBI). Single crystal analysis revealed a one-dimensional quantum-well structure for NBI in which inter-inorganic well electronic coupling is screened by organic layers. It exhibited anisotropic photoconductivity and long-lived charge carriers with milliseconds lifetime, which is higher than that of $CH_3NH_3PbI_3$. In the second part of this chapter, we have done a combined experimental and theoretical study of the structural features and optoelectronic properties of two novel, highly stable, zero-dimensional bismuth perovskites; biphenyl bis(methylammonium)$_{1.5}BiI_6$ (BPBI) and naphthalene diimide bis(ethylammonium)$_{1.5}BiI_6$ (NDBI). The role of organic cations in modulating the visible light absorption and photoconductivity of these materials was evaluated. In BPBI, biphenyl cations have strong hydrogen bonding interactions with the iodine atoms of BiI_6^{3-} octahedral units but are stacked in a disordered manner due to the lack of π-π interaction. On the other hand, naphthalene dimide cations adopt a herringbone arrangement, which brings a tight packing of inorganic octahedrons in NDBI. As a result, though both form zero-dimensional structures having no connectivity between neighboring inorganic frameworks, NDBI has a remarkably narrow bandgap (1.82 eV) than BPBI (2.06 eV). Raman spectral analysis and computed partial density of states revealed that the naphthalene diimide cations have a significant orbital contribution at the band edges of NDBI, playing a key role in reducing the optical bandgap. Moreover, the flash photolysis time-resolved microwave conductivity analysis unraveled that the photoconductivity of NDBI is about 3.7 fold higher than that of BPBI. Density functional theory calculations revealed that the enhanced photoconductivity in NDBI arises from its Type IIb band alignment, whereas Type Ib alignment was seen in BPBI. This work illustrates the important role of organic cations in the design of bismuth-based perovskite materials for functional applications.

In Chapter 4, we have fabricated an electrochemical double-layer capacitor using methylammonium bismuth iodide $(CH_3NH_3)_3Bi_2I_9$, a lead-free, zero-dimensional hybrid perovskite material. A maximum areal capacitance of 5.5 mF/cm^2 was obtained, and the device retained 84.8% of its initial maximum capacitance even after 10,000 charge-discharge cycles. Impedance spectroscopy measurements revealed that the active layer provides a high surface area for the electrolyte to access. As a result, the charge transport resistance is reasonably low, which is advantageous for delivering excellent performance.

LIST OF PUBLICATIONS

Related to Thesis

1. Zero-Dimensional Methylammonium Bismuth Iodide-Based Lead-Free Perovskite Capacitor; **Johnpaul K. Pious**, M. L. Lekshmi, Chinnadurai Muthu, R. B. Rakhi,* and Vijayakumar C. Nair**; *ACS Omega*, **2017**, *2*, 5798-5802.

2. A Zero-Dimensional Lead-Free Hybrid Perovskite-Like Material with a Quantum-Well Structure; **Johnpaul K. Pious**, Ankita Katre, Chinnadurai Muthu, Sudip Chakraborty, Swathi Krishna, and Vijayakumar C. Nair*; *Chem. Mater.* **2019**, *31*, 1941-1945.

3. Bismuth based zero-dimensional perovskite-like material: Effect of benzylammonium on dielectric confinement and photoconductivity; **Johnpaul K. Pious**, Chinnadurai Muthu, Selgiya Dani, Akinori Saeki, and Vijayakumar C. Nair*; *Chem. Mater.* **2020**, *32*, 2647-2652.

4. Anisotropic photoconductivity and long-lived charge carriers in bismuth-based one-dimensional perovskite with type-IIa band alignment; **Johnpaul K. Pious**, Manasa G. Basavarajappa, Chinnadurai Muthu, Nayana Krishna, Ryosuke Nishikubo, Akinori Saeki, Sudip Chakraborty,* and Vijayakumar C. Nair*; *J. Phys. Chem. Lett.* **2020**, *11*, 6757-6762.

5. Self-Assembled Organic Cations-Assisted Band-Edge Tailoring in Bismuth-Based Perovskites for Enhanced Visible Light Absorption and Photoconductivity; **Johnpaul K. Pious**, Manasa G. Basavarajappa, Chinnadurai Muthu, Ryosuke Nishikubo, Akinori Saeki, Sudip Chakraborty,* Atsuro Takai, Masayuki Takeuchi, and Chakkooth Vijayakumar*; *J. Phys. Chem. Lett.* **2021**, *12*, 5758-5764.

Not Related to Thesis

1. Formamidinium Lead Iodide Perovskite Nanocrystal/Squaraine Dye Composite based Visibly Opaque and Near-Infrared Transmitting Material; Chinnadurai Muthu, **Johnpaul K. Pious**, Parambatheri S. Seethal, Nayana Krishna, and C. Vijayakumar*; *Adv. Opt. Mater.* **2020**, *8*, 2001130.

2. Resistive Switching in Formamidinium Lead Iodide Perovskite Nanocrystals: A Contradiction to the Bulk Form; Chinnadurai Muthu, A. N. Resmi, **Johnpaul K. Pious**, G. Dayal, Nayana Krishna, K. B. Jinesh*, and C. Vijayakumar*; *J. Mater. Chem. C* **2021**, *9*, 288-293.

3. Stable and Efficient White Photoluminescence from Cesium Lead Halide Perovskite Nanocrystals/Polyfluorene Organogel Composite by Suppressing of Halide Ion Migration; Chinnadurai Muthu, **Johnpaul K. Pious**, Tino Thankachan, Nayana Krishna, Chakkooth Vijayakumar*; *Adv. Opt. Mater.* **2021**, DOI: 10.1002/adom.202100601.

PAPERS/POSTERS PRESENTED IN CONFERENCE

1. 'Tuning Quantum Confinement in Zero-Dimensional Lead-Free Hybrid Perovskites'; **Johnpaul K. Pious** participated and delivered an **Oral presentation** in the CSIR-Inter Institutional Students Conference (SU-CHEM Yuva), CSIR-IICT, Hyderabad, India during 24-26th July **2019**.

2. 'Zero-Dimensional Lead-Free Hybrid Perovskite-Like Material with a Quantum-Well Structure'; **Johnpaul K. Pious** participated and delivered an **Oral presentation** in National Seminar on Advanced Functional Materials for Analytical, Energy, Environmental and Biomedical Applications (NSAFM) conducted by University of Kerala, Trivandrum, India during 25-27th March **2019**.

3. 'Low-dimensional Bismuth-Based Perovskite for Energy Storage Application'; **Johnpaul K. Pious** participated and presented a **Poster** in National Conference on Emerging Trends in Science, Technology & Application of Electron Microscope (STAEM-2018) conducted by CSIR-NIIST, Trivandrum, India during 19-21st December **2018**.

4. 'Zero-Dimensional Methylammonium Bismuth Iodide-Based Lead-Free Perovskite Capacitor'; **Johnpaul K. Pious** presented a **Poster** in a Discussion Meeting on Hybrid Perovskite Materials "HyPe-2017" conducted by S.N. Bose National Centre for Basic Sciences, Kolkata, India during 14-15th December **2017**.

ACS OMEGA

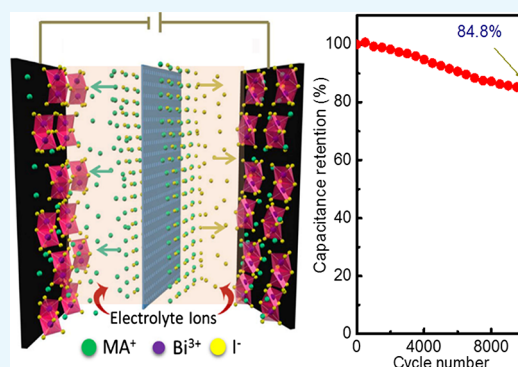# Zero-Dimensional Methylammonium Bismuth Iodide-Based Lead-Free Perovskite Capacitor

Johnpaul K. Pious,[†,‡] M. L. Lekshmi,[†] Chinnadurai Muthu,[†,‡] R. B. Rakhi,*[,†,‡] and Chakkooth Vijayakumar*[,†,‡]

†Photosciences and Photonics Section, Chemical Sciences and Technology Division, CSIR-National Institute for Interdisciplinary Science and Technology (CSIR-NIIST), Trivandrum 695 019, India

‡Academy of Scientific and Innovative Research (AcSIR), CSIR-NIIST Campus, Thiruvananthapuram 695019, Kerala, India

S Supporting Information

ABSTRACT: Symmetrical electrochemical capacitors are attracting immense attention because of their fast charging−discharging ability, high energy density, and low cost of production. The current research in this area is mainly focused on exploring novel low-cost electrode materials with higher energy and power densities. In the present work, we fabricated an electrochemical double-layer capacitor using methylammonium bismuth iodide $(CH_3NH_3)_3Bi_2I_9$, a lead-free, zero-dimensional hybrid perovskite material. A maximum areal capacitance of 5.5 mF/cm^2 was obtained, and the device retained 84.8% of its initial maximum capacitance even after 10 000 charge−discharge cycles. Impedance spectroscopy measurements revealed that the active layer provides a high surface area for the electrolyte to access. As a result, the charge transport resistance is reasonably low, which is advantageous for delivering excellent performance.

Electrolyte Ions
● MA⁺ ● Bi³⁺ ● I⁻

INTRODUCTION

Organic−inorganic halide perovskite materials captured the attention of scientific community during the past few years because of their unique optical and electronic properties.[1−5] Three-dimensional hybrid perovskites with a general formula of AMX$_3$ (A = methylammonium or formamidinium cation; M = Pb^{2+}, Sn^{2+}, etc., and X = I, Br, and Cl) are highlighted as efficient light-absorbing layers in solar cells with an efficiency surpassing 22%.[6−8] Apart from photovoltaic applications, these materials are promising for light-emitting diodes, photodetectors, sensors, memories, and so forth.[9−20] The widespread applications of this class of materials could be attributed to their properties such as tunable band gap, large absorption coefficient, high electron and hole diffusion lengths, good charge carrier mobility, ease of defect state formation, and excellent ion migration.[21−23] Even though hybrid perovskites exhibit very interesting properties and are useful for a large number of applications, the toxicity of lead and instability in the presence of moisture and oxygen are prime concerns preventing their commercialization.[24−26]

Storage of energy is as important as its production. Development of novel, environmentally friendly, and sustainable energy storage devices has attracted considerable research attention in modern times because of the rapid depletion of unsustainable fossil fuels and environmental deterioration, which are also necessary to satisfy the demands of the fast-growing electronic industry. Electrochemical capacitors with long life span, high power density, and fast charge−discharge characteristics are regarded as excellent energy storage devices,

as they have the potential to complement or even replace batteries in numerous applications.[27] However, their low energy density is a limiting factor in their widespread practical applications. Hence, the current research in electrochemical capacitors is mainly focused on exploring novel low-cost electrode materials with higher energy and power densities.[28] In this context, hybrid perovskite materials are promising because of their high ionic conductivity; a recent study suggests that the ionic conductivity of methylammonium lead iodide (MAPbI$_3$) is higher than its electronic conductivity.[29] By exploring this property, Zhao et al. have reported a MAPbI$_3$-based thin-film electrochemical double-layer capacitor (EDLC).[30] The capacitance obtained was 5.89 μF/cm^2, which proved that hybrid perovskite materials are good candidates for capacitor applications. However, the toxicity of lead is a major factor of concern here also.

RESULTS AND DISCUSSION

In this work, we have explored the potential of methylammonium bismuth iodide (MBI), which is a lead-free, zero-dimensional perovskite having a unit cell formula of $(CH_3NH_3)_3Bi_2I_9$, for energy storage applications. This bismuth-based perovskite is an environment-friendly alternative with better atmospheric stability than that of the corresponding lead-based perovskites. The unit cell of MBI consists of isolated
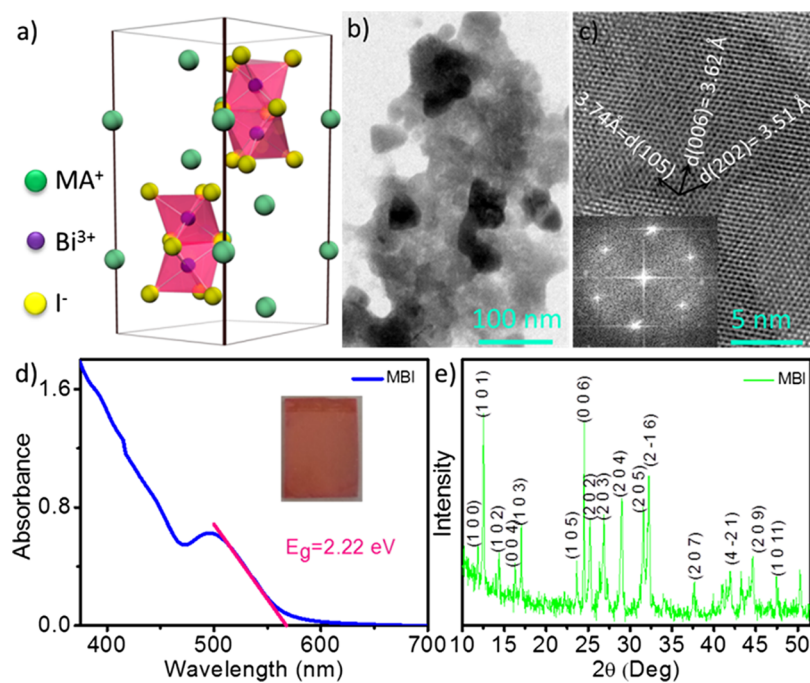
Figure 1. (a) Unit cell representation of MBI. (b) TEM image of the MBI film. (c) HRTEM image of MBI, with a fast Fourier transform image in the inset. (d) Absorption spectra of MBI in the film state. (e) Powder XRD of MBI.

$Bi_2I_9^{3-}$ units surrounded by methylammonium cations (Figure 1a). $Bi_2I_9^{3-}$ is formed through face sharing of two BiI_6^{3-} octahedra. We have hypothesized that the isolated $Bi_2I_9^{3-}$ bioctahedra can supply vacant spaces and large surface area so that the electrolyte can easily access the active material, resulting in enhanced ionic charge transport. This would lead to capacitors having high energy density. To prove this, we have fabricated capacitor devices with the MBI material and analyzed them using cyclic voltammetry (CV), galvanostatic charge–discharge, and electrochemical impedance spectroscopy (EIS) techniques. The charge transport resistance obtained from the impedance measurement was small, which was in agreement with the large surface area provided by the material.

$(CH_3NH_3)_3Bi_2I_9$ was characterized using transmission electron microscopy (TEM), ultraviolet–visible (UV–vis) absorption, and X-ray diffraction (XRD) spectroscopy. The TEM image of MBI is shown in Figure 1b which indicates that the material forms a thin film of interconnected MBI crystals. The high-resolution transmission electron microscopy (HRTEM) image of the material is shown in Figure 1c, and the corresponding electron diffraction pattern is shown in the inset. The diffraction pattern shows lattice distances of 3.51, 3.62, and 3.74 Å corresponding to the (202), (006), and (105) lattice planes, respectively. Clear visibility of the lattice planes and the hexagonal array of bright spots indicate that the material is highly crystalline. MBI exhibited a broad absorption ranging from 300 to 600 nm in the UV–vis absorption spectrum (Figure 1d). The optical band gap of MBI calculated from the onset of the absorption was 2.22 eV. XRD patterns obtained from powdered samples, which are in good agreement with the previous reports,[31] revealed the hexagonal crystal structure of the material, with the characteristic perovskite doublet peak at $2\theta = \sim12°$ (Figure 1e). The XRD profile of the material was studied over a period of 1 month (Figure S1, Supporting Information). No variation in peak position or

intensity was observed, which indicated the good stability of the material under ambient conditions.

For analyzing the electrochemical energy storage performance of the material, MBI was coated on a carbon cloth substrate having an area of 1 cm^2, which was used as the electrode. A polymer separator soaked in an electrolytic solution (30 mg/mL methylammonium iodide in butanol) was sandwiched between the MBI-containing electrodes to form a symmetric capacitor. Additives (5 wt %) such as polytetrafluoroethylene (PTFE) and activated carbon were added during the preparation of the electrode for proper binding of the perovskite material on to the carbon substrate and for improving the conductivity of the active layer. A simplified schematic representation of the device is shown in Figure 2a. The thickness of the active film was about 400 nm as measured from the cross-sectional scanning electron microscopy (SEM) image which is shown in Figure 2b. The perovskite material was uniformly coated over the carbon cloth substrate, as shown in the topological SEM image (Figure 2c). The root-mean-square roughness of the film obtained from the atomic force microscopy (AFM) height image (Figure 2d) was 16.7 nm, which means that the surface roughness of the film was reasonably high. Such a high surface roughness is good for energy storage applications because the electrolyte can strongly interact with the active layer. The high surface roughness of the film is in good agreement with the topological SEM image, which showed relatively large MBI crystals (Figure 2c).

The symmetric EDLC assembly was then sandwiched in a standard electrochemical cell (ECC-std, EL-CELL GmbH), and the capacitive performance was evaluated by CV, galvanostatic charge–discharge, and EIS techniques. The CV loops did not show any peaks during forward and reverse scans which indicates that the electrodes are charged and discharged at a constant rate during a complete voltammetric cycle (Figure 3a). It is clearly found that the areal capacitance value was
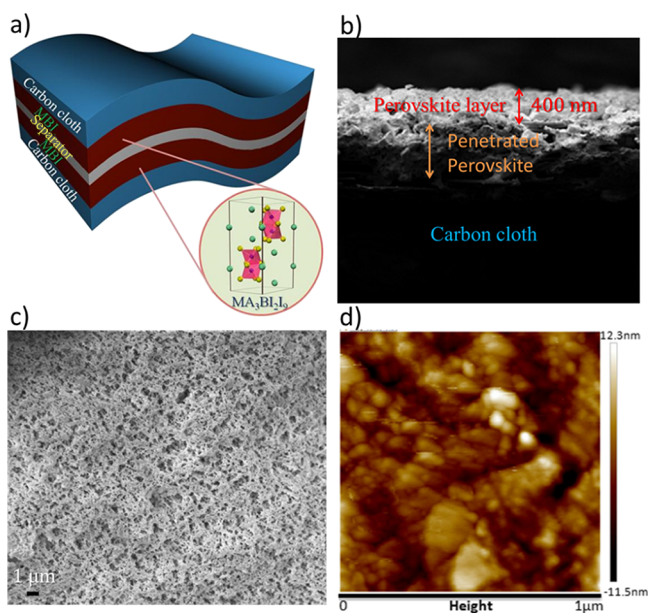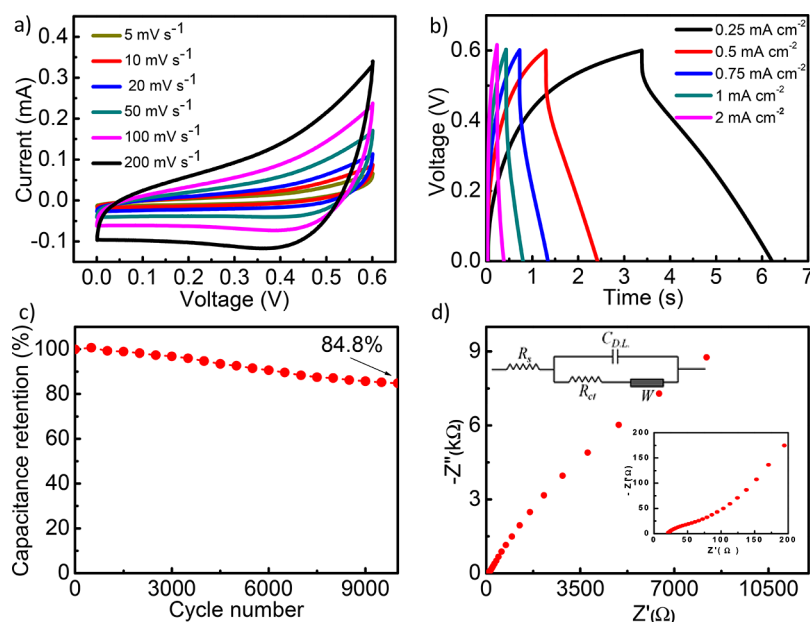
Figure 2. (a) Schematic representation of the MBI-based double-layer capacitor device. (b) Cross-sectional SEM image of the capacitor electrode. (c) Topological SEM image and (d) AFM height image of the MBI film.

decreasing with an increase in applied scan rate or current density (Figure S2, Supporting Information). This property implies the EDLC behavior of the device, which means that at lower scan rates, ions are getting enough time to occupy the vacant spaces supplied by the MBI perovskite film and at higher scan rates, the charge accumulation happens only at the electrode surface.

The galvanostatic charge−discharge curve was symmetrical, which is a characteristic of an ideal EDLC behavior (Figure 3b).[32] The results obtained from the charge−discharge measurements were in good agreement with those from CV measurements, indicating that no surface redox reactions are

happening in the device in the given voltage range. The long-term cycling stability of the capacitor device was evaluated from repetitive galvanostatic charge−discharge measurements for 10 000 cycles at a current density of 2 mA cm^{-2}. The capacitor retained 84.8% capacitance of its initial value even after 10 000 cycles (Figure 3c). The Nyquist plot and the equivalent circuit diagram are shown in Figure 3d. In the equivalent circuit diagram, the electrolyte solution resistance (R_s) was connected in series to the double-layer capacitance (C_{DL}). R_{CT} is the charge-transfer resistance of the electroactive material, and Z_W is the Warburg impedance associated with ion diffusion in the electrolyte. The charge-transfer resistance (R_{CT}) of the electroactive perovskite material was calculated from the diameter of the semicircle in the higher frequency range of the Nyquist plot and was found to be 50 Ω. The X-intercept of the semicircle arc in the Nyquist plot gives the value of R_s, which is also known as the equivalent series resistance. The lower R_s value (21 Ω) is due to the large electrolyte-accessible surface area provided by the zero-dimensional MBI. This implies that during the charging process, MA$^+$ and I$^-$ ions from the electrolyte can easily access the active perovskite material and in the discharge process, these ions move toward the electrolyte. The straight line in the low-frequency region of the Nyquist plot making an angle of 45° with the X-axis represents the Warburg impedance associated with the ion diffusion in the electrolyte.[33] On the other hand, during the discharging process, MA$^+$ and I$^-$ ions accumulated at the perovskite/electrolyte interface move toward the electrolyte. Because the Bi$_2$I$_9$$^{3-}$ octahedra are rigid, the ionic contribution from the perovskite layer will be negligibly small, and thus the perovskite layer acts as an electrode.

The MAPbI$_3$ perovskite-based electrochemical capacitor reported by Zhao et al. exhibited a capacitance of 5.89 μF/cm^2. On the other hand, our material has a capacitance of 5.5 mF/cm^2, which is almost 1000 times higher than that of the above-mentioned material. It should also be noted that the toxicity and moisture instability of MAPbI$_3$ may prevent its practical applications. The lead-free Bi-based hybrid perovskite

Figure 3. (a) CV measurements of MBI-based capacitor. (b) Galvanostatic charge−discharge curves. (c) Capacitance retention as a function of the number of cycles. (d) Nyquist plot and equivalent circuit diagram as an inset.

used in the present work was stable for several months under ambient conditions. The performance of the capacitor devices can be further enhanced by engineering the perovskite material by varying metal ions, organic cations, and electrolytes in addition to the device architecture.

■ CONCLUSIONS

In summary, for the first time, we have fabricated a lead-free perovskite material-based symmetric EDLC. A maximum areal capacitance of 5.5 mF/cm² at a scan rate of 5 mV/s was obtained. According to our knowledge, this is the highest value of capacitance reported so far for a hybrid perovskite-based EDLC. Moreover, our findings confirmed that MBI perovskite is an excellent material for EDLC applications.

■ EXPERIMENTAL SECTION

Chemicals. Bismuth(III) iodide (99.9%, Sigma-Aldrich), methylammonium iodide (98%, TCI Chemicals), and *N,N*-dimethyl formamide (99.8%, Sigma-Aldrich) were used without any further purification.

Synthesis of a Powder (CH₃NH₃)₃Bi₂I₉ (MBI) Material. Bismuth(III) iodide (0.9729 g) (1.649 mM, 1 equiv) and 0.3934 g of methylammonium iodide (2.474 mM, 1.5 equiv) were dissolved in 1 mL of dimethylformamide (DMF) and heated at 70 °C on a hot plate with constant stirring overnight for complete dissolution. Then, the solution was transferred into a Petri dish and heated to 100 °C for about 4 h for the complete removal of DMF. The obtained powder perovskite material was used for further studies.

Characterization. Electronic absorption spectra were recorded on a Shimadzu UV-2600 UV–vis spectrophotometer. For the measurement, the powder perovskite material was kept in between two transparent quartz plates and measured in the reflectance mode. Using Kubelka–Munk function, the reflectance spectra were converted into absorption spectra. XRD studies were carried out on the powder samples with Xeuss simultaneous 2D WAXS/SAXS using Cu Kα radiation (λ = 1.5418 Å). The topological and cross-sectional SEM imaging of the device was performed by subjecting the device to thin gold coating using a JEOL JFC—1200 fine coater. The probe side was inserted into a JEOL JSM-5600 LV scanning electron microscope for imaging. AFM image was recorded under ambient conditions using an NTEGRA (NT-MDT) operated in the tapping mode regime. Microfabricated thin cantilever tips (NSG 10) with a resonance frequency of 299 kHz and a spring constant of 20–80 N m⁻¹ were used. The morphology and electron diffraction pattern of the perovskite material were studied by using an FEI-Tecnai T30 high-resolution transmission electron microscope, at an accelerating voltage of 300 kV.

Preparation of Electrodes. The presynthesized MBI was mixed with a PTFE binder and activated charcoal in a weight ratio of 85:10:5 and dispersed in ethanol. The resulting mixture was homogenized by ultrasonication and coated onto a conductive carbon cloth (ELAT, NuVant Systems Inc.) substrate, having an area of 1 cm², via a drop-casting method, which was followed by drying at 60 °C for 12 h in a vacuum oven. The two electrodes were separated by a thin polymer separator (Celgard 3501) in a 30 mg/mL methylammonium iodide/butanol electrolyte and were sandwiched in a capacitor test cell (ECC-std, EL-CELL GmbH).

Electrochemical Measurements. The electrochemical properties of the capacitor electrodes were studied by symmetric assemblies of the material in a two-electrode configuration by CV, galvanostatic charge–discharge, and EIS using a VMP3 BioLogic electrochemical workstation. The two-electrode configuration is preferred as it provides the most reliable results of the performance of a material for electrochemical capacitors. The cell capacitance (C in F) was then calculated from the CV curves according to eq 1 or from the charge–discharge curves according to eq 2

$$C = \frac{i}{s} \tag{1}$$

where "i" is the average cathodic current of the CV loop and "s" is the scan rate.

$$C = \frac{I}{(\Delta V/\Delta t)} \tag{2}$$

where "I" is the constant current for charge–discharge and $\Delta V/\Delta t$ is the slope of the discharge curve. The areal capacitance (C_{areal} in F/cm²) was then calculated as

$$C_{areal} = \frac{2C}{A} \tag{3}$$

where "A" is the area of each electrode.

■ ASSOCIATED CONTENT

Ⓢ Supporting Information

The Supporting Information is available free of charge on the ACS Publications website at DOI: 10.1021/acsomega.7b00973.

Stability studies of (CH₃NH₃)₃Bi₂I₉ and graphical data representing the variation of areal capacitance with scan rate and areal current density (PDF)

■ AUTHOR INFORMATION

Corresponding Authors

*E-mail: rakhiraghavanbaby@niist.res.in (R.B.R.).
*E-mail: cvijayakumar@niist.res.in (C.V.).

ORCID Ⓞ

R. B. Rakhi: 0000-0002-0207-8595

Chakkooth Vijayakumar: 0000-0001-5347-6799

Author Contributions

The manuscript was written through the contributions of all authors.

■ REFERENCES

(1) Saparov, B.; Mitzi, D. B. Organic−Inorganic Perovskites: Structural Versatility for Functional Materials Design. *Chem. Rev.* **2016**, *116*, 4558−4596.

(2) Brenner, T. M.; Egger, D. A.; Kronik, L.; Hodes, G.; Cahen, D. Hybrid organic−inorganic perovskites: low-cost semiconductors with intriguing charge-transport properties. *Nat. Rev. Mater.* **2016**, *1*, 15007.

(3) Zhao, Y.; Zhu, K. Organic−inorganic hybrid lead halide perovskites for optoelectronic and electronic applications. *Chem. Soc. Rev.* **2016**, *45*, 655−689.

(4) Manser, J. S.; Christians, J. A.; Kamat, P. V. Intriguing Optoelectronic Properties of Metal Halide Perovskites. *Chem. Rev.* **2016**, *116*, 12956−13008.

(5) Stranks, S. D. Nonradiative Losses in Metal Halide Perovskites. *ACS Energy Lett.* **2017**, *2*, 1515−1525.

(6) Guchhait, A.; Dewi, H. A.; Leow, S. W.; Wang, H.; Han, G.; Suhaimi, F. B.; Mhaisalkar, S.; Wong, L. H.; Mathews, N. Over 20% Efficient CIGS−Perovskite Tandem Solar Cells. *ACS Energy Lett.* **2017**, *2*, 807−812.

(7) Chou, H.-H.; Chiang, Y.-H.; Li, M.-H.; Shen, P.-S.; Wei, H.-J.; Mai, C.-L.; Chen, P.; Yeh, C.-Y. Zinc Porphyrin−Ethynylaniline Conjugates as Novel Hole-Transporting Materials for Perovskite Solar Cells with Power Conversion Efficiency of 16.6%. *ACS Energy Lett.* **2016**, *1*, 956−962.

(8) NREL chart. www.nrel.gov/ncpv/images/efficiency_chart.jpg, 2017.

(9) Xiao, Z.; Kerner, R. A.; Zhao, L.; Tran, N. L.; Lee, K. M.; Koh, T.-W.; Scholes, G. D.; Rand, B. P. Efficient perovskite light-emitting diodes featuring nanometre-sized crystallites. *Nat. Photonics* **2017**, *11*, 108−115.

(10) Li, G.; Tan, Z.-K.; Di, D.; Lai, M. L.; Jiang, L.; Lim, J. H.-W.; Friend, R. H.; Greenham, N. C. Efficient Light-Emitting Diodes Based on Nanocrystalline Perovskite in a Dielectric Polymer Matrix. *Nano Lett.* **2015**, *15*, 2640−2644.

(11) Kumawat, N. K.; Dey, A.; Narasimhan, K. L.; Kabra, D. Near Infrared to Visible Electroluminescent Diodes Based on Organometallic Halide Perovskites: Structural and Optical Investigation. *ACS Photonics* **2015**, *2*, 349−354.

(12) Ding, J.; Du, S.; Zuo, Z.; Zhao, Y.; Cui, H.; Zhan, X. High Detectivity and Rapid Response in Perovskite $CsPbBr_3$ Single-Crystal Photodetector. *J. Phys. Chem. C* **2017**, *121*, 4917−4923.

(13) Tan, Z.; Wu, Y.; Hong, H.; Yin, J.; Zhang, J.; Lin, L.; Wang, M.; Sun, X.; Sun, L.; Huang, Y.; Liu, K.; Liu, Z.; Peng, H. Two-Dimensional $(C_4H_9NH_3)_2PbBr_4$ Perovskite Crystals for High-Performance Photodetector. *J. Am. Chem. Soc.* **2016**, *138*, 16612−16615.

(14) Zhou, J.; Chu, Y.; Huang, J. Photodetectors based on two-dimensional layer-structured hybrid lead iodide perovskite semiconductors. *ACS Appl. Mater. Interfaces* **2016**, *8*, 25660−25666.

(15) Kumar, P.; Muthu, C.; Nair, V. C.; Narayan, K. S. Quantum Confinement Effects in Organic Lead Tribromide Perovskite Nanoparticles. *J. Phys. Chem. C* **2016**, *120*, 18333−18339.

(16) He, M.; Chen, Y.; Liu, H.; Wang, J.; Fang, X.; Liang, Z. Chemical decoration of $CH_3NH_3PbI_3$ perovskites with graphene oxides for photodetector applications. *Chem. Commun.* **2015**, *51*, 9659−9661.

(17) Bao, C.; Yang, J.; Zhu, W.; Zhou, X.; Gao, H.; Li, F.; Fu, G.; Yu, T.; Zou, Z. A resistance change effect in perovskite $CH_3NH_3PbI_3$ films induced by ammonia. *Chem. Commun.* **2015**, *51*, 15426−15429.

(18) Muthu, C.; Nagamma, S. R.; Nair, V. C. Luminescent Hybrid Perovskite Nanoparticles as a New Platform for Selective Detection of 2,4,6-Trinitrophenol. *RSC Adv.* **2014**, *4*, 55908−55911.

(19) Gu, C.; Lee, J.-S. Flexible Hybrid Organic−Inorganic Perovskite Memory. *ACS Nano* **2016**, *10*, 5413−5418.

(20) Muthu, C.; Agarwal, S.; Vijayan, A.; Hazra, P.; Jinesh, K. B.; Nair, V. C. Hybrid Perovskite Nanoparticles for High-Performance Resistive Random Access Memory Devices: Control of Operational Parameters through Chloride Doping. *Adv. Mater. Interfaces* **2016**, *3*, 1600092.

(21) Sherkar, T. S.; Momblona, C.; Gil-Escrig, L.; Ávila, J.; Sessolo, M.; Bolink, H. J.; Koster, L. J. A. Recombination in Perovskite Solar Cells: Significance of Grain Boundaries, Interface Traps, and Defect Ions. *ACS Energy Lett.* **2017**, *2*, 1214−1222.

(22) Zheng, X.; Chen, B.; Yang, M.; Wu, C.; Orler, B.; Moore, R. B.; Zhu, K.; Priya, S. The Controlling Mechanism for Potential Loss in $CH_3NH_3PbBr_3$ Hybrid Solar Cells. *ACS Energy Lett.* **2016**, *1*, 424−430.

(23) Sutherland, B. R.; Sargent, E. H. Perovskite photonic sources. *Nat. Photonics* **2016**, *10*, 295−302.

(24) Babayigit, A.; Duy Thanh, D.; Ethirajan, A.; Manca, J.; Muller, M.; Boyen, H.-G.; Conings, B. Assessing the toxicity of Pb- and Sn-based perovskite solar cells in model organism Danio rerio. *Sci. Rep.* **2016**, *6*, 18721.

(25) Mosconi, E.; Azpiroz, J. M.; De Angelis, F. Ab Initio Molecular Dynamics Simulations of Methylammonium Lead Iodide Perovskite Degradation by Water. *Chem. Mater.* **2015**, *27*, 4885−4892.

(26) Aristidou, N.; Sanchez-molina, I.; Chotchuangchutchaval, T.; Brown, M.; Martinez, L.; Rath, T.; Haque, S. A. The Role of Oxygen in the Degradation of Methylammonium Lead Trihalide Perovskite Photoactive Layers. *Angew. Chem., Int. Ed.* **2015**, *54*, 8208−8212.

(27) Rakhi, R. B.; Chen, W.; Cha, D.; Alshareef, H. N. Nanostructured Ternary Electrodes for Energy-Storage Applications. *Adv. Energy Mater.* **2012**, *2*, 381−389.

(28) Wu, Z.-S.; Parvez, K.; Feng, X.; Müllen, K. Graphene-based in-plane micro-supercapacitors with high power and energy densities. *Nat. Commun.* **2013**, *4*, 2487.

(29) Yang, T.-Y.; Gregori, G.; Pellet, N.; Grätzel, M.; Maier, J. The Significance of Ion Conduction in a Hybrid Organic−Inorganic Lead-Iodide-Based Perovskite Photosensitizer. *Angew. Chem.* **2015**, *127*, 8016−8021.

(30) Zhou, S.; Li, L.; Yu, H.; Chen, J.; Wong, C.-P.; Zhao, N. Thin Film Electrochemical Capacitors based on Organolead Triiodide Perovskite. *Adv. Electron. Mater.* **2016**, *2*, 1600114.

(31) Eckhardt, K.; Bon, V.; Getzschmann, J.; Grothe, J.; Wisser, F. M.; Kaskel, S. Crystallographic insights into $(CH_3NH_3)_3(Bi_2I_9)$: a new lead-free hybrid organic−inorganic material as a potential absorber for photovoltaics. *Chem. Commun.* **2016**, *52*, 3058−3060.

(32) Chen, W.; Rakhi, R. B.; Hu, L.; Xie, X.; Cui, Y.; Alshareef, H. N. High-Performance Nanostructured Supercapacitors on a Sponge. *Nano Lett.* **2011**, *11*, 5165−5172.

(33) Naveen, A. N.; Selladurai, S. A 1-D/2-D Hybrid Nanostructured Manganese Cobaltite−Graphene Nanocomposite for Electrochemical Energy Storage. *RSC Adv.* **2015**, *5*, 65139−65152.

Zero-Dimensional Lead-Free Hybrid Perovskite-like Material with a Quantum-Well Structure

Johnpaul K. Pious,[†,‡] Ankita Katre,[§] Chinnadurai Muthu,[†,‡] Sudip Chakraborty,[||] Swathi Krishna,[†] and Chakkooth Vijayakumar*[,†,‡]

[†]Photosciences and Photonics Section, CSIR-National Institute for Interdisciplinary Science and Technology (NIIST), Thiruvananthapuram 695 019, India

[‡]Academy of Scientific and Innovative Research (AcSIR), Ghaziabad 201002, India

[§]Centre for Modelling and Simulation, Savitribai Phule Pune University, Ganeshkhind, Pune 411007, Maharashtra, India

[||]Materials Theory Division, Department of Physics and Astronomy, Uppsala University, Box 516, 75120 Uppsala, Sweden

S Supporting Information

ABSTRACT: Low-dimensional perovskites are an emerging class of materials with high stability and excellent optoelectronic properties. Herein, we introduce a novel, lead-free, zero-dimensional perovskite-like material, (1,3-propanediammonium)$_2$Bi$_2$I$_{10}$·2H$_2$O, for optoelectronic applications. This material exhibited good moisture and thermal stability under ambient conditions. Single-crystal X-ray diffraction analysis revealed a quantum-well structure having the inorganic Bi$_2$I$_{10}^{4-}$ clusters periodically arranged in the crystallographic "c" axis separated by a distance of 5.36 Å, sandwiched by independent layers of organic cations. The density functional theory calculations showed that the oxygen in water molecules has a significant contribution to the band edges of the material. The photodetector device fabricated using this material showed an efficient charge separation at low voltage (1 V) due to the good electronic conduction between the Bi$_2$I$_{10}^{4-}$ dimer units.
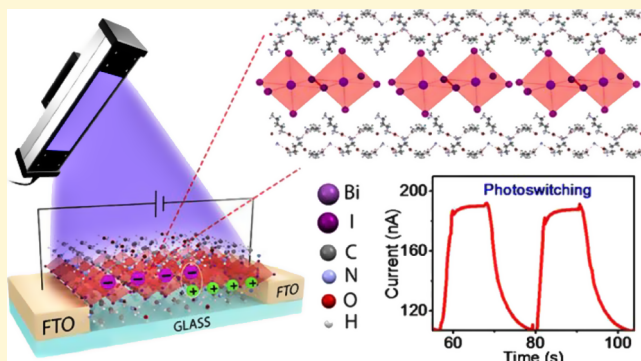
Hybrid perovskites have emerged as a unique semiconductor material for various optoelectronic device applications during the past few years.[1−3] Excellent properties such as long charge carrier diffusion length, low exciton binding energy, facile band gap tunability, and low-temperature solution processability made this material highly useful in these devices.[4−7] Nevertheless, poor stability under ambient conditions and toxicity of lead hampers their commercial usage.[8,9] Reports suggest that lower dimensional perovskites exhibit moisture tolerance to a great extent.[10−13] In order to address the toxicity issue, less toxic metal ions, such as Sn^{2+}, Bi^{3+}, Sb^{3+}, and so forth, having ns^2 electrons similar to Pb^{2+} were introduced into the perovskite structure.[14−16] Among them, tin-based materials are highly unstable due to the facile oxidation of the Sn^{2+} to Sn^{4+} state.[17] On the other hand, bismuth- and antimony-based zero-dimensional perovskites exhibited excellent moisture stability due to their rigid M$_2$X$_9^{3-}$ (M = metal, X = halogen) dimer units.[7] However, these dimer units are having a quantum dot structure with insulating organic cations as separators in all directions, resulting in poor electronic conductivity.[18]

It could be assumed that the creation of zero-dimensional perovskites with a quantum-well structure would exhibit improved electronic properties without compromising the stability aspects. This could be achieved by periodically aligning the inorganic dimer units in one of the three axes without the hindrance of the organic moieties. Keeping this in mind, in the present work, we have synthesized and characterized a novel, lead-free, zero-dimensional perovskite-like material, (PD)$_2$Bi$_2$I$_{10}$·2H$_2$O (PDBI, where PD is 1,3-propanediammonium). The Bi$_2$I$_{10}^{4-}$ dimers were formed by the edge sharing of BiI$_6^{3-}$ octahedra, and the organic cations formed independent layers sandwiching the inorganic structures. Photodetector devices were fabricated using PDBI, which showed consistent and repeatable photocurrent in several light on/off cycles, highlighting the material as a promising candidate for optoelectronic applications.

PDBI was prepared by treating PD iodide and bismuth-(III)iodide in the aqueous solution of hydrogen iodide at 90 °C for 3 h. The solution was filtered under hot conditions, and the filtrate was dried under vacuum, yielding the crude product as a red powder. Single crystals of PDBI were prepared by the antisolvent diffusion technique using methanol as the good solvent and chloroform as the poor solvent. Needle-like single

crystals having several millimeters of lengths were obtained (Figure S1a). The high-resolution transmission electron microscopy image showed a well-defined atomic lattice with a spacing of 1.3 Å (Figure S1b). Bright diffraction spots in the fast Fourier transform image indicated the high crystallinity of the material.

Structure characterization of PDBI was performed by single-crystal XRD analysis. The crystal system was found to be trigonal with the $P3_121$ space group (Figure 1a). Single crystals
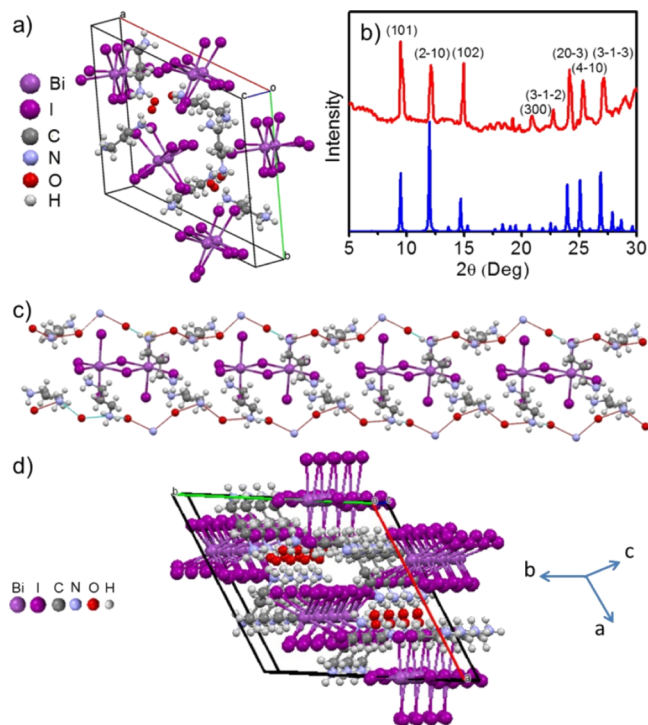

Figure 1. (a) Unit cell of PDBI; the crystal system is trigonal with the $P3_121$ space group. (b) Simulated (blue line) and experimental (red line) X-ray diffraction (XRD) patterns of PDBI obtained from the single crystal sample. (c) $Bi_2I_{10}^{4-}$ dimer layer sandwiched between the organic layers. (d) Crystal growth of PDBI along the crystallographic "c" axis. $Bi_2I_{10}^{4-}$ dimers are aligned in this direction without the hindrance of organic cations. The dimer $Bi_2I_{10}^{4-}$ is formed by the edge sharing of two BiI_6^{3-} octahedrons.

were powdered, and the measured powder XRD patterns were well matched with the simulated patterns obtained from single-crystal analysis (Figure 1b). The crystals have a preferential growth along the crystallographic a and b axes showing an intense characteristic peak around $2\theta = 12.5°$ corresponding to the $(2 −1\ 0)$ plane. Each $Bi_2I_{10}^{4-}$ dimer was formed by the edge sharing of two tilted BiI_6^{3-} octahedrons with two different bridging I−Bi−I bond lengths (3.19 and 3.25 Å). Previously reported bismuth- and antimony-based zero-dimensional perovskites such as $(CH_3NH_3)_3Bi_2I_9$, $(CH_3NH_3)_3Sb_2I_9$, $(NH_4)_3Bi_2I_9$, and $Cs_3Bi_2I_9$ are formed by the face sharing of octahedra.[19−22] In the present material, the BiI_6^{3-} octahedral units were separated by propane diammonium cations, which are connected through hydrogen bonding from water molecules (Figure 1c). Well-aligned inorganic units along the crystallographic "c" axis and the sandwiched organic cation layers on either side result in a quantum-well structure. Figure 1d provides the three-dimensional view of the quantum-well structure of PDBI. Compared to the distance between the

neighboring $Bi_2I_9^{3-}$ dimers in $(CH_3NH_3)_3Bi_2I_9$ (14.3 Å), the $Bi_2I_{10}^{4-}$ clusters in PDBI are separated by a distance of only 5.36 Å (Figure S2). This is beneficial to improve the electronic communication between the inorganic clusters in PDBI than that in the former. Water molecules in the PDBI structure are assumed to be trapped during the crystallization process because of the hygroscopic nature of the propane diammonium cation. The presence of water molecules was confirmed from the Fourier transform infrared spectroscopy analysis, which showed a broad O−H stretching frequency at 3500 cm^{-1} (Figure S3).

Further characterization of the material was carried out by Raman, UV−vis absorption, and fluorescence spectroscopy techniques. Intense Raman signals were observed from PDBI on excitation with a 785 nm laser source (Figure 2a). Peaks
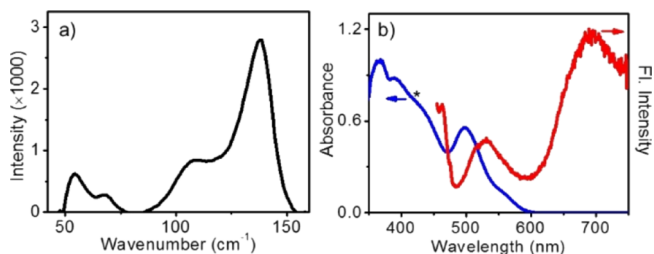
Figure 2. (a) Raman and (b) absorption (blue line) and emission (red line) spectra of PDBI on a glass substrate. The samples were excited at 785 nm for the Raman spectrum and at 425 nm for emission.

observed below 100 cm^{-1} corresponds to Bi−I bending vibrational modes, whereas peaks close to 100 and 150 cm^{-1} correspond to terminal Bi−I asymmetric and symmetric stretching modes, respectively, in the $Bi_2I_{10}^{4-}$ dimer units.[23] The powder samples of PDBI exhibited a broad absorption spectrum (Figure 2b, left) in the visible region ranging from 350 to 600 nm. A well-defined narrow excitonic peak was observed at 500 nm in the absorption spectrum. The emission spectrum of PDBI exhibited two peaks centered at 530 and 690 nm (Figure 2a, right). Similar emission features were observed for $(CH_3NH_3)_3Bi_2I_9$ also, which was attributed to the existence of direct and indirect band gaps in the material.[24]

Density functional theory (DFT)-based electronic structure calculations were performed to explore the optical properties of PDBI. The computed density of states (DOS) for the experimentally synthesized PDBI is shown in Figure 3a. DOS
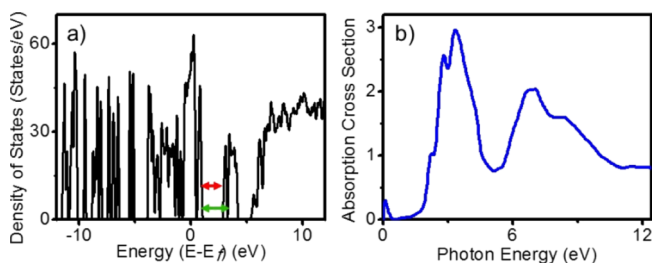
Figure 3. (a) Total DOSs plot for the calculated band structure of PDBI marked with arrows indicating lower (↔) and higher (↔) energy end of the split conduction band. (b) Calculated optical absorption spectra of PDBI from the single-crystal data. Peaks at 2.47, 2.95 and 3.58 eV correspond to electronic transitions from $^1S_0$ to $^3P_1$, $^3P_2$, and $^1P_1$ states, respectively.[25]

calculations revealed the presence of the split conduction band with a higher energy transition at 2.3 eV and a lower energy transition at 1.8 eV. These values were comparable with the experimentally observed direct and indirect band gap values deduced from the Tauc plot (Figure S4). Hence, the emission at 530 and 690 nm may be originated from the higher and lower energy ends of the split conduction band. The corresponding projected DOS is shown in Figure S5, which reveals the contribution of each atomic species to the total DOS and helps to find out which states are dominant near band gap. A significant contribution from iodine can be readily observed from the plot. A peak arising because of oxygen is also visible near the valence band maximum. A near conduction band minimum and hybridization between iodine and oxygen are also evident. The reflection of the DOSs calculations could be observed in the optical absorption spectrum as depicted in Figure 3b. We can observe the first optical peak near the lower photon energy range, which is corresponding to the water molecules coordinated with the organic layer. Two of the most prominent peaks are observed in the range of 2−4 eV, whereas the second most prominent absorption peak is observed between 6.5 and 7 eV. The nature of the optical absorption spectrum follows the similar trend as observed experimentally, depicted in Figure 2a, where one can observe the highest optical response around 250−620 nm.

The thermal and moisture stability of perovskites are important for its practical applications, which were evaluated using thermogravimetric analysis (TGA) and XRD analysis. The TGA revealed that the PDBI was thermally stable up to 284 °C; above this temperature, the propane diammonium cation was sublimed and resulted in weight loss (Figure S6). Moisture stability of the perovskite is related to its structural rigidity; here, the edge sharing of BiI_6^{3-} octahedra provides rigidity to the perovskite framework, which in turn provided better moisture tolerance to the material. XRD measurements were further confirmed that PDBI was stable under ambient conditions for weeks (Figure S7). Differential scanning calorimetry (DSC) analysis was performed for evaluating the phase stability of the material. An endothermic peak was observed in the first cycle at 90 °C due to the removal of the adsorbed water molecules from the sample, which was absent in the second and third DSC cycles (Figure S8). XRD analysis at 80 and 120 °C did not exhibit any apparent change in the XRD pattern, implying the excellent phase stability of the material (Figure S9).

Photodetectors that capture incident light (photons) and convert it to electrical signals instantaneously have many important applications including imaging, optical communication, remote control, chemical/biological sensing, and so on.[26] Very recently, hybrid perovskite materials found special attention for photodetector device application.[27−29] This could be attributed to the ability of hybrid perovskites to efficiently absorb the incident light even if the thickness of the film is only a few hundred nanometers. In such thin films, the photogenerated charge carriers need to travel only small distances resulting in a fast and efficient photoresponse. In order to evaluate the light harvesting and charge separation properties of PDBI, photodetector devices were fabricated using PDBI as the active layer. For this purpose, PDBI dissolved in dimethylformamide was spin-coated between the prepatterned fluorine-doped tin oxide (FTO) electrodes having an electrode separation of 0.5 cm and annealed at 110 °C for 10 min. The crystallites formed during film

formation had a rodlike morphology with several micrometers in size as evident from the topological scanning electron microscopy (SEM) image (Figure 4a). In order to avoid
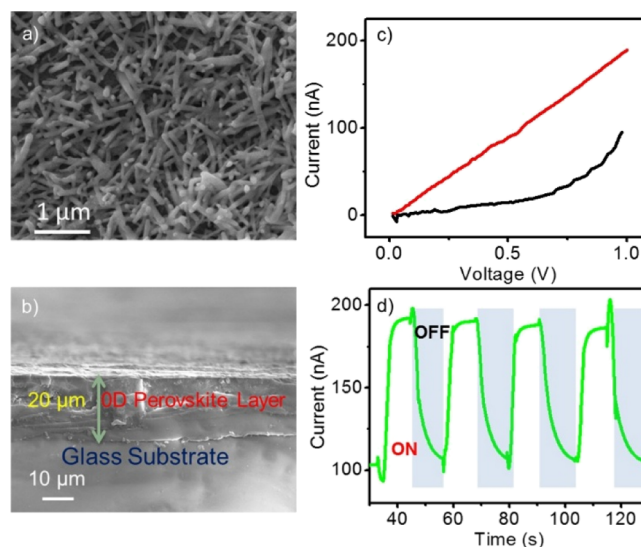
Figure 4. (a) Topographical SEM image of PDBI over a glass substrate. (b) Cross-sectional SEM image of a photodetector device fabricated using PDBI as the active layer. (c) I−V curves of the PDBI photodetector measured in dark (black line) and under illumination (red line). (d) Time-dependent photocurrent response of the PDBI photodetector under chopped light irradiation (365 nm; 350 μW/cm^2) at a bias voltage of 1 V showing no obvious attenuation after multiple cycles.

pinholes and to ensure the interconnectivity between the crystallites, thicker films were prepared. From the cross-sectional SEM analysis, the thickness of the PDBI layer was obtained as 20 μm (Figure 4b). The photoconductivity (I−V) measurements (dark and light) were carried out by illuminating the fabricated photodetector device with a 365 nm UV lamp (350 μW/cm^2; Spectroline model CM-10A) connected to a Keithley 2450 semiconductor characterization system.

On illumination, the photogenerated charge carriers on the surface need to be transported through the PDBI crystal grains and injected into the electrodes. Though the PDBI microcrystals carry a substantial amount of insulating propane diammonium chains, a lower bias voltage (1 V) was enough to overcome the energetic barrier for charge injection at the electrodes and initiate a charge transfer between adjacent microcrystals compared to the zero-dimensional $(CH_3NH_3)_3Sb_2I_9$ (3 V) and one-dimensional $(C_6H_{14}N_4)_3I_3BiI_6$ (5 V) perovskite-based photodetectors.[29,30] The above mentioned observation could be explained by the quantum-well structure of PDBI, which ensures better electronic dimensionality. In addition to that, the thin-film XRD pattern of PDBI over the glass substrate showed a preferential orientation along the (101) crystal plane (Figure S10); this plane is primarily composed of $Bi_2I_{10}^{4-}$ inorganic units which facilitate the interelectronic conduction between the $Bi_2I_{10}^{4-}$ dimers (Figure S11).

Under illumination, photogenerated charges at the PDBI surface were extracted to the electrodes to generate the signal. Therefore, a constant bias was applied to generate a potential, which separates electrons (e−) and holes (h+) to the injecting

electrodes. In the dark, the charge transport across grain boundaries occurs between the electrodes with an average distance of 0.5 cm due to the electric field of the applied voltage (Figure S12). In this device, the electronic conduction occurs exclusively through the PDBI crystallites because of the absence of any other charge-transporting layers. The device exhibited 194 nA photocurrent and 94 nA dark current as shown in the $I-V$ curves (Figure 4c). The high dark current in our device is attributed to the injection of charge carriers from the FTO electrodes because of the absence of electron-/hole-blocking layers.[31] The nonlinear $I-V$ curve in the dark implies a Schottky contact at the FTO/PDBI interface.[30] However, the devices exhibited an ohmic contact under illumination, which was beneficial for efficient charge collection at the electrodes. The on/off ratio of the PDBI photodetector was calculated from light (194 nA) and dark current (94 nA) measurements as 2.1, which is comparable with the on/off ratio of one-dimensional perovskites reported in the literature such as $(C_6H_{13}N)_2BiI_5$ (on/off ratio = 2.9) and $(N,N,N',N'$-tetramethyl-piperazine$)_{1.5}[Bi_2I_7Cl_2]$ (on/off ratio = 3).[32,33] The responsivity of the device was obtained as 1.14 mA/W. In addition to the responsivity, other important figures of merits for the photodetector devices are specific detectivity and the number of electrons probed per incident photon (external quantum efficiency). For PDBI, these parameters were estimated to be 1.9×10^6 Jones and 0.4%, respectively. More importantly, the photocurrent was consistent and repeatable over several photoswitching cycles (Figure 4d).

Properties of PDBI described above and the comparison of that with other lead-free, zero-dimensional perovskite revealed that the former is an excellent candidate for optoelectronic device applications. Study of Irvine et al. with $(CH_3NH_3)_3Bi_2I_9$ perovskites is particularly important in this context.[18] Organic cations of this material separate the $Bi_2I_9{}^{3-}$ moiety by a distance of 14.3 Å, which results in a core−shell quantum dot structure. This hinders the particle−particle electronic communication resulting in poor optoelectronic performances. On the other hand, the "quantum-well" structure of PDBI brings the $Bi_2I_{10}{}^{4-}$ dimer units to a close proximity of 5.36 Å enabling better interinorganic cluster electronic communication. Excellent photoresponse properties comparable to that of one-dimensional perovskites reiterated this aspect.

In conclusion, we have synthesized and characterized a novel, lead-free, zero-dimensional perovskite-like material consisting of $Bi_2I_{10}{}^{4-}$ dimers formed by the edge sharing of $BiI_6{}^{3-}$ octahedra. This material exhibited excellent photo-absorption and environmental stability. Experimentally observed optical properties of PDBI are in accordance with the DFT calculations. The thin-film photodetector fabricated using PDBI showed consistent and repeatable photocurrent in several light on/off cycles under a low bias voltage. This work may open up a new direction in crystal engineering of zero-dimensional, lead-free perovskites to improve the optoelectronic properties for advanced device applications.

ASSOCIATED CONTENT

$\mathbf{S}$ Supporting Information

The Supporting Information is available free of charge on the ACS Publications website at DOI: 10.1021/acs.chemmater.8b04642.

Experimental and synthetic procedures and stability studies (PDF)

Crystallographic (refinement) data and additional crystal structures (CIF)

AUTHOR INFORMATION

Corresponding Author
*E-mail: cvijayakumar@niist.res.in.

ORCID
Sudip Chakraborty: 0000-0002-6765-2084
Chakkooth Vijayakumar: 0000-0001-5347-6799

Author Contributions
The manuscript was written through contributions of all the authors. All the authors have given approval to the final version of the manuscript

Notes
The authors declare no competing financial interest.

REFERENCES

(1) Manser, J. S.; Christians, J. A.; Kamat, P. V. Intriguing Optoelectronic Properties of Metal Halide Perovskites. *Chem. Rev.* **2016**, *116*, 12956−13008.

(2) Saparov, B.; Mitzi, D. B. Organic-Inorganic Perovskites: Structural Versatility for Functional Materials Design. *Chem. Rev.* **2016**, *116*, 4558−4596.

(3) Li, W.; Wang, Z.; Deschler, F.; Gao, S.; Friend, R. H.; Cheetham, A. K. Chemically Diverse and Multifunctional Hybrid Organic-Inorganic Perovskites. *Nat. Rev. Mater.* **2017**, *2*, 16099.

(4) Sutherland, B. R.; Sargent, E. H. Perovskite Photonic Sources. *Nat. Photonics* **2016**, *10*, 295−302.

(5) Brenner, T. M.; Egger, D. A.; Kronik, L.; Hodes, G.; Cahen, D. Hybrid Organic—inorganic Perovskites: Low-Cost Semiconductors with Intriguing Charge-Transport Properties. *Nat. Rev. Mater.* **2016**, *1*, 15007.

(6) Muthu, C.; Agarwal, S.; Vijayan, A.; Hazra, P.; Jinesh, K. B.; Nair, V. C. Hybrid Perovskite Nanoparticles for High-Performance Resistive Random Access Memory Devices: Control of Operational Parameters through Chloride Doping. *Adv. Mater. Interfaces* **2016**, *3*, 1600092.

(7) Pious, J. K.; Lekshmi, M. L.; Muthu, C.; Rakhi, R. B.; Nair, V. C. Zero-Dimensional Methylammonium Bismuth Iodide-Based Lead-Free Perovskite Capacitor. *ACS Omega* **2017**, *2*, 5798−5802.

(8) Shi, Z.; Guo, J.; Chen, Y.; Li, Q.; Pan, Y.; Zhang, H.; Xia, Y.; Huang, W. Lead-Free Organic-Inorganic Hybrid Perovskites for Photovoltaic Applications: Recent Advances and Perspectives. *Adv. Mater.* **2017**, *29*, 1605005.

(9) Khazaee, M.; Sardashti, K.; Sun, J.-P.; Zhou, H.; Clegg, C.; Hill, I. G.; Jones, J. L.; Lupascu, D. C.; Mitzi, D. B. A Versatile Thin-Film Deposition Method for Multidimensional Semiconducting Bismuth Halides. *Chem. Mater.* **2018**, *30*, 3538−3544.

(10) Tsai, H.; Nie, W.; Blancon, J.-C.; Stoumpos, C. C.; Asadpour, R.; Harutyunyan, B.; Neukirch, A. J.; Verduzco, R.; Crochet, J. J.; Tretiak, S.; Pedesseau, L.; Even, J.; Alam, M. A.; Gupta, G.; Lou, J.; Ajayan, P. M.; Bedzyk, M. J.; Kanatzidis, M. G.; Mohite, A. D. High-Efficiency Two-Dimensional Ruddlesden-Popper Perovskite Solar Cells. *Nature* **2016**, *536*, 312−316.

(11) Lu, Y.-B.; Guan, C.; sun, H.; Cong, W.-Y.; Yang, H.; Zhang, P. Investigation on Enhanced Moisture Resistance of Two-Dimensional Layered Hybrid Organic-Inorganic Perovskites (C4H9NH3)2PbI4. *J. Phys. Chem. C* **2018**, *122*, 11862−11869.

(12) Tsai, H.; Nie, W.; Blancon, J. C.; Stoumpos, C. C.; Soe, C. M. M.; Yoo, J.; Crochet, J.; Tretiak, S.; Even, J.; Sadhanala, A. Stable Light-Emitting Diodes Using Phase-Pure Ruddlesden−Popper Layered Perovskites. *Adv. Mater.* **2018**, *30*, 1704217.

(13) Zhang, X.; Ren, X.; Liu, B.; Munir, R.; Zhu, X.; Yang, D.; Li, J.; Liu, Y.; Smilgies, D.-M.; Li, R.; Yang, Z.; Niu, T.; Wang, X.; Amassian, A.; Zhao, K.; Liu, S. Stable High Efficiency Two-Dimensional Perovskite Solar Cells via Cesium Doping. *Energy Environ. Sci.* **2017**, *10*, 2095−2102.

(14) Noel, N. K.; Stranks, S. D.; Abate, A.; Wehrenfennig, C.; Guarnera, S.; Haghighirad, A.-A.; Sadhanala, A.; Eperon, G. E.; Pathak, S. K.; Johnston, M. B.; Petrozza, A.; Herz, L. M.; Snaith, H. J. Lead-free organic-inorganic tin halide perovskites for photovoltaic applications. *Energy Environ. Sci.* **2014**, *7*, 3061−3068.

(15) Abulikemu, M.; Ould-Chikh, S.; Miao, X.; Alarousu, E.; Murali, B.; Ngongang Ndjawa, G. O.; Barbé, J.; El Labban, A.; Amassian, A.; Del Gobbo, S. Optoelectronic and Photovoltaic Properties of the Air-Stable Organohalide Semiconductor $(CH_3NH_3)_3Bi_2I_9$. *J. Mater. Chem. A* **2016**, *4*, 12504−12515.

(16) Hebig, J.-C.; Kühn, I.; Flohre, J.; Kirchartz, T. Optoelectronic Properties of $(CH_3NH_3)_3Sb_2I_9$ Thin Films for Photovoltaic Applications. *ACS Energy Lett.* **2016**, *1*, 309−314.

(17) Wang, A.; Guo, Y.; Muhammad, F.; Deng, Z. Controlled Synthesis of Lead-Free Cesium Tin Halide Perovskite Cubic Nanocages with High Stability. *Chem. Mater.* **2017**, *29*, 6493−6501.

(18) Ni, C.; Hedley, G.; Payne, J.; Svrcek, V.; McDonald, C.; Jagadamma, L. K.; Edwards, P.; Martin, R.; Jain, G.; Carolan, D.; Mariotti, D.; Maguire, P.; Samuel, I.; Irvine, J. Charge Carrier Localised in Zero-Dimensional $(CH_3NH_3)_3Bi_2I_9$ clusters. *Nat. Commun.* **2017**, *8*, 170.

(19) Zhang, Z.; Li, X.; Xia, X.; Wang, Z.; Huang, Z.; Lei, B.; Gao, Y. High-Quality $(CH_3NH_3)_3Bi_2I_9$ Film-Based Solar Cells: Pushing Efficiency up to 1.64%. *J. Phys. Chem. Lett.* **2017**, *8*, 4300−4307.

(20) Boopathi, K. M.; Karuppuswamy, P.; Singh, A.; Hanmandlu, C.; Lin, L.; Abbas, S. A.; Chang, C. C.; Wang, P. C.; Li, G.; Chu, C. W. Solution-Processable Antimony-Based Light-Absorbing Materials beyond Lead Halide Perovskites. *J. Mater. Chem. A* **2017**, *5*, 20843−20850.

(21) Sun, S.; Tominaka, S.; Lee, J. H.; Xie, F.; Bristowe, P. D.; Cheetham, A. K. Synthesis, Crystal Structure, and Properties of a Perovskite-Related Bismuth Phase, $(NH_4)_3Bi_2I_9$. *APL Mater.* **2016**, *4*, 031101.

(22) Park, B.-W.; Philippe, B.; Zhang, X.; Rensmo, H.; Boschloo, G.; Johansson, E. M. J. Bismuth Based Hybrid Perovskites $A_3Bi_2I_9$ (A: Methylammonium or Cesium) for Solar Cell Application. *Adv. Mater.* **2015**, *27*, 6806−6813.

(23) McCall, K. M.; Stoumpos, C. C.; Kostina, S. S.; Kanatzidi, M. G.; Wessels, B. W. Strong Electron−Phonon Coupling and Self-Trapped Excitons in the Defect Halide Perovskites $A_3M_2I_9$ (A = Cs, Rb; M = Bi, Sb). *Chem. Mater.* **2017**, *29*, 4129−4145.

(24) Hoye, R. L. Z.; Brandt, R. E.; Osherov, A.; Stevanovic, V.; Stranks, S. D.; Wilson, M. W. B.; Kim, H.; Akey, A. J.; Perkins, J. D.; Kurchin, R. C. Methylammonium Bismuth Iodide as a Lead-Free, Stable Hybrid Organic-Inorganic Solar Absorber. *Chem.—Eur. J.* **2016**, *22*, 2605−2610.

(25) Ran, C.; Wu, Z.; Xi, J.; Yuan, F.; Dong, H.; Lei, T.; He, X.; Hou, X. Construction of Compact Methylammonium Bismuth Iodide Film Promoting Lead-Free Inverted Planar Heterojunction Organohalide Solar Cells with Open-Circuit Voltage over 0.8 V. *J. Phys. Chem. Lett.* **2017**, *8*, 394−400.

(26) García de Arquer, F. P.; Armin, A.; Meredith, P.; Sargent, E. H. Solution-processed semiconductors for next-generation photodetectors. *Nat. Mater.* **2017**, *2*, 16100.

(27) Tong, X.-W.; Kong, W.-Y.; Wang, Y.-Y.; Zhu, J.-M.; Luo, L.-B.; Wang, Z.-H. High-Performance Red-Light Photodetector Based on

Lead-Free Bismuth Halide Perovskite Film. *ACS Appl. Mater. Interfaces* **2017**, *9*, 18977−18985.

(28) Ji, C.; Wang, P.; Wu, Z.; Sun, Z.; Li, L.; Zhang, J.; Hu, W.; Hong, M.; Luo, J. Inch-Size Single Crystal of a Lead-Free Organic−Inorganic Hybrid Perovskite for High-Performance Photodetector. *Adv. Funct. Mater.* **2018**, *28*, 1705467.

(29) Zhang, W.; Liu, X.; Li, L.; Sun, Z.; Han, S.; Wu, Z.; Luo, J. Triiodide-Induced Band-Edge Reconstruction of a Lead-Free Perovskite-Derivative Hybrid for Strong Light Absorption. *Chem. Mater.* **2018**, *30*, 4081−4088.

(30) Yang, B.; Li, Y. J.; Tang, Y. X.; Mao, X.; Luo, C.; Wang, M. S.; Deng, W. Q.; Han, K. L. Constructing Sensitive and Fast Lead-Free Single-Crystalline Perovskite Photodetectors. *J. Phys. Chem. Lett.* **2018**, *9*, 3087−3092.

(31) Wang, H.; Kim, D. H. Perovskite-based photodetectors: materials and devices. *Chem. Soc. Rev.* **2017**, *46*, 5204−5236.

(32) Zhang, W.; Tao, K.; Ji, C.; Sun, Z.; Han, S.; Zhang, J.; Wu, Z.; Luo, J. $(C_6H_{13}N)_2BiI_5$: A One-Dimensional Lead-Free Perovskite-Derivative Photoconductive Light Absorber. *Inorg. Chem.* **2018**, *57*, 4239−4243.

(33) Li, M.-Q.; Hu, Y.-Q.; Bi, L.-Y.; Zhang, H.-L.; Wang, Y.; Zheng, Y.-Z. Structure Tunable Organic-Inorganic Bismuth Halides for an Enhanced Two-Dimensional Lead-Free Light-Harvesting Material. *Chem. Mater.* **2017**, *29*, 5463−5467.

Bismuth-Based Zero-Dimensional Perovskite-like Materials: Effect of Benzylammonium on Dielectric Confinement and Photoconductivity

Johnpaul K. Pious, Chinnadurai Muthu, Selgiya Dani, Akinori Saeki, and Chakkooth Vijayakumar*

ACCESS | Metrics & More | Article Recommendations | SI Supporting Information

ABSTRACT: Bismuth-based perovskite-like materials are considered as promising alternatives to lead-based perovskites for optoelectronic applications. However, the major drawbacks of these materials are high exciton binding energy and poor charge-carrier separation efficiency. These issues are attributed to the strong quantum and dielectric confinements associated with these materials. In this work, we have used a simple methodology to reduce the dielectric confinement in hybrid $A_3Bi_2I_9$ type perovskite-like materials (A is an organic cation) to improve the charge-carrier separation efficiency. For that, the electronically inert methylammonium (MA) was replaced with a polarizable benzylammonium (BA) cation in the well-studied $MA_3Bi_2I_9$ (MBI) structure. The single-crystal X-ray diffraction (XRD) and ultraviolet−visible (UV−vis) absorption spectroscopy analyses suggested similar quantum confinement in both $(BA)_3Bi_2I_9$ (BBI) and MBI materials. This enabled us to precisely investigate the role of polarizable benzylammonium cations in the dielectric confinement in BBI. Flash-photolysis time-resolved microwave conductivity studies revealed about 2.5-fold enhancement of $\varphi\sum\mu$ (the product of charge-carrier generation quantum yield and the sum of charge-carrier mobilities) for BBI when compared to that of MBI, which is attributed to the low dielectric confinement in the former.
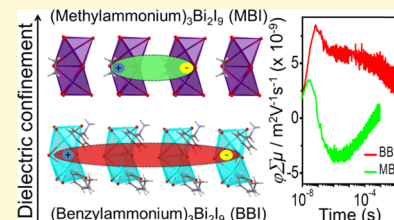
L ead-free perovskites are currently receiving intense research interest for optoelectronic device applications due to less toxicity and better moisture stability compared to the lead-based analogues.[1−3] Bismuth-based perovskite-like materials having a general formula of $A_3Bi_2I_9$ is a promising class of materials in this context. Due to the presence of ns^2 electrons in their structure, these materials are known to exhibit p−p electronic transition yielding a high molar extinction coefficient.[4] Moreover, these electrons could screen the charged defect sites in the structure, resulting in long charge-carrier lifetimes.[5] However, the major drawbacks of bismuth-based perovskites are high exciton binding energy and poor charge-carrier separation efficiency due to strong quantum and dielectric confinements. Quantum confinement in perovskites is related to their size and dimensionality, whereas dielectric confinement arises from the mismatch of dielectric permittivity of the inorganic framework and the organic counterparts. The dielectric mismatch leads to an "image charge effect" resulting in bound excitons with low mobility.[6,7] Since these materials have zero-dimensional crystal structures, the density of states will be discrete at the band edges due to its strong quantum confinement, which leads to high exciton binding energy.[8] Most of the $A_3Bi_2I_9$ structures reported so far consist of organic spacers with low dielectric constants having high dielectric confinement. Coupled with strong quantum confinement, these perovskite-like structures exhibit poor optoelectronic performances.

To address the quantum confinement bottleneck, the dimensionality of bismuth-based perovskites was increased from zero-dimensional (0D) to three-dimensional (3D), which

resulted in the improvement in photovoltaic performance.[2,9,10] In this context, we have recently reported that the quantum confinement in 0D bismuth perovskites could be reduced by enhancing the inter-inorganic cluster electronic coupling.[11] We observed that the quantum-well arrangement of inorganic clusters ($Bi_2I_{10}^{4-}$) in $PD_2Bi_2I_{10}$ (PD: propanediammonium) resulted in the formation of delocalized excitons. This enabled the separation of the excitons into free charge carriers at a voltage as low as 1 V. Recent reports from various groups suggest that dielectric confinement is as important as quantum confinement in determining the exciton binding energy of perovskites.[12,13] Although quantum confinement and its modulation in bismuth-based zero-dimensional perovskites were well-studied, research on dielectric confinement in such systems is still elusive. However, dielectric confinement in lead and tin-based two-dimensional (2D) perovskites were studied in detail. For example, Ishihara and co-workers observed low exciton binding energy for $(PEA)_2[PbI_4]$ due to low dielectric confinement $(PEA = C_6H_5(CH_2)_2NH_3^+)$.[14] This was attributed to the greater polarizability of the aromatic groups in the organic layers, compared to alkyl groups. Zhang's and Wu's groups have reported the improvement in the conductivity of
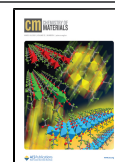
perovskite quantum dots using benzylamine and 3-phenyl-2-propen-1-amine as the capping ligands.[15,16] This conductivity enhancement was an outcome of the delocalization of the electronic wave function over the quantum dots via the aromatic ligands. Chen and co-workers revealed that aromatic polarizable cations could lower the dielectric confinement yielding efficient exciton dissociation in 2D tin-based perovskites.[12] This was further supported by the reports from Zeng's and Sargent's groups in 2D lead-based perovskites; they suggested that lowering of dielectric confinement forms a type-II band alignment, which facilitates efficient exciton dissociation.[17,18]

The above-mentioned reports imply that polar aromatic organic spacers are good candidates for reducing the exciton binding energy in low-dimensional perovskites by lowering the dielectric confinement. However, the "A" site organic cations have a significant structure-directing ability on bismuth-based $A_3Bi_2I_9$-type perovskites, and hence, it is challenging to incorporate a polarizable organic spacer at that site without distorting the crystal structure. In the present work, we have achieved this by introducing the aromatic benzylammonium (BA) cations via crystal engineering. The novel perovskite material we developed has the formula $BA_3Bi_2I_9$ (BBI). Both BBI and the well-studied methylammonium (MA) analogue, $(CH_3NH_3)_3Bi_2I_9$ (MBI), perovskites are isostructural. This enabled us to precisely investigate the role of the benzylammonium cation in the dielectric confinement in BBI.
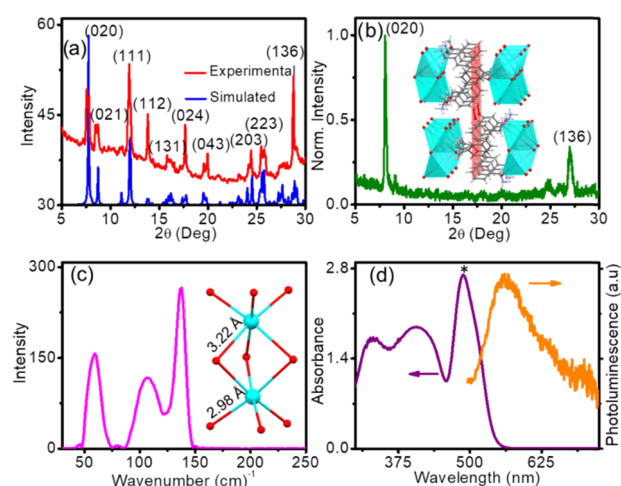
The single crystals of BBI were synthesized by the solvent layering technique. Briefly, BiI_3 in 57% aq. hydrogen iodide (HI) and benzylammonium iodide in methanol were carefully taken in a glass vial as separate layers and single crystals were formed by the slow reaction at the sharp interface of the two solutions. Millimeter-sized rod-shaped crystals were formed after several hours (Figure 1a,b). The interatomic plane distance of BBI was calculated from the high-resolution transmission electron microscopy (HRTEM) analysis as 0.44 nm (Figure 1c). The bright diffraction spots in the fast Fourier transform (FFT) image indicate high crystallinity of the
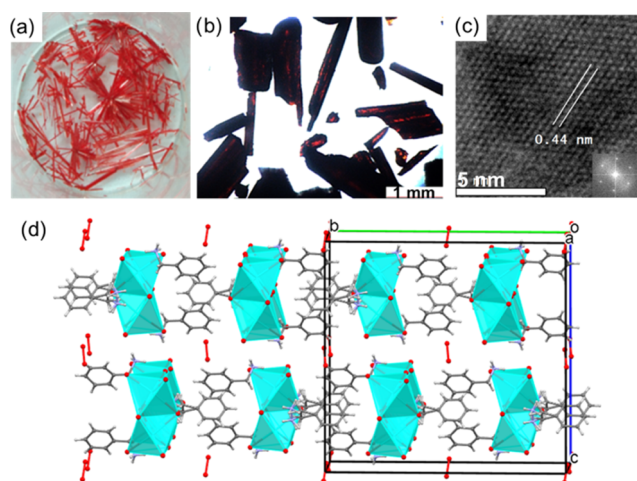
material. The single-crystal X-ray diffraction (SCXRD) measurement was done at room temperature, but crystal structure refinement was not possible due to the poor electron density in the organic part. Subsequently, the crystal structure was resolved through SCXRD analysis at 180 K. The unit cell of BBI represents a monoclinic crystal system with a $C2/c$ space group (Figure 1d). BBI belongs to the category of zero-dimensional perovskites due to the isolated nature of $Bi_2I_9^{3-}$ bi-octahedra. As the crystal structure shows, these bi-octahedral units are formed by face sharing of two BiI_6^{3-} octahedra. It was also observed that HI molecules are trapped in the crystal structure of BBI. SCXRD analysis also proved that BBI is isostructural compared with MBI (Figure S1);[19] both BBI and MBI consist of $Bi_2I_9^{3-}$ bi-octahedra surrounded by benzylammonium and methylammonium cations, respectively. Similar quantum confinement is expected in both MBI and BBI materials because the thickness of $Bi_2I_9^{3-}$ inorganic layers is the same in both the materials ($n = 2$ along the "b" axis, where "n" is the no. of octahedra). In BBI, the benzylammonium cations adopted an edge-to-face arrangement making an angle of 71.92° with a minimum separation distance of 3.26 Å. This enables an edge−face $\pi-\pi$ stacking of benzylammonium cations. This self-assembly of benzylammonium cations in the "ac" crystallographic plane brings the $Bi_2I_9^{3-}$ bi-octahedra to a close proximity of 4.13 Å along the crystallographic "a" axis. Importantly, the tight packing of inorganic units provides structural rigidity to the BBI perovskite framework.

The powder X-ray diffraction (XRD) pattern of BBI is comparable with the simulated one obtained from the SCXRD analysis (Figure 2a), which indicates the phase purity of the powder samples. XRD analysis of thin films over fluorine-doped tin oxide (FTO) substrates revealed a preferential orientation of BBI crystallites along the (020) crystallographic plane (Figure 2b). Interestingly, this crystallographic plane is

Figure 1. (a) Photograph and (b) optical polarization microscope image of BBI single crystals. (c) High-resolution transmission electron microscopic image of the BBI thin film. The corresponding fast Fourier transform image in the inset. (d) Three-dimensional crystallographic packing of BBI obtained from single-crystal X-ray diffraction analysis. The unit cell is represented with the crystallographic axes a, b, and c.

Figure 2. (a) Comparison of the experimental XRD pattern of crushed BBI crystals and simulated XRD patterns obtained from the single-crystal analysis. (b) Thin-film XRD of BBI coated over the FTO substrate; the inset showing the preferentially oriented (020) plane. (c) Raman spectrum of BBI crystals upon 785 nm laser excitation. The inset shows the $Bi_2I_9^{3-}$ dimer units labeled with two different Bi−I bond lengths, 2.98 and 3.22 Å. (d) Absorption and emission spectra of BBI thin films coated over FTO substrates. The asterisk indicates the excitonic peak corresponding to the $^1S_0-^3P_1$ electronic transition.

composed of benzylammonium cations. This implies that the organic part is playing a major role in the assembly of perovskite crystallites. In other words, our observation proved that the growth and orientation of perovskite crystallites can be controlled by the rational selection of organic cations. Further control over the packing could be achieved using organic chromophores with strong $\pi-\pi$ stacking abilities.

We also observed that BBI thin films obtained via single-step solution processing on FTO substrates exhibited better uniform coverage (Figures S2 and S3) than that of MBI. This would be beneficial for fabricating devices for optoelectronic applications. The Raman spectrum of BBI crystals was recorded at 785 nm laser excitation (Figure 2c). The peak at 50 cm^{-1} corresponds to the bending vibrations of the Bi−I bridging bond and the peaks close to 100 and 150 cm^{-1} are attributed to the asymmetric and symmetric stretching vibrations of the terminal Bi−I bonds, respectively.[20] The thermal stability of BBI was evaluated using thermogravimetry, which revealed that BBI is thermally stable up to 250 °C and further heating resulted in the sublimation of the organic component (Figure S4). Phase stability of the material was monitored by differential scanning calorimetry (DSC) analysis. It exhibited excellent phase stability up to 250 °C without showing any endo/exothermic peaks during the temperature scans (Figure S5).

The optical properties of BBI were studied using UV−visible absorption and fluorescence spectroscopy (Figure 2d). The absorption spectrum is spanning from the UV region up to 550 nm with a well-defined excitonic peak at 490 nm corresponding to $^1S_0-^3P_1$ electronic transition.[21] The sharp excitonic peak indicates strong quantum confinement in BBI. The optical band gap of the material was calculated from the Tauc plot as 2.34 eV (Figure S6). BBI exhibited weak photoluminescence (PL) with an emission maximum at 560 nm (2.21 eV). Since the emission maximum is close to the excitonic absorption peak and from the narrow emission feature, it could be assumed as excitonic emission.[22] The small Stokes shift between the optical band gap and emission maximum in BBI is a piece of evidence for its low exciton binding energy.[3] Exciton nonlocality effects[23] on the position of the PL maximum of BBI could be ruled out due to strong quantum confinement in BBI as a result of relatively large inter-inorganic cluster separation (4.13 Å; Figure S7). From the optical band gap and PL maximum, the exciton binding energy of BBI at room temperature was estimated as 130 meV.

To compare the optical properties of BBI and MBI, we have synthesized the single crystals of MBI (Figure S8a). Similar to BBI, MBI also exhibited a well-defined band edge excitonic absorption peak at 490 nm corresponding to the $^1S_0-^3P_1$ electronic transition occurring in their $Bi_2I_9^{3-}$ clusters (Figure S8b). We have calculated the band gap of MBI as 2.26 eV from the Tauc plot (Figure S8c), which is comparable with previous reports.[19,24] The excitonic emission from MBI was observed at 620 nm (2 eV; Figure S8b). Thus, the exciton binding energy for MBI was calculated as 260 meV. This is also comparable with previous reports.[24−26] The lower exciton binding energy of BBI compared to that of MBI could be attributed to the weak dielectric confinement in the former due to the effective screening of Coulomb's interaction induced by the polarizable organic spacer present in it.[27] This can result in facile dissociation of excitons into charge carriers. In other words, higher photoconductivity can be expected in BBI than that in MBI.

To validate the above-mentioned point, we have performed flash-photolysis time-resolved microwave conductivity (FP-TRMC) analysis. TRMC measurement is an excellent electrode-less technique to gain insight into the photo-generated charge-carrier mobility and its dynamics of functional materials.[28−30] For the TRMC measurements, the powdered single crystals of BBI and MBI were excited using a 355 nm laser and transient photoconductivity was probed using microwave radiation. The product of mobility ($\sum \mu$) and dissociation yield of charge carriers at the end-of-pulse (φ) for BBI (8.4×10^{-9} m^2/V s) was about 2.5-fold higher than that for MBI (3.3×10^{-9} m^2/V s, Figure 3), which is a direct piece
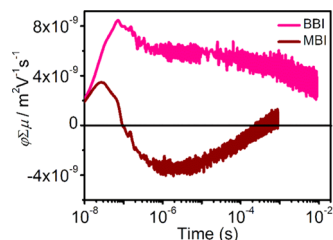
Figure 3. Product of TRMC mobility and yield dissociation of free charges as a function of time for BBI and MBI powder samples.

of evidence of a larger charge-carrier mobility and/or the facile dissociation of excitons into free charge carriers in BBI compared to MBI.[31] The lower $\varphi \sum \mu$ value of MBI could be attributed to the presence of bound excitons, which does not separate into free charge carriers and contribute to the TRMC signal intensity. This was further supported by the anomalous TRMC signal transition of MBI from positive to negative with time. This is due to the decrease in the dielectric permittivity of MBI upon photoexcitation. In detail, methylammonium dipoles are disordered in the ground state of MBI, which leads to a high dielectric permittivity of 7.94 μC/cm^2.[32] Upon photoexcitation, the localized excitons will restrict the free rotation of methylammonium cations and subsequently reduce the dielectric permittivity of the material. This dielectric permittivity change resulted in the unusual TRMC signal for MBI. A similar anomalous TRMC signal transition in the case of MAPb$_{1-x}$Sn$_x$X$_3$ (x = 0−1, X = I and Br) perovskites was reported recently.[33] In contrast, the higher and long-lived TRMC signal for BBI is due to the facile dissociation of excitons into free charge carriers. This could be attributed to the lower dielectric confinement in BBI. The C≡C bonds in benzylammonium are more polarizable than the C−H bond in methylammonium. As a result, benzylammonium could reduce the dielectric confinement in BBI compared with the methylammonium in MBI.

In summary, we have successfully synthesized and characterized a novel lead-free zero-dimensional perovskite material that consists of isolated $Bi_2I_9^{3-}$ bi-octahedra separated by benzylammonium cations. Comparable quantum confinement was observed for both BBI and MBI materials due to their identical structural dimensionality (0D). The polarizable benzylammonium cations in BBI reduced the dielectric mismatch between the inorganic $Bi_2I_9^{3-}$ clusters and their organic counterpart. From the TRMC studies, the higher product of mobility and yield dissociation of charge carriers for BBI compared to MBI revealed that the benzylammonium cation induced low dielectric confinement in BBI. More importantly, we have also proved that it is possible to control

the packing orientation of hybrid perovskite materials with the rational choice of organic cations. This would have far-reaching implications on the design and synthesis of tailor-made hybrid perovskites for functional applications.

■ EXPERIMENTAL SECTION

Chemicals. Bismuth (III) iodide (99.9%, Sigma-Aldrich), benzylamine (98%, Spectrochem), hydriodic acid (57 wt % in H_2O, 99.95%, Sigma-Aldrich), dichloromethane (99.0%, Merck), and methanol (99.7%, Merck) were used without any further purification.

Synthesis of Benzylammonium Iodide. Benzylamine (3 mL, 27.4 mmol, 1 equiv) was taken in an RB flask, and 57% aq hydriodic acid (4.62 mL, 102.9 mmol, 3.75 equiv) was added to it at 0 °C with constant stirring for an hour. A white precipitate of benzylammonium iodide was formed, which was then purified by dissolving in a minimum amount of ethanol followed by reprecipitation using diethyl ether.

Preparation of $(BA)_3Bi_2I_9 \cdot HI$ Single Crystals. Single crystals of $BA_3Bi_2I_9 \cdot HI$ were prepared by the solvent layering technique using a 57% aqueous hydriodic acid solution of BiI_3 (60 mg, 1 mmol, 2 equiv) and methanol solution of benzylammonium iodide (36 mg, 1.5 mmol, 3 equiv) in a glass vial. Red, block-shaped crystals were formed at the interface of the two solutions by a slow reaction.

Preparation of $(MA)_3Bi_2I_9$ Single Crystals. BiI_3 (589.69 mg, 1 mmol, 2 equiv) and methylammonium iodide (238 mg, 1.5 mmol, 3 equiv) were dissolved in 1 mL of dimethylformamide (DMF) and immersed in a 100 mL beaker containing chloroform, and the mouth of the beaker was covered with parafilm. Dark, red single crystals of $(MA)_3Bi_2I_9$ were formed after several days.

Characterization Methods. Electronic absorption spectra were recorded on a Shimadzu UV-2600 ultraviolet−visible (UV−vis) spectrophotometer. The measurement was made in the reflectance mode. Using the Kubelka−Munk function, the reflectance spectrum was converted into absorption spectra. Emission spectra were recorded on a SPEX-Fluorolog spectrofluorimeter. X-ray diffraction studies were carried out on powder samples with Xeuss Simultaneous 2D WAXs/SAXs using Cu Kα radiation (λ = 1.5418 Å). The single-crystal diffraction data were collected on a Bruker AXS Smart Apex CCD diffractometer at 180 K. The data were deduced using SAINTPLUS, and an empirical absorption correction was applied using the SADABS program. The crystal structure was solved by direct methods using SHELXS97 and refined using SHELXL97 present in SHELXTL V6.14. Full-matrix least-squares structure refinement against F^2 was carried out using the WINGX package of programs. Thermogravimetric analysis (TGA) was done using TA Q50 under a nitrogen gas atmosphere at a heating rate of 10 °C/min. Differential scanning calorimetric (DSC) measurements were carried out using a TA Instrument DSC Q2000 model equipped with a refrigerated cooling system. The powdered $(BA)_3Bi_2I_9 \cdot HI$ crystals were heated from room temperature to 700 °C at a heating rate of 10 °C/min, under a nitrogen atmosphere. Raman spectroscopic measurements were carried out in a WITec Raman microscope (WITec Inc. Germany, α 300R) with a laser beam directed to the sample through 20x objective and a Peltier cooled CCD detector. Samples were excited with a 785 nm excitation wavelength laser, and Stokes-shifted Raman spectra were collected in the range of 0−250 cm^{-1} with 1 cm^{-1} resolution. Prior to every measurement, calibration with a silicon standard was performed. The WITec Project plus (v2.1) software package was used for data evaluation. Transient conductivity was measured by the flash-photolysis time-resolved microwave conductivity (FP-TRMC) technique. A resonant cavity was used to obtain a high degree of sensitivity in the measurement. The resonant frequency and the microwave power were set at 9.1 GHz and 3 mW, respectively, so that the electric field of the microwave was sufficiently small and does not disturb the motion of charge carriers. The value of conductivity is converted into the product of the quantum yield (φ) and the sum of charge-carrier mobilities ($\sum \mu$), by the following equation

$$\varphi \sum \mu = \frac{1}{eAI_0 F_{\text{light}}} \times \frac{\Delta P_{\text{r}}}{P_{\text{r}}}$$

where e, A, I_0, F_{light}, ΔP_{r}, and P_{r} are the unit charge of a single electron, the sensitivity factor $[(S \, m^{-1})^{-1}]$, the incident photon density of the excitation laser (photons per m^2), the correction (or filling) factor (m^{-1}), the change in the reflected microwave power, and the power of the reflected microwave, respectively. The change in conductivity is equivalent to $\Delta P_{\text{r}}/(AP_{\text{r}})$. A 355 nm laser light with a photon density of 9.1×10^{15} photons per cm^2 was used as the excitation source. The sample was set at the highest electric field in a resonant cavity. The experiments were carried out at room temperature.

Exciton Binding Energy Calculation. The exciton binding energy was estimated using the following equation[34]

$$h\nu = E_{\text{g}} - E_{\text{x}}$$

where $h\nu$ is the emitted photon energy (corresponds to the excitonic emission maximum), E_{g} is the optical band gap (from Tauc's plot), and E_{x} is the exciton binding energy.

■ ASSOCIATED CONTENT

ⓢ Supporting Information

The Supporting Information is available free of charge at https://pubs.acs.org/doi/10.1021/acs.chemmater.0c00390.

Crystal structure of BBI and MBI; SEM analysis; film quality analysis; TGA and DSC; Tauc plot; inter inorganic cluster distance calculation; characterization of MBI (PDF)

Crystal structure of BBI (CIF)

■ AUTHOR INFORMATION

Corresponding Author

Chakkooth Vijayakumar − *Photosciences and Photonics Section, CSIR—National Institute for Interdisciplinary Science and Technology (NIIST), Thiruvananthapuram 695 019, India; Academy of Scientific and Innovative Research (AcSIR), Ghaziabad 201 002, India;* ⓞ orcid.org/0000-0001-5347-6799; Email: cvijayakumar@niist.res.in

Authors

Johnpaul K. Pious − *Photosciences and Photonics Section, CSIR—National Institute for Interdisciplinary Science and Technology (NIIST), Thiruvananthapuram 695 019, India; Academy of Scientific and Innovative Research (AcSIR), Ghaziabad 201 002, India*

Chinnadurai Muthu − *Photosciences and Photonics Section, CSIR—National Institute for Interdisciplinary Science and Technology (NIIST), Thiruvananthapuram 695 019, India; Academy of Scientific and Innovative Research (AcSIR), Ghaziabad 201 002, India*

Selgiya Dani − *Photosciences and Photonics Section, CSIR—National Institute for Interdisciplinary Science and Technology (NIIST), Thiruvananthapuram 695 019, India*

Akinori Saeki − *Department of Applied Chemistry, Graduate School of Engineering, Osaka University, Suita, Osaka 565 0871, Japan;* ⓞ orcid.org/0000-0001-7429-2200

Complete contact information is available at:
https://pubs.acs.org/10.1021/acs.chemmater.0c00390

Author Contributions

The manuscript was written through contributions of all authors. All authors have given approval to the final version of the manuscript.

REFERENCES

(1) Eckhardt, K.; Bon, V.; Getzschmann, J.; Grothe, J.; Wisser, F. M.; Kaskel, S. Crystallographic Insights into $(CH_3NH_3)_3(Bi_2I_9)$: A New Lead-Free Hybrid Organic-Inorganic Material as a Potential Absorber for Photovoltaics. *Chem. Commun.* **2016**, *52*, 3058−3060.

(2) Park, B. W.; Philippe, B.; Zhang, X.; Rensmo, H.; Boschloo, G.; Johansson, E. M. J. Bismuth Based Hybrid Perovskites $A_3Bi_2I_9$ (A: Methylammonium or Cesium) for Solar Cell Application. *Adv. Mater.* **2015**, *27*, 6806−6813.

(3) McCall, K. M.; Stoumpos, C. C.; Kostina, S. S.; Kanatzidis, M. G.; Wessels, B. W. Strong Electron-Phonon Coupling and Self-Trapped Excitons in the Defect Halide Perovskites $A_3Bi_2I_9$ (A = Cs, Rb; M = Bi, Sb). *Chem. Mater.* **2017**, *29*, 4129−4145.

(4) Jana, M. K.; Janke, S. M.; Dirkes, D. J.; Dovletgeldi, S.; Liu, C.; Qin, X.; Gundogdu, K.; You, W.; Blum, V.; Mitzi, D. B. Direct-Bandgap 2D Silver-Bismuth Iodide Double Perovskite: The Structure-Directing Influence of an Oligothiophene Spacer Cation. *J. Am. Chem. Soc.* **2019**, *141*, 7955−7964.

(5) Hoye, R. L. Z.; Brandt, R. E.; Osherov, A.; Stevanovic, V.; Stranks, S. D.; Wilson, M. W. B.; Kim, H.; Akey, A. J.; Perkins, J. D.; Kurchin, R. C.; Poindexter, J. R.; Wang, E. N.; Bawendi, M. G.; Bulović, V.; Buonassisi, T. Methylammonium Bismuth Iodide as a Lead-Free, Stable Hybrid Organic-Inorganic Solar Absorber. *Chem. - Eur. J.* **2016**, *22*, 2605−2610.

(6) Katan, C.; Mercier, N.; Even, J. Quantum and Dielectric Confinement Effects in Lower-Dimensional Hybrid Perovskite Semiconductors. *Chem. Rev.* **2019**, *119*, 3140−3192.

(7) Lehner, A. J.; Fabini, D. H.; Evans, H. A.; Hébert, C. A.; Smock, S. R.; Hu, J.; Wang, H.; Zwanziger, J. W.; Chabinyc, M. L.; Seshadri, R. Crystal and Electronic Structures of Complex Bismuth Iodides $A_3Bi_2I_9$ (A = K, Rb, Cs) Related to Perovskite: Aiding the Rational Design of Photovoltaics. *Chem. Mater.* **2015**, *27*, 7137−7148.

(8) Cohen, B.-E.; Wierzbowska, M.; Etgar, L. High Efficiency Quasi 2D Lead Bromide Perovskite Solar Cells Using Various Barrier Molecules. *Sustainable Energy Fuels* **2017**, *1*, 1935−1943.

(9) Li, T.; Hu, Y.; Morrison, C. A.; Wu, W.; Han, H.; Robertson, N. Lead-Free Pseudo-Three-Dimensional Organic-Inorganic Iodobismuthates for Photovoltaic Applications. *Sustainable Energy Fuels* **2017**, *1*, 308−316.

(10) Igbari, F.; Wang, R.; Wang, Z. K.; Ma, X. J.; Wang, Q.; Wang, K. L.; Zhang, Y.; Liao, L. S.; Yang, Y. Composition Stoichiometry of $Cs_2AgBiBr_6$ Films for Highly Efficient Lead-Free Perovskite Solar Cells. *Nano Lett.* **2019**, *19*, 2066−2073.

(11) Pious, J. K.; Katre, A.; Muthu, C.; Chakraborty, S.; Krishna, S.; Nair, V. C. Zero-Dimensional Lead-Free Hybrid Perovskite-like Material with a Quantum-Well Structure. *Chem. Mater.* **2019**, *31*, 1941−1945.

(12) Lin, J. T.; Liao, C. C.; Hsu, C. S.; Chen, D. G.; Chen, H. M.; Tsai, M. K.; Chou, P. T.; Chiu, C. W. Harnessing Dielectric Confinement on Tin Perovskites to Achieve Emission Quantum Yield up to 21%. *J. Am. Chem. Soc.* **2019**, *141*, 10324−10330.

(13) Cheng, B.; Li, T.-Y.; Maity, P.; Wei, P.-C.; Nordlund, D.; Ho, K.-T.; Lien, D.-H.; Lin, C.-H.; Liang, R.-Z.; Miao, X.; Ajia, I. A.; Yin, J.; Sokaras, D.; Javey, A.; Roqan, I. S.; Mohammed, O. F.; He, J.-H. Extremely Reduced Dielectric Confinement in Two-Dimensional Hybrid Perovskites with Large Polar Organics. *Commun. Phys.* **2018**, *1*, No. 80.

(14) Hong, X.; Ishihara, T.; Nurmikko, A. V. Dielectric Confinement Effect on Excitons in PbI_4-Based Layered Semiconductors. *Phys. Rev. B* **1992**, *45*, 6961−6964.

(15) Vickers, E. T.; Graham, T. A.; Chowdhury, A. H.; Bahrami, B.; Dreskin, B. W.; Lindley, S.; Naghadeh, S. B.; Qiao, Q.; Zhang, J. Z. Improving Charge Carrier Delocalization in Perovskite Quantum Dots by Surface Passivation with Conductive Aromatic Ligands. *ACS Energy Lett.* **2018**, *3*, 2931−2939.

(16) Dai, J.; Xi, J.; Li, L.; Zhao, J. F.; Shi, Y.; Zhang, W.; Ran, C.; Jiao, B.; Hou, X.; Duan, X.; Wu, Z. Charge Transport between Coupling Colloidal Perovskite Quantum Dots Assisted by Functional Conjugated Ligands. *Angew. Chem., Int. Ed.* **2018**, *57*, 5754−5758.

(17) Ju, M.-G.; Dai, J.; Ma, L.; Zhou, Y.; Liang, W.; Zeng, X. C. Lead-Free Low-Dimensional Tin Halide Perovskites with Functional Organic Spacers: Breaking the Charge-Transport Bottleneck. *J. Mater. Chem. A* **2019**, *7*, 16742−16747.

(18) Quintero-Bermudez, R.; Proppe, A. H.; Mahata, A.; Todorovic, P.; Kelley, S. O.; De Angelis, F.; Sargent, E. H. Ligand-Induced Surface Charge Density Modulation Generates Local Type-II Band Alignment in Reduced-Dimensional Perovskites. *J. Am. Chem. Soc.* **2019**, *141*, 13459−13467.

(19) Abulikemu, M.; Ould-Chikh, S.; Miao, X.; Alarousu, E.; Murali, B.; Ngongang Ndjawa, G. O.; Barbé, J.; El Labban, A.; Amassian, A.; Del Gobbo, S. Optoelectronic and Photovoltaic Properties of the Air-Stable Organohalide Semiconductor $(CH_3NH_3)_3Bi_2I_9$. *J. Mater. Chem. A* **2016**, *4*, 12504−12515.

(20) Laane, J.; Jagodzinski, P. W. Low-Frequency Vibrational Spectra of Bromo- and Iodobismuthates and the Observation of a Trans Effect. *Inorg. Chem.* **1980**, *19*, 44−49.

(21) Ran, C.; Wu, Z.; Xi, J.; Yuan, F.; Dong, H.; Lei, T.; He, X.; Hou, X. Construction of Compact Methylammonium Bismuth Iodide Film Promoting Lead-Free Inverted Planar Heterojunction Organohalide Solar Cells with Open-Circuit Voltage over 0.8 V. *J. Phys. Chem. Lett.* **2017**, *8*, 394−400.

(22) Zhang, R.; Mao, X.; Yang, Y.; Yang, S.; Zhao, W.; Wumaier, T.; Wei, D.; Deng, W.; Han, K. Air-Stable, Lead-Free Zero-Dimensional Mixed Bismuth-Antimony Perovskite Single Crystals with Ultra-Broadband Emission. *Angew. Chem., Int. Ed.* **2019**, *58*, 2725−2729.

(23) Berestennikov, A. S.; Li, Y.; Iorsh, I. V.; Zakhidov, A. A.; Rogach, A. L.; Makarov, S. V. *Nanoscale* **2019**, *11*, 6747−6754.

(24) Zhang, Z.; Li, X.; Xia, X.; Wang, Z.; Huang, Z.; Lei, B.; Gao, Y. High-Quality $(CH_3NH_3)_3Bi_2I_9$ Film-Based Solar Cells: Pushing Efficiency up to 1.64%. *J. Phys. Chem. Lett.* **2017**, *8*, 4300−4307.

(25) Kawai, T.; Ishii, A.; Kitamura, T.; Shimanuki, S.; Iwata, M.; Ishibashi, Y. Optical Absorption in Band-Edge Region of $(CH_3NH_3)_3Bi_2I_9$ Single Crystals. *J. Phys. Soc. Jpn.* **1996**, *65*, 1464−1468.

(26) Ni, C.; Hedley, G.; Payne, J.; Svrcek, V.; McDonald, C.; Jagadamma, L. K.; Edwards, P.; Martin, R.; Jain, G.; Carolan, D.; Mariotti, D.; Maguire, P.; Samuel, I.; Irvine, J. Charge Carrier Localised in Zero-Dimensional $(CH_3NH_3)_3Bi_2I_9$ clusters. *Nat. Commun.* **2017**, *8*, No. 170.

(27) Jain, S. M.; Phuyal, D.; Davies, M. L.; Li, M.; Philippe, B.; De Castro, C.; Tsoi, C.; Karis, O.; Rensmo, H.; Edvinsson, T.; et al. An effective approach of vapour assisted morphological tailoring for reducing metal defect sites in lead-free, $(CH_3NH_3)_3Bi_2I_9$ Bismuth-based Perovskite solar cells for improved performance and long-term stability. *Nano Energy* **2018**, *49*, 614−624.

(28) Oga, H.; Saeki, A.; Ogomi, Y.; Hayase, S.; Seki, S. Improved Understanding of the Electronic and Energetic Landscapes of Perovskite Solar Cells: High Local Charge Carrier Mobility, Reduced Recombination, and Extremely Shallow Traps. *J. Am. Chem. Soc.* **2014**, *136*, 13818−13825.

(29) Ghosh, T.; Gopal, A.; Nagasawa, S.; Mohan, N.; Saeki, A.; Nair, V. C. Following the TRMC Trail: Optimization of Photovoltaic Efficiency and Structure-Property Correlation of Thiophene Oligomers. *ACS Appl. Mater. Interfaces* **2016**, *8*, 25396−25404.

(30) Peng, J.; Chen, Y.; Zheng, K.; Pullerits, T.; Liang, Z. Insights into Charge Carrier Dynamics in Organo-Metal Halide Perovskites:

From Neat Films to Solar Cells. *Chem. Soc. Rev.* **2017**, *46*, 5714−5729.

(31) Hartono, N. T. P.; Sun, S.; Gélvez-Rueda, M. C.; Pierone, P. J.; Erodici, M. P.; Yoo, J.; Wei, F.; Bawendi, M.; Grozema, F. C.; Sher, M.; Buonassisi, T.; Correa-Baena, J.-P. The Effect of Structural Dimensionality on Carrier Mobility in Lead-Halide Perovskites. *J. Mater. Chem. A* **2019**, *7*, 23949−23957.

(32) Kamminga, M. E.; Stroppa, A.; Picozzi, S.; Chislov, M.; Zvereva, I. A.; Baas, J.; Meetsma, A.; Blake, G. R.; Palstra, T. T. M. Polar Nature of $(CH_3NH_3)_3Bi_2I_9$ Perovskite-Like Hybrids. *Inorg. Chem.* **2017**, *56*, 33−41.

(33) Yamada, K.; Nishikubo, R.; Oga, H.; Ogomi, Y.; Hayase, S.; Kanno, S.; Imamura, Y.; Hada, M.; Saeki, A. Anomalous Dielectric Behavior of a Pb/Sn Perovskite: Effect of Trapped Charges on Complex Photoconductivity. *ACS Photonics* **2018**, *5*, 3189−3197.

(34) Blancon, J.-C.; Stier, A. V.; Tsai, H.; Nie, W.; Stoumpos, C. C.; Traoré, B.; Pedesseau, L.; Kepenekian, M.; Katsutani, F.; Noe, G. T.; Kono, J.; Tretiak, S.; Crooker, S. A.; Katan, C.; Kanatzidis, M. G.; Crochet, J. J.; Even, J.; Mohite, A. D. Scaling Law for Excitons in 2D Perovskite Quantum Wells. *Nat. Commun.* **2018**, *9*, No. 2254.

Letter

Anisotropic Photoconductivity and Long-Lived Charge Carriers in Bismuth-Based One-Dimensional Perovskite with Type-IIa Band Alignment

Johnpaul K. Pious, Manasa G. Basavarajappa, Chinnadurai Muthu, Nayana Krishna, Ryosuke Nishikubo, Akinori Saeki, Sudip Chakraborty,* and Chakkooth Vijayakumar*

Cite This: *J. Phys. Chem. Lett.* 2020, 11, 6757–6762

Read Online

ACCESS | Metrics & More | Article Recommendations | SI Supporting Information

ABSTRACT: Bismuth-based perovskites are attracting intense scientific interest due to low toxicity and excellent moisture stability compared to lead-based analogues. However, high exciton binding energy, poor charge carrier separation, and transport efficiencies lower their optoelectronic performances. To address these issues, we have integrated an electronically active organic cation, naphthalimide ethylammonium, between the $[BiI_5^{2-}]_n$ chains via crystal engineering to form a novel perovskite-like material (naphthalimide ethyl-ammonium)$_2$BiI$_5$ (NBI). Single crystal analysis revealed a one-dimensional quantum-well structure for NBI in which inter-inorganic well electronic coupling is screened by organic layers. It exhibited anisotropic photoconductivity and long-lived charge carriers with milliseconds lifetime, which is higher than that of CH$_3$NH$_3$PbI$_3$. Density functional theory calculations confirmed type-IIa band alignment between organic cations and inorganic chains, allowing the former to electronically contribute to the overall charge transport properties of the material.
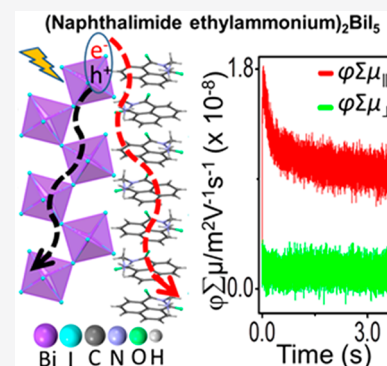
Lead halide perovskite materials have made remarkable advancements in the field of optoelectronics due to their unique properties such as low exciton binding energy, long charge carrier diffusion length, defect tolerance, and broadband spectral tunability.[1−4] However, high toxicity and poor moisture stability limit their commercial applications. In search of nontoxic, environmentally friendly alternatives, bismuth is on the front line of choices of metals, since it is isoelectronic to lead. Moreover, the antibonding interactions of 6s² electrons in bismuth could reduce the defect states at the band edges.[5] Bismuth-based perovskites are found to be suitable for solar cells, photodetectors, X-ray detectors, memory, and ferroelectric device applications.[6−10] Bismuth has a propensity to form one-dimensional (1D) chains of bismuth-halide octahedra of varying connectivity such as $[BiI_5^{2-}]_n$, $[BiI_4^-]_n$, $[Bi_2I_7^{2-}]_n$, and $[Bi_3I_{11}^{2-}]_n$.[11] Importantly, the optical and electronic properties of these materials can be easily tuned by tailoring their connectivity through the rational selection of organic cations.[12] Nevertheless, the +3 oxidation state of bismuth restricts it from directly replacing Pb²⁺ in the conventional three-dimensional perovskite structure. In addition to that, the +3 oxidation state leads to the formation of metal-deficient low-dimensional perovskites.[13] The lower dimensionality results in high exciton binding energy, low charge carrier mobility, and small electron/hole diffusion lengths.[14−16]

In order to address the poor conductivity of low-dimensional perovskites, the introduction of π-conjugated aromatic organic spacers in the perovskite framework is suggested as an efficient strategy.[17] They can reduce the conductivity barrier between the organic and inorganic constituents leading to the delocalization of electronic wave function.[18] This strategy was successfully implemented in lead-based perovskites of different forms including nanocrystals.[19−22] A similar approach was adopted in lead-free 1D perovskites such as $(C_7H_7)SbI_4$ and $(C_7H_7)BiI_4$, which are reported to form charge-separated states by the photoinduced electron transfer from inorganic layers to the π−π stacked tropilium cations.[23] A charge-transfer semiconductor was formed consisting of conduction and valence bands composed of tropylium cations and inorganic chains, respectively. In addition to the improved conductivity induced by the aromatic organic cations, the polarizability of these moieties could lower the exciton binding energy by reducing the dielectric confinement. In this regard, we have recently reported a novel perovskite-like material, (benzylammonium)$_3$Bi$_2$I$_9$ (BBI), with low dielectric confinement and efficient exciton dissociation compared to the isostructural $(CH_3NH_3)_3Bi_2I_9$.[24] However, charge transfer interaction
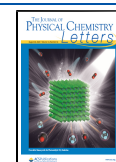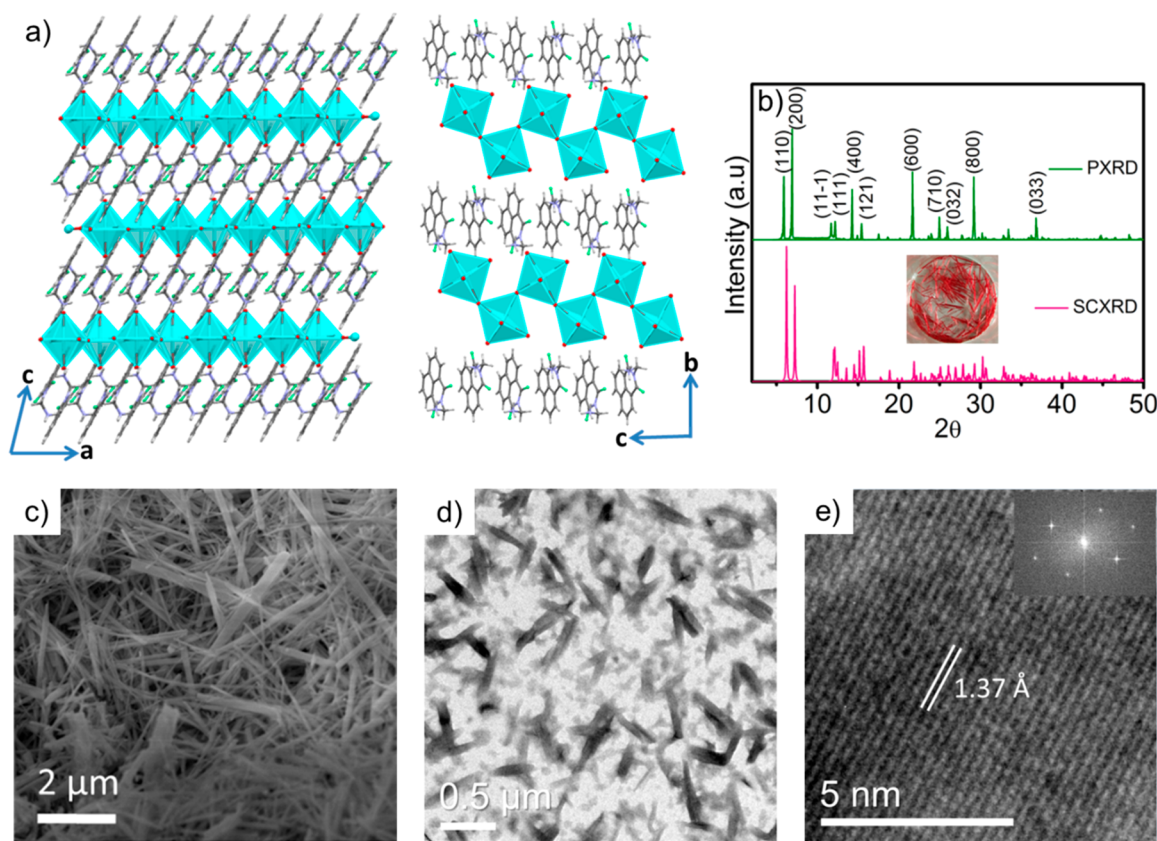
Figure 1. (a) Lateral (along b axis) and top view (along a axis) of the crystal packing of NBI showing a multiple quantum well structure. (b) Powder and single-crystal X-ray diffraction patterns of NBI. Inset shows the photograph of the needle-shaped single crystals. (c) Scanning electron microscope and (d) transmission electron microscope images of NBI thin films. (e) High-resolution transmission electron microscope image of NBI shows a lattice spacing of 1.37 Å. Inset shows the fast Fourier transform image with bright diffraction spots arranged in a distorted hexagonal shape.

between the inorganic and organic units in BBI was absent even though benzylammonium is a π-conjugated system. This was attributed to the lack of extended $\pi-\pi$ stacking of benzylammonium cations.

Though the incorporation of aromatic organic cations in the perovskite framework is a good strategy for improving the optoelectronic properties of 1D perovskites, generation of long-lived charge carriers, a requirement for several optoelectronic devices, is still elusive. Highly ordered and efficiently $\pi-\pi$ stacked (face-on) organic semiconductors within the perovskite structure is necessary for achieving this, which is very challenging. In this context, self-organized naphthalene imides are excellent electron transporting semiconductors widely used in organic thin-film transistors.[25,26] Herein, we report the use of naphthalene monoimide to overcome the charge transfer bottleneck in low-dimensional bismuth-based perovskites. For that, we have interdigitated naphthalene monoimide derived ligands between the inorganic $[BiI_5^{2-}]_n$ chains to form a perovskite-like material, (naphthalimide ethylammonium)$_2$BiI$_5$ (NBI). The high electron affinity of naphthalimide created a type-IIa band alignment at the organic−inorganic heterojunction. This facilitated the efficient separation of electron−hole pairs, and the highly ordered self-assembly of naphthalene chromophores resulted in long charge carrier lifetimes. Moreover, the NBI single crystals exhibited high anisotropic photoconductivity along the crystal long axis due to the directional growth of $[BiI_5^{2-}]_n$ inorganic chains.

Single crystals of NBI were synthesized from the aqueous hydrogen iodide (HI) solution containing a 1:1 molar ratio of naphthalimide ethylammonium iodide and BiI$_3$. Red needle-like single crystals having several millimeters in length were harvested from the HI solution after 24 h. X-ray diffraction (XRD) analysis of the crystals at 297 K revealed that NBI has a monoclinic crystal structure and belongs to the $P2_1/c$ space group (Figure 1a). It also revealed that NBI has a 1D perovskite-like structure consisting of inorganic $[BiI_5^{2-}]_n$ chains formed by the corner-sharing of BiI$_6^{3-}$ octahedra. The organic counterpart, naphthalene monoimides, adopted a face-on $\pi-\pi$ stacking arrangement with an average distance of 3.5 Å, which hinted at a potential charge transport pathway. On the other hand, the inorganic chains are stacked one above the other with zero octahedral unit displacement along the crystallographic b axis. These chains are separated by bilayers of monovalent naphthalimide cations resulting in a multiple-quantum-well (MQW) structure at the molecular level. In this structure, inorganic chains will act as conducting wells and the organic molecules as screening layers for interwell charge hopping. To the best of our knowledge, this is the first perovskite material exhibiting an eclipsed packing of zigzag $[BiI_5^{2-}]_n$ chains separated by organic monocations.

Single-crystal XRD analysis revealed that the aromatic face-on $\pi-\pi$ interactions between the rigid organic spacers stabilize the unique crystal packing in NBI. Powder and single-crystal XRD patterns match well without any secondary phase peaks, suggesting the phase purity of the crystals (Figure 1b). The
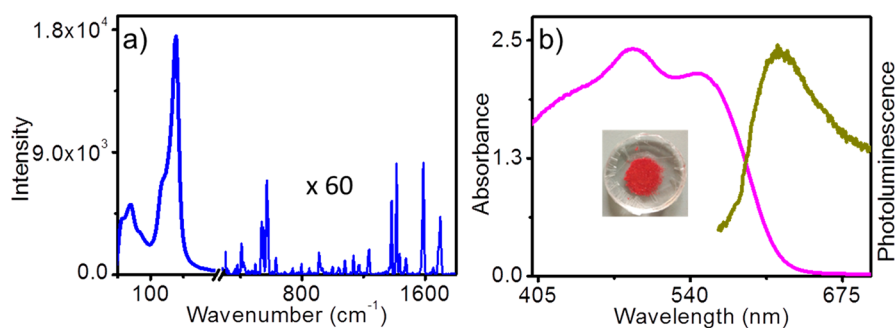
Figure 2. (a) Raman spectrum of NBI single crystals upon 785 nm laser excitation. (The region corresponding to the vibrational modes of naphthalimide cations, 300−1800 cm^{-1}, is enhanced by 60× for visibility.) (b) Absorption and emission spectra of the NBI powder sample. The inset shows the photograph of the powder sample.
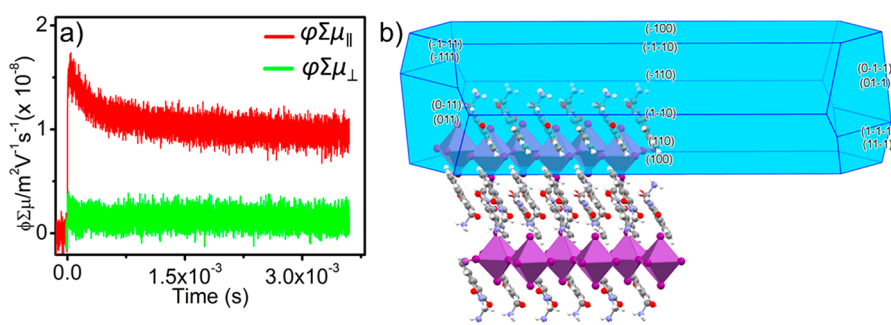

Figure 3. (a) Flash photolysis time-resolved microwave conductivity kinetics of NBI single crystals measured parallel ($\varphi\Sigma\mu_{\parallel}$) and perpendicular ($\varphi\Sigma\mu_{\perp}$) to the crystal long axis (500 nm laser source was used as the excitation source). (b) Crystal shape and packing of NBI simulated using Bravais-Friedel-Donnay-Harker method by the Mercury software.[32]

zigzag connectivity of BiI_6^{3-} octahedra in the $[BiI_5^{2-}]_n$ chains imparted a layered structure to NBI, which was in good agreement with the observed intense ⟨110⟩ plane reflection in the single crystal XRD pattern. Equidistant ⟨100⟩ reflections in the powder XRD pattern further confirmed that the inorganic layers are arranged one above the other separated by the organic spacers. The scanning electron microscope (SEM) and transmission electron microscope (TEM) analysis showed a needle-like 1D growth morphology similar to the bulk single crystals (Figure 1c and d, respectively). The high-resolution TEM image showed a well-defined atomic lattice with a lattice separation of 1.37 Å corresponding to a ⟨61$\bar{2}$⟩ plane (Figure 1e). Bright diffraction spots in the fast Fourier transformation image are attributed to the highly crystalline nature of NBI.

Raman spectrum provides direct evidence for electron−phonon coupling in perovskites. Generally, intense Raman active vibrational modes imply a strong electron−phonon coupling.[27,28] The Raman spectrum of NBI at 785 nm laser excitation showed two prominent peaks corresponding to Bi−I bond bending, and symmetric stretching vibrations at 69 and 138 cm^{-1}, respectively (Figure 2a).[28] In addition to this, vibrational modes of naphthalimide cations were observed between 300 and 1800 cm^{-1}. This implies that the excited electrons are coupled with the vibrational modes of both organic and inorganic moieties. In other words, the naphthalimide cations are contributing to the electronic properties of NBI. The intensity of the peaks corresponding to the vibrational modes of BiI_5^{2-} units were remarkably high compared to the naphthalimide cations. This implies that the vibrational modes of inorganic units are more strongly coupled to the excited electrons than the organic units. The optical absorption spectrum of NBI spans from 400 to 600 nm with a

well-defined excitonic absorption peak at 548 nm and an additional peak at 490 nm (Figure 2b). The peaks at 548 and 490 nm could be attributed to the $^1S_0-^3P_1$ and $^1S_0-^3P_2$ electronic transitions of the Bi^{3+} ions in the BiI_5^{2-} units, respectively.[29−31] This indicates that the ground-state electronic transitions are occurring within the BiI_6^{3-} inorganic units. NBI showed weak photoluminescence (PL) upon 500 nm excitation with a PL maximum at 619 nm. Since the emission peak is narrow and close to the absorption continuum, it is likely originated from excitonic radiative recombination (Figure 2b). The optical band gap of NBI was estimated from the Tauc plot as 2.06 eV (Figure S1). Thermal and phase stability of NBI were confirmed using thermogravimetry (TG, Figure S2) and differential scanning calorimetry (DSC, Figure S3) analyses. TG profile showed a 5% initial weight loss at 290 °C, corresponding to the decomposition of the organic component. Neither endothermic nor exothermic peaks were observed in the DSC profile proving the phase stability of NBI in the measured temperature range.

To evaluate the photoconductivity properties of NBI, flash photolysis time-resolved microwave conductivity (FP-TRMC) analysis was performed. This is a widely accepted technique for assessing the photoconductivity of semiconducting materials including perovskites.[33−35] It is an electrode-less technique in which microwave radiation is used to probe the radiative and nonradiative recombination of all free mobile charge carriers in the material on photoexcitation.[36] The absorption of microwave radiation varies with the photoconductivity changes, which is recorded to calculate the product of mobility ($\Sigma\mu$) and dissociation yield of charge carriers (φ). Since NBI crystals are of needle shape, the measurement was performed parallel ($\varphi\Sigma\mu_{\parallel}$) and perpendicular ($\varphi\Sigma\mu_{\perp}$) to the crystal long axis. It
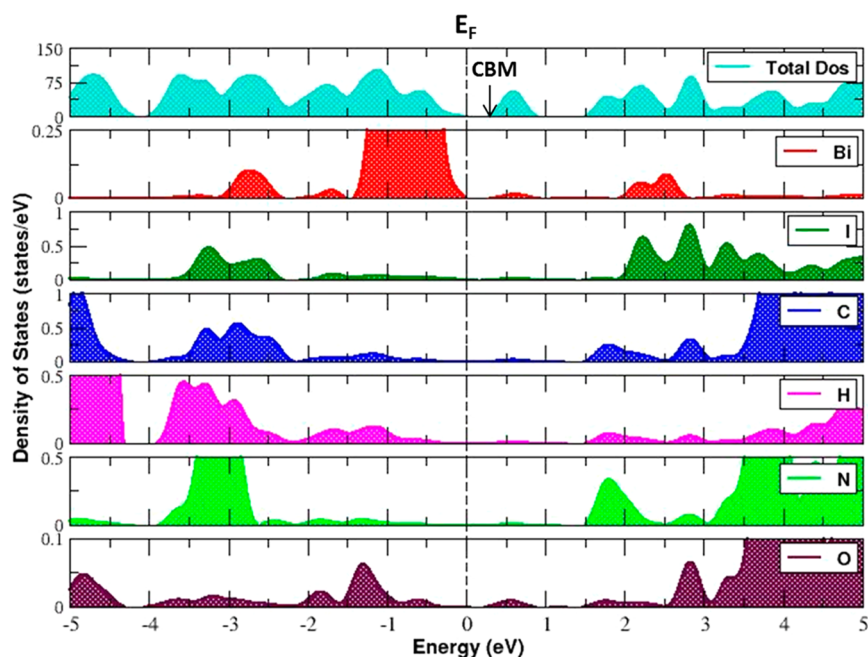
Figure 4. Total density of states plot for the calculated band structure of NBI and the corresponding partial density of state contribution from the organic and inorganic counterparts. E_F (Fermi energy level) has been considered as the valence band maximum (VBM), while the conduction band minimum (CBM) has been indicated with an arrow in the panel of total density of states.

was observed that $\varphi\Sigma\mu_\parallel$ (1.64×10^{-8} m^2/(V s)) was 8.2-fold higher than $\varphi\Sigma\mu_\perp$ (2×10^{-9} m^2/(V s)) (Figure 3a). High anisotropic photoconductivity in NBI suggests that it would be a promising candidate for field-effect transistor and photodetector applications. To get a better understanding of the anisotropic conductivity, the crystal shape and packing direction were simulated using the Bravais-Friedel-Donnay-Harker (BFDH) method. It revealed that the inorganic $[BiI_5^{2-}]_n$ chains and stacked naphthalimide cations are arranged along the crystal long axis, resembling one-dimensional conductor structures for both of them (Figure 3b). This arrangement provides a facile route for the charge carriers to move along the crystal long axis yielding a higher $\varphi\Sigma\mu_\parallel$. On the other hand, along the perpendicular direction, the charge carriers have to hop from inorganic chains to organic stacks sequentially. Since the latter is a poor conductor compared to the former, such hoping is not favored, resulting in a lower $\varphi\Sigma\mu_\perp$.

The $\varphi\Sigma\mu_\parallel$ signal showed a charge carrier lifetime of 18 ms (Figure S4), which is significantly higher than the TRMC lifetimes reported for 3D perovskites such as MAPbI$_3$, Cs$_2$AgBiBr$_6$, and Cs$_2$AgBiTlBr$_6$.[37,38] The long carrier lifetime of NBI implies a critical aspect that the organic moieties are taking part in the charge transport along with the inorganic chains. In other words, the holes move through the one-dimensional $[BiI_5^{2-}]_n$ chains, whereas electrons travel through $\pi-\pi$ stacked naphthalimide moieties. It has been theoretically proven that perylene and naphthalene based organic cations could provide potential charge transport pathways for electrons in hybrid perovskites.[17] The observation of long-lived carriers in NBI is an experimental proof for this theoretical prediction. In most of the 1D bismuth-based perovskites, only the inorganic moieties involved in the charge transport and the organic cations remain electronically inactive.[10,39−42] Making the organic cations contribute to the electronic properties of perovskites has remarkable implications in the performance of

corresponding optoelectronic devices. More importantly, it also opens up an avenue for developing perovskites with tailor-made features for specific applications.

To understand the role of the organic cations and the inorganic elements in the electronic properties of NBI, density functional theory (DFT) calculations were performed. After getting the minimum energy configurations, the corresponding projected density of states (PDOS) was estimated for the profound understanding of the electronic structure of NBI (Figure 4). From the PDOS, it is clear that the valence band maximum is composed of bismuth orbitals, whereas, at the conduction band, a dominant hybridization between bismuth and iodine orbitals is observed in addition to the orbital contributions from the naphthalimide cations. The stronger hybridization of bismuth and iodine orbitals led to the stability of BiI$_6^{3-}$ octahedra. The lowest energy electronic transition in BiI$_6^{3-}$ units occurs at 2 eV, consistent with the observed absorption near the band edges (2.06 eV). In the conduction band, strong hybridization between C, H, N, and O elements of naphthalimide cation is observed at a lower energy (1.8 eV) compared to the BiI$_6^{3-}$ units. One of the prime observations that we can make from this is to relate the electronic structure of NBI to the type-IIa band alignment.[43] For the type-IIa alignment, the contribution of the inorganic elements has prevailed in the vicinity of valence band maxima, whereas organic cations contribute to the deeper electronic levels of the valence bands. The scenario changes in the case of the conduction band regime, where the organic contributions have prevailed nearer to the Fermi level compared to the inorganic counterpart. In other words, the valence band maximum and conduction band minimum states are derived from the BiI$_6^{3-}$ and naphthalimide units, respectively. This band alignment promotes the photoinduced electron transfer from the inorganic Bi−I lattice to the unoccupied frontier molecular orbitals of naphthalimide moieties, whereas the holes will

reside in the inorganic framework leading to the observed long-lived charge carriers.

In summary, we have synthesized a novel lead-free 1D perovskite-like material with a quantum-well structure having the inorganic chains separated by $\pi-\pi$ stacked, face-on oriented organic cations. The material exhibited excellent conductivity parallel to the crystal long axis and long charge carrier lifetime. The latter is ascribed to the charge carrier's separation at the naphthalimide$-[\mathrm{BiI}_5{}^{2-}]_n$ chain interface followed by their transport through the organic and inorganic semiconducting channels. This was confirmed by DFT calculations, which unraveled a type-IIa band alignment at the organic−inorganic heterojunction. This work opens up a new avenue for improving the optoelectronic properties of low-dimensional lead-free perovskite materials through the incorporation of electronically compatible organic moieties with the inorganic structures.

ASSOCIATED CONTENT

Supporting Information

The Supporting Information is available free of charge at https://pubs.acs.org/doi/10.1021/acs.jpclett.0c01772.

> Experimental and synthetic procedures, Tauc plot, TGA, DSC, and TRMC carrier lifetime fitted plot (PDF)

AUTHOR INFORMATION

Corresponding Authors

Sudip Chakraborty − *Discipline of Physics, Indian Institute of Technology Indore, Indore 453 552, India;* orcid.org/0000-0002-6765-2084; Email: sudiphys@gmail.com

Chakkooth Vijayakumar − *Photosciences and Photonics Section, CSIR-National Institute for Interdisciplinary Science and Technology (NIIST), Thiruvananthapuram 695 019, India; Academy of Scientific and Innovative Research (AcSIR), Ghaziabad 201 001, India;* orcid.org/0000-0001-5347-6799; Email: cvijayakumar@niist.res.in

Authors

Johnpaul K. Pious − *Photosciences and Photonics Section, CSIR-National Institute for Interdisciplinary Science and Technology (NIIST), Thiruvananthapuram 695 019, India; Academy of Scientific and Innovative Research (AcSIR), Ghaziabad 201 001, India*

Manasa G. Basavarajappa − *Discipline of Physics, Indian Institute of Technology Indore, Indore 453 552, India*

Chinnadurai Muthu − *Photosciences and Photonics Section, CSIR-National Institute for Interdisciplinary Science and Technology (NIIST), Thiruvananthapuram 695 019, India; Academy of Scientific and Innovative Research (AcSIR), Ghaziabad 201 001, India*

Nayana Krishna − *Photosciences and Photonics Section, CSIR-National Institute for Interdisciplinary Science and Technology (NIIST), Thiruvananthapuram 695 019, India*

Ryosuke Nishikubo − *Department of Applied Chemistry, Graduate School of Engineering, Osaka University, Suita, Osaka 565-0871, Japan*

Akinori Saeki − *Department of Applied Chemistry, Graduate School of Engineering, Osaka University, Suita, Osaka 565-0871, Japan;* orcid.org/0000-0001-7429-2200

Complete contact information is available at:
https://pubs.acs.org/10.1021/acs.jpclett.0c01772

Notes

The authors declare no competing financial interest.

REFERENCES

(1) Zheng, X.; Hou, Y.; Bao, C.; Yin, J.; Yuan, F.; Huang, Z.; Song, K.; Liu, J.; Troughton, J.; Gasparini, N.; Zhou, C.; Lin, Y.; Xue, D.-J.; Chen, B.; Johnston, A. K.; Wei, N.; Hedhili, M. N.; Wei, M.; Al-salloum, A. Y.; Maity, P.; Turedi, B.; Yang, C.; Baran, D.; Anthopoulos, T. D.; Han, Y.; Lu, Z.-H.; Mohammed, O. F.; Gao, F.; Sargent, E. H.; Bakr, O. M. Managing Grains and Interfaces via Ligand Anchoring Enables 22.3%-Efficiency Inverted Perovskite Solar Cells. *Nat. Energy* **2020**, *5*, 131−140.

(2) Fu, F.; Feurer, T.; Jäger, T.; Avancini, E.; Bissig, B.; Yoon, S.; Buecheler, S.; Tiwari, A. N. Low-Temperature-Processed Efficient Semi-Transparent Planar Perovskite Solar Cells for Bifacial and Tandem Applications. *Nat. Commun.* **2015**, *6*, 1−9.

(3) Ghimire, S.; Takahashi, K.; Takano, Y.; Nakamura, T.; Biju, V. Photon-Recycling by Energy Transfer in Piezochemically Synthesized and Close-packed Methyl Ammonium Lead Halide Perovskites. *J. Phys. Chem. C* **2019**, *123*, 27752−27758.

(4) Markina, D. I.; Tiguntseva, E. Y.; Pushkarev, A. P.; Samsonov, M. A.; Vengris, M.; Munkhbat, B.; Shegai, T.; Hix, G.; Zakhidov, A. A.; Makarov, S. V. Photophysical Properties of Halide Perovskite $\mathrm{CsPb(Br}_{1-x}\mathrm{I}_x)_3$ Thin Films and Nanowires. *J. Lumin.* **2020**, *220*, 116985.

(5) Ganose, A. M.; Savory, C. N.; Scanlon, D. O. Beyond Methylammonium Lead Iodide: Prospects for the Emergent Field of ns^2 Containing Solar Absorbers. *Chem. Commun.* **2017**, *53*, 20−44.

(6) Jain, S. M.; Phuyal, D.; Davies, M. L.; Li, M.; Philippe, B.; De Castro, C.; Qiu, Z.; Kim, J.; Watson, T.; Tsoi, W. C.; Karis, O.; Rensmo, H.; Boschloo, G.; Edvinsson, T.; Durrant, J. R. An Effective Approach of Vapour Assisted Morphological Tailoring for Reducing Metal Defect Sites in Lead-free, $(\mathrm{CH}_3\mathrm{NH}_3)_3\mathrm{Bi}_2\mathrm{I}_9$ Bismuth-based Perovskite Solar Cells for Improved Performance and Long-term Stability. *Nano Energy* **2018**, *49*, 614−624.

(7) Hussain, A. A.; Rana, A. K.; Ranjan, M. Air-Stable Lead-free Hybrid Perovskite Employing Self-Powered Photodetection with an Electron/Hole-Conductor-free Device Geometry. *Nanoscale* **2019**, *11*, 1217−1227.

(8) Ji, C.; Wang, S.; Wang, Y.; Chen, H.; Li, L.; Sun, Z.; Sui, Y.; Wang, S.; Luo, J. 2D Hybrid Perovskite Ferroelectric Enables Highly Sensitive X-Ray Detection with Low Driving Voltage. *Adv. Funct. Mater.* **2020**, *30*, 1905529.

(9) Mazur, T.; Zawal, P.; Szaciłowski, K. Synaptic Plasticity, Meta-Plasticity and Memory Effects in Hybrid Organic-Inorganic Bismuth-based Materials. *Nanoscale* **2019**, *11*, 1080−1090.

(10) Zhang, H.-Y.; Wei, Z.; Li, P.-F.; Tang, Y.-Y.; Liao, W.-Q.; Ye, H.-Y.; Cai, H.; Xiong, R.-G. The Narrowest Band Gap Observed in Molecular Ferroelectrics: Hexanethylenediammonium Penta-Iodo Bismuth(III). *Angew. Chem.* **2018**, *130*, 535−539.

(11) Li, T.; Hu, Y.; Morrison, C. A.; Wu, W.; Han, H.; Robertson, N. Lead-free Pseudo-Three-Dimensional Organic-Inorganic Iodobismu-thates for Photovoltaic Applications. *Sustain. Energy Fuels* **2017**, *1*, 308−316.

(12) Oswald, I. W. H.; Ahn, H.; Neilson, J. R. Influence of Organic Cation Planarity on Structural Templating in Hybrid Metal-Halides. *Dalton Trans.* **2019**, *48*, 16340−16349.

(13) Lehner, A. J.; Fabini, D. H.; Evans, H. A.; Hébert, C. A.; Smock, S. R.; Hu, J.; Wang, H.; Zwanziger, J. W.; Chabinyc, M. L.; Seshadri, R. Crystal and Electronic Structures of Complex Bismuth Iodides

$A_3Bi_2I_9$ (A = K, Rb, Cs) Related to Perovskite: Aiding the Rational Design of Photovoltaics. *Chem. Mater.* **2015**, *27*, 7137−7148.

(14) Ke, W.; Kanatzidis, M. G. Prospects for Low-Toxicity Lead-free Perovskite Solar Cells. *Nat. Commun.* **2019**, *10*, 965.

(15) Pazoki, M.; Johansson, M. B.; Zhu, H.; Broqvist, P.; Edvinsson, T.; Boschloo, G.; Johansson, E. M. J. Bismuth Iodide Perovskite Materials for Solar Cell Applications: Electronic Structure, Optical Transitions and Directional Charge Transport. *J. Phys. Chem. C* **2016**, *120*, 29039−29046.

(16) Fu, H. Review of Lead-free Halide Perovskites as Light-Absorbers for Photovoltaic Applications: From Materials to Solar Cells. *Sol. Energy Mater. Sol. Cells* **2019**, *193*, 107−132.

(17) Maheshwari, S.; Savenije, T. J.; Renaud, N.; Grozema, F. C. Computational Design of 2D Perovskites with Functional Organic Cations. *J. Phys. Chem. C* **2018**, *122*, 17118−17122.

(18) Dai, J.; Xi, J.; Li, L.; Zhao, J. F.; Shi, Y.; Zhang, W.; Ran, C.; Jiao, B.; Hou, X.; Duan, X.; Wu, Z. Functional Conjugated Ligands Assisted Charge Transport between Coupling Colloidal Perovskite Quantum Dots. *Angew. Chem., Int. Ed.* **2018**, *57*, 5754−5758.

(19) Febriansyah, B.; Koh, T. M.; John, R. A.; Ganguly, R.; Li, Y.; Bruno, A.; Mhaisalkar, S. G.; England, J. Inducing Panchromatic Absorption and Photoconductivity in Polycrystalline Molecular 1D Lead-Iodide Perovskites through π-Stacked Viologens. *Chem. Mater.* **2018**, *30*, 5827−5830.

(20) Gao, Y.; Shi, E.; Deng, S.; Shiring, S. B.; Snaider, J. M.; Liang, C.; Yuan, B.; Song, R.; Janke, S. M.; Peláez, A. L.; Yoo, P.; Zeller, M.; Boudouris, B. W.; Liao, P.; Zhu, C.; Blum, V.; Yu, Y.; Savoie, B. M.; Huang, L.; Dou, L. Molecular Engineering of Organic-Inorganic Hybrid Perovskites Quantum Wells. *Nat. Chem.* **2019**, *11*, 1151−1157.

(21) Li, X.; Yang, J.; Song, Z.; Chen, R.; Ma, L.; Li, H.; Jia, J.; Meng, J.; Li, X.; Yi, M.; Sun, X. Naphthalene Diimide Ammonium Directed Single-Crystalline Perovskites with 'Atypical' Ambipolar Charge Transport Signatures in Two-Dimensional Limit. *ACS Appl. Energy Mater.* **2018**, *1*, 4467−4472.

(22) Vickers, E. T.; Graham, T. A.; Chowdhury, A. H.; Bahrami, B.; Dreskin, B. W.; Lindley, S.; Naghadeh, S. B.; Qiao, Q.; Zhang, J. Z. Improving Charge Carrier Delocalization in Perovskite Quantum Dots by Surface Passivation with Conductive Aromatic Ligands. *ACS Energy Lett.* **2018**, *3*, 2931−2939.

(23) Oswald, I. W. H.; Mozur, E. M.; Moseley, I. P.; Ahn, H.; Neilson, J. R. Hybrid Charge-Transfer Semiconductors: $(C_7H_7)SbI_4$, $(C_7H_7)BiI_4$, and Their Halide Congeners. *Inorg. Chem.* **2019**, *58*, 5818−5826.

(24) Pious, J. K.; Muthu, C.; Dani, S.; Saeki, A.; Nair, V. C. Bismuth-Based Zero-Dimensional Perovskite-like Materials: Effect of Benzylammonium on Dielectric Confinement and Photoconductivity. *Chem. Mater.* **2020**, *32*, 2647−2652.

(25) Zhu, G.; Zhang, Y.; Hu, Y.; Zhao, X.; Yuan, Z.; Chen, Y. Conjugated Polymers Based on 1, 8-Naphthalene Monoimide with High Electron Mobility. *J. Polym. Sci., Part A: Polym. Chem.* **2018**, *56*, 276−281.

(26) Liu, Z.; Zhang, G.; Cai, Z.; Chen, X.; Luo, H.; Li, Y.; Wang, J.; Zhang, D. New Organic Semiconductors with Imide/Amide-Containing Molecular Systems. *Adv. Mater.* **2014**, *26*, 6965−6977.

(27) Gong, X.; Voznyy, O.; Jain, A.; Liu, W.; Sabatini, R.; Piontkowski, Z.; Walters, G.; Bappi, G.; Nokhrin, S.; Bushuyev, O.; Yuan, M.; Comin, R.; McCamant, D.; Kelley, S. O.; Sargent, E. H. Electron-Phonon Interaction in Efficient Perovskite Blue Emitters. *Nat. Mater.* **2018**, *17*, 550−556.

(28) McCall, K. M.; Stoumpos, C. C.; Kostina, S. S.; Kanatzidis, M. G.; Wessels, B. W. Strong Electron-Phonon Coupling and Self-Trapped Excitons in the Defect Halide Perovskites $A_3M_2I_9$ (A = Cs, Rb; M = Bi, Sb). *Chem. Mater.* **2017**, *29*, 4129−4145.

(29) Kawai, T.; Ishii, A.; Kitamura, T.; Shimanuki, S.; Iwata, M.; Ishibashi, Y. Optical Absorption in Band-Edge Region of $(CH_3NH_3)_3Bi_2I_9$ Single Crystals. *J. Phys. Soc. Jpn.* **1996**, *65*, 1464−1468.

(30) Abulikemu, M.; Ould-Chikh, S.; Miao, X.; Alarousu, E.; Murali, B.; Ngongang, N. G. O.; Barbé, J.; El Labban, A.; Amassian, A.; Del Gobbo, S. Optoelectronic and Photovoltaic Properties of the Air-Stable Organohalide Semiconductor $(CH_3NH_3)_3Bi_2I_9$. *J. Mater. Chem. A* **2016**, *4*, 12504−12515.

(31) Ran, C.; Wu, Z.; Xi, J.; Yuan, F.; Dong, H.; Lei, T.; He, X.; Hou, X. Construction of Compact Methylammonium Bismuth Iodide Film Promoting Lead-Free Inverted Planar Heterojunction Organohalide Solar Cells with Open-Circuit Voltage over 0.8 V. *J. Phys. Chem. Lett.* **2017**, *8*, 394−400.

(32) Macrae, C. F.; Edgington, P. R.; Mccabe, P.; Pidcock, E.; Shields, G. P.; Taylor, R.; Towler, M.; Van De Streek, J. Mercury: Visualization and Analysis of Crystal Structures. *J. Appl. Crystallogr.* **2006**, *39*, 453−457.

(33) Oga, H.; Saeki, A.; Ogomi, Y.; Hayase, S.; Seki, S. Improved Understanding of the Electronic and Energetic Landscapes of Perovskite Solar Cells: High Local Charge Carrier Mobility, Reduced Re-combination, and Extremely Shallow Traps. *J. Am. Chem. Soc.* **2014**, *136*, 13818−13825.

(34) Ghosh, T.; Gopal, A.; Nagasawa, S.; Mohan, N.; Saeki, A.; Nair, V. C. Following the TRMC Trail: Optimization of Photovoltaic Efficiency and Structure-Property Correlation of Thiophene Oligomers. *ACS Appl. Mater. Interfaces* **2016**, *8*, 25396−25404.

(35) Marchal, N.; Van Gompel, W.; Gélvez-Rueda, M. C.; Vandewal, K.; Van Hecke, K.; Boyen, H.; Conings, B.; Herckens, R.; Maheshwari, S.; Lutsen, L.; Quarti, C.; Grozema, F. C.; Vanderzande, D.; Beljonne, D. Lead-Halide Perovskites Meet Donor-Acceptor Charge-Transfer Complexes. *Chem. Mater.* **2019**, *31*, 6880−6888.

(36) Savenije, T. J.; Guo, D.; Caselli, V. M.; Hutter, E. M. Quantifying Charge-Carrier Mobilities and Recombination Rates in Metal Halide Perovskites from Time-Resolved Microwave Photoconductivity Measurements. *Adv. Energy Mater.* **2020**, *10*, 1903788.

(37) Bi, Y.; Hutter, E. M.; Fang, Y.; Dong, Q.; Huang, J.; Savenije, T. J. Charge Carrier Lifetimes Exceeding 15 Microseconds in Methylammonium Lead Iodide Single Crystals. *J. Phys. Chem. Lett.* **2016**, *7*, 923−928.

(38) Slavney, A. H.; Leppert, L.; Bartesaghi, D.; Gold-Parker, A.; Toney, M. F.; Savenije, T. J.; Neaton, J. B.; Karunadasa, H. I. Defect-Induced Band-Edge Reconstruction of a Bismuth-Halide Double Perovskite for Visible-Light Absorption. *J. Am. Chem. Soc.* **2017**, *139*, 5015−5018.

(39) Li, M.-Q.; Hu, Y.-Q.; Bi, L.-Y.; Zhang, H.-L.; Wang, Y.; Zheng, Y.-Z. Structure Tunable Organic-Inorganic Bismuth Halides for an Enhanced Two-Dimensional Lead-Free Light-Harvesting Material. *Chem. Mater.* **2017**, *29*, 5463−5467.

(40) Tao, K.; Li, Y.; Ji, C.; Liu, X.; Wu, Z.; Han, S.; Sun, Z.; Luo, J. A Lead-Free Hybrid Iodide with Quantitative Response to X-ray Radiation. *Chem. Mater.* **2019**, *31*, 5927−5932.

(41) Zhang, W.; Tao, K.; Ji, C.; Sun, Z.; Han, S.; Zhang, J.; Wu, Z.; Luo, J. $(C_6H_{13}N)_2BiI_5$: A One-Dimensional Lead-Free Perovskite-Derivative Photoconductive Light Absorber. *Inorg. Chem.* **2018**, *57*, 4239−4243.

(42) Yao, L.; Niu, G.; Yin, L.; Du, X.; Lin, Y.; Den, X.; Zhang, J.; Tang, J. Bismuth Halide Perovskite Derivatives for Direct X-ray Detection. *J. Mater. Chem. C* **2020**, *8*, 1239−1243.

(43) Liu, C.; Huhn, W.; Du, K.-Z.; Mayagoitia, A. V.; Dirkes, D.; You, W.; Kanai, Y.; Mitzi, D. B.; Blum, V. Tunable Semiconductors: Control over Carrier States and Excitations in Layered Hybrid Organic-Inorganic Perovskites. *Phys. Rev. Lett.* **2018**, *121*, 146401.

Letter

Self-Assembled Organic Cations-Assisted Band-Edge Tailoring in Bismuth-Based Perovskites for Enhanced Visible Light Absorption and Photoconductivity

Johnpaul K. Pious, Manasa G. Basavarajappa, Chinnadurai Muthu, Ryosuke Nishikubo, Akinori Saeki, Sudip Chakraborty,* Atsuro Takai, Masayuki Takeuchi, and Chakkooth Vijayakumar*

Read Online

ACCESS | Metrics & More | Article Recommendations | SI Supporting Information

ABSTRACT: Bismuth-based zero-dimensional perovskites garner high research interest because of their advantages, such as excellent moisture stability and lower toxicity in comparison to lead-based congeners. However, the wide optical bandgap (>2 eV) and poor photoconductivity of these materials are the bottlenecks for their optoelectronic applications. Herein, we report a combined experimental and theoretical study of the structural features and optoelectronic properties of two novel and stable zero-dimensional bismuth perovskites: (biphenyl bis(methylammonium))$_{1.5}$BiI$_6$·2H$_2$O (BPBI) and (naphthalene diimide bis-(ethylammonium))$_{1.5}$BiI$_6$·2H$_2$O (NDBI). NDBI features a remarkably narrower bandgap (1.82 eV) than BPBI (2.06 eV) because of the significant orbital contribution of self-assembled naphthalene diimide cations at the band edges of NDBI. Further, the FP-TRMC analysis revealed that the photoconductivity of NDBI is about 3.7-fold greater than that of BPBI. DFT calculations showed that the enhanced photoconductivity in NDBI arises from its type-IIa band alignment, whereas type-Ib alignment was seen in BPBI.
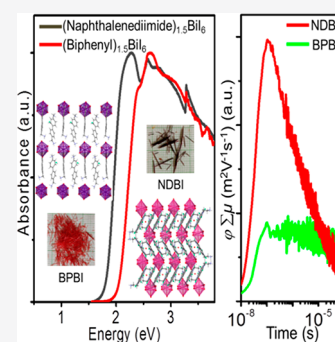
L ead-free halide perovskites are gaining significant research attention because of their excellent moisture stability and less toxicity in comparison to lead-based analogues.[1−5] Many lead-free perovskites based on metal ions such as Sn^{2+}, Cu$^+$, In^{3+}, Mn^{2+}, and Bi^{3+} have already been synthesized and employed for various optoelectronic applications.[6−10] Among them, Sn-based materials are generally unstable in the presence of moisture and undergo facile oxidation from Sn^{2+} to Sn^{4+} state because of their high-energy 5s electrons.[11,12] Most of the perovskites based on Cu$^+$, In^{3+}, and Mn^{2+} have a wide optical bandgap and are not ideal for most optoelectronic applications.[9,13−16] In 2015, a new class of halide perovskites based on bismuth with a general formula A$_3$Bi$_2$I$_9$ (A = methylammonium, formamidinium, cesium) emerged.[17] During the past few years, a large number of novel materials were added to this class because of the propensity of bismuth-halide octahedrons to form polyanions of various connectivity and dimensionality.[18−21] Nevertheless, the device performance of these materials was inferior when compared to the lead-based perovskites, which is attributed to a wide optical bandgap (>2 eV) and high exciton binding energy (~300 meV), resulting in poor visible light absorption and inefficient exciton dissociation into free charge carriers, respectively.[22−24]

To improve the visible light absorption in bismuth-based perovskites, Karunadasa et al. introduced a new material design strategy in which Bi^{3+} ions were partially substituted with monovalent Ag$^+$ ions to form a double perovskite, Cs$_2$AgBiBr$_6$. This material has a 3D crystal structure and exhibited a long

carrier lifetime and an appreciable optical bandgap (1.95 eV).[25] The optical bandgap of this material was further reduced to 1.30 eV by alloying it with Tl$^+$ ions. The 6s^2 and 6p^0 orbitals of Tl introduced hybridized energy levels at the band edges, resulting in lowering the bandgap.[26] Murugan et al. reconstructed the band structure of (CH$_3$NH$_3$)$_3$Bi$_2$I$_9$ by in situ doping of sulfur from the Bi(ethyl xanthate)$_3$ precursor, narrowing its bandgap from 2.04 to 1.45 eV.[27] Triiodide-induced band structure reconstruction reported by Luo et al. is another efficient method to improve the visible light absorption of bismuth perovskites.[28] The optical bandgap of (4-methylpiperidinium)$_3$Bi$_2$I$_9$ (2.02 eV) and (bis(2-dimethylaminoethyl)ether)Bi$_2$I$_8$ (1.91 eV) was reduced to 1.58 and 1.59 eV, respectively, by incorporating triiodide into the crystal structures. Neilson's group successfully demonstrated the bandgap tuning of (tropylium)BiX$_4$ (X = Cl$^-$, Br$^-$, I$^-$) by halide substitution.[29] While increasing the size of halide ions, the Bi-halide bond length got elongated, and the stereochemical activity of the Bi^{3+} lone pair was reduced, which subsequently leads to the narrowing of the bandgap.
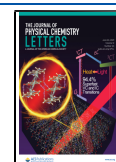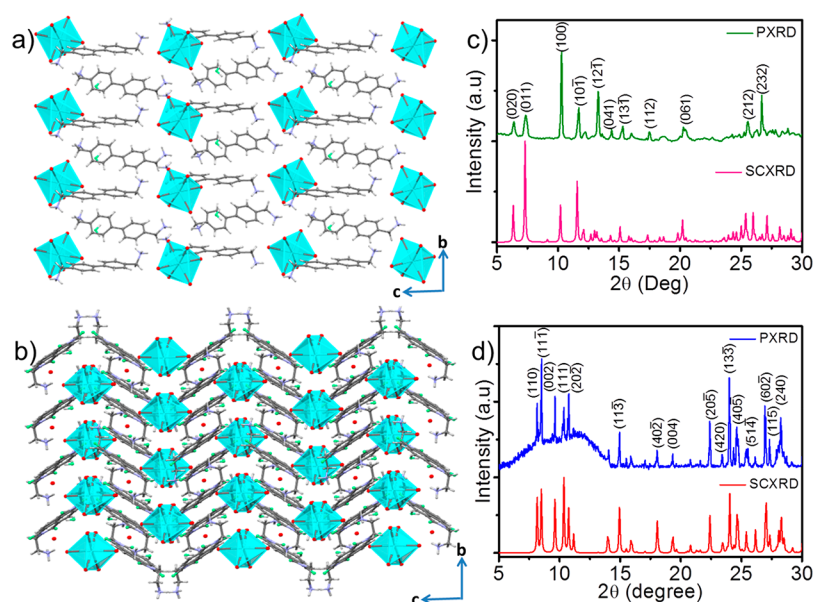
Figure 1. Crystal packing along the "*b*" and "*c*" crystallographic axes of (a) BPBI and (b) NDBI single crystals. Comparison of the powder and single-crystal X-ray diffraction patterns of (c) BPBI and (d) NDBI. All the intense powder X-ray diffraction peaks were indexed using Mercury software.

Though several successful attempts were made to reduce the bandgap and improve the visible-light-harvesting property of low dimensional bismuth halide perovskites, only a few attempts were made to enhance their photoconductivity. We have addressed this issue in $(CH_3NH_3)_3Bi_2I_9$ by replacing the aliphatic methylammonium cations with aromatic benzylammonium cations, resulting in low exciton binding energy and high photoconductivity.[30] The improved photophysical properties of (benzylammonium)$_3$Bi$_2$I$_9$ were due to the reduced dielectric confinement in the material induced by the polarizable benzylammonium cations. Another strategy we employed to improve the photoconductivity in bismuth perovskites was creating a type-II heterojunction at the organic−inorganic interface.[31] This was achieved by interdigitating semiconducting naphthalimide spacer cations between the inorganic frameworks. The time-resolved microwave conductivity (TRMC) analysis revealed that the carrier lifetime of the material was 18 μs, which is higher than that of state-of-the-art lead halide perovskite material $(CH_3NH_3)PbI_3$. Although several bismuth halide perovskites with improved properties have been reported, simultaneous enhancement of visible light absorption and photoconductivity was not observed in most cases. The trade-off between optical bandgap and photoconductivity in perovskites is due to the dependence of their photophysical properties on numerous factors such as metal−halide bond length, octahedral distortions, bond angle variance, quantum confinement, dielectric confinement, and band structure.[32−35] Hence, it is imperative to design and synthesize perovskite materials with engineered organic spacer cations to understand and optimize their optoelectronic properties.

Herein, we combined experimental techniques and density functional theory (DFT) calculations to analyze the structural, optical, and electronic properties of two novel bismuth halide perovskites: (biphenyl bis(methylammonium))$_{1.5}$BiI$_6$·2H$_2$O (BPBI) and (naphthalene diimide bis-(ethylammonium))$_{1.5}$BiI$_6$·2H$_2$O (NDBI). The title compounds were prepared by the slow cooling-induced crystal-

lization method from the respective precursor solutions in 57% aq HI. Room-temperature single-crystal X-ray diffraction (SCXRD) analysis revealed the zero-dimensional (0D) crystal structures of BPBI and NDBI (Figure 1a,b). The former belongs to the $P2_1/c$ space group, whereas the latter belongs to the $C2/c$ space group. BPBI and NDBI consist of isolated BiI_6^{3-} octahedral units surrounded by biphenyl bis-(methylammonium) and naphthalene diimide bis-(ethylammonium) cations, respectively. It may be noted that only a few Bi−I perovskites with completely isolated octahedral units were reported to date to the best of our knowledge.[18,36] Most of the bismuth perovskite structures exist as dimers or 1D chains ($Bi_2I_9^{3-}$, BiI_4^-, and BiI_5^{2-}) with face, edge, and corner-sharing connectivity of octahedrons.[17,28−31] They do not fall under the classical "perovskite structure" classification and are called perovskite-like or perovskitoid materials.[37] The formation of completely isolated inorganic octahedrons (BiI_6^{3-}) in the materials under study could be attributed to the large geometrical strain imposed by the bulkier biphenyl and naphthalimide cations. Biphenyl cations in BPBI exhibited strong hydrogen-bonding interactions with the iodine atoms of BiI_6^{3-} octahedral units (Figure S1a). However, they are arranged in a disordered manner because of the lack of $\pi−\pi$ stacking interaction between the adjacent biphenyl moieties. In NDBI, the hydrogen-bonding between naphthalene diimide and inorganic units was observed in the form of HCH···I and H$_2$NH···I interactions (Figure S1b). Moreover, the naphthalimide cations are self-assembled in a tilted-T fashion or otherwise called the herringbone arrangement (Figure S2a).[38] The stacking of naphthalimide cations resembles the "picket fence" arrangement of terphenyl moiety in poly(3-"fenced"-thiophene) (Figure S2b).[39] Powder XRD patterns of both materials are in good agreement with the respective SCXRD patterns suggesting the phase purity of the synthesized perovskite single crystals (Figure 1c,d). The X-ray photoelectron spectroscopic (XPS) analysis of the title compounds exhibited a similar pattern, with two prominent peaks at 158 and 163 eV ascribed to the binding energies of

Bi^{3+} $4f_{7/2}$ and Bi^{3+} $4f_{5/2}$ states, respectively (Figure S3).[40] The absence of signals corresponding to the metallic bismuth (Bi^0) in the XPS spectra further confirms the phase purity of the samples. The thermal stability of the materials was evaluated using thermogravimetry analysis (TGA). The initial 5% weight loss for BPBI and NDBI was observed at 273 and 291 °C, respectively (Figure S4). The higher thermal stability of NDBI could be attributed to the rigidity and strong intermolecular interactions of the interdigitated naphthalimide cations.

The isostructural feature of the inorganic moieties (BiI_6^{3-}) in these two perovskites enabled us to precisely investigate the role of organic cations in their optical and electronic properties. Both BPBI and NDBI featured broad visible light absorption across 400−600 and 400−680 nm, respectively (Figure 2a). The steep absorption onset and sharp excitonic
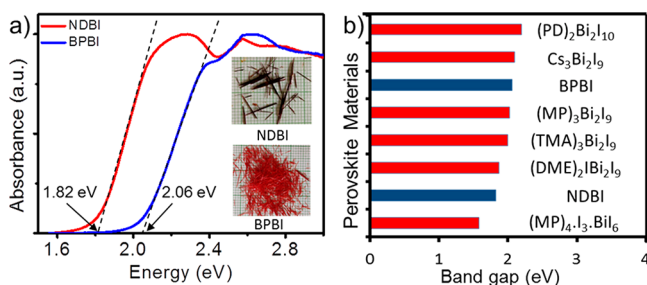

Figure 2. (a) Absorption spectra of BPBI and NDBI powder samples derived from diffuse reflectance spectra using the Kubelka−Munk function. The optical bandgap was calculated by extrapolating the steep absorption feature of both materials. Insets show photographs of millimeter-sized single crystals of the materials. (b) Plot showing the comparison of the optical bandgaps of various 0D bismuth halide perovskites, including BPBI and NDBI of this study. The abbreviations are PD, 1,3-propane diammonium; MP, 4-methylpiperidinium; TMA, trimethylammonium; and DME, bis(2-dimethylaminoethyl)ether.[17,28,41−43]

features in the optical absorption spectrum indicate the direct bandgap nature of these materials.[18,24] The optical bandgap of BPBI ($E_{g,BPBI}$) and NDBI ($E_{g,NDBI}$) were estimated from the absorption onset as 2.06 and 1.82 eV, respectively. The significant difference in the optical bandgaps was reflected in the color of their crystals: red for BPBI and blackish red for NDBI (inset of Figure 2a). The optical bandgap of these materials compared with that of the 0D bismuth halide perovskites reported in the literature is shown in Figure 2b. The lower bandgap of NDBI than most reported materials implies its capability for efficient visible light absorption and potential for photovoltaic and photodetector device applications.

Recent reports suggest that metal−halide bond length and distortion of inorganic octahedrons are highly influential in tuning the optical bandgap of perovskites. If the average Bi−I bond length is shorter, the BiI_6^{3-} octahedron will experience a less negative chemical pressure and subsequently leads to a narrow bandgap.[32] The average Bi−I bond length in BPBI and NDBI is 3.075 and 3.081 Å, respectively (Figure S5). Because the mean Bi−I bond length difference is marginal, it could not be correlated to the observed optical bandgap variation in these materials. Another parameter influencing the optical bandgap is the octahedral distortion (Δd), which is calculated using the equation $\Delta d = \left(\frac{1}{6}\right)\sum (d_i - d)^2/d^2$ (where d_i denotes the six individual Bi−I bond lengths and d is the

average of them). The tilting of inorganic octahedrons leads to poor metal and halide orbital mixing, which will decrease the bandwidth and results in the widening of the optical bandgap.[33] The Δd values for BPBI and NDBI were calculated as 2.94×10^{-4} and 6.35×10^{-4}, respectively. The calculated Δd values contradict the observed difference in the optical bandgaps of BPBI ($E_{g,BPBI}$ = 2.06 eV) and NDBI ($E_{g,NDBI}$ = 1.82 eV) materials. Therefore, it is likely that the optical bandgap variation in both the materials arises from reasons other than the slight differences in their inorganic BiI_6^{3-} anion frameworks. Electronic effects such as quantum and dielectric confinements also could modulate the optical bandgap of halide perovskites. The quantum confinement effect varies with structural dimensionality or inorganic layer thickness. Because BPBI and NDBI have identical structural dimensionality (i.e., 0D), their quantum confinement effect on optical properties is expected to be similar. Another electronic property called dielectric confinement arises from the mismatch in the dielectric constants of inorganic units and the surrounding organic cations. Because both perovskites are composed of aromatic π-conjugated spacer cations, the dielectric environment provided by the organic medium would be comparable.

By ruling out these electronic possibilities, we hypothesized that the observed substantial red-shift (~80 nm) in the absorption spectrum (and hence a better coverage of the visible region) of NDBI compared to that of BPBI might originate from the differences in the organic molecular orbital contribution to the overall band structure of these materials. It is well-established that the coupling of electronic excitations with the vibrational modes of the organic cations in hybrid perovskites could be monitored using Raman spectroscopy.[44] This analysis could reveal the involvement of organic spacer cations in the electronic transitions of BPBI and NDBI. Single crystals of the respective materials were used for this study. A 633 nm laser, which is very close to the optical band-to-band electronic transition energy of the materials, was used as the excitation source. At this near band edge excitation, both materials showed intense Raman signals between 50 and 200 cm^{-1} corresponding to the Bi−I bond vibrations (Figure 3).[30,31,41] The low energies of inorganic vibrational modes are due to their high reduced mass. Interestingly, the vibrational signatures of naphthalimide cations in the range of 500−1800 cm^{-1} were observed in the Raman spectrum of NDBI. This observation implies that the molecular orbitals of both naphthalimide and bismuth-iodide moieties are involved in the absorption of NDBI. On the other hand, signatures of
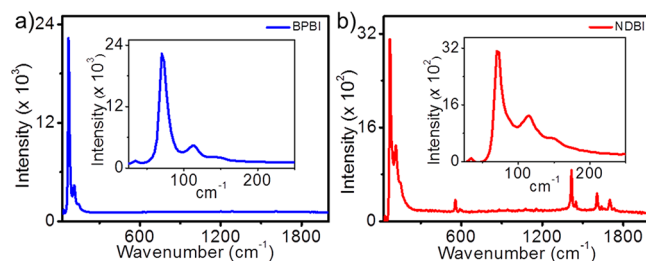
Figure 3. Raman spectra of the single crystals of (a) BPBI and (b) NDBI. The crystals were excited with a 633 nm laser source. Insets show the zoomed low-energy vibrational modes originating from the inorganic octahedrons. The intense Raman peaks at 70 and 113 cm^{-1} for both the materials are attributed to the Bi−I bond bending and stretching vibrational modes, respectively.
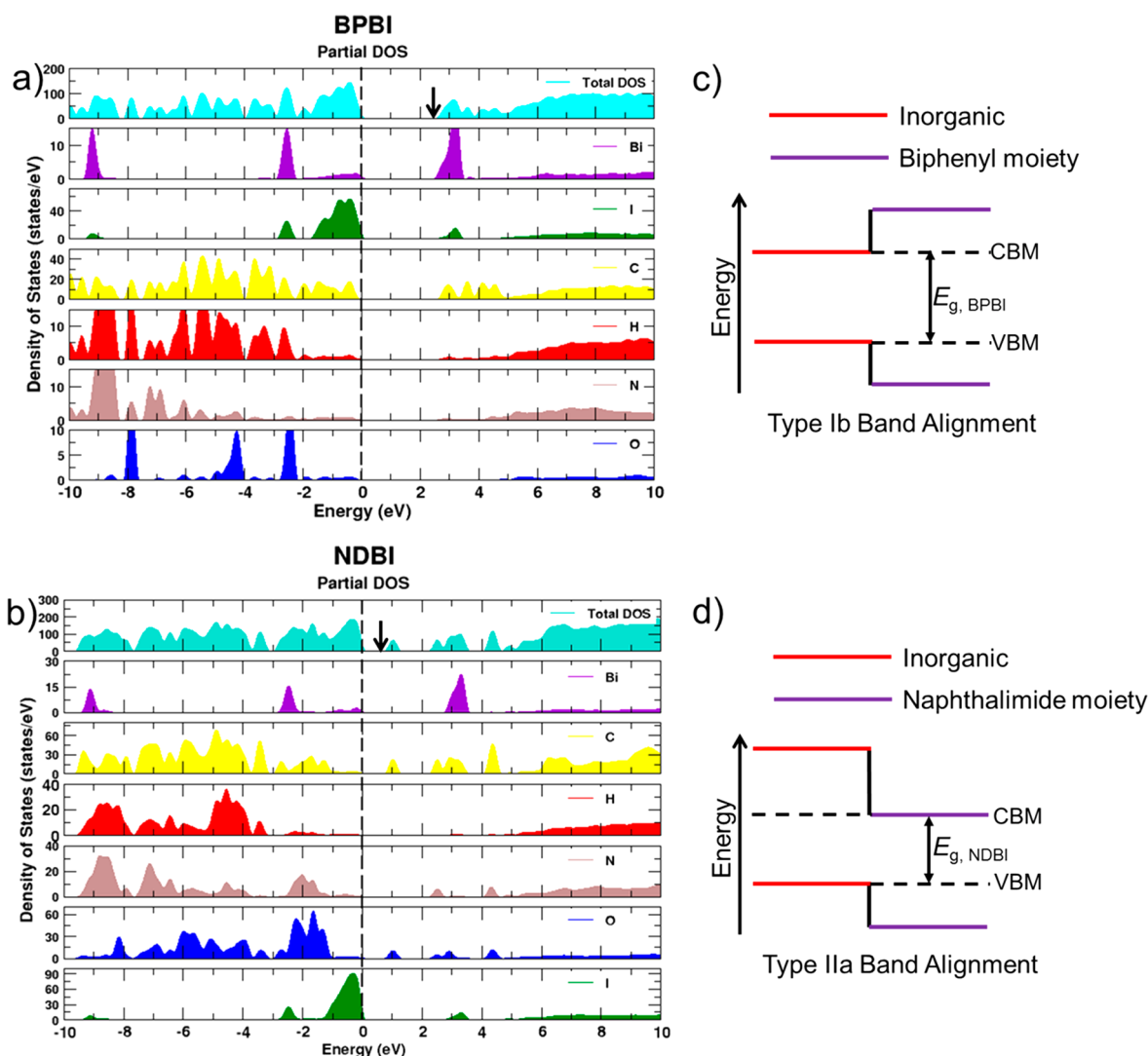
Figure 4. Computed partial density of states for (a) BPBI and (b) NDBI. The upper panels in both figures show the total density of states of the respective materials. The dotted line indicates the Fermi energy level or valence band maximum. The conduction band minimum is indicated with an arrow in the total density of states plot. Simplified schematic representations of (c) type-Ib and (d) type-IIa band alignments.

biphenyl cations were not visible in the Raman spectrum of BPBI, indicating the absence of contribution from the organic cations in the overall electronic properties of BPBI.

Density functional theory (DFT) calculations were performed to understand the influence of organic spacer cations on the electronic bandgap of BPBI and NDBI. The electronic bandgap values calculated from the total density of states plots (Figure 4a,b) for BPBI and NDBI were 2.6 eV ($E_{g,BPBI}$) and 0.8 eV ($E_{g,NDBI}$), respectively. The computed optical absorption spectra of these materials exhibited absorption onset identical to their calculated electronic bandgaps (Figure S6). Moreover, the electronic bandgaps estimated from the DFT calculations showed a trend similar to that of experimentally observed optical bandgaps with $E_{g,BPBI} >$ $E_{g,NDBI}$. The observed difference in the experimental and theoretical bandgap is due to the limitation of the generalized gradient approximation (GGA)-based exchange−correlation functional used in DFT calculations, which could not effectively correct the self-interaction errors.[45] Most importantly, the partial density of states analyses revealed a type-Ib band alignment for BPBI and type-IIa band alignment for NDBI.[46] In type-Ib band alignment, both valence band

maximum (VBM) and conduction band minimum (CBM) density of states is composed of inorganic atomic orbitals (Figure 4c). In contrast, for type-IIa band alignment, VBM and CBM energy levels are contributed by inorganic and organic atomic orbitals, respectively (Figure 4d). In other words, the band edge states are exclusively constructed of inorganic orbitals in BPBI, and the biphenyl atomic orbitals have contributions only above the bandgap. This implies that the lower-energy electron−hole pairs will reside in the highly confined BiI_6^{3-} clusters. In contrast, for NDBI, the VBM energy levels are derived from the inorganic framework, and the CBM states have a major contribution from naphthalimide molecular orbitals. Given these observations, it could be concluded that the observed narrow bandgap for NDBI compared to BPBI is due to the additional contribution from naphthalimide cations to the density of states at the band edges of the former. Notably, the type-IIa band alignment in NDBI will enable a facile dissociation of excitons into free charge carriers at the organic−inorganic interface due to the presence of lower-energy electron acceptor levels.

The photoconductivity of BPBI and NDBI single crystals was evaluated using flash-photolysis time-resolved microwave

conductivity (FP-TRMC) analysis. FP-TRMC is an electrodeless technique based on the interaction between the electric field component of high-frequency (GHz) microwave radiation and photoinduced mobile charge carriers. Hence, FP-TRMC analysis could avoid the interfacial effects and undesired chemical reactions between the semiconducting material and electrodes. To evaluate the potential of the materials for optoelectronic applications, we have measured the product of the mobility and charge separation efficiency ($\phi\Sigma\mu$) of BPBI and NDBI single crystals (Figure 5). The measurement was done along the long axis of the crystals because the intermolecular interaction is stronger in this direction.
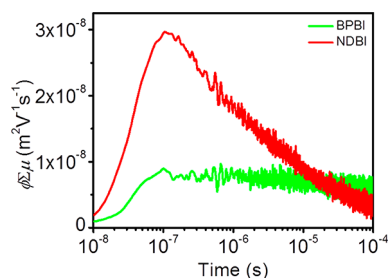
Figure 5. Product of charge carrier mobility (both electron and hole; $\Sigma\mu$) and dissociation yield of free charges (ϕ) as a function of time measured along the long crystal axis of BPBI and NDBI single crystals.

Both materials exhibited intense TRMC signals with a $\phi\Sigma\mu_{max}$ of 8×10^{-9} m^2/V s for BPBI and 2.95×10^{-8} m^2/V s for NDBI. The signal intensity was about one order higher when compared to that of most of the 0D bismuth halide perovskite materials reported in the literature, including $(CH_3NH_3)_3Bi_2I_9$ (3.3×10^{-9} m^2/V s).[30] The observed 3.7-fold higher TRMC signal for NDBI compared to that of BPBI stems from the type-IIa band alignment in the former. The energy level landscape at the interface of BiI_6^{3-} octahedron and naphthalimide moiety provides the driving force for the dissociation of excitons into free charge carriers. In contrast, the excitons generated in BPBI are strongly confined in the isolated BiI_6^{3-} octahedrons and subsequently resulted in a weak TRMC signal. There are several reports of using zero-dimensional bismuth halide perovskites as a light-absorbing layer in photovoltaic devices.[22,23,47] Our materials may also be suitable for such devices, particularly NDBI, which has a relatively low bandgap. Further, these materials may be employed as a top cell light absorber in tandem solar cells consisting of c-Si or CIGS as the bottom cells to improve the overall efficiencies. Moreover, similar materials are being reported as suitable for photodetector applications owing to their high photoconductivity, strong visible light absorption, good thermal stability, and low toxicity.[10,48,49]

In summary, we have designed and synthesized two novel bismuth halide zero-dimensional perovskite materials, BPBI and NDBI, consisting of isolated BiI_6^{3-} octahedrons templated by biphenyl and naphthalimide-based organic cations. We have precisely investigated the influence of the self-assembly of the organic cations within the perovskite structure in modulating the optical bandgap and electronic properties of the resultant materials. Raman spectroscopy analysis revealed the involvement of both organic and inorganic molecular orbitals in the electronic transitions of naphthalimide-containing perovskite. DFT calculations have confirmed that the orbital contribution from naphthalimide cations at the CBM states of NDBI is

responsible for its narrow optical bandgap compared to that of BPBI. Further, we found that naphthalimide cations form a type-IIa heterojunction with inorganic units (BiI_6^{3-}), whereas the biphenyl cations form type-Ib band alignment with inorganic clusters. NDBI exhibited a 3.7-fold higher photoconductivity signal than BPBI, which could be ascribed to the type-IIa band alignment in the former, which offered an energy level offset at the organic–inorganic interface that facilitated efficient exciton dissociation into free charge carriers. Our studies on the structure–property relationships of these materials open a new avenue of material design strategy to precisely control the optical bandgap and photoconductivity of zero-dimensional bismuth halide perovskites for optoelectronic applications.

■ ASSOCIATED CONTENT

ⓈⒾ Supporting Information

The Supporting Information is available free of charge at https://pubs.acs.org/doi/10.1021/acs.jpclett.1c01321.

Experimental and synthetic procedures, computational methodology, crystal packing and intermolecular interactions, XPS, and TGA (PDF)

■ AUTHOR INFORMATION

Corresponding Authors

Sudip Chakraborty — *Discipline of Physics, Indian Institute of Technology Indore, Indore 453 552, India; Materials Theory for Energy Scavenging (MATES) Lab, Harish-Chandra Research Institute (HRI) Allahabad, HBNI, Jhusi 211 019, India;* ⓞ orcid.org/0000-0002-6765-2084; Email: sudipchakraborty@hri.res.in, sudiphys@gmail.com

Chakkooth Vijayakumar — *Photosciences and Photonics Section, CSIR-National Institute for Interdisciplinary Science and Technology (NIIST), Thiruvananthapuram 695 019, India; Academy of Scientific and Innovative Research (AcSIR), Ghaziabad 201 002, India;* ⓞ orcid.org/0000-0001-5347-6799; Email: cvijayakumar@niist.res.in

Authors

Johnpaul K. Pious — *Photosciences and Photonics Section, CSIR-National Institute for Interdisciplinary Science and Technology (NIIST), Thiruvananthapuram 695 019, India; Academy of Scientific and Innovative Research (AcSIR), Ghaziabad 201 002, India*

Manasa G. Basavarajappa — *Discipline of Physics, Indian Institute of Technology Indore, Indore 453 552, India; Materials Theory for Energy Scavenging (MATES) Lab, Harish-Chandra Research Institute (HRI) Allahabad, HBNI, Jhusi 211 019, India*

Chinnadurai Muthu — *Photosciences and Photonics Section, CSIR-National Institute for Interdisciplinary Science and Technology (NIIST), Thiruvananthapuram 695 019, India; Academy of Scientific and Innovative Research (AcSIR), Ghaziabad 201 002, India*

Ryosuke Nishikubo — *Department of Applied Chemistry, Graduate School of Engineering, Osaka University, Suita, Osaka 565 0871, Japan*

Akinori Saeki — *Department of Applied Chemistry, Graduate School of Engineering, Osaka University, Suita, Osaka 565 0871, Japan;* ⓞ orcid.org/0000-0001-7429-2200

Atsuro Takai − *Molecular Design and Function Group, National Institute for Materials Science (NIMS), Tsukuba 305 0047, Japan;* ⊙ orcid.org/0000-0003-3457-3352

Masayuki Takeuchi − *Molecular Design and Function Group, National Institute for Materials Science (NIMS), Tsukuba 305 0047, Japan;* ⊙ orcid.org/0000-0002-0207-0665

Complete contact information is available at:
https://pubs.acs.org/10.1021/acs.jpclett.1c01321

Notes
The authors declare no competing financial interest.

■ REFERENCES

(1) Wu, C.; Zhang, Q.; Liu, G.; Zhang, Z.; Wang, D.; Qu, B.; Chen, Z.; Xiao, L. From Pb to Bi: A Promising Family of Pb-Free Optoelectronic Materials and Devices. *Adv. Energy Mater.* **2020**, *10*, 1902496.

(2) Attique, S.; Ali, N.; Ali, S.; Khatoon, R.; Li, N.; Khesro, A.; Rauf, S.; Yang, S.; Wu, H. A Potential Checkmate to Lead: Bismuth in Organometal Halide Perovskites, Structure, Properties, and Applications. *Adv. Sci.* **2020**, *7*, 1903143.

(3) Nie, R.; Sumukam, R. R.; Reddy, S. H.; Banavoth, M.; Seok, S. I. Lead-Free Perovskite Solar Cells Enabled by Hetero-Valent Substitutes. *Energy Environ. Sci.* **2020**, *13*, 2363−2385.

(4) Ushakova, E. V.; Cherevkov, S. A.; Kuznetsova, V. A.; Baranov, A. V. Lead-Free Perovskites for Lighting and Lasing Applications: A Minireview. *Materials* **2019**, *12*, 3845.

(5) Li, M.; Xia, Z. Recent Progress of Zero-Dimensional Luminescent Metal halides. *Chem. Soc. Rev.* **2021**, *50*, 2626−2662.

(6) Li, P.; Dong, H.; Xu, J.; Chen, J.; Jiao, B.; Hou, X.; Li, J.; Wu, Z. Ligand Orientation Induced Lattice Robustness for High Efficient and Stable Tin-Based Perovskite Solar Cells. *ACS Energy Lett.* **2020**, *5*, 2327−2334.

(7) Li, S.; Xu, J.; Li, Z.; Zeng, Z.; Li, W.; Cui, M.; Qin, C.; Du, Y. One-Dimensional Lead-free Halide with Near-unity Greenish-Yellow Light Emission. *Chem. Mater.* **2020**, *32*, 6525−6531.

(8) Chen, Da.; Hao, S.; Zhou, G.; Deng, C.; Liu, Q.; Ma, S.; Wolverton, C.; Zhao, J.; Xia, Z. Lead-Free Broadband Orange-Emitting Zero-Dimensional Hybrid (PMA)$_3$InBr$_6$ with Direct Band Gap. *Inorg. Chem.* **2019**, *58*, 15602−15609.

(9) Mao, L.; Guo, P.; Wang, S.; Cheetham, A. K.; Seshadri, R. Design Principles for Enhancing Photoluminescence Quantum Yield in Hybrid Manganese Bromides. *J. Am. Chem. Soc.* **2020**, *142*, 13582−13589.

(10) Hussain, A. A. Constructing Caesium Based Lead-Free Perovskite Photodetector Enabling Self-Powered Operation with Extended Spectral Response. *ACS Appl. Mater. Interfaces* **2020**, *12*, 46317−46329.

(11) Lin, R.; Xiao, K.; Qin, Z.; Han, Q.; Zhang, C.; Wei, M.; Saidaminov, M. I.; Gao, Y.; Xu, J.; Xiao, M.; Li, A.; Zhu, J.; Sargent, E. H.; Tan, H. Monolithic All-Perovskite Tandem Solar Cells with 24.8% Efficiency Exploiting Comproportionation to Suppress Sn(II) Oxidation in Precursor Ink. *Nature Energy* **2019**, *4*, 864−873.

(12) Saidaminov, M. I.; Spanopoulos, I.; Abed, J.; Ke, W.; Wicks, J.; Kanatzidis, M. G.; Sargent, E. H. Conventional Solvent Oxidizes Sn(II) in Perovskite Inks. *ACS Energy Lett.* **2020**, *5*, 1153−1155.

(13) Peng, H.; Guo, Y.; Zhi, R.; Wang, X.; Yao, S.; Ge, F.; Tian, Y.; Wang, J.; Zou, B. High Efficient Self-Trapped Exciton Emission of a (MA)$_4$Cu$_2$Br$_6$ Single Crystal. *J. Phys. Chem. Lett.* **2020**, *11*, 4703−4710.

(14) Lin, R.; Guo, Q.; Zhu, Q.; Zhu, Y.; Zheng, W.; Huang, F. All-Inorganic CsCu$_2$I$_3$ Single Crystal with High-PLQY (≈15.7%) Intrinsic White-Light Emission via Strongly Localized 1D Excitonic Recombination. *Adv. Mater.* **2019**, *31*, 1905079.

(15) Zhou, L.; Liao, J.-F.; Huang, Z.-G.; Wei, J.-H.; Wang, X.-D.; Chen, H.-Y.; Kuang, D.-B. Intrinsic Self-Trapped Emission in 0D Lead-Free (C$_4$H$_{14}$N$_2$)$_2$In$_2$Br$_{10}$ Single Crystal. *Angew. Chem., Int. Ed.* **2019**, *58*, 15435−15440.

(16) Zhou, L.; Liao, J.-F.; Huang, Z.-G.; Wei, J.-H.; Wang, X.-D.; Li, W.-G.; Chen, H.-Y.; Kuang, D.-B.; Su, C.-Y. Highly Red Emissive Lead-Free Indium-Based Perovskite Single Crystal for Sensitive Water Detection. *Angew. Chem., Int. Ed.* **2019**, *58*, 5277−5281.

(17) Park, B.-W.; Philippe, B.; Zhang, X.; Rensmo, H.; Boschloo, G.; Johansson, E. M. J. Bismuth Based Hybrid Perovskites A$_3$Bi$_2$I$_9$ (A: Methylammonium or Cesium) for Solar Cell Application. *Adv. Mater.* **2015**, *27*, 6806−6813.

(18) Yao, L.; Niu, G.; Yin, L.; Du, X.; Lin, Y.; Den, X.; Zhang, J.; Tang, J. Bismuth Halide Perovskite Derivatives for Direct X-ray Detection. *J. Mater. Chem. C* **2020**, *8*, 1239−1243.

(19) Ji, C.; Wang, P.; Wu, Z.; Sun, Z.; Li, L.; Zhang, J.; Hu, W.; Hong, M.; Luo, J. Inch-Size Single Crystal of a Lead-Free Organic−Inorganic Hybrid Perovskite for High-Performance Photodetector. *Adv. Funct. Mater.* **2018**, *28*, 1705467.

(20) Jana, M. K.; Janke, S. M.; Dirkes, D. J.; Dovletgeldi, S.; Liu, C.; Qin, X.; Gundogdu, K.; You, W.; Blum, V.; Mitzi, D. B. Direct-Bandgap 2D Silver-Bismuth Iodide Double Perovskite: The Structure-Directing Influence of an Oligothiophene Spacer Cation. *J. Am. Chem. Soc.* **2019**, *141*, 7955−7964.

(21) Ji, F.; Klarbring, J.; Wang, F.; Ning, W.; Wang, L.; Yin, C.; Figueroa, J. S. M.; Christensen, C. K.; Etter, M.; Ederth, T.; Sun, L.; Simak, S. I.; Abrikosov, I. A.; Gao, F. Lead-Free Halide Double Perovskite Cs$_2$AgBiBr$_6$ with Decreased Bandgap. *Angew. Chem., Int. Ed.* **2020**, *59*, 15191−15194.

(22) Zhang, Z.; Li, X.; Xia, X.; Wang, Z.; Huang, Z.; Lei, B.; Gao, Y. High-Quality (CH$_3$NH$_3$)$_3$Bi$_2$I$_9$ Film-Based Solar Cells: Pushing Efficiency up to 1.64%. *J. Phys. Chem. Lett.* **2017**, *8*, 4300−4307.

(23) Jain, S. M.; Phuyal, D.; Davies, M. L.; Li, M.; Philippe, B.; De Castro, C.; Qiu, Z.; Kim, J.; Watson, T.; Tsoi, W. C.; Karis, O.; Rensmo, H.; Boschloo, G.; Edvinsson, T.; Durrant, J. R. An Effective Approach of Vapour Assisted Morphological Tailoring for Reducing Metal Defect Sites in Lead-Free, (CH$_3$NH$_3$)$_3$Bi$_2$I$_9$ Bismuth-Based Perovskite Solar cells for Improved Performance and Long-Term Stability. *Nano Energy* **2018**, *49*, 614−624.

(24) Ni, C.; Hedley, G.; Payne, J.; Svrcek, V.; McDonald, C.; Jagadamma, L. K.; Edwards, P.; Martin, R.; Jain, G.; Carolan, D.; Mariotti, D.; Maguire, P.; Samuel, I.; Irvine, J. Charge Carrier Localised in Zero-Dimensional (CH$_3$NH$_3$)$_3$Bi$_2$I$_9$ Clusters. *Nat. Commun.* **2017**, *8*, 170.

(25) Slavney, A. H.; Hu, T.; Lindenberg, A. M.; Karunadasa, H. I. A Bismuth-Halide Double Perovskite with Long Carrier Recombination Lifetime for Photovoltaic Applications. *J. Am. Chem. Soc.* **2016**, *138*, 2138−2141.

(26) Slavney, A. H.; Leppert, L.; Bartesaghi, D.; Gold-Parker, A.; Toney, M. F.; Savenije, T. J.; Neaton, J. B.; Karunadasa, H. I. Defect-Induced Band-Edge Reconstruction of a Bismuth-Halide Double Perovskite for Visible-Light Absorption. *J. Am. Chem. Soc.* **2017**, *139*, 5015−5018.

(27) Vigneshwaran, M.; Ohta, T.; Iikubo, S.; Kapil, G.; Ripolles, T. S.; Ogomi, Y.; Ma, T.; Pandey, S. S.; Shen, Q.; Toyoda, T.; Yoshino, K.; Minemoto, T.; Hayase, S. Facile Synthesis and Characterization of Sulfur Doped Low Bandgap Bismuth Based Perovskites by Soluble Precursor Route. *Chem. Mater.* **2016**, *28*, 6436−6440.

(28) Zhang, W.; Liu, X.; Li, L.; Sun, Z.; Han, S.; Wu, Z.; Luo, J. Triiodide-Induced Band-Edge Reconstruction of a Lead-Free Perov-

skite-Derivative Hybrid for Strong Light Absorption. *Chem. Mater.* **2018**, *30*, 4081−4088.

(29) Oswald, I. W. H.; Mozur, E. M.; Moseley, I. P.; Ahn, H.; Neilson, J. R. Hybrid Charge-Transfer Semiconductors: $(C_7H_7)SbI_4$, $(C_7H_7)BiI_4$, and Their Halide Congeners. *Inorg. Chem.* **2019**, *58*, 5818−5826.

(30) Pious, J. K.; Muthu, C.; Dani, S.; Saeki, A.; Nair, V. C. Bismuth-Based Zero-Dimensional Perovskite-Like Materials: Effect of Benzylammonium on Dielectric Confinement and Photoconductivity. *Chem. Mater.* **2020**, *32*, 2647−2652.

(31) Pious, J. K.; Basavarajappa, M. G.; Muthu, C.; Krishna, N.; Nishikubo, R.; Saeki, A.; Chakraborty, S.; Nair, V. C. Anisotropic Photoconductivity and Long-Lived Charge Carriers in Bismuth-Based One-Dimensional Perovskite with Type-IIa Band Alignment. *J. Phys. Chem. Lett.* **2020**, *11*, 6757−6762.

(32) Li, X.; Fu, Y.; Pedesseau, L.; Guo, P.; Cuthriell, S.; Hadar, I.; Even, J.; Katan, C.; Stoumpos, C. C.; Schaller, R. D.; Harel, E.; Kanatzidis, M. G. Negative Pressure Engineering with Large Cage Cations in 2D Halide Perovskites Causes Lattice Softening. *J. Am. Chem. Soc.* **2020**, *142*, 11486−11496.

(33) Mao, L.; Guo, P.; Kepenekian, M.; Spanopoulos, I.; He, Y.; Katan, C.; Even, J.; Schaller, R. D.; Seshadri, R.; Stoumpos, C. C.; Kanatzidis, M. G. Organic Cation Alloying on Intralayer A and Interlayer A' sites in 2D Hybrid Dion-Jacobson Lead Bromide Perovskites (A')(A)Pb_2Br_7. *J. Am. Chem. Soc.* **2020**, *142*, 8342−8351.

(34) Cao, D. H.; Stoumpos, C. C.; Farha, O. K. J.; Hupp, T.; Kanatzidis, M. G. 2D Homologous Perovskites as Light-Absorbing Materials for Solar Cell Applications. *J. Am. Chem. Soc.* **2015**, *137*, 7843−7850.

(35) Cohen, B.-E.; Wierzbowska, M.; Etgar, L. High Efficiency Quasi 2D Lead Bromide Perovskite Solar Cells Using Various Barrier Molecules. *Sustainable Energy Fuels* **2017**, *1*, 1935−1943.

(36) Evans, H. A.; Labram, J. G.; Smock, S. R.; Wu, G.; Chabinyc, M. L.; Seshadri, R.; Wudl, F. Mono- and Mixed-Valence Tetrathiafulvalene Semiconductors $(TTF)BiI_4$ and $(TTF)_4BiI_6$ with 1D and 0D Bismuth-Iodide Networks. *Inorg. Chem.* **2017**, *56*, 395−401.

(37) Hoffman, J. M.; Che, X.; Sidhik, S.; Li, X.; Hadar, I.; Blancon, J.-C.; Yamaguchi, H.; Kepenekian, M.; Katan, C.; Even, J.; Stoumpos, C. C.; Mohite, A. D.; Kanatzidis, M. G. From 2D to 1D Electronic Dimensionality in Halide Perovskites with Stepped and Flat Layers Using Propylammonium as a Spacer. *J. Am. Chem. Soc.* **2019**, *141*, 10661−10676.

(38) Jana, M. K.; Liu, C.; Lidin, S.; Dirkes, D. J.; You, W.; Blum, V.; Mitzi, D. B. Resolving Rotational Stacking Disorder and Electronic Level Alignment in a 2D Oligothiophene-Based Lead Iodide Perovskite. *Chem. Mater.* **2019**, *31*, 8523−8532.

(39) Pan, C.; Sugiyasu, K.; Aimi, J.; Sato, A.; Takeuchi, M. Picket-Fence Polythiophene and its Diblock Copolymers that Afford Microphase Separations Comprising a Stacked and an Isolated Polythiophene Ensemble. *Angew. Chem., Int. Ed.* **2014**, *53*, 8870−8875.

(40) Li, T.; Hu, Y.; Morrison, C. A.; Wu, W.; Han, H.; Robertson, N. Lead-Free Pseudo-Three-Dimensional Organic-Inorganic Iodobismuthates for Photovoltaic Applications. *Sustainable Energy Fuels* **2017**, *1*, 308−316.

(41) Pious, J. K.; Katre, A.; Muthu, C.; Chakraborty, S.; Krishna, S.; Nair, V. C. Zero-Dimensional Lead-Free Hybrid Perovskite-like Material with a Quantum-Well Structure. *Chem. Mater.* **2019**, *31*, 1941−1945.

(42) Zhang, J.; Han, S.; Ji, C.; Zhang, W.; Wang, Y.; Tao, K.; Sun, Z.; Luo, J. $[(CH_3)_3NH]_3Bi_2I_9$: A Polar Lead-Free Hybrid Perovskite-Like Material as a Potential Semiconducting Absorber. *Chem. - Eur. J.* **2017**, *23*, 17304−17310.

(43) Kou, B.; Zhang, W.; Ji, C.; Wu, Z.; Zhang, S.; Liu, X.; Luo, J. Tunable Optical Absorption in Lead-Free Perovskite-Like Hybrids by Iodide Management. *Chem. Commun.* **2019**, *55*, 14174−14177.

(44) Gong, X.; Voznyy, O.; Jain, A.; Liu, W.; Sabatini, R.; Piontkowski, Z.; Walters, G.; Bappi, G.; Nokhrin, S.; Bushuyev, O.; Yuan, M.; Comin, R.; McCamant, D.; Kelley, S. O.; Sargent, E. H. Electron-Phonon Interaction in Efficient Perovskite Blue Emitters. *Nat. Mater.* **2018**, *17*, 550−556.

(45) Du, M.-H. Density Functional Calculations of Native Defects in $CH_3NH_3PbI_3$: Effects of Spin-Orbit Coupling and Self-Interaction Error. *J. Phys. Chem. Lett.* **2015**, *6*, 1461−1466.

(46) Liu, C.; Huhn, W.; Du, K.-Z.; Vazquez-Mayagoitia, A.; Dirkes, D.; You, W.; Kanai, Y.; Mitzi, D. B.; Blum, V. Tunable Semiconductors: Control Over Carrier States and Excitations in Layered Hybrid Organic-Inorganic Perovskites. *Phys. Rev. Lett.* **2018**, *121*, 146401.

(47) Jia, Q.; Li, C.; Tian, W.; Johansson, M. B.; Johansson, E. M. J.; Yang, R. Large-Grained All-Inorganic Bismuth-Based Perovskites with Narrow Band Gap via Lewis Acid−Base Adduct Approach. *ACS Appl. Mater. Interfaces* **2020**, *12*, 43876−43884.

(48) Hussain, A. A.; Rana, A. K.; Ranjan, M. Air-stable lead-free hybrid perovskite employing self-powered photodetection with an electron/hole-conductor-free device geometry. *Nanoscale* **2019**, *11*, 1217−1227.

(49) Li, W.-G.; Wang, X.-D.; Liao, J.-F.; Jiang, Y.; Kuang, D.-B. Enhanced On-Off Ratio Photodetectors Based on Lead-Free $Cs_3Bi_2I_9$ Single Crystal Thin Films. *Adv. Funct. Mater.* **2020**, *30*, 1909701.